MM

RESEARCH INTO AIR CUSHION STABILITY: 1979 REPORT

Prepared by

P. A. Sullivan, M. J. Hinchey, P. V. Hartmann, A. Dupuis,

G. M. Green, and T. A. Graham

Transport Canada / Transports Canada
Library and Information Centre /
Centre de Documentation GSLA
Ottawa, Canada K1A 0N5

for

Transportation Development Centre
Transport Canada
Montreal, Quebec

TP 3109 E

TDC File D-500-431-1

January, 1982

The contents of this report reflect the views of the Contractor and not necessarily the official views or policies of the Transportation Development Centre.

REPORT DOCUMENTATION FORM

1. Transport Canada Report No. TP 3109E	2. TDC Project No 7479	3. Recipient's Catalogue No

4. Title and Subtitle

RESEARCH INTO AIR CUSHION STABILITY, 1979 REPORT

5. Report Date

January 1982

6. Performing Organization Report No

7. Author(s)

P. A. Sullivan, M. J. Hinchey, P. V. Hartmann,
A. Dupuis, G. M. Green and T. A. Graham

8. Transport Canada File No

D1460-125-1

9. Performing Organization Name and Address

University of Toronto, Institute for Aerospace Studies
(UTIAS),
4925 Dufferin Street,
Downsview, Ontario, M3H 5T6

10. DSS File No

T8200-7-7513

11. DSS or Transport Canada Contract No

OSU-77-00208

12. Sponsoring Agency Name and Address

Transportation Development Centre (TDC),
1000 Sherbrooke St. West,
Suite 2421,
Montreal, Quebec, H3A 2R3

13. Type of Report and Period Covered

Yearly - 1979

14. Sponsoring Agency Code

7479

15. Supplementary Notes

See also: "Research into Air Cushion Stability, 1978 Report", Sullivan et al, TP 1760, January 1981

16. TDC Project Officer

J. E. Laframboise

17. Abstract This is the second of two reports describing research on selected topics in air cushion vehicle (ACV) dynamics undertaken from July 1977 to April 1980. The work had three objectives: (i) investigation of the dynamical properties of an uncompartmented segmented skirt cushion, (ii) development of methods for the prediction of the onset of self-excited oscillations, and (iii) investigation of structural stability characteristics of flexible skirts. This report describes results of an experiment designed to verify the very large duct effects on the dynamic stability of air cushions predicted in the first report (TP 1760). The main feature of the experiment is the use of a very large volume between the fan and the cushion to completely uncouple the dynamics of the air cushion from that of the air supply system. The validity of the various assumptions used in stability calculations is reviewed. A theory for the static pitch and roll stiffness characteristics of the uncompartmented segmented skirt cushion is developed, and the predictions are compared with experimental results obtained on a 2.44m x 1.22m model. Excellent agreement is obtained for segments made from a urethane-coated nylon fabric material, whereas with segments made from extruded polyethylene film, the stiffness characteristics display a large hysteresis. System parameter identification techniques are applied to the interpretation of the pitch-heave dynamics of the UTIAS circular track test vehicle, Vampire 1, equipped with the uncompartmented segmented skirt cushion. It is concluded that hysteresis of the type observed in the static experiments has a major effect on the dynamics. Development of a finite element computer programme for the analysis of partly wrinkled membrane structures is described. Results of a preliminary theoretical investigation on the heave stability of air cushions hovering over water are also presented.

18. Key Words Air cushion stability, flexible skirted air cushion, hovercraft dynamics, pneumatic stability.	19. Distribution Statement Limited number of copies available at TDC.

20. Security Classification (of this report) None	21. Security Classification (of this page) None	22. No. of Pages 275 app.	23. Price -

TDC CDT 79-005

FORMULE DE DOCUMENTATION POUR RAPPORT

1 Nº du rapport Transports Canada
TP 3109E

2. Nº de l'étude — CDT
7479

3 Nº de catalogue du destinataire

4 Titre et sous-titre
RESEARCH INTO AIR CUSHION STABILITY, 1979 REPORT

5 Date du rapport
janvier 1982

6 Nº du rapport de l'organisme exécutant

7 Auteur(s)
P. A. Sullivan, M. J. Hinchey, P. V. Hartmann,
A Dupuis, G. M. Green and T. A. Graham

8 Nº de dossier Transports Canada
D1460-125-1

9 Nom et adresse de l'organisme exécutant
University of Toronto, Institute for Aerospace Studies
(UTIAS),
4925 Dufferin Street,
Downsview, Ontario, Canada, M3H 5T6

10 Nº de dossier — ASC
T8200-7-7513

11. Nº de contrat — ASC ou Transports Canada
OSU-77-00208

12 Nom et adresse de l'organisme parrain
Centre de développement des transports (Cdt),
1000 rue Sherbrooke, ouest,
Suite 2421,
Montréal, Québec, H3A 2R3

13. Genre de rapport et période visée
Annuel - 1979

14. Code de l'organisme parrain
7479

15 Remarques additionnelles
Voir aussi: "Research into Air Cushion Stability, 1978 Report", Sullivan et al, TP 1760, janvier 1981.

16 Agent de projet — CDT
J. E. Laframboise

17 Résumé

Ce rapport constitue la seconde partie du programme de recherche sur la dynamique des aéroglisseurs effectuée de juillet 1977 à avril 1980. Le programme comprend trois objectifs: (i) investigation des propriétés dynamiques d'une jupe à segments non compartimentée, (ii) développement de méthodes pour la prédiction d'oscillations auto-générées, (iii) investigation des paramètres affectant la stabilité structurale des jupes flexibles. Les résultats expérimentaux pour vérifier l'effet des conduites d'alimentation sur la stabilité dynamique des coussins d'air sont également inclus. L'expérience consiste principalement en l'utilisation d'un très grand volume entre le ventilateur et le coussin afin de découpler les parties dynamiques du coussin d'air de celles du système d'alimentation. La justification des différentes hypothèses utilisées dans les calculs de stabilité est aussi examinée. Une théorie est developpée pour la stabilité en tangage et en roulis et les valeurs prédites sont comparées avec les résultats expérimentaux obtenus sur un modèle réduit de 2.44m x 1.22m. Une excellente corrélation est obtenue pour les segments d'uréthane enduits d'une couche de nylon alors qu'avec les segments obtenus à partir d'une extrusion de polyéthylene, on observe une très grande hystérésis en rigidité. Les techniques d'identification des paramètres d'un système sont utilisées afin d'interpréter la dynamique en oscillation verticale et en tangage du prototype équipé de la jupe à segments non compartimentée sur la piste circulaire de l'UTIAS. On en conclut que l'hystérésis observée durant les tests statiques a un effet important sur la dynamique. Le développement d'un programme d'éléments finis pour l'analyse d'une membrane partiellement affaissée et les résultats préliminaires d'une théorie sur la stabilité en oscillation verticale des aéroglisseurs planant sur l'eau sont également inclus.

18. Mots-clés
Stabilité des coussins d'air; jupes souples, dynamique des aéroglisseurs, instabilité pneumatique.

19. Diffusion
Nombre limité de copies disponibles auprés du Cdt.

20. Classification de sécurité (de ce rapport)
Aucune

21. Classification de sécurité (de cette page)
Aucune

22 Nombre de pages
275 app.

23 Prix
-

PREFACE AND ACKNOWLEDGEMENTS

This is the second of two reports which describe research on some basic aspects of air cushion vehicle (ACV) technology initiated at this Institute as part of a contract with the Transportation Development Centre (TDC) during the period 1 July, 1977 to 1 January, 1980, (TDC File D-500-431). As for previous research for TDC completed at this Institute, although the research was broad ranging in nature, it was oriented towards projects of current Canadian interest. For example, a major emphasis in the present programme has been the investigation of the dynamical properties of an uncompartmented segmented skirt cushion which has been developed in Canada for application to low speed cross-river ferries. The work described in this and the first report (TP1760) was also partly funded by the first author's Natural Sciences and Engineering Research Council (NSERC) Operating Grant (A3378) and Core Grant (A1613). In general, although NSERC funds have been used to support work of a basic nature, no clear cut distinction has been made between specific projects supported by TDC and those supported by NSERC.

As in past work for TDC, examination of cushion geometries of specific interest to TDC has led to the definition of work of a more fundamental nature. Understanding of these basic questions is often essential to development of design and testing methods, in addition to having intrinsic academic interest. We are very grateful to TDC for allowing us the flexibility to explore these basic questions.

Finally the first author would like to note that since about 1968, he has been attempting to build up a high quality research programme in this new field, one that is recognized as both having the intellectual challenge characteristic of the research tradition at UTIAS and yet at the same time being perceived as relevant to TDC's mission. At the start in 1968 he knew nothing about air cushion technology, and the task has been very difficult; at times it has seemed to be impossible. The first report reflects to some extent the process of establishing competence in certain techniques, rather than achieving specific results. However, it now seems fair to say that, at the time of writing of this preface, the programme is well established. This is particularly evident in this report, in which three major achievements are described.

The first author would like to express his deep gratitude to Mr. P. L. Eggleton and Mr. J. E. Laframboise of TDC for their sustained financial support, encouragement, and flexibility in allowing him to meet the two success criteria noted above, especially since at times they seemed to be in conflict. The encouragement of his academic colleagues and the efforts of his students have been instrumental in achieving this success. However, most of all, the author would like to record here his deep gratitude to Dr. Michael Hinchey for his efforts, skill and perseverence, first as a student, then as a colleague.

CONTENTS

Page

1. INTRODUCTION 1

1.1 Overall Objective 1
1.2 Projects Identified for the Present Contract 3

1.2.1 Experimental Measurement of Dynamic Stability Boundaries of Simple Air Cushions 3
1.2.2 Investigation of the Static Pitch and Roll Stiffness Characteristics of the HSL Cushion 3
1.2.3 Investigation of the Pitch-Heave Dynamics of the Segmented Skirt (HSL) Cushion 4
1.2.4 Buckling of Skirt Material 5
1.2.5 Stability Over Water 6

2. EXPERIMENTAL MEASUREMENT OF DYNAMIC STABILITY BOUNDARIES FOR SIMPLE AIR CUSHIONS 7

2.1 Introduction 7
2.2 Review of Equations and Assumptions Used in Analysis 9

2.2.1 Equations for Simplified Model 9
2.2.2 Assumptions 14

2.2.2.1 Quasisteady Fan Law Approximation (Equation 1) 14
2.2.2.2 Modelling of the Duct Flow as a Lumped Inertance (Equation 5) 16
2.2.2.3 Lumped Volume Approximation (Equation 8) 17
2.2.2.4 Compressibility of the Air in the Plenum Chamber (Equation 8a) 22
2.2.2.5 Isentropic Compression-Expansion Assumption (Equation 9) 24
2.2.2.6 Quasisteady Incompressible Orifice Flow Assumption (Equations 6 and 10) 25
2.2.2.7 Concluding Remarks 27

2.3 Design of the Experiment 27

2.3.1 Original Concept 27
2.3.2 Results Obtained Prior to Present Contract 29
2.3.3 Initial Comparisons Between Theory and Experiment on Heave Table Facility 29
2.3.4 Design of a Critical Experiment: The Sphere Facility 29
2.3.5 Procedures Used for Determining Stability Boundaries 34

2.4 Sphere Facility Results 39

2.4.1 Duct Effects for Rigid and Flexible Skirts 39
2.4.2 Comparison of Methods of Boundary Determination 44
2.4.3 Internal Flow Effects 44

Contents - Continued

Page

2.5 Conclusions: Implications for Practical Stability Calculations 44

2.5.1 General 44
2.5.2 Improved Modelling for Heave Table Facility 48

3. STATIC PITCH AND ROLL STIFFNESS CHARACTERISTICS OF A SEGMENTED SKIRT CUSHION 50

3.1 Introduction 50

3.1.1 Background 50
3.1.2 Details of HSL Skirts Built for UTIAS Facilities 52
3.1.3 Detailed Objectives of the Work Described in this Section 52

3.2 Theoretical Development 55

3.2.1 Pitch and Roll Stiffness Theory 55

3.2.1.1 Basic Assumptions 55
3.2.1.2 Measurement of Skirt Geometrical Parameters 57
3.2.1.3 Formulation of the Roll Stiffness Equations 61
3.2.1.4 Formulation for Pitching Motion 67
3.2.1.5 Exact and Approximate Solution 67

3.2.2 Dimensional Analysis 68

3.2.2.1 Analysis for the Ideal-Model Skirt Material 68
3.2.2.2 Scaling of Skirt Material 70

3.3 Results for Nylon-Urethane Skirt 72

3.3.1 General Comparison of Theory and Experiment 72

3.3.1.1 Roll Characteristics 72
3.3.1.2 Pitch Characteristics 72
3.3.1.3 Effect of Approximations to Shape of Cushion Footprint 81

3.3.2 Other Experimental Results 81

3.4 Experimental Results for Polytehylene Skirt Material 89

3.4.1 Roll Characteristics 89
3.4.2 Pitch Characteristics 89

3.5 Experimental Results for Loop-Segment Skirt 89

3.6 Conclusions 97

Contents - Continued

Page

4. PITCH-HEAVE DYNAMICS OF THE SEGMENTED SKIRT CUSHION 100

4.1 Introduction 100

4.1.1 General Objective 100
4.1.2 Choice of Skirt Material 100

4.2 Static Pitch and Heave Stiffness Measurements 105

4.2.1 Description of the Experiment 105
4.2.2 Static Experiment Results 105

4.3 Theoretical Model of Pitch-Heave Dynamics 112

4.3.1 Assumptions 112
4.3.2 Equations 112
4.3.3 Nondimensionalization 113
4.3.4 Linearized Equations 114

4.4 Dynamic Experiments and Results 117

4.4.1 Experiments 117
4.4.2 Dynamic Test Results 120

4.5 Correlation of Dynamic and Static Measurements 123

4.5.1 Estimation of Dynamic Coefficients from Static Data 123
4.5.2 Discussion of Dynamic and Static Results 129

4.6 Conclusions 133

5. BUCKLING OF SKIRT MATERIAL 134

5.1 Introduction 134

5.1.1 Preamble 134
5.1.2 Definitions of Stability and Analytical Approaches 135

5.2 Previous Work 139

5.2.1 Historical Review of Wrinkling Theory 139
5.2.2 Wrinkling of Skirt Systems on ACV's 152

5.3 Finite Element Formulation of Wrinkled Region 157

5.3.1 Finite Element Formulation 157
5.3.2 Formulation of Stress Resultant 157
5.3.3 Wrinkling Criterion for Finite Element Cylinder 162

Contents - Continued

Page

5.4 Performance Tests 168

5.4.1 Curvilinear Shell Element Test 169

5.5 Numerical Results and Discussions 175

5.5.1 Isotropic Case 175
5.5.2 Orthotropic Case 177
5.5.3 Rectilinear Anisotropic Case 184

5.6 Suggestions for Future Work 185

5.7 Conclusions 188

6. HEAVE STABILITY OVER WATER 189

6.1 Introduction 189
6.2 Pressure-Water Surface Interaction 189
6.3 Lip Flow 194
6.4 Stability Considerations 194
6.5 Results for HEX-5 197
6.6 Discussion 198

REFERENCES 199

APPENDIX A: CONTRACT WORK STATEMENT 204

A.1 Objectives 204
A.2 Work Statement 204

A.2.1 HDL Stability Limits 204
A.2.2 Pneumatic Circuit Stability 205
A.2.3 Buckling of Skirt Material 205

APPENDIX B: SCALING ARGUMENTS FOR GEOMETRICALLY SIMILAR AIR CUSHION SYSTEMS 206

B.1 Rigid Plenum Air Cushion with a Constant Pressure Source 206
B.2 Rigid Plenum Air Cushion with a Duct and a Constant Pressure Source 207

APPENDIX C: DERIVATION OF A 24 DEGREE OF FREEDOM CURVILINEAR SHELL FINITE ELEMENT FOR A RECTILINEAR ANISOTROPIC MATERIAL 210

C.1 Strain Energy 212
C.2 Stiffness Matrix Derivation 214

C.2.1 Trial Functions 214
C.2.2 Membrane Stiffness Matrix 214
C.2.3 Bending Stiffness Matrix 215
C.2.4 Curvilinear Coupling Stiffness Matrix 220

Contents - Continued

Page

C.3 Consistent Force Vector Calculation 225
C.4 Stress Formulation 227

C.4.1 Stress Formulation at the Nodes 228
C.4.2 Stress Formulation at the Centre of the Element 230
C.4.3 Curvature Calculation 231

APPENDIX D: UNSTEADY ORIFICE FLOW 232

APPENDIX E: SEQUENCE OF FUNCTIONS USED IN HSL ROLL AND PITCH STIFFNESS ANALYSIS 236

APPENDIX F: VAMPIRE 1 STEADY STATE FAN CHARACTERISTIC 240

APPENDIX G: THE UTIAS CIRCULAR TRACK FACILITY 247

LIST OF FIGURES

Page

FIG. 1.1 HSL's PROTOTYPE VEHICLE 2

FIG. 1.2 UTIAS TEST VEHICLE, VAMPIRE I, FLYING OVER RAMP 2

FIG. 2.1 FAN-DUCT-PLENUM CHAMBER MODEL USED IN STABILITY CALCULATIONS 8

FIG. 2.2A TYPICAL FINITE ELEMENT HEAVE STABILITY RESULTS; CASES 1 TO 6 HAVE RATIOS OF L_D/D_D OF 0.125, 4.0, 8.0, 11.25, 16.0 AND 64 RESPECTIVELY 10

FIG. 2.2B COMPARISON OF FINITE ELEMENT AND LUMPED INERTANCE RESULTS. CASE 3, $L_D/D_D = 8$, CASE 6, $L_D/D_D = 64$ 11

FIG. 2.3 HOVER-JAK SINGLE CELL RIG 18

FIG. 2.4 INTERNAL FLOW EFFECT ON HEAVE STABILITY 18

FIG. 2.5A VELOCITY VECTOR PLOT OF TURBULENT FLOW INSIDE A PLENUM CHAMBER AIR CUSHION. HOVERGAP $h_e/D_p = 0.0125$, AND DUCT REYNOLDS NUMBER $Re_D = 10^4$. 19

FIG. 2.5B VELOCITY VECTOR PLOT OF FLOW INSIDE AN AIR CUSHION HOVERGAP $h_e/D_p = 0.05$, $Re_D = 10^5$. 20

FIG. 2.6 VELOCITY VECTOR PLOT FOR AN AIR CUSHION WITH A BAFFLE PLATE. $h_e/D_p = 0.05$, $Re_D = 10^5$ 21

FIG. 2.7 STREAMLINE PATTERN FOR STEADY INVISCID ORIFICE FLOW 23

FIG. 2.8 IDEALIZATION OF AN AIR CUSHION VOLUME 23

FIG. 2.9 SCHEMATIC DIAGRAM OF ORIGINAL HEAVE TABLE FACILITY 28

FIG. 2.10 TYPICAL STABILITY RESULT OBTAINED USING HEAVE TABLE FACILITY 30

FIG. 2.11 FIRST MODEL USED FOR STABILITY MEASUREMENTS 30

FIG. 2.12 AN INTERNAL FLOW EFFECT OBTAINED ON HEAVE TABLE FACILITY 31

FIG. 2.13 SCHEMATIC DIAGRAM OF SPHERE FACILITY 33

FIG. 2.14 DETAILS OF THE EXPERIMENT USED UNDER THE SPHERE FACILITY 33

FIG. 2.15 TYPICAL EXAMPLES OF STABLE AND UNSTABLE MOTION NEAR A STABILITY BOUNDARY 35

FIG. 2.16 DAMPING DECREMENTS USED IN EXTRAPOLATED DECREMENT METHOD OF DETERMINING STABILITY BOUNDARY 36

FIG. 2.17 TYPICAL DATA OBTAINED FOR THE EXTRAPOLATED DECREMENT OF DETERMINING STABILITY BOUNDARIES. FOR THIS EXTRAPOLATION, X_2 IS USED 37

FIG. 2.18 EXTRAPOLATED DECREMENT METHOD WITH X_2 APPLIED TO DATA 38

List of Figures - Continued

Page

FIG. 2.19 COMPARISON OF THEORETICAL RESULTS FOR AN ISOTHERMAL AND ISENTROPIC CUSHION PROCESS WITH EXPERIMENTAL RESULTS FOR SHORT DUCT RIGID SKIRT CASE 40

FIG. 2.20 MEASURED STABILITY DATA FOR RIGID AND FLEXIBLE SKIRTS, SHORT DUCT CASE 41

FIG. 2.21 COMPARISON OF THEORY AND EXPERIMENT FOR SHORT DUCT FLEXIBLE SKIRT CASE 42

FIG. 2.22 COMPARISON OF THEORY AND EXPERIMENT FOR THE LONG DUCT AND FLEXIBLE SKIRT CASE 43

FIG. 2.23 ILLUSTRATION OF REPEATABILITY OF THE EXPERIMENTAL DATA 43

FIG. 2.24 COMPARISON OF METHODS OF ASCERTAINING STABILITY BOUNDARIES WITH THEORETICAL PREDICTIONS FOR L_d = 1.71m. THEORY, LUMPED INERTANCE DUCT MODEL OF REF. 21, CURVE A; LUMPED INERTANCE MODEL OF REF. 1, CURVE B; FINITE ELEMENT MODEL OF REF. 1, CURVE C. DATA POINTS, EXTRAPOLATED DECREMENT METHOD INCLUDING ERROR BARS: x; OBSERVED MOTION METHOD: O. 45

FIG. 2.25 EXPERIMENTAL RESULTS OBTAINED IN SPHERE FACILITY SHOWING AN INTERNAL FLOW EFFECT 46

FIG. 2.26 THEORETICAL RESULTS FOR RADIAL WALL-JET MODEL OF AN INTERNAL FLOW EFFECT FOR MODEL TESTED IN THE SPHERE FACILITY 47

FIG. 2.27 IMPROVED THEORETICAL PREDICTION OF STABILITY BOUNDARIES OBTAINED TEST FACILITY DEPICTED IN FIGURE 2.9 WHEN MODELLING OF THE SUPPLY DUCT IS INCLUDED 49

FIG. 3.1 BASIC CONCEPT OF HOVERCRAFT DEVELOPMENT LIMITED (HDL) SKIRT. 51

FIG. 3.2 DETAILS OF HOVERLIFT SYSTEMS LIMITED (HSL) SEGMENTS USED AT UTIAS. 53

FIG. 3.3 PHOTOGRAPH OF HSL SKIRT MODEL ON CUSHION DYNAMIC TABLE HOVERING AT A SCALED VALUE OF CUSHION AIR FLOW RATE AND AT PITCH ANGLE. 54

(a) SIDE VIEW
(b) END VIEW

FIG. 3.4 BASIC PARAMETERS DEFINING THE GEOMETRY OF THE HSL SKIRT AT ZERO PITCH AND ROLL. 58

FIG. 3.5 DETAILS OF THE GEOMETRY OF THE HSL SKIRT ASSUMED FOR COMPUTING PITCH AND ROLL STIFFNESS. CASE I: BELOW THE KNEE REGION. 60

FIG. 3.6 DETAILS OF THE GEOMETRY OF THE HSL SKIRT ASSUMED FOR COMPUTING PITCH AND ROLL STIFFNESS. CASE II: ABOVE THE KNEE REGION. 62

List of Figures - Continued

Page

FIG. 3.7 PHOTOGRAPH OF SKIRT SEGMENTS ON PITCH-DOWN SIDE SHOWING EFFECTIVE SEAL. 64
(a) BEFORE SEGMENT BUCKLING
(b) AFTER SEGMENT BUCKLING

FIG. 3.8 ASSUMED FOOTPRINT SHAPE FOR ROLL AND PITCH STIFFNESS CALCULATIONS. 66

FIG. 3.9 COMPARISON OF TYPICAL ROLL STIFFNESS TEST RESULTS WITH THEORY FOR THE HSL SKIRT ON THE CUSHION DYNAMICS FACILITY. POLYURETHANE COATED NYLON IS THE SKIRT MATERIAL. 73

FIG. 3.10 COMPARISON OF PREDICTED AND MEASURED CENTRE OF MASS MOTION DURING ROLL FOR CUSHION DYNAMICS FACILITY WITH HSL SKIRT. SKIRT MATERIAL IS POLYURETHANE COATED NYLON. 74

FIG. 3.11 COMPARISON OF PREDICTED AND MEASURED CUSHION PRESSURE DURING ROLL FOR CUSHION DYNAMICS FACILITY WITH HSL SKIRT. SKIRT MATERIAL IS POLYURETHANE COATED NYLON. 75

FIG. 3.12 EXPERIMENTAL RESULTS SHOWING THE EFFECT OF LIFT FAN SLOPE ON ROLL STIFFNESS OF CUSHION DYNAMICS FACILITY WITH HSL SKIRT. SKIRT MATERIAL IS POLYURETHANE COATED NYLON. 76

FIG. 3.13 THEORETICAL DEPENDENCE OF ROLL STIFFNESS CHARACTERISTIC ON FAN SLOPE COEFFICIENT (C_{SC}) FOR CUSHION DYNAMICS FACILITY WITH HSL SKIRT. 77

FIG. 3.14 THEORETICAL AND EXPERIMENTAL VALUES OF PITCH STIFFNESS OF CUSHION DYNAMICS FACILITY WITH HSL SKIRT. SKIRT MATERIAL IS POLYURETHANE COATED NYLON. 78

FIG. 3.15 THEORETICAL AND EXPERIMENTAL CURVES OF CENTRE OF MASS MOTION DURING PITCH CYCLE FOR CUSHION DYNAMICS FACILITY WITH HSL SKIRT. SKIRT MATERIAL IS POLYURETHANE COATED NYLON. 79

FIG. 3.16 THEORETICAL AND EXPERIMENTAL CURVES OF CUSHION PRESSURE VARIATION DURING PITCH CYCLE FOR CUSHION DYNAMICS FACILITY WITH HSL SKIRT. SKIRT MATERIAL IS POLYURETHANE COATED NYLON. 80

List of Figures - Continued

Page

FIG. 3.17 COMPARISON OF AN EXPERIMENTAL ROLL STIFFNESS CHARACTERISTIC TO THEORETICAL PREDICTIONS BASED ON DIFFERENT ASSUMPTIONS ABOUT FOOTPRINT SHAPE. 82

FIG. 3.18 EFFECT OF PARTIAL ROLL ON THE ROLL STIFFNESS CHARACTERISTIC OF THE CUSHION DYNAMICS FACILITY WITH THE HSL SKIRT. SKIRT MATERIAL IS POLYURETHANE COATED NYLON. 83

FIG. 3.19 EFFECT OF GROSS MODEL WEIGHT ON THE ROLL STIFFNESS CHARACTERISTIC OF THE CUSHION DYNAMICS FACILITY WITH HSL SKIRT. SKIRT MATERIAL IS POLYURETHANE COATED NYLON. 84

FIG. 3.20 EFFECT OF SKIRT GROUND FRICTION ON THE ROLL STIFFNESS CHARACTERISTIC OF THE CUSHION DYNAMICS FACILITY WITH THE HSL SKIRT. SKIRT MATERIAL IS POLYURETHANE COATED NYLON. 85

FIG. 3.21 EFFECT OF GROSS MODEL WEIGHT ON ROLL STIFFNESS CHARACTERISTIC OF CUSHION DYNAMICS MODEL WHEN HELD AT CONSTANT ROLL ANGLE. MATERIAL FOR HSL SKIRT IS POLYURETHANE COATED NYLON. 86

FIG. 3.22 EFFECT OF CUSHION PRESSURE COEFFICIENT (C_{PC}) ON ROLL STIFFNESS CHARACTERISTIC OF CUSHION DYNAMICS MODEL EQUIPPED WITH HSL SKIRT. SKIRT MATERIAL IS POLYURETHANE COATED NYLON. 87

FIG. 3.23 CUSHION PRESSURE DISTRIBUTION ACROSS GROUNDBOARD DIRECTLY UNDER TIPS OF SEGMENTS (A), AND AT MIDPOINT (B).
(a) ROLL ANGLE, $\alpha = 0°$
(b) ROLL ANGLE, $\alpha = 7.2°$ 88

FIG. 3.24 EFFECT OF MOMENT INCREMENT SIZE ON ROLL STIFFNESS CHARACTERISTIC OF CUSHION DYNAMICS MODEL EQUIPPED WITH HSL SKIRT. SKIRT MATERIAL IS POLYURETHANE COATED NYLON. 90

FIG. 3.25 TYPICAL CUSHION PRESSURE VERSUS VOLUME FLOW CURVE FOR CUSHION DYNAMICS FACILITY EQUIPPED WITH HSL SKIRT. 91

FIG. 3.26 ROLL STIFFNESS CHARACTERISTIC OF CUSHION DYNAMICS MODEL EQUIPPED WITH HSL SKIRT INCLUDING THE EFFECT OF SKIRT-GROUND FRICTION. SKIRT MATERIAL IS POLYETHYLENE FILM. 92

List of Figures - Continued

Page

FIG. 3.27 EXPERIMENTAL PITCH STIFFNESS MEASUREMENTS FOR THE CUSHION DYNAMICS MODEL EQUIPPED WITH THE POLYETHYLENE HSL SKIRT. 93

FIG. 3.28 NONDIMENSIONAL HEIGHT VERSUS PITCH ANGLE, θ, FOR THE CUSHION DYNAMICS MODEL EQUIPPED WITH THE POLYETHYLENE HSL SKIRT. 94

FIG. 3.29 NONDIMENSIONAL PRESSURE VERSUS PITCH ANGLE, θ, FOR THE CUSHION DYNAMICS MODEL EQUIPPED WITH THE POLYETHYLENE HSL SKIRT. 95

FIG. 3.30 ROLL STIFFNESS CHARACTERISTICS OF CUSHION DYNAMICS MODEL EQUIPPED WITH A SINGLE PLENUM CHAMBER LOOP AND SEGMENT SKIRT INCLUDING THE EFFECT OF SKIRT-GROUND FRICTION. SKIRT MATERIAL IS AN ELASTOMER COATED FABRIC. 96

FIG. 3.31 ROLL STIFFNESS CHARACTERISTICS OF CUSHION DYNAMICS MODEL EQUIPPED WITH A SINGLE PLENUM CHAMBER LOOP AND SEGMENT SKIRT, INCLUDING THE EFFECT OF SKIRT-GROUND FRICTION. ELASTOMER COATED FABRIC IS USED FOR THE SKIRT MATERIAL. 98

FIG. 3.32 EFFECT OF MODEL WEIGHT ON THE MEASURED ROLL STIFFNESS OF THE CUSHION DYNAMICS MODEL EQUIPPED WITH THE ELASTOMER COATED FABRIC LOOP AND SEGMENT SKIRT SYSTEM. 99

FIG. 4.1 THEORETICAL ROLL RESPONSE WHEN STATIC HYSTERESIS IS INTERPRETED AS A VISCOUS LOSS. 101

FIG. 4.2 TYPICAL STATIC ROLL STIFFNESS CURVE SHOWING HYSTERESIS WITH THE HSL SKIRT. .02

FIG. 4.3 PITCH RESPONSE TO DISTURBANCE FOR POLYETHYLENE SKIRT.

(a) $\theta_o = 2.6°$
(b) $\theta_o = 4.0°$ 103

FIG. 4.4 PITCH RESPONSE TO DISTURBANCE FOR NYLON URETHANE SKIRT.

(a) $\theta_o = 2.6°$
(b) $\theta_o = 4.0°$ 104

List of Figures - Continued

Page

FIG. 4.5 EXPERIMENTAL SETUP FOR STATIC PITCH-HEAVE MEASUREMENTS - VAMPIRE I. 106

FIG. 4.6 BEARING ASSEMBLY FOR STATIC PITCH-HEAVE EXPERIMENT. 106

FIG. 4.7 STATIC PITCH-HEAVE EXPERIMENTAL RESULTS FOR 1800 RPM FAN SPEED.
(a) AIR MASS FLOW RATE vs θ-SINGLE LINE FIT TO DATA.
(b) ROLL ANGLE vs θ-SINGLE LINE FIT TO DATA.
(c) HEAVE HEIGHT vs θ-SINGLE LINE FIT TO DATA.
(d) PITCH STIFFNESS CURVE. 107

FIG. 4.8 STATIC PITCH-HEAVE EXPERIMENTAL RESULTS FOR 2000 RPM FAN SPEED.
(a) AIR MASS FLOW RATE vs θ-SINGLE LINE FIT TO DATA.
(b) ROLL ANGLE vs θ-SINGLE LINE FIT TO DATA.
(c) HEAVE HEIGHT vs θ-SINGLE LINE FIT TO DATA.
(d) PITCH STIFFNESS CURVE. 108

FIG. 4.9 STATIC PITCH-HEAVE EXPERIMENTAL RESULTS FOR 2200 RPM FAN SPEED.
(a) AIR MASS FLOW RATE vs θ-SINGLE LINE FIT TO DATA.
(b) ROLL ANGLE vs θ-SINGLE LINE FIT TO DATA.
(c) HEAVE HEIGHT vs θ-SINGLE LINE FIT TO DATA.
(d) PITCH STIFFNESS CURVE. 109

FIG. 4.10 COMPARISON OF SINGLE LINE AND HYSTERESIS LINE FITS TO AIR FLOW, ROLL ANGLE AND HEAVE DATA FOR VARIOUS FAN SPEEDS.
(a) N = 1800 RPM
(b) N = 2000 RPM
(c) N = 2200 RPM 111

FIG. 4.11 UTIAS CIRCULAR TRACK VIEW. 118

FIG. 4.12 TEST VEHICLE IN FLIGHT OVER RAMP. 118

FIG. 4.13 UNDERSIDE OF TEST VEHICLE TAKEN DURING CENTRE OF GRAVITY MEASUREMENTS. 119

List of Figures - Continued

Page

FIG. 4.14 TRAILING ARM SENSOR RESPONSE TO RAMP DISTURBANCE. 121

FIG. 4.15 VEHICLE RESPONSE TO RAMP DISTURBANCE — TIME HISTORIES FROM POINT WHERE LAST TRAILING ARM HAS LEFT RAMP. 122

FIG. 4.16 COMPARISON OF SPI PREDICTED RESPONSE AND MEASURED VEHICLE RESPONSE. 124

FIG. 5.1 ADJACENT EQUILIBRIUM BUCKLED STATE 136

FIG. 5.2 NON-ADJACENT EQUILIBRIUM BUCKLED STATE 137

FIG. 5.3 COLLAPSE OF A STRUCTURE 138

FIG. 5.4 LOADS FOR PRESSURIZED CYLINDERS 140

FIG. 5.5 MOMENT-CURVATURE RELATIONSHIP FOR THE BENDING OF A PRESSURIZED CYLINDER 140

FIG. 5.6 COMPARISON OF WRINKLED REGION IN PRESSURIZED CYLINDRICAL MEMBRANE IN BENDING WITH COMPRESSION REGION IN CYLINDRICAL SHELL WITH SAME LOADING (REF. 5.2) 142

FIG. 5.7 MOMENT CURVATURE RELATIONSHIP FOR MYLAR CYLINDERS IN BENDING (REF. 5.2) 143

FIG. 5.8 LOADS AND DEFORMATIONS FOR PRESSURIZED CYLINDER 145

FIG. 5.9 CURVATURE AND LONGITUDINAL STRESS DISTRIBUTION IN CYLINDER 145

FIG. 5.10 LOAD-DEFLECTION CURVE FOR $\bar{p}$ = 1.20 (REF. 5.5) 147

FIG. 5.11 MEASURED LOAD DISTRIBUTION AROUND CIRCUMFERENCE OF ATLAS AT STATION S84 COMPARED WITH PREDICTED-TEST 3 (FLAT PORTION OF CURVES INDICATES PORTION OF TANK SKIN THAT HAS WRINKLED) (REF. 5.7) 149

FIG. 5.12 TORQUE-ROTATION RESULTS FOR WRINKLING OF A CIRCULAR MEMBRANE BY ROTATION OF ATTACHED HUB (REF. 5.9) 153

FIG. 5.13 SCHEMATIC OF ROLL INSTABILITY EXPERIMENT 154

FIG. 5.13 SCHEMATIC OF ROLL INSTABILITY EXPERIMENT 154

FIG. 5.14 155

FIG. 5.15 155

FIG. 5.16 WRINKLED REGION ON SEGMENTED SKIRT 156

FIG. 5.17 WRINKLING AND COLLAPSE ANGLE FOR CONICAL CELL OVER A SMOOTH SURFACE 158

FIG. 5.18 LOADING AND COORDINATE SYSTEM FOR FINITE ELEMENT ANALYSIS 160

FIG. 5.19 CROSS-SECTIONAL VIEW OF WRINKLED REGION 161

FIG. 5.20 FINITE ELEMENT REPRESENTATION OF CYLINDER WITH CURVED RECTANGULAR ELEMENTS 161

FIG. 5.21 LOADS FOR PRESSURIZED CYLINDER 163

FIG. 5.22 SPRING ANALOGY OF ELEMENTS 167

FIG. 5.23 COMPARISON OF FINITE ELEMENT ANALYSIS WITH EXACT SOLUTION FOR A CYLINDER WITH A UNIFORM CIRCUMFERENTIAL LOAD APPLIED AT MIDLENGTH 170

FIG. 5.24 COMPARISON OF FINITE ELEMENT ANALYSIS WITH STEIN AND HEDGEPETH'S THEORY (40 ELEMENTS) 176

FIG. 5.25 COMPARISON OF FINITE ELEMENT ANALYSIS WITH STEIN AND HEDGEPETH'S THEORY (80 ELEMENTS) 178

FIG. 5.26 COMPARISON FOR INCREASE OF TOTAL APPLIED AXIAL LOAD 179

FIG. 5.27 COMPARISON FOR L/r = 5 180

FIG. 5.28 NORMAL DISPLACEMENT VERSUS AXIAL COORDINATE ALONG TOP OF CYLINDER 181

FIG. 5.29 MOMENT-CURVATURE RELATIONSHIP FOR HJ-15 CELL 182

FIG. 5.30 MOMENT-CURVATURE RELATIONSHIP FOR ORTHOTROPIC CYLINDER 183

FIG. 5.31 HYPERBOLOIDAL CONFIGURATION OF ANISOTROPIC CYLINDER 186

FIG. 5.32 TWISTING OF ANISOTROPIC CYLINDER 186

FIG. 5.33 NONUNIFORMITY OF COMPRESSION REGION FOR ANISOTROPIC CYLINDER 187

FIG. 6.1 AIR CUSHION HOVERING OVER WATER AT ZERO FORWARD SPEED 190

FIG. 6.2 INVERTED BOX AT THE SURFACE OF AN INFINITELY DEEP INFINITE EXPANSE OF WATER 190

FIG. 6.3 WATER COMPLIANCE FREQUENCY RESPONSE FUNCTION 193
FIG. 6.4 SIMPLE MODEL OF AIR ESCAPE UNDER CUSHION LID 195
FIG. D.1 SLOT ORIFICE FLOW APPROXIMATION 233
FIG. G.1 VAMPIRE I BASIC DIMENSIONS (m) 244
FIG. G.2 UTIAS CIRCULAR TRACK CONTROL ROOM 245

LIST OF TABLES

		Page
TABLE 2.1	DIMENSIONS OF SPHERE FACILITY EXPERIMENT	32
TABLE 3.1	GEOMETRIC DETAILS OF HSL SKIRT SEGMENTS USED ON UTIAS MODELS	56
TABLE 4.1	TABLE OF ESTIMATED AND CALCULATED PARAMETERS	130
TABLE 5.1	CIRVULINEAR TEST FOR ISOTROPIC CASE	171
TABLE 5.2	CURVILINEAR TEST FOR ORTHOTROPIC CASE	172
TABLE 5.3	CURVILINEAR TEST WITH SMALL BENDING MOMENT APPLIED	173
TABLE C.1		218
TABLE C.2		223
TABLE C.3	BENDING LOAD CONSISTENT FORCE VECTOR	226
TABLE C.4	MEMBRANE LOAD CONSISTENT FORCE VECTOR	227
TABLE C.5		229

NOTATION

Section 2

Roman

A	cross-sectional area.
A_{ref}	reference area for C_{QC}, $A_{ref} = \pi/4\ D_p^2$ here.
a	atmospheric sound speed.
C_c	cushion volume capacitance, $C_c = V_c/\rho_a a^2$
C_m	mass discharge coefficient.
C_{PQ}	non-dimensional fan slope coefficient, see equation 2.
C_{QC}	cushion flow coefficient = $Q_e\ (\rho_a/2WA_{ref})^{1/2}$.
D_p	diameter of plenum chamber.
f	frequency of cushion oscillations
g	acceleration due to gravity
h	hovergap
j	$\sqrt{-1}$
K_j	coefficient for radial wall-jet effect as determined from finite difference calculation of turbulent flow structure
L_p	height of plenum chamber as defined in Figure 2.1
ℓ_p	length of perimeter of cushion, here $\ell_p = \pi D_p$
$\dot{m}$	mass flux rate
n	polytropic exponent P/ρ^n = constant,
n	rotational speed of cushion fan
N_R	number of blades in fan rotor
p	pressure in gauge units (atmospheric as datum)
P	absolute pressure
q	speed of air in duct
Q_i	volume flow rate into i-th volume
R	ratio of cushion volume residence time to cushion oscillation period τ_c

Re_D	Reynolds number based on diameter of plenum chamber and cushion air entrance velocity V_j
R_m	ratio of local to convective acceleration terms in Eulers equations for fluid flow.
s	Laplace variable $s = \sigma + j\omega$
s	distance along a steamline
S_a	cushion support area, here $S_a = \pi/4D_p^2$
t	time
V	volume
V_d	"dead" volume of a
V_j	jet entrance velocity to cushion, $V_j = q_a$ here
W	weight supported by cushion

Greek

α	coefficient in Ohashi's theory [Ref 2.10] for unsteady blade aerodynamics
γ	isentropic exponent
ϕ	flow coefficient
λ_R	stagger angle of fan rotor blades
ρ	density
ω	Im (s)
ω_R	reduced frequency of rotor blades, $\omega_R = 2\pi\alpha\tau rf$
α	Re (s)
τ	time constant
τ_c	period of cushion oscillation = f
τ_p	time of passage of fluid particle through rotor blad system
τ_R	critical time constant in Ohashi's unsteady blade aerodynamic theory [Ref 2.10]

Subscripts

a	atmospheric, to atmosphere
c	pertaining to cushion voluem
d	duct, except V_d = dead volume of cushion
d_c	duct, cushion end
d_f	duct, fan end
e	equilibrium
f	fan

NOTATION

Section 3

Roman

A_{ref}	reference area - base area of vehicle
a_e	cushion air escape area
a_f	cushion footprint area
B	vehicle hard structure width
B_s	skirt width at segment bottoms
C_D	discharge coefficient
C_m	moment coefficient
C_{MR}	roll moment coefficient
C_{MP}	pitch moment coefficient
C_{PC}	cushion pressure coefficient
C_{QC}	cushion flow coefficient
C_{SC}	fan slope coefficient
$C_0, C_1, C_2, \ldots$	fan characteristic coefficients
E_1	viscoelastic storage modulus
E_2	viscoelastic loss modulus
g	gravitational acceleration
$g_1, g_2, g_3, \ldots$	skirt geometry dimensions
H	$\triangleq H_S + H_P$
H_L	cushion air leakage height
H_P	distance of centre of mass from base of box
H_S	skirt reference height
h_p	height of centre of mass above ground board
i	$\sqrt{-1}$
k_f	equilibrium dimensionless cushion pressure

L	vehicle hard structure length
L_S	skirt length at segment bottoms
$L_1 \rightarrow L_5$	skirt segment dimensions
M	roll moment
P_{ce}	cushion pressure at equilibrium
p_c	cushion pressure
p_f	fan exit pressure
Q_{ce}	cushion flow at equilibrium
q_c	cushion exit flow
q_f	fan exit flow
Re	Reynolds number
t	skirt thickness
V_j	air exit velocity
W	vehicle weight

Greek

α	roll angle
β	segment angle
ϵ	strain
$\dot{\epsilon}$	strain rate
θ	pitch angle
ξ	segment angle
$\pi_1, \pi_2, \ldots$	dimensionless coefficients
ρ_a	atmospheric density
σ	stress
Φ	segment angle with ground at 0° roll and pitch
ψ	segment angle

Subscripts

C, c	cushion

e	equilibrium
f	fan
f	full scale
m	model
s	skirt

NOTATION

Section 4

Roman

a	Speed of Sound
a_e	Air Escape Area
a_f	Footprint Area
B	Vehicle Width
C_1, C_2, C_3	Fan Characteristic Coefficients
C_c	Cushion Capacitance
C_D	Discharge Coefficient at Lip
C_{sc}	Fan Slope Coefficient
CG	Centre of Gravity
F	Force
g	Gravitational Acceleration
g_{12}	Moment Arm From Centre of Pressure to Centre of Gravity
h	Heave Height of Centre of Gravity
I	Moment of Inertia
L	Vehicle Length
M	Pitching Moment
N	Fan Speed
P_c	Cushion Pressure
P_{co}	Fan Characteristic Constant
q_c	Cushion Exit Flow
q_f	Fan Exit Flow
t	Time
V_c	Cushion Volume
W	Vehicle Weight

Greek

α	Roll Angle
θ	Pitch Angle
ξ_h	Heave Damping Co-efficient
ξ_θ	Pitch Damping Co-efficient
ρ	Cushion Air Density
ρ_a	Atmospheric Air Density
ω_p	Pitch Frequency (Rad/S)

NOTATION

Section 5

Roman

A	cross-sectional area of cylinder wall ($2\pi rt$)
b	distance along cylinder which has wrinkled
E	Young's modulus
E_{11},E_{22}	orthotropic moduli
G_{12}	shear modulus
k	curvature
ℓ	length of cylinder
M	applied bending moment
N'	defined by equation 3.2-12
N_B	pure bending moment acting at end of cylinder
N_x,N_o	stress resultants in longitudinal and hoop direction
N_c	critical wrinkling load
N_{AX}	uniform load acting at end of cylinder
P	total axial load acting at end of cylinder ($p\pi r^2 - P_{AX}$)
p	internal pressure
P_{AX}	axial load
r	radius of cylinder
t	thickness of cylinder wall
w	displacement normal to cylinder wall
x	axial coordinate
$\tilde{y}$	circumferential coordinate
$\bar{y}$	effective centroid

Greek

α	wrinkling angle
$\varepsilon_x,\varepsilon_y,\gamma_{xy}$	longitudinal, hoop and shear strain
ν,ν_{21},ν_{12}	isotropic, minor and major Poisson's ratio

ρ	curvature of cylinder $(-w,_{xx})$
ρ'	constant defined in equation 4.1-2
σ_1 σ_2	principal stresses
$\sigma_x, \sigma_y, \tau_{xy}$	longitudinal, hoop and shear stress
ϕ	$\tilde{y}/r$
ϕ_o	defined in equation 3.2-1
χ	angle between material axis and structural axis

NOTATION

Section 6

Roman

a	sound speed in air
b	vehicle semi-width
C_c	lumped preumatic Capacitance
C_e	Euler's constant
C_m	discharge coefficient
C_{PQ}	slope of fan pressure - flow characteristic
$f(z)$, (z)	auxiliary exponential integral functions
g	gravitational acceleration
h	hover gap
j	$\sqrt{-1}$
ℓ	cushion perimeter
L_n	natural logarithm
M	suspension mass
N	transfer function relating the averaged motion of the water surface inside the plenum to the cushion pressure
p	pressure
Q	volume flow rate
R	gas constant
R_a	outlet origice resistance
R_c	inlet origice resistance
s	Laplace variable
t	time
T	absolute temperature
V	volume
x	horizontal coordinate
y	vertical coordinate
z	Y+iy

Greek

α_a	hover gap flow parameter
∇^2	Laplacian operator
Δ	perturbation
γ	polytropic coefficient = 1.4 (isentropic)
η	deflection of wave from surface
λ	wavelength
ν	wave number of generated waves
ω	angular frequency
ϕ	velocity potential
ρ	density

Subscripts

a	air
c	cushion
e	equilibrium
t	partial derivative w.r.t. line
w	water
y	partial derivative w.r.t. vertical coordinate

NOTATION

Appendix B

Roman

C_c	cushion or plenum capacitance
C_{PQ}	fan slope coefficient
D	diameter
I_d	duct inertance
m	mass
R	linearized flow resistance
S_a	support area

Greek

α_a	hover-gap flow parameter

Subscripts

a	air
p	cushion or plenum

Appendix C

Roman

a	length of element in x-direction
a_{ij}	coefficients of $w(x,y)$ trial function
$\bar{a}_{ij}$	coefficients of $w(3,\eta)$ trial function
$\{a'\}$	column vector of $\bar{a}ij$'s
A	area of element
A_i	$i=1,8$ entries in $[K_M]$
$[A_w]$	matrix relating $\{a'\}$ to $\{\delta_B\}$
b	length of element in y-direction
b'_i	$i=1,2$; coefficients of $u_{,x}(x,y)$
$\bar{b}_i$	$i=1,2$; coefficients of $u_{,x}(\xi,\eta)$
$<b'>$	row vector of $\bar{b}_i$'s

$[B_u]$	matrix realting $\{b'\}$ to $\{\delta\}$
B_i	i=1,5; entries in $[K_m]$
C_i	coefficients of $v_{,y}\ (x,y)$
$\bar{C}_i$	coefficients of $v_{,y}(\xi,\eta)$
$<c>$	row vector of $\bar{c}_i$'s
$[C_v]$	matrix relating $\{c\}$ to $\{\delta\}$
$[C]$	matrix relating $\{\delta_B\}$ to $\{\alpha\}$
$[D]$	diagonal matrix
e_x, e_y, e_{xy}	displacements defined by equation A-7
E	Young's modulus
E_{11}, E_{22}	orthotropic muduli
f_i	i=1,2; coefficients of $u_{,y}(x,y)$
$\bar{f}_i$	i=1,2; coefficients of $u_{,y}(\xi,\eta)$
$<f>$	row vector of $\bar{f}_i$'s
$[F_u]$	matrix relating $\{f\}$ to $\{\delta\}$
g_i	i=1,2; coefficients of $v_{,x}(x,y)$
$\bar{g}_i$	i=1,2; coefficients of $v_{,x}(\xi,\eta)$
$<g>$	row vector of $\bar{g}_i$'s
$[G_v]$	matrix relating $\{g\}$ to $\{\delta\}$
G_{12}	orthotropic shear modulus
h	thickness of cylinder wall
I_i	i=1,5; integrals forming the coupling stiffness
I_i	i=1,5; integrals forming the coupling stiffness
k_x, k_y, k_{xy}	rotations defined in equations A-8
$[K^*]$	global stiffness matrix
$[K_B]$	bending stiffness matrix
$[K_i]$	i=1,5; component stiffness matrices of $[K_{MC}]$
$[K_M]$	membrane stiffness matrix
$[K_{MC}]$	coupling stiffness matrix

$[K_T]$	total element stiffness matrix
ℓ	length of cylinder
m	$\cos(\chi)$
$[M_i]$	$i=1,6$; integral coefficients matrices in calculation of $[K_B]$
n	$\sin(\chi)$
P_u, P_v	applied membrane loads
P_w	applied bending loads
$\{P\}$	total column vector of applied loads
$\{P_B\}$	column vector of applied bending loads
$\{P_M\}$	column vector of applied membrane loads
$\{P^*\}$	global column matrix of total applied loads
Q	internal pressure
$\bar{Q}_{ij}$	coefficients relating the stresses to the strains defined by equation A-2
Q_{ij}	defined by equations A-3 and A-4
Q^*_{ij}	$h\bar{Q}_{ij}$
Q^+_{ij}	$h^3\bar{Q}_{ij}/12$
r	radius of cylinder
$\{S\}$	integral weighting vector or $\{S_B\}$ in consistent load vector calculation.
u	axial displacement
u_{ij}	Axial displacement at node i,j
U	total strain energy
U_B	bending strain energy
U_M	membrane strain energy
U_{MC}	curvilinear coupling strain energy
v	circumferential displacement

v_{ij}	circumferential displacement at node i,j
w	normal displacement
w_{ij}	normal displacement at node i,j
W	work done by external loading
W_1, W_2, W_3	work done by out and in plane loads
x	axial coordinate
(X)	integral coefficient matrix formed while evaluating $[K_{MC}]$
y	circumferential coordinate
$[Y]$	integral coefficient matrix formed while evaluating $[K_{MC}]$
z	radial coordinate from middle surface
$[Z]$	integral coefficient matrix formed while evaluating $[K_{MC}]$

Greek

$\{\alpha\}$	column vector of coefficients resulting from expansion of w(s,y)
γ_{xy}	shear strain with respect to structural axes (x,y)
$\{\delta\}$	total column vector of element degrees of freedom (displacements and rotations)
$\{\delta_B\}$	column vector of out of plane displacements and rotations
$\{\delta_M\}$	column vector of membrane displacements
$\{\delta^*\}$	global column vector of degrees of freedom
ϵ_x, ϵ_y	normal strains with respect to structural
η	y/b
θ	y/r
υ	Poisson's ratio
$\upsilon_{12}, \upsilon_{21}$	major and minor Poisson's ratios
ξ	x/a

$\Pi\rho$	total potential energy
σ_x, σ_y	axial and circumferential stresses
τ_{xy}	shear stress
χ	fibre orientation with respect to the longitudinal cylinder axis
$(\ )_{,xy}$	$\frac{\partial^2}{\partial\chi\partial y}$
$\{\ \}$	column vector
$<\ >$	row vector
$[\ ]$	matrix
$[\ ]^T$	transpose of matrix
$[\ ]^{-1}$	inverse of matrix

NOTATION

Appendix D

Roman

A	area
C_m	discharge coefficient
L	length
p	pressure
R	ratio
r	radial coordinate
s	streamline coordinate
T	time
v	velocity

Greek

Δ	small perturbation
π	3.14159
ρ	density
ω	frequency

Subscripts

c	cushion or plenum
e	equilibrium
σ	orifice

1) INTRODUCTION

1.1) Overall Objective

This report describes the results obtained from a programme of research on the dynamical and stability properties of flexible skirted air cushions undertaken at the Institute for Aerospace Studies of the University of Toronto (UTIAS) under contract with Transport Development Centre (TDC) during the period July, 1977 to December, 1979. The Work Statement of this Contract (TDC File D-500-431) is given in Appendix A. Considerable progress has been made in the reporting period for this Contract, and a number of important basic results have been obtained. However, since the Contract covers a specific interval of time, some of the work reported in this document is incomplete from a scientific viewpoint.

The overall long-term objective of the UTIAS air cushion technology research programme is to develop carefully validated analytical descriptions or "mathematical models" of the dynamical processes that can occur in flexible skirted air cushion systems. It is our intention that these mathematical models be of use to the air cushion vehicle (ACV) designer, in the first instance to provide basic qualitative insights, but also in some cases, to obtain quantitative design data. Furthermore, an appreciation of these models can facilitate the interpretation of laboratory scale physical model tests. Since the objective is to produce aids to design, it is very important to develop these mathematical models which are the simplest that can be used to obtain a suitable level of accuracy for engineering prediction purposes.

An overriding consideration of the programme is the use of carefully defined and well controlled experiments which are capable of unequivocal confirmation of various theoretically predicted effects. It is intended that the experiments relate as closely as possible to problems of current technical interest, but in many cases the technical problems encountered are so complex that highly simplified experiments have to be defined in order to provide the desired unequivocal interpretation. Once having obtained satisfactory agreement in such simplified situations, the investigations can then proceed by systematically incorporating selected aspects in order to build up a comprehensive picture of the pertinent phenomena.

The relevance of this and previous UTIAS research to TDC's mission is perhaps most easily assessed in terms of the use of particular cushion geometries to provide guidance for emphasis on certain problems. These cushion geometries usually are similar to those currently being developed in industrial programmes funded by TDC or other Canadian Government departments. For work undertaken for TDC prior to the present Contract, the cushion systems of interest were of the multicell type [Refs. 1.1 and 1.2]. For the present Contract, the cushion geometry used in much of the testing is an uncompartmented segmented skirt cushion resembling designs developed by Hoverlift Systems Limited (HSL) of Calgary. The latter skirt is, in turn, based on the ideas of Hovercraft Development Limited (HDL) of Britain. HSL's prototype vehicle is shown in Figure 1.1. Figure 1.2 is a photograph of the UTIAS 43m Circular Track test vehicle Vampire I flying with this skirt. It is to be noted that, although UTIAS experience with these two radically different cushion types has resulted in the definition of problems that are perhaps peculiar to each type, the most striking feature has been the emergence of a number of problems of a basic nature which require careful investigation and which occur in one

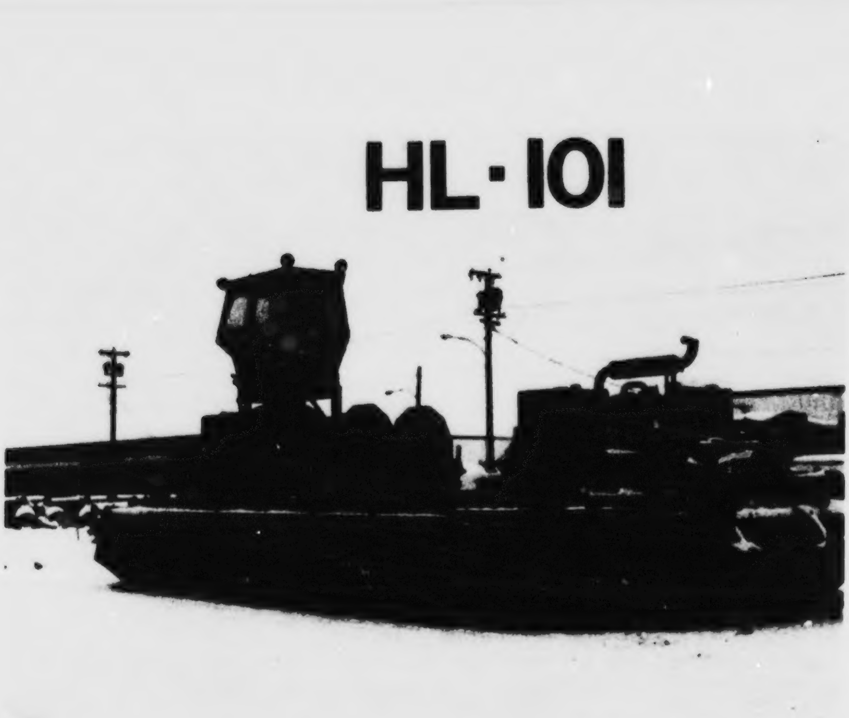

FIG. 1.1 HSL's PROTOTYPE VEHICLE

FIG. 1.2 UTIAS TEST VEHICLE, VAMPIRE I, FLYING OVER RAMP.

form or another in both cushion systems.

The work described here was also supported by the author's Natural Sciences and Engineering Research Council (NSERC) Grants, and individual projects in the UTIAS air cushion technology research programme cannot in general be considered as support by either agency. Hence the following description gives an overview of the entire programme.

1.2) Projects Identified for the Present Contract

1.2.1) Experimental Measurement of Dynamic Stability Boundaries of Simple Air Cushions

Because the dynamic stability of air cushion suspensions is affected by so many factors, the design of a suitable experiment to test theoretical models represented a formidable task. Section 2 presents the design of such a critical experiment, the results of which confirm the large duct effects predicted by our earlier theoretical work. An important feature of the experiment is the use of a large pneumatic filter between the fan and the duct-plenum system studied which effectively removed or isolated fan dynamics. Section 2 uses the opportunity provided by the experiment to assess the usefulness of the available mathematical models of air cushion dynamics. In particular, the implications of the many assumptions employed by the models are explored.

1.2.2) Investigation of the Static Pitch and Roll Stiffness Characteristics of the HSL Cushion

This project involved construction of suitably scaled segmented skirt cushion systems similar to the HSL designs for both the Circular Track Vehicle and the Pitch and Roll Table model. The aim was to develop a simple theory for heave, pitch and roll stiffness based on the plenum chamber assumption, one-dimensional orifice flow laws and the ideal-model skirt concept; and then to compare this with experimental results obtained for the two models. Requirements of the theory are to describe the method of generating restoring forces, predict cushion pressure and flow, and model the vehicle motion.

The restoring forces, cushion pressure and centre of gravity motion are intrinsically coupled. For example, the movement of the centre of mass that occurs during a rolling manoeuvre must be known to reasonably accuracy in order to be able to apply Newton's laws of mechanics. Also, application of the basic cushion mass flux conservation law requires information about the mass flux of air escaping from the cushion, and this in turn has to be calculated, since a direct measurement of this time varying quantity is impossible. This in turn requires knowledge of both the history of the cushion pressure and the effective air escape area generated by the cushion as a result of its motion. Thus, as a minimum, a knowledge of skirt geometry during motion and a description of the fan characteristic are necessary. Geometrical information on the HSL cushion system is presented in Section 3.

A notable feature of roll and pitch stiffness characteristics presented in References [1.1] and [1.2] is the occurrence of hysteresis. The experimental results for the HSL skirt presented in Section 3 show that the amount of hysteresis depends on the type of material used for the skirt and in the case of low hysteresis good agreement with the theory is obtained. The question of proper scaling of skirt material properties is therefore addressed in Section 3 briefly.

1.2.3) Investigation of the Pitch-Heave Dynamics of the Segmented Skirt (HSL) Cushion

This project involves measuring the dynamic response of the HSL skirt equipped Circular Track Vehicle. Data is generated by flight over a ramp type disturbance. The aim is to use the disturbance to excite motion in pitch and heave, but without any rolling. This appears to be a relatively simple yet practical case. Pitching motion, which might be considered to be the major feature of vehicle response to disturbances which are aligned at right angles to the forward motion direction, cannot be considered to be uncoupled from the motion that occurs in heave. A characteristic feature of flexible skirt systems is that pitching or rolling usually involves simultaneous vertical translations of the centre of mass of the vehicle, or heaving; this aspect of vehicle motion is discussed in Section 3 of this report. The work has two specific targets:

(i) evaluation of the accuracy with which the theory developed for the description of the cushion static behaviour in the project described in Section 1.2.2 predicts the effect of the static cushion properties in vehicle dynamic behaviour,

(ii) evaluation of the relative importance of the various possible sources of cushion damping in the Circular Track Vehicle motion, together with interpretation of the relative significance at full scale.

There are at least four possible sources of damping or energy dissipation that can occur in ACV dynamics. Firstly, the air that is being pumped into and is escaping from the cushion periphery carries with it energy. Both processes involve turbulent dissipation and the motion of the vehicle can modulate the flows in such a way as to cause both positive and negative damping of the vehicle motion. The latter case is the source of the dynamic instabilities discussed elsewhere in this report, and the possibility of its occurrence is not so intuitively evident. The former case is however; simply put the cushion volume is equivalent to the cylinder of a dashpot or "shock absorber", while the motion of the ground relative to the base of the vehicle is equivalent to the piston in that dashpot. The second source of damping is that due to the hysteretic phenomenon mentioned in Section 1.2.2. Thirdly, sliding or dry friction forces generated by those parts of the skirt in contact with the ground and which move relative to it as a result of vehicle motion. Finally, the external aerodynamics can contribute significant damping at high enough vehicle speeds.

It is expected that, for the low speeds which are characteristic of presently considered applications of the HSL cushion, the contribution from the external aerodynamics is small, so that it is not examined in the present work. Furthermore, since this cushion relies on skirt-ground contact to generate its heave, pitch and roll stiffness characteristics the possibility that sliding friction might make significant contributions to damping has to be considered.

The project involved five key steps:

(i) design, construction and installation of an HSL type segmented skirt cushion for the Circular Track Vehicle, Vampire I,

(ii) formulation of a suitable theoretical model of the pitch-heave dynamics of this vehicle,

(iii) development of a computer programme for the analysis of the Circular Track test flight data,

(iv) design and development of a digital data acquisition system for serial transmission of data along a light cable to the data acquisition computer,

(v) implementation of a test program using Vampire I to assess the accuracy of the theoretical model.

The first item is a straightforward exercise, the third is discussed in detail by Sullivan et al [Ref. 1.3] and the fourth is detailed by Ribner [Ref. 1.4]. Items (ii) and (v) are dealt with in Section 4 where a linear pitch-heave model of the dynamics is derived and the results of static and dynamic tests using Vampire I are presented.

1.2.4) Buckling of Skirt Material

A "single-wrinkle-creep" phenomenon encountered at one stage in the UTIAS programme [1.2] raised the expectation that, for design purposes on practical cushion geometries, one might be able to bypass the complex process of analysis of a partly wrinkled structure. It was envisaged that one would simply use inelastic membrane theory to predict the initiation of wrinkling, and assume that buckling occurred soon after. However, the results given in reference 1.3 clearly indicate that, for isotropic materials at least, wrinkling can occur well before the structure may have failed.

Hence this project was focussed on two points:

(i) exploration and development of methods for the analysis of partly wrinkled membrane structures, and

(ii) investigation of the nature of the wrinkling/buckling process for elastomer-fabric materials.

As discussed in reference [1.3], the wrinkling process may be characterized by a highly nonlinear orthotropic elastic material which is very soft in compression. Because of this relationship between the two objectives it was decided to focus attention on the development of a finite element numerical computer programme to analyse the buckling properties of shells made from orthotropic materials. Section 5 gives the details of the program and the results obtained.

1.2.5) Stability Over Water

There are many potential Canadian uses for slow moving air cushion suspension systems that can operate over water as well as over land. However, unlike overland stability, very little is known about overwater stability. Section 6 presents some preliminary work on the heave stability overwater problem. The effect of the cushion volume pumping resulting from the water surface motion is explored and is shown to have a large stabilizing effect for the geometry considered. This does not agree with field observations of stability recently made by Fowler. It is believed that the reason for the discrepancy is the crude model used for the air flow at the lip of the cushion. This model did not take into account the flow modulation which would result from water surface motion in the neighbourhood of the lip. More recent work, not reported here, has confirmed the above suspicion. Understanding the overwater stability question is important because, among other things, a vehicle that could be made to oscillate at any desired amplitude over water could be used to set up a train of outgoing waves that could augment the ice breaking capability of existing slow moving air cushion ice breakers, which is probably the most important application of air cushion technology in Canada to date.

2) EXPERIMENTAL MEASUREMENT OF DYNAMIC STABILITY BOUNDARIES FOR SIMPLE AIR CUSHIONS

2.1) Introduction

This section describes the experiments undertaken to verify the theoretical predictions of the linear dynamical stability boundaries for simple air cushion geometries given in the report to TDC covering progress in the 1977-78 period [Ref. 2.1]. Although these experiments are confined to consideration of a very simple case, namely a single plenum chamber which is supplied with air through a duct and which is constrained to move only in heave, they nevertheless provide an important foundation which allows the more complex geometries and motions characteristic of practical systems to be investigated in a systematic way. It is to be noted that very little information is available in the open technical literature describing experimental confirmations of analyses of the dynamic behaviour of air cushions. Indeed the authors of this report are aware of only one investigation which provides some experimental data on the stability aspect of this general problem [Ref. 2.2]. Most of the work described in this section formed part of a general investigation of the stability problem undertaken for a Ph.D. programme at the University of Toronto [Ref. 2.3].

The major geometrical features of the system used in the theory are given in Figure 2.1. A fan or other source supplies air to a straight duct having length L_D and cross-sectional area A_d. This duct, which is fixed in the laboratory frame of reference, supplies air through a flexible bellows to a rigid-wall plenum chamber cushion which is constrained to allow only heaving motion; that is, translation in the vertical direction. The cushion cell is a circular cylinder having diameter D_p and height L_p. When the cushion is hovering in dynamic equilibrium it forms a hovergap h_e relative to a flat horizontal ground plane.

Typical theoretically predicted stability boundaries for this system obtained by the analysis described in Ref. 2.1 are given in Figure 2.2. The curves give the equilibrium gauge cushion pressure p_{ce} at the onset of instability as a function of h_e/D_p, for selected ratios of length to diameter of a circular duct. The hatched sides of the curves are unstable. The Routh-Hurwitz criteria for the lumped capacitance model indicate that, at the onset of instability, the cushion gauge pressure p_c, expressed as a fraction of atmospheric pressure, should be the same for systems of different size but having the same geometric proportions (see Appendix B). This is the rationale for the present format.

The quantity h_e/D_p is related to the cushion flow coefficient C_{QC} [Ref. 2.4]

$$C_{QC} = Q_e(\rho/2WA_{ref})^{\frac{1}{2}} \qquad (1)$$

In equation (1), Q_e is the cushion equilibrium flow rate, ρ_a is the atmospheric density, W the total weight carried by the cushion, A_{ref} is a reference area, and C_m is the usual orifice discharge coefficient. Here,

$$W = \frac{\pi}{4} D_p^2 \, p_{ce} \quad \text{and} \quad A_{ref} = \frac{\pi}{4} D_p^2$$

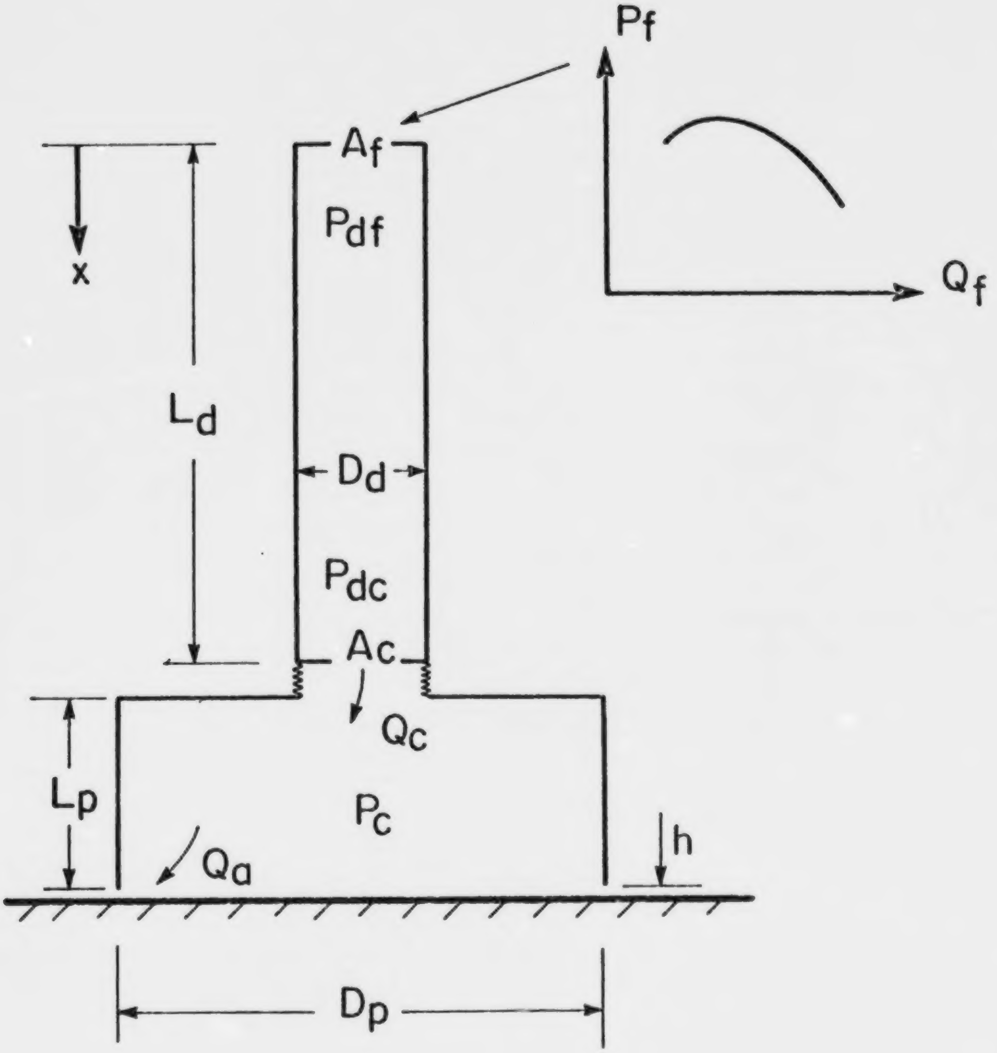
Pf
Qf
Af
Pdf
x
Ld
Dd
Pdc
Ac
Qc
Lp
Pc
h
Qa
Dp

FIGURE 2.1 FAN-DUCT-PLENUM CHAMBER MODEL USED IN STABILITY CALCULATIONS.

Hence these results correspond to cushion flows in the range $0.004 \leq C_{QC} \leq 0.01$. This is typical of values used in practice [Ref. 2.4].

Two types of reference conditions for the air source or fan are used in Figure 2.2. The first is a constant pressure source, denoted by $C_{PQ} = 0$, which may be considered as resulting from the use of a very large fan; and the second is a constant volume flow source, corresponding to $C_{PQ} = -\infty$, which corresponds to a very small fan. The constant pressure source is a particularly useful reference condition for comparison purposes, since it corresponds to the idealized condition in which all fan and other air supply system dynamics have been eliminated. It is the analog of a constant voltage source used in electric circuit theory. All of the hatched curves given in Figure 2.2 correspond to a constant pressure source.

Several features of these curves should be noted. First, a commonly held belief is that for a given system, increase in cushion pressure favours the onset of instability. While, as is noted in Ref 2.3, for simple systems this is generally true, the results given in Figure 2.2 show that the reverse can occur. Typically, for $h_e/D_p = 0.001$ and duct geometry 3 - corresponding to $L_D/D_D = 8$ - as the cushion pressure p_c/P_a is increased from zero, the system is initially stable, then becomes unstable at $p_c/P_a = 0.002$ and stable again at $p_{ce}/P_a = 0.018$. Another major feature is that all of the systems become unstable for sufficiently small h_e/D_p. Finally, as the duct lengths are increased the stability boundaries approach that obtained for a constant mass flow source. Detailed theoretical explanations for these features of the stability boundary structure are given in Section 2 of Ref. 2.1, but here it is sufficient to note that the very large effects that even moderately long ducting has on stability is associated primarily with the inertia of the air in the duct. This is shown in Figure 2.2b.

It is observed that the analyses of cushion dynamics and stability used in the work undertaken for the present contract and elsewhere are based on a relatively large number of assumptions. These assumptions may not always apply to the various ACV configurations encountered in practice, and it is very important to have a clear appreciation of their limitations. The experimental results described herein were obtained under conditions which provided an unusual opportunity for a critical comparison of theory and experiment. It is therefore considered appropriate to describe briefly the equations for the simplest possible theoretical model of the cushion-duct system used in the experiments and review the associated assumptions. This is done in the next section. It is noted here that the theoretical results for the duct problem described in the 1978 Report [Ref. 2.1] were obtained well before conception of the experimental set-up described herein; and the only experimentally measured quantity used by the theory is the discharge coefficient for the steady flow out of the cushion.

2.2) Review of Equations and Assumptions Used in Analysis

2.2.1) Equations for Simplified Model

The fan or other air source is assumed to have a given static supply characteristic for pressure p_f as a function of volume flow Q_f expressed in the functional form

$$p_f = p_f(Q_f) \tag{1}$$

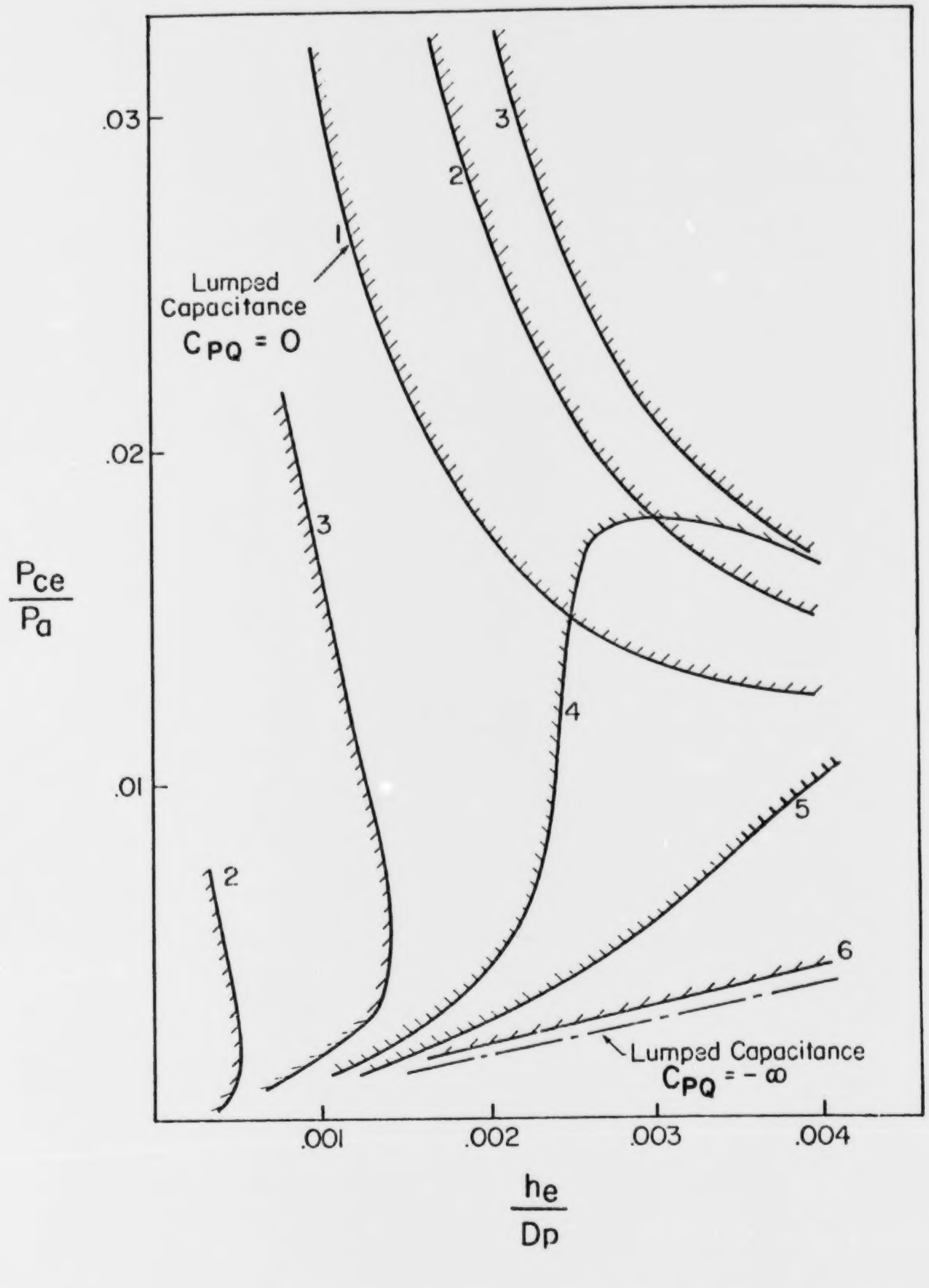

FIGURE 2.2A TYPICAL FINITE ELEMENT HEAVE STABILITY RESULTS; CASES 1 TO 6 HAVE RATIOS OF L_D/D_D OF 0.125, 4.0, 8.0, 11.25, 16.0 and 64 RESPECTIVELY.

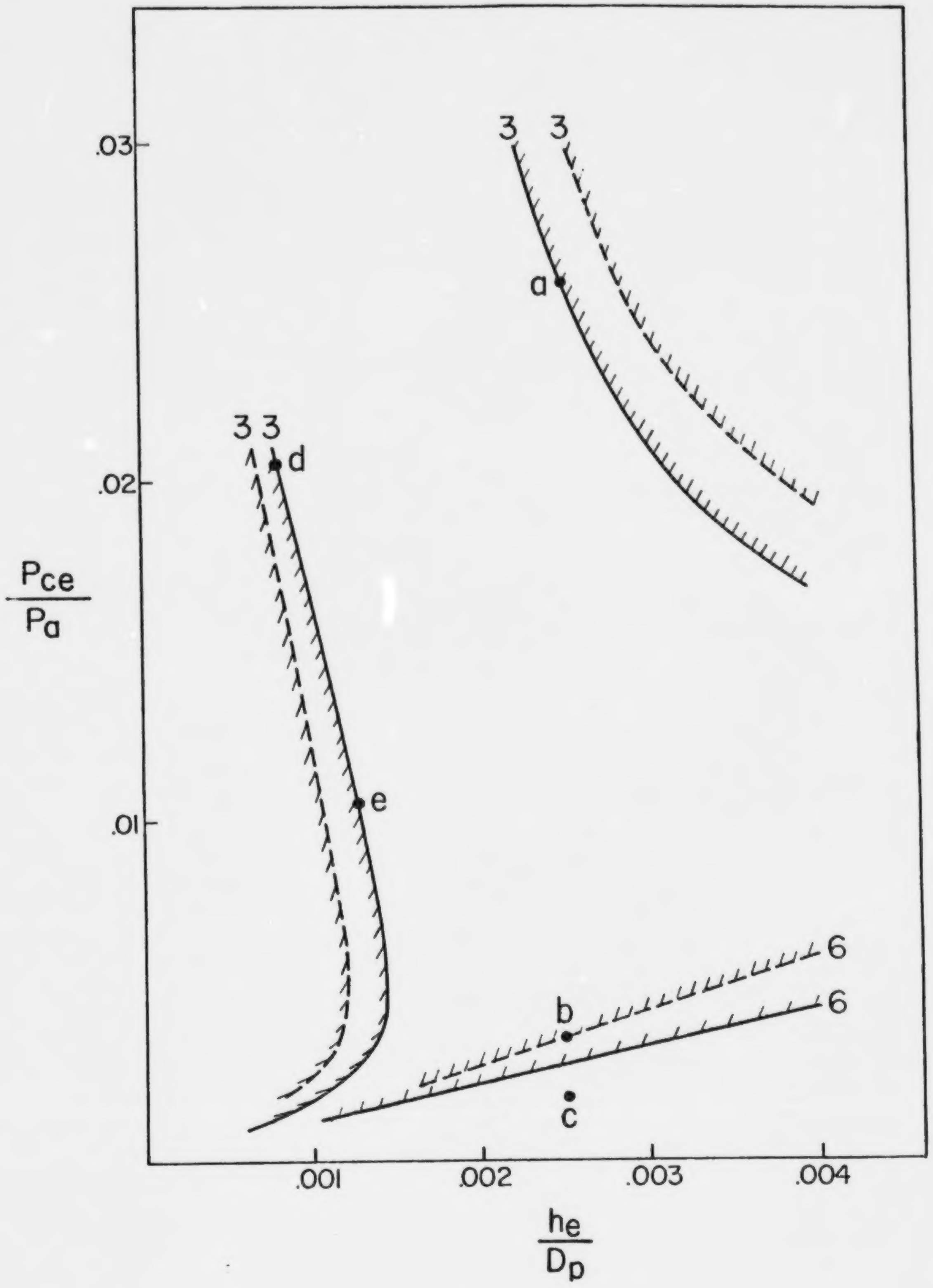

FIGURE 2.2B COMPARISON OF FINITE ELEMENT AND LUMPED INERTANCE RESULTS. CASE 3, L_D / D_D = 8, CASE 6, L_D / D_D = 64

In order that the cushion be statically stable, at the operating point on this curve - denoted by the subscript "e" - this characteristic must have a negative slope, that is one must have

$$C_{PQ} = \frac{Q_f}{p_f} \frac{dp_f}{dQ_f}\bigg|_e < 0, \tag{2}$$

unless a stabilizing resistance-orifice is incorporated at some point downstream. During dynamic motion of the cushion system, changes in fan supply pressure and volume flow are assumed to be still governed by equation (1); the fan is said to behave "quasistatically".

The air flow in the duct is modelled as a lumped inertance, that is, it is assumed to move as if it is a single rigid mass, with a velocity given by the instantaneous mass-average velocity associated with the volume flux through the duct

$$q_d(t) = Q_d(t)/A_d \tag{3}$$

In this approximation, the volume flux at any instant into the duct at the fan end is equal to the flux out at the cushion end. Changes in $q_d(t)$ are therefore caused by differences in p_{df} and p_{dc}, the pressures at the fan and at the cushion end of the duct respectively. Usually $p_{dfe} \leq p_{fe}$, and if no stabilizing resistance orifice is included at the downstream end, $p_{dce} \cong p_{ce}$, the cushion pressure. The equation relating end pressure differences to $q_d(t)$ is simply Newton's law for a single mass, which is[1]

$$\rho L_d A_d \frac{dq_d}{dt} = p_{df} A_d - p_{dc} A_d + F_f(t) \tag{4}$$

Here $\rho L_d A_d$ is the mass or inertia of the air in the duct and F_f is any resultant frictional forces. For low enough mean q_d, the frictional forces are small, and are neglected in the simplified model. Equation (4) can be expressed in terms of the volume flux as follows:

$$\left(\frac{\rho L_d}{A_d}\right) \frac{dQ_d}{dt} = p_{df} - p_{dc} \tag{5}$$

The quantity $\rho L_d/A_d$ is called the inertance by virtue of the analogy with electric circuit problems involving inductances. The analog of pressure, the voltage $e(t)$ applied to an inductance coil, is given by $L di/dt$, where $i(t)$ is the instantaneous current passing through the inductance L.

If a stabilizing orifice is included between the duct and the cushion volume, the flow through this is assumed to be described at each instant of time by the steady incompressible orifice flow law:

$$Q_d = C_m A_{dc} \sqrt{\frac{2(p_{dc} - p_c)}{\rho}} \tag{6}$$

where A_{dc} is the area of the orifice separating the duct and the cushion, and C_m is an orifice flow discharge coefficient.

---

[1] Equation (4) also follows from the equations of one-dimensional unsteady flow together with the assumption of incompressibility and constant cross-sectional area of the duct.

The vertical motion of the cushion is assumed to be governed by Newton's law for a single rigid mass,

$$\frac{W}{g}\frac{d^2h}{dt^2} = S_a p_c - W \qquad (7)$$

where W is the total weight supported by the cushion, g is the acceleration due to gravity, h is the heave height, S_a is the support area over which the cushion pressure acts.

The relationship between p_c and air mass fluxes is governed by the conservation of mass applied to the varying cushion volume, which is

$$\frac{d}{dt}(\rho_c V_c) = \dot{m}_c - \dot{m}_a \qquad (8a)$$

in which ρ_c is the density of the air in the cushion, V_c is the total cushion volume, $\dot{m}_c$ is the mass flux of air into the cushion, and $\dot{m}_a$ is the mass flux that escapes to atmosphere. The cushion volume V_c comprises two parts, the fixed or "dead" volume V_d enclosed by the cell walls, which is $V_d = \pi/4 \cdot D_p{}^2 L_p$; and the changing or active volume V_a generated by the hovergap, which is the product of the cushion footprint area S_a and the hovergap, that is

$$V_c = V_d + S_a h \qquad (8b)$$

The compression-expansion process in the cushion volume is assumed to be isentropic: with the atmospheric pressure p denoted by P_a, one has

$$\frac{(p_c + P_a)}{\rho^\gamma} = \text{constant} \qquad (9)$$

Finally the unsteady air escape process from the cushion is assumed to be governed by the steady incompressible orifice flow law coupled to a varying hovergap; that is

$$\dot{m}_a = C_m \ell_p h \sqrt{2 p_c \rho_c} \qquad (10)$$

where ℓ_p is the length of the cushion lip; here $\ell_p = \pi D_p$.

Linear stability boundaries for this system of equations may be obtained by standard techniques, these are described in Ref. 2.1 and in more detail in Ref. 2.3. In these analyses, the nonlinear aspects which arise from the cushion fan law, the cushion conservation law and the Bernoulli law for the orifice and cushion lip flows are all replaced by their linearized small perturbation equivalents. The cushion conservation law is modelled as a lumped pneumatic capacitance, in which case, equations (8) and (9) are replaced by

$$\frac{dV_c}{dt} + C_c \frac{dp_c}{dt} = Q_c - Q_a \qquad (11)$$

In this equation, C_c is the cushion capacitance, and the quantities Q_c and Q_a are the volume fluxes into the cushion and to atmosphere respectively. The cushion capacitance is given by

$$C_c = \frac{V_c}{\rho a^2} \qquad (12)$$

where a is the sound speed, which for a calorically perfect gas such as air at atmospheric conditions is given by $a^2 = \gamma RT_a$.

In Section 4 of Ref. 2.1, the importance of nonlinear effects is discussed in some detail. It is suggested that, for cushions operating at moderate pressures, the nonlinear deviations from the capacitance law are very small. Furthermore, for many but not all cushion systems, the static and dynamic motion entails only relatively small deviations along the fan characteristic from the operating point. The most important nonlinearities are those associated with the use of the Bernoulli laws for orifice and cushion lip flows, and the phenomenon of "shut-off". The analysis given in Section 4 of Ref. 2.1 suggests that they generally cause a cushion system operating at conditions which make it unstable in the linear sense to enter a stable finite amplitude oscillation or limit cycle. The present experiments are limited to measurement of linear stability boundaries.

The applicability of the assumptions implied in the use of the equations is now reviewed.

2.2.2) Assumptions

2.2.2.1) Quasisteady Fan Law Approximation (Equation 1)

It has been noted elsewhere that, during dynamic operation of an air cushion system, the effective fan characteristic can deviate significantly from that determined in a static test [Refs. 2.5 to 2.11]. For the fans used in ACV's, it is expected that such deviations can arise from two sources. One is the inertance of the air in the volute of a centrifugal fan or the annulus of an axial flow fan. The second is the unsteady blade aerodynamics in the fan rotor-stator system itself. Thompson and others [Ref. 2.8] developed a combined capacitance-inertance model for the annulus and other volumes of a single stage axial flow fan, but did not consider unsteady blade aerodynamics. For the frequencies of interest to them, this model appeared to account for most of the observed unsteady effects. However it is to be noted that, for anything but the simplest fan geometries similar to the one used in Ref. 2.8, accurate computation of the numerical values of effective inertance and capacitance from the given fan geometry may be difficult. This difficulty might be expected to be especially acute in the case of centrifugal fans directly feeding into a duct, such as that used by Goldschmied and Wormley [Ref. 2.7] and in the experiments first used here.

The situation is greatly complicated if the cushion oscillation frequencies are high enough to excite unsteady fan blade aerodynamics. However, one would expect that this would only occur if the time of passage of a typical fluid particle through the rotor τ_p is of the same order of magnitude as the period of the cushion oscillation τ_c. For most cushion and fan geometries one might expect that $\tau_p << \tau_c$. Ohashi [Ref. 2.10], who conducted an extensive investigation of the dynamic characteristics of turbopumps, gives a criterion for the onset of significant unsteady blade aerodynamics. For his analytical development, he assumed that the pump could be approximated by a two-dimensional linear cascade of airfoils, but in his experiments, he used a centrifugal water pump. He suggested that the blade aerodynamic response at low frequencies could be given approximately by a first order lag having the form

$$\frac{\Delta p_f(s)}{\Delta Q_f(s)} = \frac{dp_f/dQ_f|_e}{\tau_R s + 1} \tag{13}$$

Here $s = \sigma + j\omega$ is the Laplace variable, τ_R is the critical time constant:

$$\tau_R \cong \frac{1}{\alpha} \frac{\cos\lambda_R}{2\pi N_R \phi n} \tag{14}$$

Here α is a constant for a particular fan geometry determined by either theory or experiment. The angle λ_R is the stagger angle of the rotor blades, N_R is the number of rotor blades, and n is the rotational speed. The quantity ϕ is the usual low coefficient, the ratio of the axial flow velocity to a representative rotor blade velocity; the latter is taken by Ohashi to be that at the tip of the rotor or impeller. The quantity τ_R is directly proportional to the time τ_p required for a typical air particle in the cascade to travel one blade chord length. The "reduced frequency", ω_R of any system oscillation of frequency f is simply given by $\omega_R = 2\pi\alpha\,\tau_R f$. According to Ohashi's theory $\alpha = 0.3$; however his experimental results obtained using a centrifugal pump indicated that α could be as low as 0.1; this implies a significant increase in the possibility that unsteady blade aerodynamics may be important. Note that the frequency response characteristics of a first order lag indicate that a 10% reduction in amplitude response from its quasisteady value occurs for oscillations having a period of $2\tau_R$.

For high enough frequencies, the first-order lag approximation breaks down, since both Ohashi's theory and his experiments indicate that the phase lag for high ω_R approaches 45° instead of that appropriate to equation (13), namely a lag of 90°. In an attempt to circumvent this difficulty, Goldschmied and Wormley [Ref. 2.7] modified the empirical fit suggested by Ohashi [Ref. 2.10] to give the correct phase lag at large ω by setting

$$\frac{\Delta p_f(s)}{\Delta Q_f(s)} = \frac{dp_f/dQ_f|_e}{\sqrt{\tau_R s + 1}} \tag{15}$$

Ohashi's results suggest that, for self excited oscillations, as far as the fan blade or rotor aerodynamics is concerned, the flow should be quasi-steady. Hinchey [Ref. 2.3] calculates that for a 15.0 tonne towed raft operating at half load $\tau_R \cong 0.03$ seconds, whereas the period of a typical oscillation is 0.25 second or longer. However he also notes that for very heavy loads operating at low cushion flows, which corresponds to a reduction in ϕ, the value of τ_R could become large enough to have significant effects. However fan blade stall might occur first as ϕ is reduced. For certain other ACV dynamics problems, the blade aerodynamics is likely to be highly unsteady. One example is the heave dynamics and ride habitability of an ACV moving at high speed over water waves. In such cases a model such as equation (15) must be used.

This discussion suggests that considerable care has to be taken in the selection of a fan system for cushion dynamics experiments; otherwise the interpretation of results may be greatly complicated. For example, the authors initially selected a standard industrial centrifugal blower which had a volume flow capacity sufficient to encompass the range required for the experiments. For cushion models operating at correctly scaled values of C_{QC}, and with computed oscillation frequencies in the range 10 to 15 Hz, the critical frequency for the onset of unsteady blade aerodynamics was estimated from equation (14) to be in the range 1.5 to 3 Hz. However, these conditions involved operating at a point on the steady state characteristic for which $dp_f/dQ_f|_e$ was small, so that the contribution to the overall dynamic characteristic might be small compared to those caused by the inertance and capacitance of the air in the fan volume. An additional problem was that some of the test conditions required operation at points on the steady state characteristic for which $dp_f/dQ_f|_e > 0$, and this implied that surging might occur.

Considerations such as these led the authors to conclude that it might be necessary to determine the true unsteady fan characteristic by direct experiment, so that one can distinguish between fan dynamic effects and true cushion effects. This entails the measurement of the true unsteady volume flow at the exit of the fan and the fitting of a suitable dynamic model - such as a first order lead-lag - to the data. An alternative route is to develop a configuration which clearly minimizes or eliminates any possible fan dynamic contribution to the experiments. The latter route was finally chosen for experiments described here.

2.2.2.2) Modelling of the Duct Flow as a Lumped Inertance (Equation 5)

The theoretical investigation of duct effects completed in the 1978 reporting period [Ref. 2.1], which used the well-known partial differential equations for one-dimensional hydraulic transients [Ref. 2.12], provides the most comprehensive and fundamental treatment of duct effects on cushion stability available to date. This shows that the lumped inertance concept describes the major features of the stability curves, but for accurate descriptions to a typical accuracy acceptable to engineers, a more refined model is required. Most of the discrepancy appears to be associated with the pneumatic capacitance of the duct [Ref. 2.3]. Other possible effects such as wall friction have been found to be negligible for most practical duct lengths. Hinchey [Ref. 2.3] states that for most geometries of practical interest, the duct capacitance can be adequately modelled by lumping it with the cushion capacitance.

In an earlier treatment of the duct problem, Sweet, Richardson and Wormley [Ref. 2.2] modelled the duct flow by the equations of one-dimensional acoustics for distributed volume flow and pressure perturbations, and included duct friction by lumping it as equivalent resistance orifices at the ends. In their frequency response analysis, the transfer functions relating the pressure $p_{dc}(t)$ and flow $Q_{df}(t)$ at the end of the duct to the corresponding values at the cushion end $p_{dc}(t)$ and $Q_{dc}(t)$ introduce hyperbolic functions of the Laplace variable $s = \sigma + j\omega$, as is characteristic of wave propagation phenomena. For low frequency behaviour these functions may be approximated by truncation of infinite order product representations. They note that, for many practical systems, an accurate representation may be obtained by using only the first term in this product. This is, in effect, a combined lead-lag network in which the lead and lag constants involved relate directly to the inertance and capacitance respectively.

2.2.2.3) Lumped Volume Approximation (Equation 8)

The cushion conservation equation (8) assumes that any effects of internal flow structure inside the cushion volume can be ignored, so that it can be modelled as a reservoir. Now it is clear that, if cushion equilibrium flow rates are increased sufficiently, internal flow structure can be made to have a significant effect. Typically, for the model depicted in Figure 2.1, at sufficiently high Q and large associated hovergap h_e, the cushion may begin to act as if it is a jet directed vertically downwards against the ground-board. The crucial question is: for the cushion geometries typical of those used in practice, do such effects occur at representative cushion flow rates?

Some preliminary experiments, undertaken prior to the present Contract, suggested that internal flow effects which may be of practical significance do actually occur. The system used for these tests is depicted in Figure 2.3, and representative data is given in Figure 2.4. A large change in the location of a stability boundary was obtained by altering the cushion feed geometry from a single central feed hole to a set of eight holes having the same total area and located much nearer the periphery of the cell. This change was thought to be associated with changes of internal flow within the cushion cell itself because the air was supplied through a plenum box, not a duct similar to that depicted in Figure 2.1.

In an attempt to obtain some insight into this aspect of the stability problem, steady state or equilibrium flow structures for cushion geometries representative of those used for the analysis described in Ref. 2.1 were obtained by a finite difference numerical computation technique applied to the equations used for modelling recirculating turbulent flows [Section 6 of Ref. 2.1]. This technique was based on the computer programme developed by Gosman and Ideriah [Ref. 2.13]. Typical velocity-vector diagrams, taken from Section 6 of Ref. 2.1, are given in Figures 2.5 and 2.6. The first of these diagrams, which give effectively the shape of the streamlines of the turbulent mean flow, suggest that the two major features are the radial wall-jet and a very weak viscous ring-vortex. Figure 2.6 demonstrates the effect of inclusion of a deflector plate directly under the inlet flow.

These results suggest one possible way in which internal flow structure might have an effect on cushion dynamics and stability. For the higher levels of cushion flow rates, the radial wall-jet of Figure 2.3 can generate flow in the neighbourhood of the cushion exit region directed towards the exit and which has a dynamic head comparable to the effective cushion pressure. This means that the quasisteady Bernoulli law (Equation 10 of Section 2.2.1) has to be modified to include this head:

$$\dot{m}_c = C_m \ell_p h \sqrt{2\rho_c \left(p_c + \frac{K_{jet}}{2} \rho_c V_j^2 \right)} \qquad (16)$$

where V_j is the uniform jet velocity at the cushion inlet, and K_{jet} is a dimensionless factor determined from the numerical solution. Furthermore,

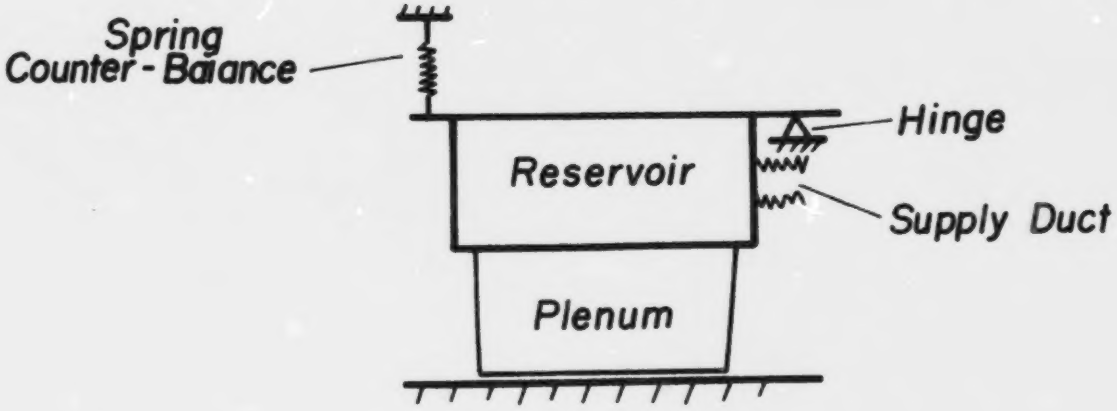
Spring
Counter - Balance
Hinge
Reservoir
Supply Duct
Plenum

FIG. 2.3 HOVER-JAK SINGLE CELL RIG

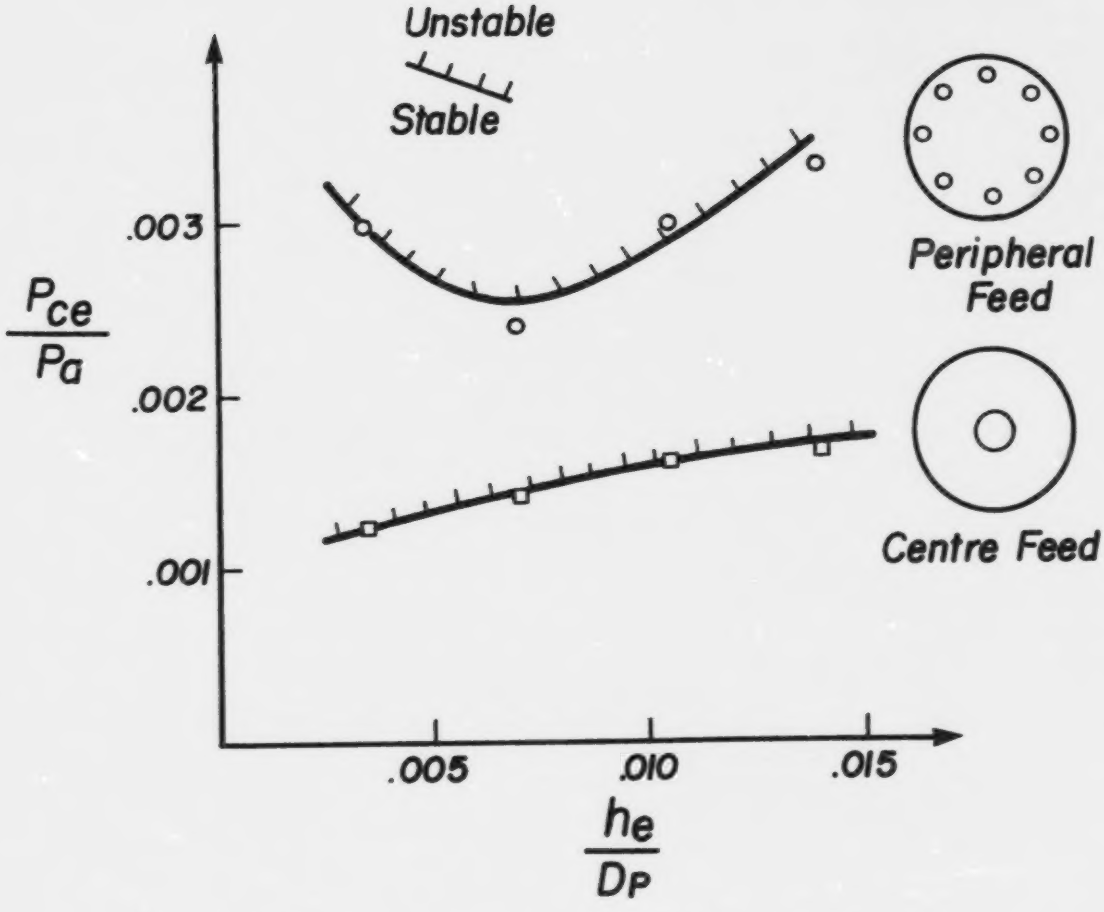

FIG. 2.4 INTERNAL FLOW EFFECT ON HEAVE STABILITY

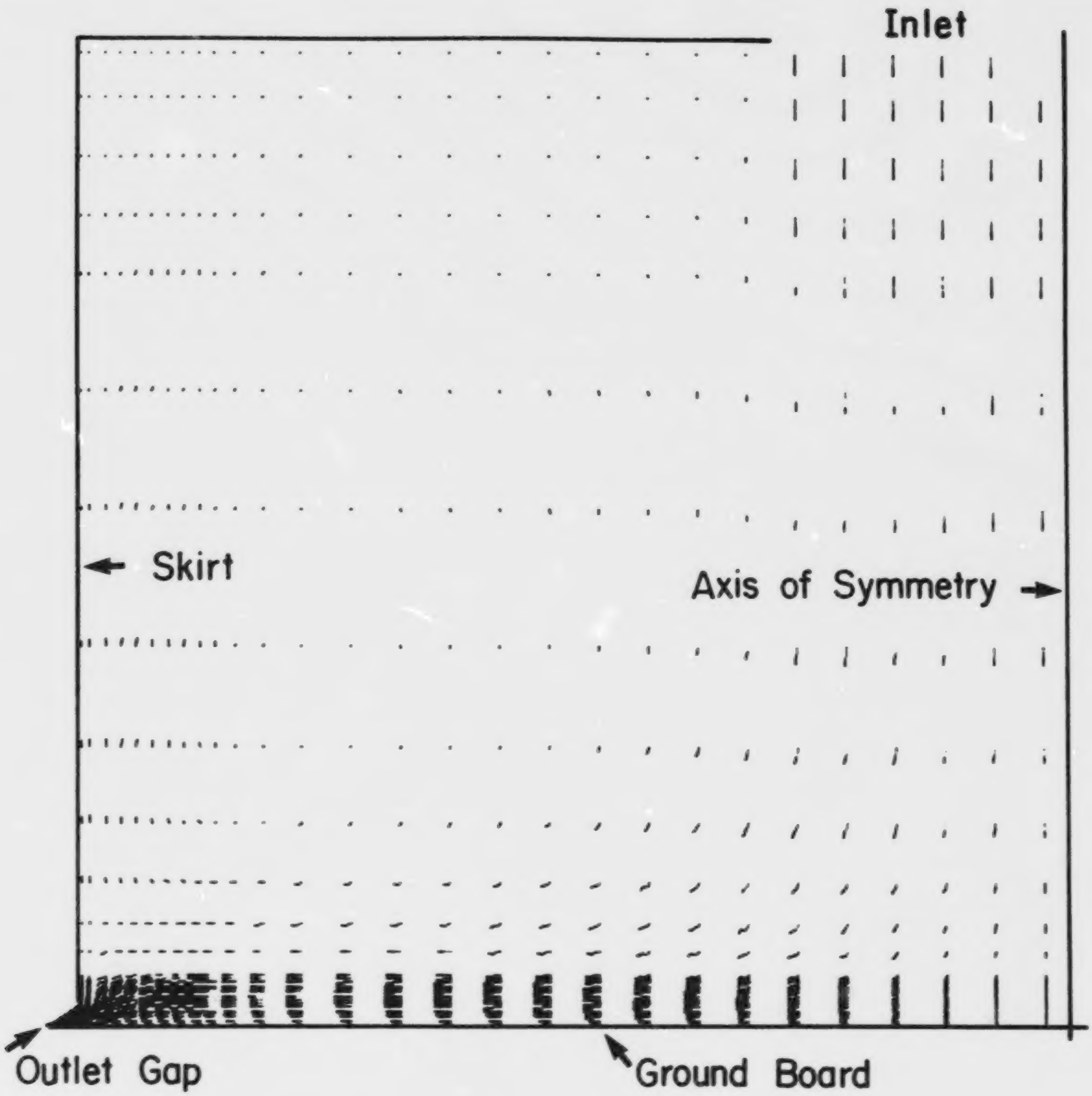

FIGURE 2.5A VELOCITY VECTOR PLOT OF TURBULENT FLOW INSIDE A PLENUM CHAMBER AIR CUSHION. HOVERGAP $h_e/D_p = 0.0125$, AND DUCT REYNOLDS NUMBER $R_{ED} = 10^4$.

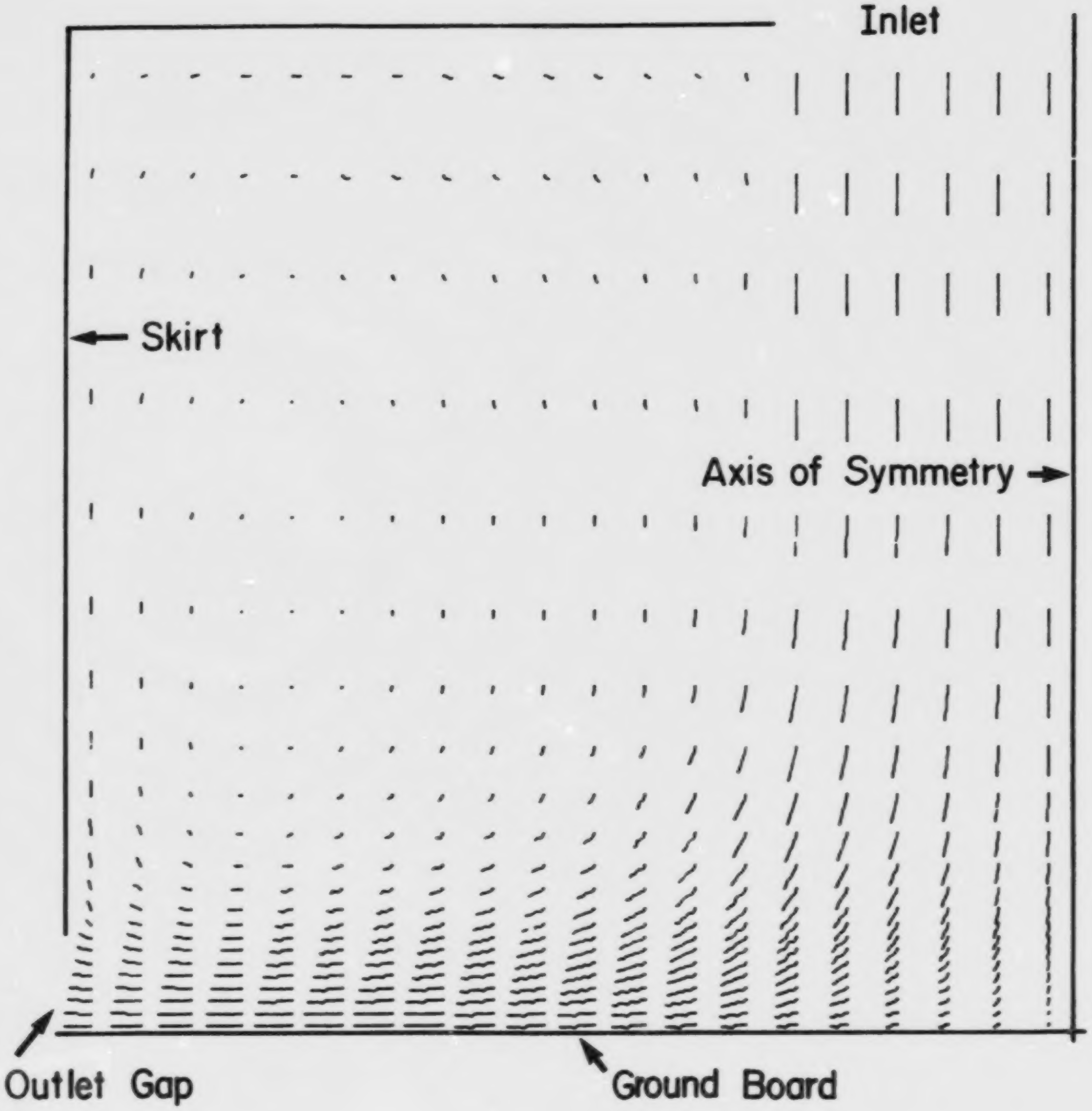

FIGURE 2.5B VELOCITY VECTOR PLOT OF FLOW INSIDE AN AIR CUSHION HOVERGAP $h_e/D_p = 0.05$, $R_{ED} = 10^5$.

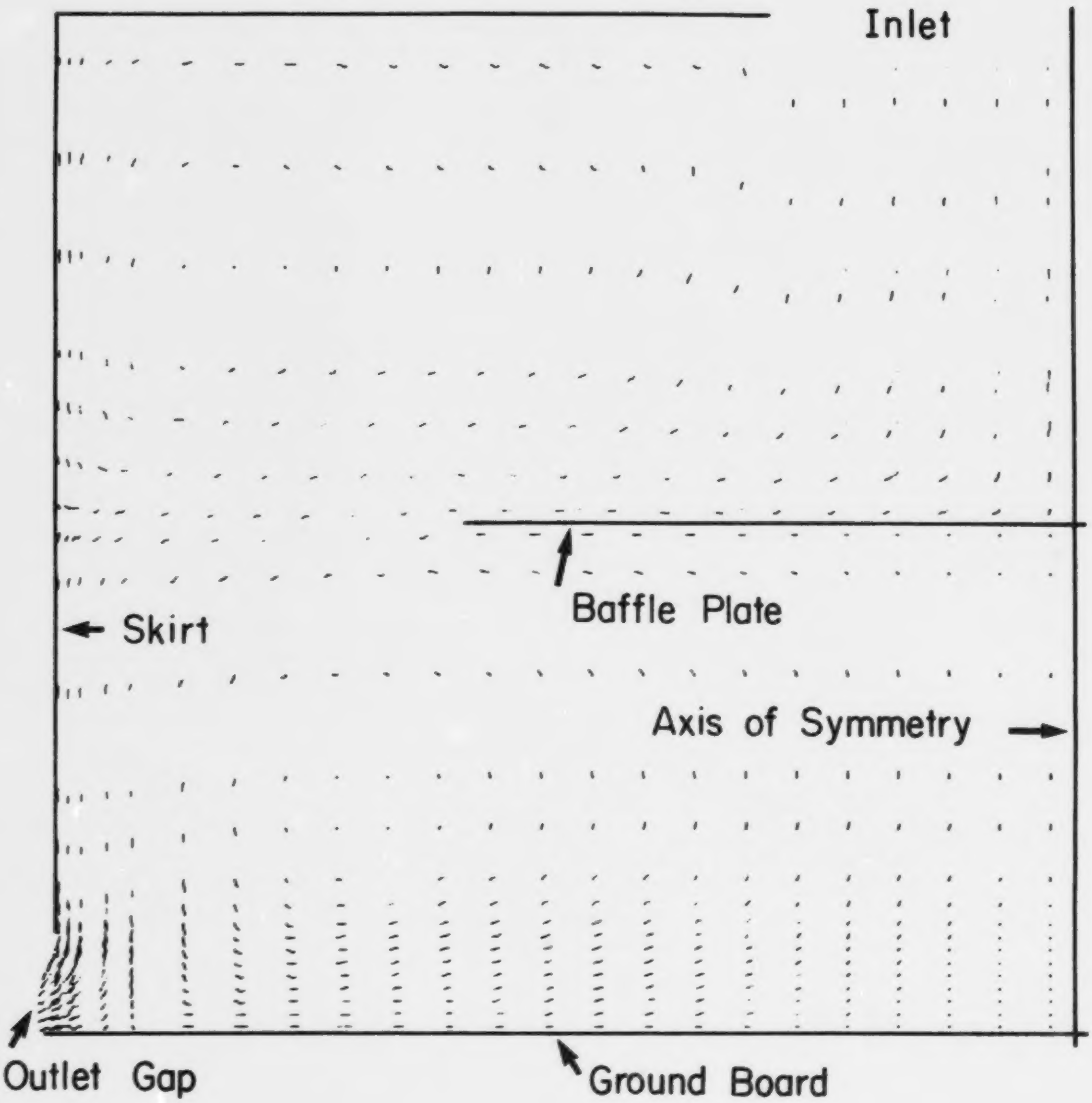

FIGURE 2.6 VELOCITY VECTOR PLOT FOR AN AIR CUSHION WITH A BAFFLE PLATE. $h_e/D_p = 0.05$, $R_{ED} = 10^5$.

because much of the fluid just inside the cushion lip has a significant velocity component parallel to the outlet flow direction, the discharge coefficient C_m may be somewhat higher than the classic vena contracta value of 0.61.* As may be seen in Figure 2.7 (page 23), the sink-like behaviour of the flow field upstream of the orifice in the flow from a reservoir shows that most of the vena contracta is associated with turning the fluid particles that approach the orifice along the wall. In the radial wall-jet case, the fluid is already flowing towards the exit region. Calculations of stability boundaries for some representative geometries given in Section 6 of Ref. 2.1 indicated that the wall-jet phenomena might have a significant destabilizing effect for cushion flow rates at the high end of the practical range. It is to be noted that the flow patterns given in Figure 2.6 strongly suggest that a baffle plate can be used to break up the wall jet and thereby eliminate the internal flow effects. Hence in the experiments, the use of a baffle plate provides a simple critical test of their significance.

Finally, the identification of a specific mechanism for possible internal flow effects provides some guidance on their possible importance for cushion geometries other than that used here. The latter is representative of multicell cushions in which the size of the individual cells is relatively small. For uncompartmented cushions, such as the HDL type discussed elsewhere in this report, if the inlet is mounted not too far from the centre of the cushion, any wall-jet should be greatly attenuated by the time any part of it has reached the periphery. Furthermore, on multicell cusions, for a variety of reasons, it is a common practice to include a screen or baffle to break up the jet. This discussion therefore suggests that, with the possible exception of certain special geometries, generally one might expect that internal flow effects are not significant.

2.2.2.4) Compressibility of the Air in the Plenum Chamber (Equation 8a)

The fact that it is necessary to assume that the air in the cushion volume is compressible (Equation 8a), even though the cushion pressure may be low enough to use an incompressible formulation for the flow processes into and out of the cushion (Equations 6 and 10), was first pointed out by Ribich and Richardson in 1967 [Ref. 2.14]. Earlier treatments of cushion dynamics sometimes ignored the cushion air compressibility. The physical reason why it must be included is now described briefly.

The heave dynamics of the cushion is coupled to the cushion flow processes by the cushion conservation law (Equation 8) and the cushion air escape law (Equation 10). For a single cell fed directly from a constant pressure source through a stabilizing resistance orifice, if the air in the cushion volume is assumed incompressible, equations (8), (9) and (10) reduce to, since $\rho_c = \rho_a$ = constant, and $V_c = V_d + S_a h$,

$$\frac{dV_c}{dt} = S_a \frac{dh}{dt} = Q_f(p_c) - \frac{C_m \ell_p}{\sqrt{\rho_a}} h \sqrt{2p_c} \qquad (17)$$

---

*Recent measurements suggest that C_m may be as high as 0.75 in the presence of a radial wall-jet.

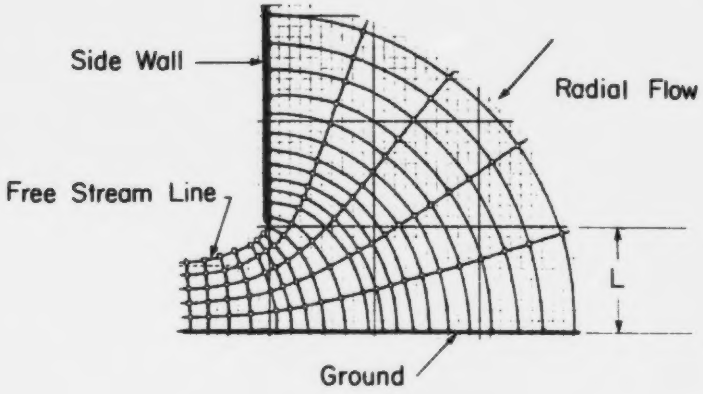
Side Wall
Radial Flow
Free Stream Line
L
Ground

FIGURE 2.7 STREAMLINE PATTERN FOR STEADY INVISCID ORIFICE FLOW.

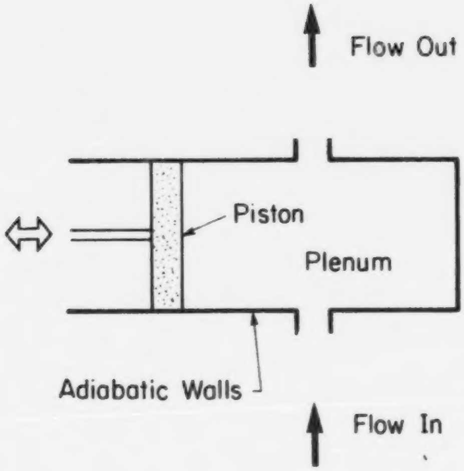
Flow Out
Piston
Plenum
Adiabatic Walls
Flow In

FIGURE 2.8 IDEALIZATION OF AN AIR CUSHION VOLUME

Generally $S_a h/V_d \ll 1$; that is, changes in the total cushion volume caused by vehicle motion are very small. Consequently, the variations in the mass of air stored in V_c due to variations in h are also very small, and may be of the same order of magnitude of variations of the mass of air stored in V_c due to small density variations. Hence cushion air compressibility must generally be included, and a consistent first order asymptotic approximation in the limit of small cushion pressures $p_c/P_a \ll 1$ to a completely compressible formulation for all processes is the linear cushion capacitance model for the cushion conservation law, together with the incompressible approximation for the cushion air escape law.

One very effective way of demonstrating the fundamental importance of cushion air compressibility is to show the effect of omitting it from the dynamics of the simplest case: a single rigid wall cell fed from a constant pressure source through a resistance orifice. The differential equations for this case are those described in Section 2.2.1 with Equations 3, 4 and 5 omitted. Linearization of these equations followed by application of the Laplace Transform leads to the following equation:

$$\Bigg[\underbrace{\left\{ \frac{mV_c}{\rho a^2} \right\}}_{\text{I}} s^3 + \underbrace{\left\{ \frac{mQ_e p_o}{2p_{ce}(p_o - p_{ce})} \right\}}_{\text{II}} s^2 + \underbrace{\left\{ S_a^{\,2} \right\}}_{\text{III}} s + \underbrace{\left\{ \frac{S_a Q_e}{h_e} \right\}}_{\text{IV}} \Bigg] \bar{h}(s) = D\bar{z}(s) \qquad (18)$$

where $s = \sigma + j\omega$ is the Laplace variable, $\bar{h}(s)$ is the Laplace transform of $h(t)$ and $\bar{z}(s)$ is the transform of an input. Static stability of the system requires $p_o > p_{ce}$, so that all the coefficients in the { } brackets are positive for a system that can hover. A physical insight into the meaning of this equation can be obtained by setting $s = j\omega$; this corresponds to a steady state oscillation, which of course only occurs at a stability boundary in a linear system. In terms of a classical mass-spring-dashpot system, term IV is the effective spring stiffness, term III is the damping and term II is associated with the system mass. Term I, which is zero if the cushion capacitance $C_c = V_c/\rho a^2 = 0$, is effectively a frequency-dependent negative damping, because if $s = j\omega$, then $s^3 = -j\omega^3$. Hence term I tends to cancel the effect of term III. It is therefore the source of the instability, since a second order system with positive damping is always stable. This explanation is essentially that given by Sweet, Richardson and Wormley [Ref. 2.2].

2.2.2.5) Isentropic Compression-Expansion Assumption (Equation 9)

The classical derivation of the isentrope law, P/ρ^γ = constant, is based on the concept of an adiabatic reversible process. One considers a fixed mass of gas contained in a thermally insulated cylinder and acted upon by a piston which moves sufficiently slowly to prevent generation of significant viscous forces or temperature gradients inside the gas. For an air cushion this is obviously an approximation, since significant amounts of air may flow into and out of the cushion volume during the period of a typical vehicle oscillation. It is useful in this regard, to consider the idealization of an air cushion volume shown in Figure 2.8. A critical parameter for this system is the ratio, R, of the volume residence time of a typical particle to the period of a small amplitude piston oscillation. One might expect that a necessary condition for the process to be approximately isentropic is that R be sufficiently large. Alternatively for R < 1, as R decreases, it should become isothermal.

Computation of typical residence times and frequencies suggests that R should be moderately large. Typically, for the "short duct" case described in the experiments below, the predicted period is about 0.08 seconds, whereas residence times ranged from 0.56 to 1.28 seconds, which gives $7 \leq R \leq 16$. For the "long duct" case $5 \leq R \leq 10$ approximately. Typically, R is much larger than unity but not so large that one can confidently ignore the effect of the cushion volume air exchange on the compression-expansion process.

Other factors can play a significant role in determining the applicability of the isentropic model. Heat transfer between the cushion air and the surrounding "hardware" occurs, and for some geometries it might be significant. It is worth noting that computational models of the pneumatic hammer process in air bearings - a phenomenon closely analogous to that being investigated here - frequently use an isothermal model. The rationale for this is clear; air bearings generally consist of passages having widths which are very small when compared to a typical bearing dimension. They have, in effect, a very large surface area to volume quotient; and the thicknesses of any thermal boundary layers developed in the process are likely to be comparable to the passage widths. In contrast, cushion geometries are at the other end of the range of the possibilities. Hence this argument and the one relating to cushion air exchange effects both suggest that the cushion air process should be much nearer isentropic than isothermal.

An appreciation of the possible significance of errors in modelling the cushion process by the isentrope law may be obtained by determining the predicted stability boundaries for a gas which obeys the polytropic law P/ρ^n = constant, and then examining the changes that occur as the exponent "n" is varied in the limits $1 \leq n \leq \gamma$. Consider the single rigid-wall cell system discussed in Section 2.2.2.4. It is possible to obtain simple algebraic expressions for the cushion pressure at the onset of instability as a function of h_e for the two limiting cases of a constant pressure and a constant volume flow source. Following the analysis given in Section 2 of Ref. 2.1 one has, for these two cases respectively:

Constant pressure source:
$$\frac{p_{ce}}{P_a} = n \frac{S_a h_e}{2V_{ce}} \left(1 + \frac{A_f^2}{\ell_p^2 h_e^2} \right) \qquad (18a)$$

Constant flow source:
$$\frac{p_{ce}}{P_a} = n \frac{S_a h_e}{2V_{ce}} \qquad (18b)$$

For both cases p_{ce} is directly proportional to the exponent "n". Hence one can conclude that even relatively large deviations from the isentrope model should generate only modest errors, although for prediction of results to a good engineering accuracy, it should be checked.

2.2.2.6) Quasisteady Incompressible Orifice Flow Assumption (Equations 6 and 10)

As discussed in the previous two sections, the air in the cushion must be considered compressible even though the cushion pressure is small enough to allow use of an incompressible orifice flow approximation. Typically for cushion pressures less than about $4kP_a$ the error is less than 1%. The other major assumption associated with the use of equations (6) and (10) is that, in Euler's equations for inviscid flow, the local or unsteady inertia terms are small compared to the convective terms. If the equations are written in streamline or natural coordinates, Euler's equation for the forces acting along the streamline direction is

$$\rho \frac{\partial V}{\partial t} + \rho V \frac{\partial V}{\partial s} + \frac{\partial p}{\partial s} = 0 \qquad (19)$$

The "quasi-steady" approximation implies that the local term $\rho(\partial V/\partial t)$ must be negligible compared to the perturbation in the convective term $\rho V(\partial V/\partial s)$.

An estimate of the limitations of the quasi-steady approximation for the present problem may be obtained as follows. Now, it is known from potential flow theory that, at radial distances greater than about one characteristic length L upstream of an orifice, where for a slot orifice L is the slot half-width while for a circular orifice L is the orifice radius, steady flow is very much like sink flow with streamlines almost radial. This is shown in Figure 2.7, which is taken from Ref. 2.15. Thus, for steady flow, simple continuity arguments can be used to relate approximately the velocities at various radial positions in the converging streamline channels to the velocity at the vena contracta. During a small amplitude system oscillation, the pressure difference across the orifice will be given approximately by

$$p_o = p_{ce} + \Delta p_o \sin\omega t \qquad (20)$$

where the subscript 'e' indicates an equilibrium value and the symbol 'Δ' indicates a small disturbance from equilibrium. Now, if the flow can be assumed quasi-steady, one can, with the aid of the simple geometrical arguments, estimate the local term $\partial\Delta V/\partial t$. Similarly, the geometrical arguments and the quasi-static assumption can be used to estimate the perturbations in the convective term

$$\Delta V \frac{\partial V_e}{\partial s} + V_e \frac{\partial \Delta V}{\partial s} \qquad (21)$$

Let r be the radial distance upstream from the centre of the orfice. Then, with the notation $|a|$ denoting the amplitude of oscillating quantities, define

$$R_m = \left(\left| \frac{\partial \Delta V}{\partial t} \right|_{r=r_o} \right) \Big/ \left(\left| \Delta V \frac{\partial Ve}{\partial s} + Ve \frac{\partial \Delta V}{\partial s} \right|_{r=r_o} \right) \qquad (22)$$

where r_o is that value of r for which the convective term is a maximum. The quasisteady assumption requires $R_m \ll 1$. Calculations described in Appendix D show that the maximum value of the convective term occurs near $r_o = L$ and that

$$R_m = \alpha L\omega/V_{oe} \qquad (23)$$

in which V_{oe} is the equilibrium speed at the vena contracta. At the cushion lip, $V_{oe} = (2p_{ce}/\rho_a)^{1/2}$ and L = he. The value of α is 1.3 for slots and 0.82 for circular orifices.

Application of this criterion generally suggests that for self-excited oscillations, the orifice flows should be quasisteady. However, as with fan blade aerodynamics, for other ACV dynamics problems involving higher frequencies, the orifice flows are likely to be unsteady. For the experiments described below, R_m for the cushion exit flow was about 0.01, but for the duct inlet R_m could be as high as 0.1.

2.2.2.7) Concluding Remarks

The above review of the assumptions widely employed in the investigation of ACV dynamics indicates that considerable care is required in their use. With some important exceptions, there is virtually no experimental data available which gives insight into the limitations of the assumptions. Hence it is concluded that a sequence of experiments carefully designed to ascertain these limitations is required. The experiments described in the remainder of this section represent a first step in this direction.

2.3) Design of the Experiment

2.3.1) Original Concept

It is appropriate to describe briefly the early attempts made at UTIAS to compare experimental measurements of stability boundaries with theoretical predictions, since these give a useful insight into the difficulties that can occur in making such measurements, and ultimately, an example of the application of the theory to a "practical" system not specifically chosen to facilitate interpretation of the theory.

The major features of the geometry of the system initially used is given in Figure 2.9. A centrifugal fan capable of supplying air at pressures up to about 2 kPa and at volume flows up to 1.5 m^3/sec provided air through a supply duct system to several air cushion experiments. The facility intended for cushion dynamics experiments was located at the end of the 0.305 metre diameter air supply duct, or about 6.1 metres from the fan. It included a servohaudrically driven moving ground-board or table which was capable of injecting sinusoidal heave or combined pitch and heave oscillations into the cushion model under test. It was initially envisaged that direct determination of repeatable stability boundaries might be difficult, owing to such potential problems as the effect of unaccounted residual or "parasitic" damping, and the obvious difficulty of making measurements in an unstable region. Consequently, the planned approach was based on experimental confirmation of the theoretical results at operating conditions in stable regions close to stability boundaries, and then use of these models to infer the location of stability boundaries.

The facility as originally set up did not incorporate the 2.55 m^3 isolating volume shown in Figure 2.9, but during the experimental investigation of the frequency response of a cushion geometry designed for use on tracked ACV's relatively large pressure oscillations were observed at the inlet of the cushion [Ref. 2.16]. The 2.55 m^3 isolating volume was installed in an attempt to eliminate, or at least greatly reduce, these pressure oscillations. Considerable improvement was obtained, and it was concluded that, for these tests, the isolating volume made the supply system behave like an ideal constant pressure source.

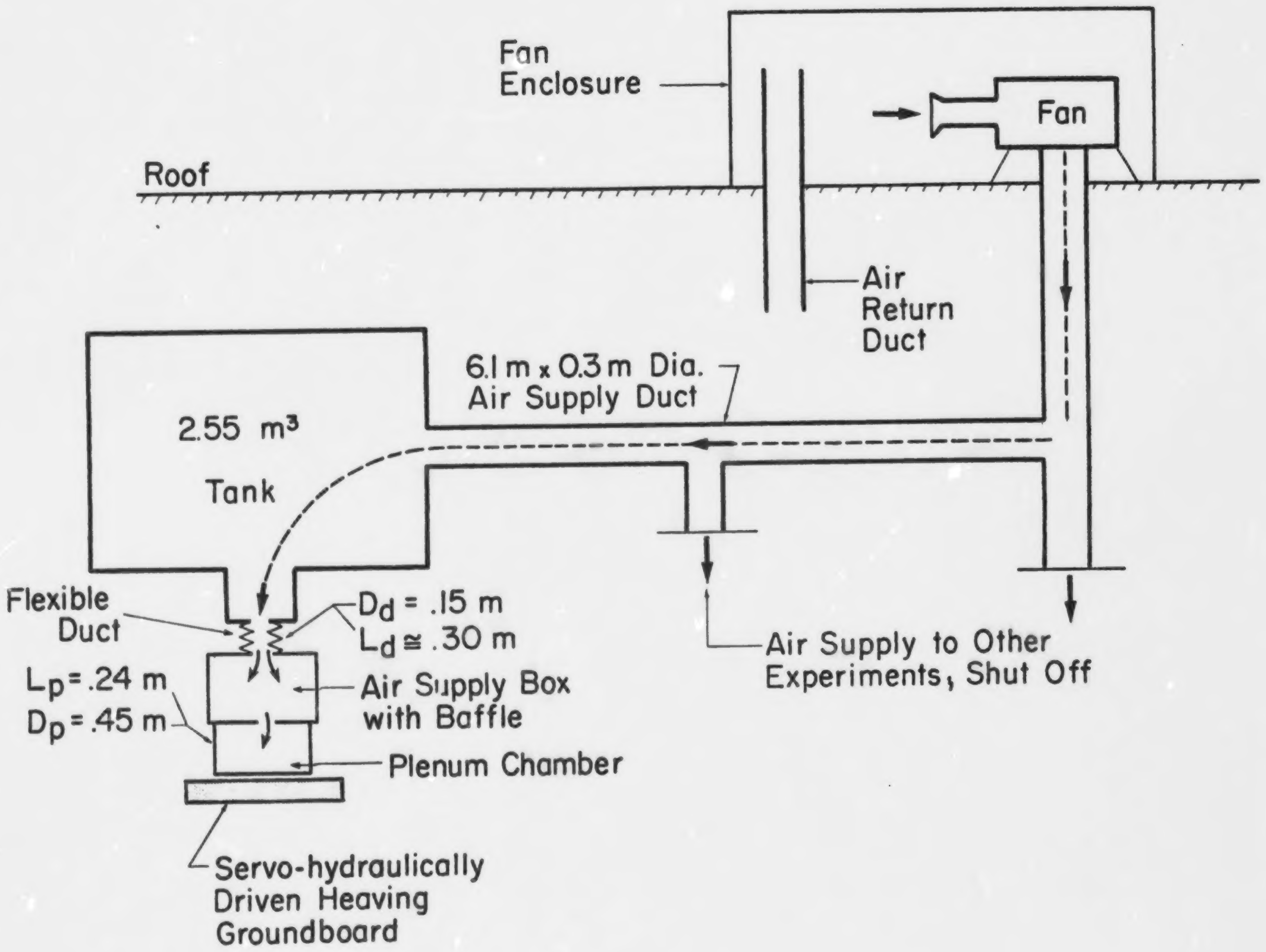
Fan
Enclosure
Fan
Roof
Air
Return
Duct
6.1 m x 0.3 m Dia.
Air Supply Duct
2.55 m³
Tank
Flexible
Duct
D_d = .15 m
L_d ≅ .30 m
L_p = .24 m
D_p = .45 m
Air Supply Box
with Baffle
Plenum Chamber
Air Supply to Other
Experiments, Shut Off
Servo-hydraulically
Driven Heaving
Groundboard

FIGURE 2.9 SCHEMATIC DIAGRAM OF ORIGINAL HEAVE TABLE FACILITY.

2.3.2) Results Obtained Prior to Present Contract

As is discussed in Ref. 2.1, work undertaken under a previous contract with TDC and during cooperative field trials with a Canadian ACV manufacturer had suggested two major points. First, observations of the behaviour of cushion systems had indicated that well defined and repeatable stability boundaries could be obtained by the simple expedient of manually disturbing the cushion in a relatively arbitrary manner, and then releasing it and observing the subsequent motion. It is noted that the practicability of this approach was due in part to the use of flexible skirts. This generally enabled operation for short intervals in unstable regions without damaging the test model. It also implied that the cumbersome procedure described above for obtaining well defined stability boundaries might be circumvented for many tests. The second point suggested by this prior work was that for the cushion geometries of current interest to TDC - which were mainly of the multicell type - the details of the flow structure in a given cell seemed to be the dominant factor not included in the analyses then available.

The theoretical investigation of duct effects, which was completed in 1978 and is described in Ref. 2.1, was first encountered during the process of exploration of the suitability of the finite element method for treating the effect of such distributed properties as internal flow structure. It was found that even the relatively short ducts that might be used on some ACV designs could have the extremely large effects on stability boundaries. Thus, according to the analysis, and for the geometries encompassed in Figure 2.1, moderate changes in duct length-to-diameter ratio could, at correctly scaled cushion flow rates, change the maximum operable cushion pressure at the onset of instability by factors of ten and more. These predicted changes were far in excess of any observed internal flow effect, and it was clear that an experimental confirmation was required.

2.3.3) Initial Comparisons Between Theory and Experiment on Heave Table Facility

Figure 2.10 is a comparison of the test results obtained on the heave table facility for the model depicted in Figure 2.11 with the predictions of the theory described in Section 2.2 and the assumption that the 2.55 m^3 isolating tank approximated the behaviour of a constant pressure source. The theoretical predictions and experimental results seem to be totally unrelated. Note that, whereas the theory indicated that, at a given cushion pressure p_{ce}, as C_{QC} or h_e/D_p is increased the system becomes unstable, the exact opposite was found experimentally. Apparently the isolating volume did not act as a constant pressure source, it allowed the system to interact with the supply ducting.

Figure 2.12 shows an observed internal flow effect for this set-up. It is relatively small.

2.3.4) Design of a Critical Experiment: The Sphere Facility

Calculations based on the finite element theory and which incorporated the supply duct geometry indicated that the tank volume would have to be increased by a factor of several hundred for the tank to act as a constant pressure source. In the heave table facility such a modification

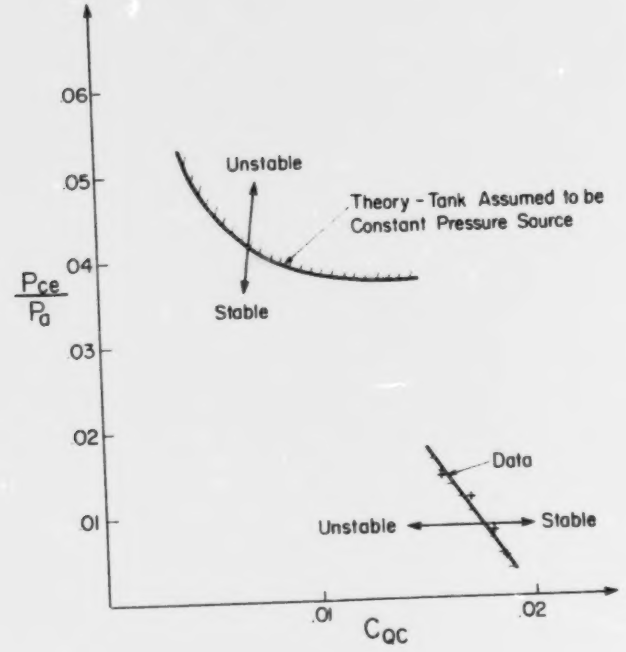

FIGURE 2.10 TYPICAL STABILITY RESULT OBTAINED USING HEAVE TABLE FACILITY.

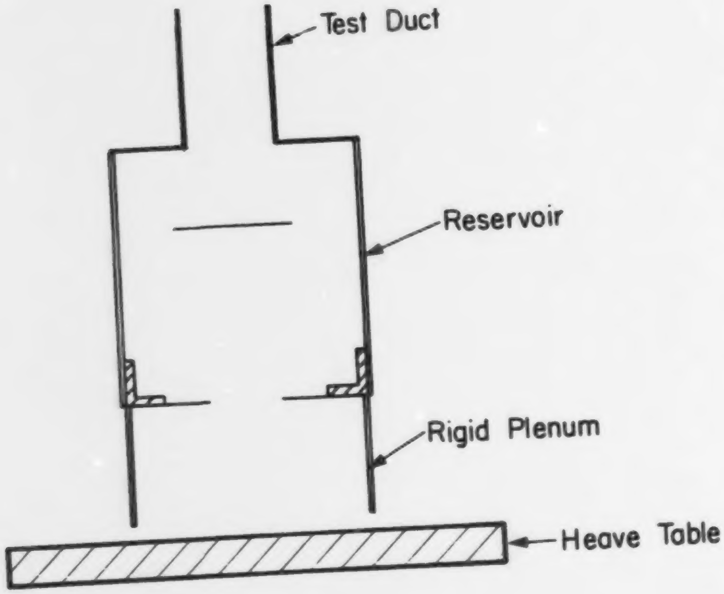
Test Duct
Reservoir
Rigid Plenum
Heave Table

FIGURE 2.11 FIRST MODEL USED FOR STABILITY MEASUREMENTS.

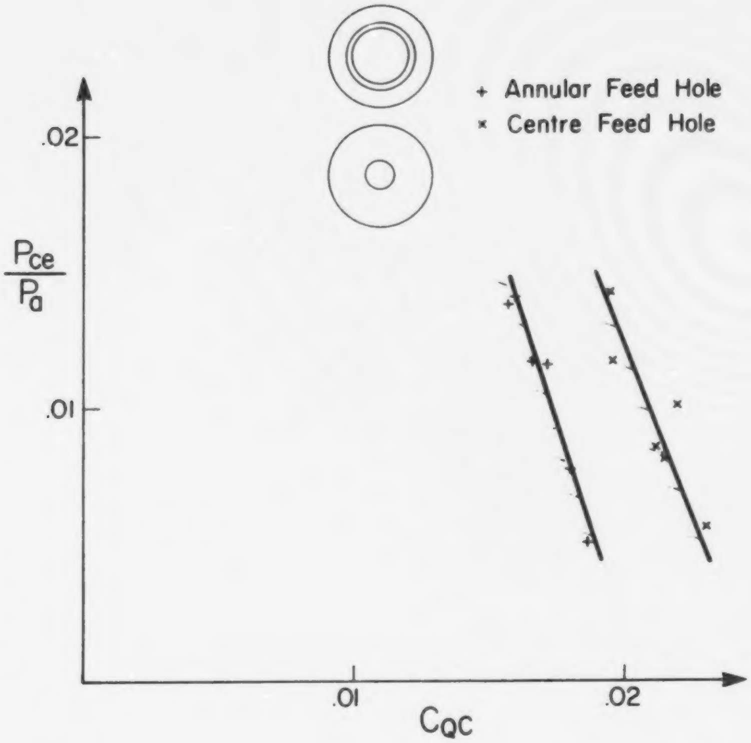

FIGURE 2.12 AN INTERNAL FLOW EFFECT OBTAINED ON HEAVE TABLE FACILITY.

was impractical. Fortunately, at UTIAS a 12.2m diameter vacuum sphere was available; and a facility, designed to isolate supply duct and fan dynamics from test duct cushion dynamics, was built around it. The sphere facility is shown schematically in Figures 2.13 and 2.14. Its dimensions are given in Table 2.1. It basically consisted of a standard industrial centrifugal fan which supplied air to the sphere and thus pressurized it. The sphere supplied air to an aluminium test duct, which, in turn, supplied the air to a single cell plenum chamber and a manually operated relief valve. The plenum hovered freely over a rigid flat table and moved vertically in heave only as it was constrained from any other motion by a linear recirculating ball bearing assembly. It was coupled to the test duct by a short length of flexible ducting. The test duct itself was fixed in the inertial reference frame. The table and the bearing assembly were supported by a steel I-beam structure which was bolted to a concrete foundation.

Table 2.1

Dimensions of Sphere Facility Experiment

Sphere diameter		=	12.2 m (40 ft)
Skirt diameter	Top	=	0.508 m (1.67 ft)
	Bottom	=	0.467 m (1.53 ft)
Skirt height		=	0.213 m (0.70 ft)
Duct length	Long	=	3.26 m (10.7 ft)
	Short	=	1.71 m (5.6 ft)
Duct diameter		=	0.0779 m (0.256 ft)
Basic model weight	Flexible	=	49.35 N (11.09 lbs)
	Rigid	=	58.96 N (13.25 lbs)
Duct flow friction factor		=	0.01656
Lip discharge coefficient	Flexible	=	0.567
	Rigid	=	0.60

Duct discharges directly into the cushion.

Flexible Skirt

Material = Uniroyal Fiberthin 131 (Rubber coated fabric)

Thickness ≅ 0.51 mm

Weight = 6.97 Pa

Rigid Skirt

Material = Aluminum

Thickness ≅ 1.25 mm

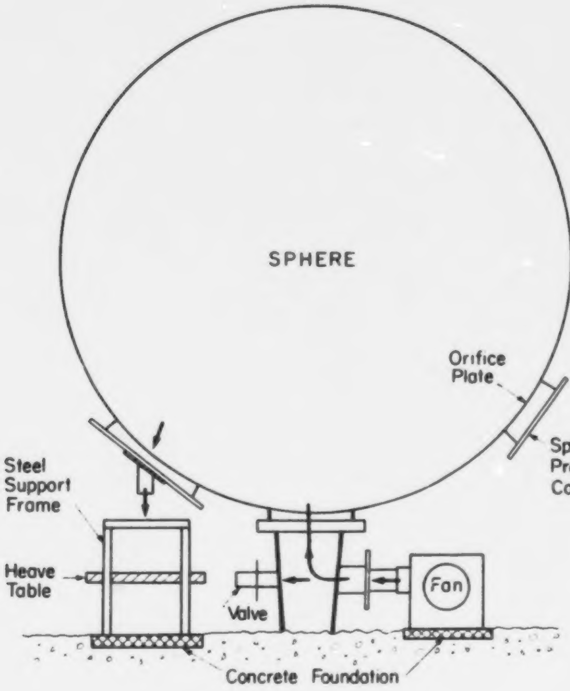
SPHERE
Orifice Plate
Sphere Pressure Control
Steel Support Frame
Heave Table
Valve
Fan
Concrete Foundation

FIGURE 2.13 SCHEMATIC DIAGRAM OF SPHERE FACILITY.

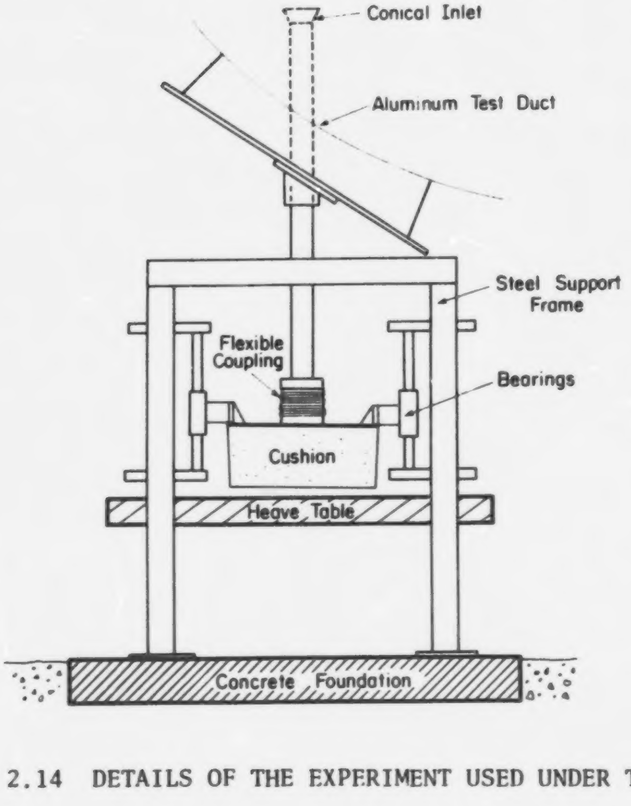
Conical Inlet
Aluminum Test Duct
Steel Support Frame
Flexible Coupling
Bearings
Cushion
Heave Table
Concrete Foundation

FIGURE 2.14 DETAILS OF THE EXPERIMENT USED UNDER THE SPHERE FACILITY.

To ensure accurate measurement of the cushion flow rate at a given equilibrium of operating condition, this quantity was measured at the entrance to the test duct by using a conical inlet [Ref. 2.17], which in turn was calibrated using an ASME standard orifice plate [Ref. 2.18]. A baffle-plate, positioned on the table immediately below the inlet to the plenum,was used to minimize internal flow effects.

As noted in the table, two skirts were used. One was rigid and one was made from flexible material. During the preliminary experimental programme described above it was found that, with suitable care, it was possible to ascertain stability boundaries for a rigid-walled cell without incurring damage to the cushion lip or the precisely machined cushion table. The flexible material was chosen to be relatively thick in order to be both inelastic on the scale of the experiment, and structurally stable enough to be cut at its bottom edge - the cushion lip - so that it was parallel to the table. It is worth noting that, even though the material was perhaps a factor of 5 or 10 thicker than that which might be used to produce a scaled skirt, the accuracy of the experiment was such as to detect a slight "skirt flexibility" effect.*

The cushion lip discharge coefficients C_m were determined experimentally after the cushion was installed. It is noted that the C_m for the flexible skirt (Table 2.1) was significantly below that given for a slot orifice by inviscid flow theory, namely $C_m = 0.611$. This difference was attributed to the slight taper incorporated to ensure stable deployment.

2.3.5) Procedures Used for Determining Stability Boundaries

Two procedures were used to obtain data points on a stability boundary. In the first, called the "observed motion method", the model weight was fixed; this determined the cushion operating pressure. The pressure in the sphere was adjusted so that the cushion pressure-flow equilibrium operating point was in a stable region. The equilibrium flow was then reduced gradually by lowering the sphere pressure in small steps until the model developed a heave oscillation when subjected to a slight manual disturbance. When an oscillation developed, the sphere pressure was adjusted to bring the pressure-flow operating point back into the stable region; the whole process was repeated a number of times so that the readings for a particular data point finally recorded represent averages.

The second, more involved procedure, called the "extrapolated decrement method", obtained a boundary point for a given weight by measuring the damping at a number of equilibrium conditions in the stable region. Figure 2.15 shows oscilloscope traces of cushion motion near a stability boundary obtained from the output of a displacement transducer attached to the cushion. The damping determined from traces such as that shown in Figure 2.15b by measuring the decrements χ_1 and χ_2 defined in Figure 2.16. The functional dependence of the damping ratios on cushion flow was determined from measurements taken over a range of cushion flows in an equilibrium region. Typical data is shown in Figures 2.17 and 2.18. The value of h_e or C_{QC} corresponding to the boundary point, $\chi_1 = \chi_2 = 1$, was ascertained by mean-square fitting a polynomial to the data and then extrapolating [Ref. 2.19], as is shown in Figures 2.17 and 2.18.

---

*It is assumed that the appropriate scaling parameter is the quantity C_{SW} discussed in Section 3 of this report.

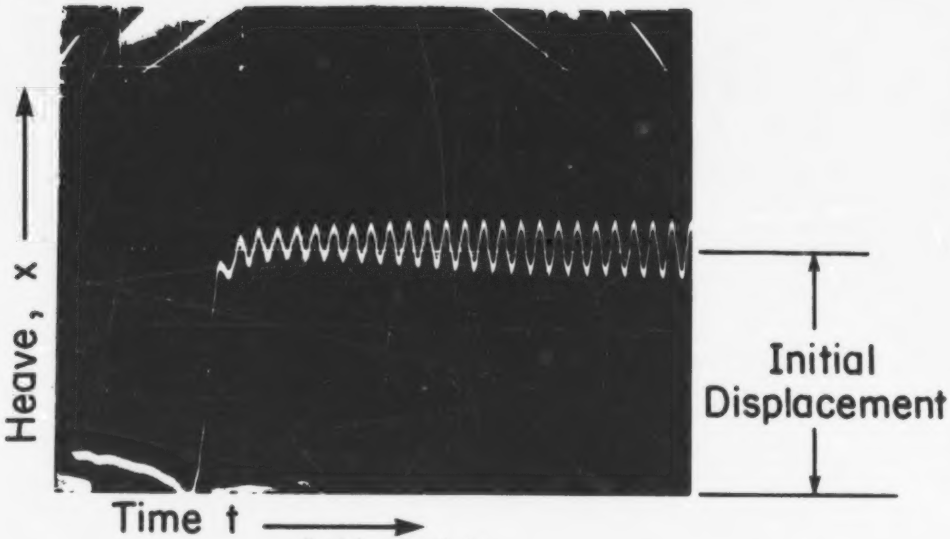

a) Unstable

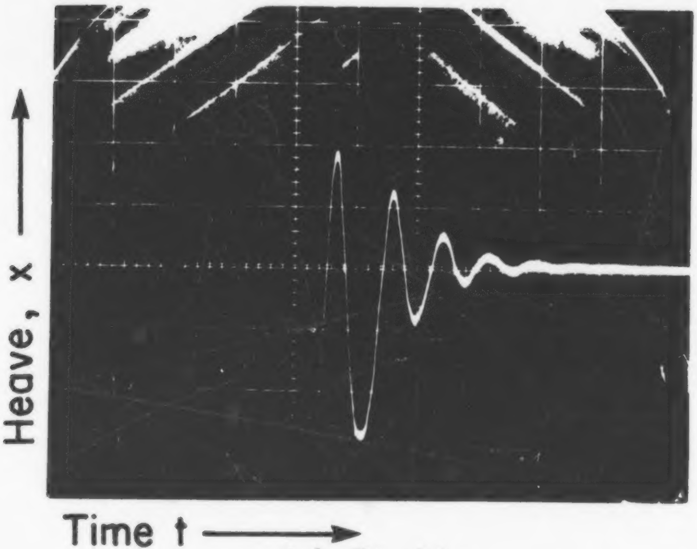

b) Stable

FIGURE 2.15 TYPICAL EXAMPLES OF STABLE AND UNSTABLE MOTION NEAR A STABILITY BOUNDARY

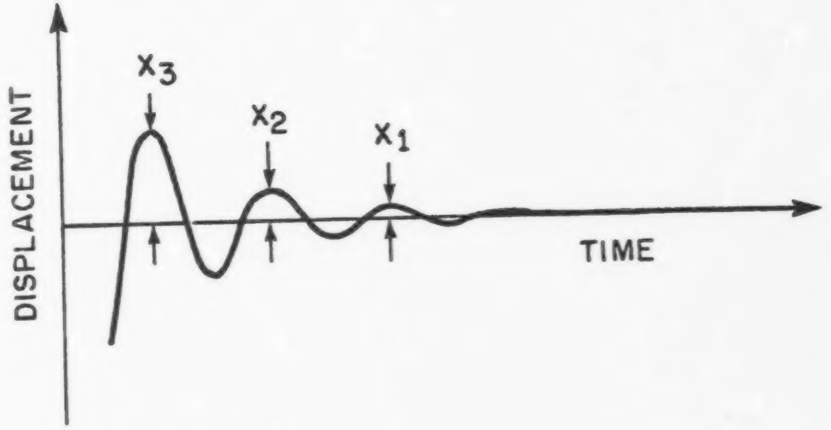
DISPLACEMENT
TIME
x_3
x_2
x_1

$$X_1 = \frac{x_1}{x_2}$$

$$X_2 = \frac{1}{2}\left(\frac{x_1}{x_2} + \frac{x_2}{x_3}\right)$$

FIGURE 2.16 DAMPING DECREMENTS USED IN EXTRAPOLATED DECREMENT METHOD OF DETERMINING STABILITY BOUNDARY.

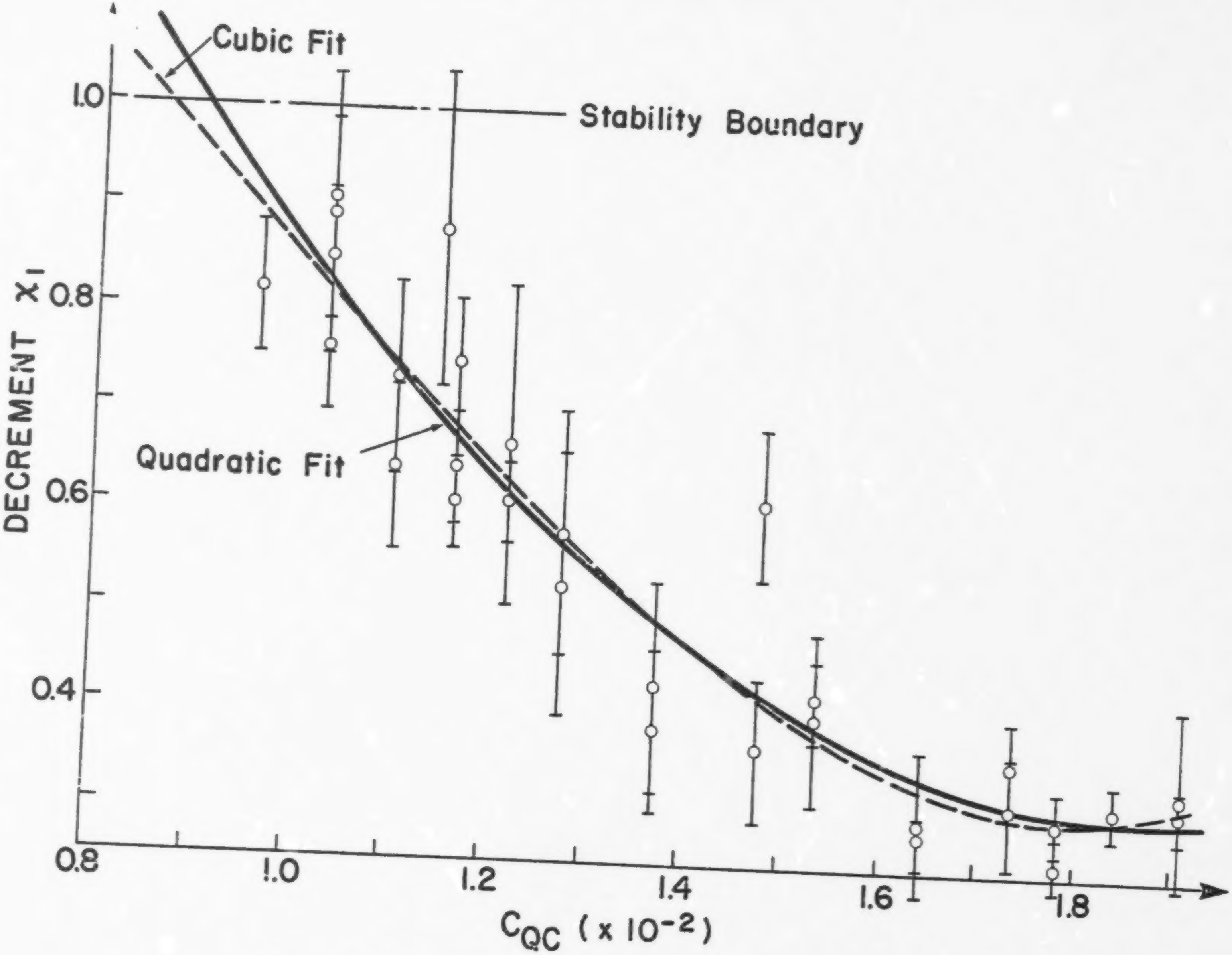

FIGURE 2.17 TYPICAL DATA OBTAINED FOR THE EXTRAPOLATED DECREMENT OF DETERMINING STABILITY BOUNDAIRES. FOR THIS EXTRAPOLATION, X_2 IS USED.

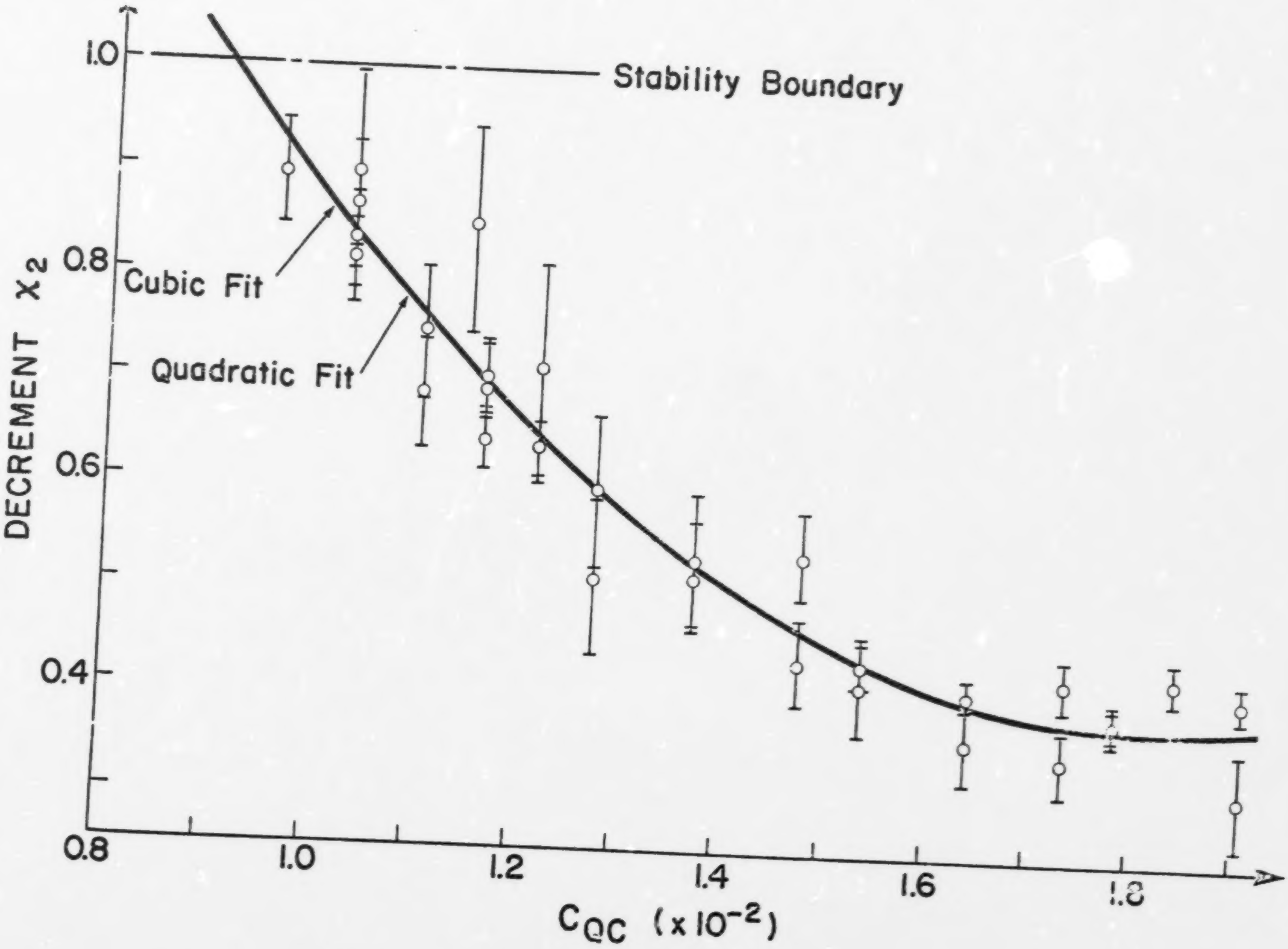

FIGURE 2.18 EXTRAPOLATED DECREMENT METHOD WITH X_2 APPLIED TO DATA.

As discussed below, the observed motion method of determining stability boundaries gave, for the present set of experiments, remarkably unambiguous results. It is believed that this was partly fortuitous, because the theoretical analysis showed that the real parts of the eigenvalues of the stability matrix were very rapidly varying functions of the equilibrium hovergap h_e, or its equivalent C_{QC}. For other configurations, or at other operating conditions this may not be the case; so that the stability boundaries would be much less well-defined. It was also found that, presumably also as a result of the well-defined boundaries, one could use the observed motion method to ascertain stability boundaries of rigid "skirts".

2.4) Sphere Facility Results

2.4.1) Duct Effects for Rigid and Flexible Skirts

A typical result showing a duct effect obtained by the observed motion procedure is given in Figure 2.19. As noted previously, the hatched side of the curve denotes the unstable region. The duct length was 1.71m and the skirt was rigid (Table 2.1). As can be seen, the agreement between the theory for an isentropic cushion process and the experiment is very good. The effects occur for values of C_{QC} in the practical operating range noted in previous reports.

Figure 2.20 compares the stability boundaries obtained for the rigid and flexible skirts described in Table 2.1. To obtain these boundaries, a set of measurements was taken with the flexible skirt installed, then with the rigid skirt installed and finally with the flexible skirt installed again. The results are indicated by the open circles, squares and closed circles respectively. The observed motion method was again used for these and the remaining results of Section 2.4.1. The excellent repeatability of the results indicates that the difference is a true flexibility effect. In the present case, as might be expected, since the flexible skirt is very thick, this effect is very small. However, it is interesting to note that a theoretical estimate of the flexibility effect taking into account its static stiffness properties suggested that the effect should be much larger. The discrepancy is believed to be due to dynamic stiffness or other viscoelastic properties of the skirt material [Ref. 2.20].

Figure 2.21 compares theory and experiment for the short duct, flexible skirt case. The data shown in Figure 2.20 was used to determine an equivalent static material stiffness coefficient for correcting the flexible skirt theoretical results.

Figure 2.22 compares theory and experiment for a duct length $L_D = 3.26$ m, and Figure 2.23 is another demonstration of the repeatability that was obtained. It is noted that the two sets of runs were obtained on different days; and the effect of atmospheric density changes is incorporated in the nondimensional presentation of the data.

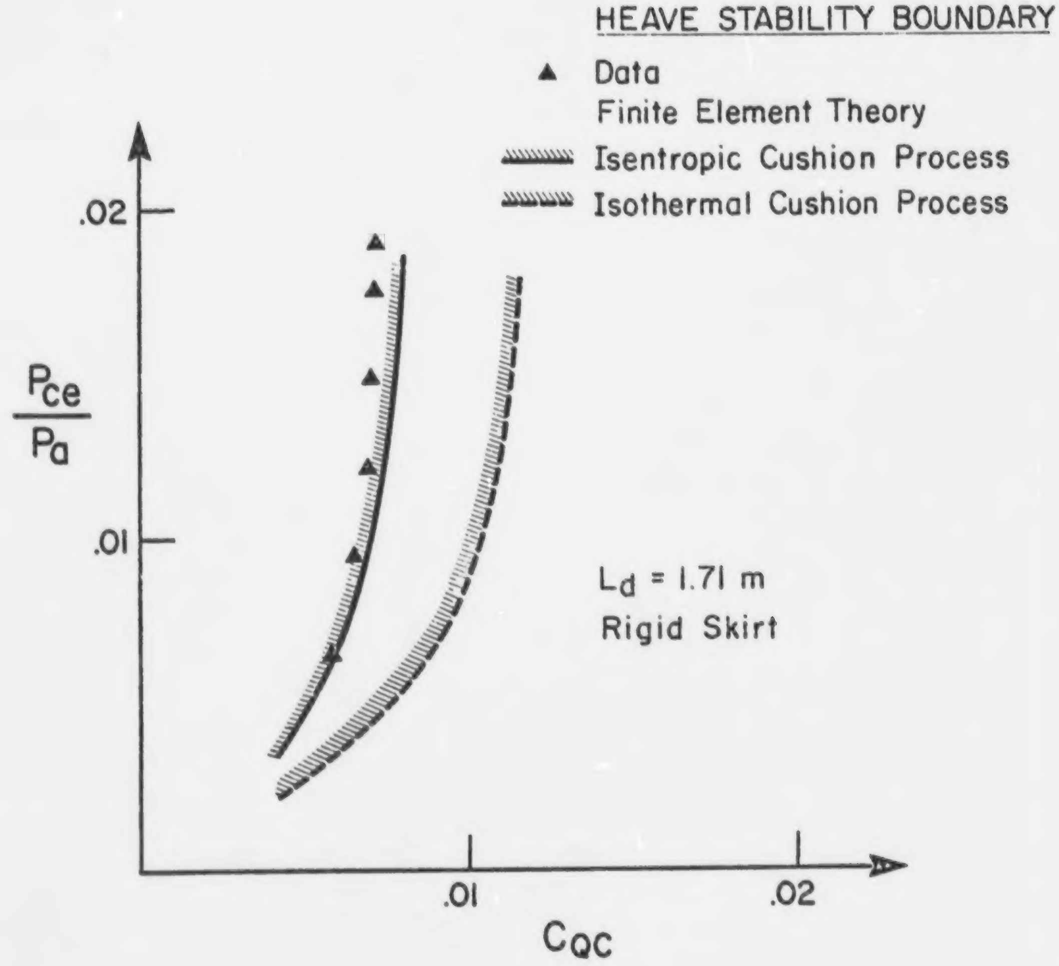

FIGURE 2.19 COMPARISON OF THEORETICAL RESULTS FOR AN ISOTHERMAL AND ISENTROPIC CUSHION PROCESS WITH EXPERIMENTAL RESULTS FOR SHORT DUCT RIGID SKIRT CASE.

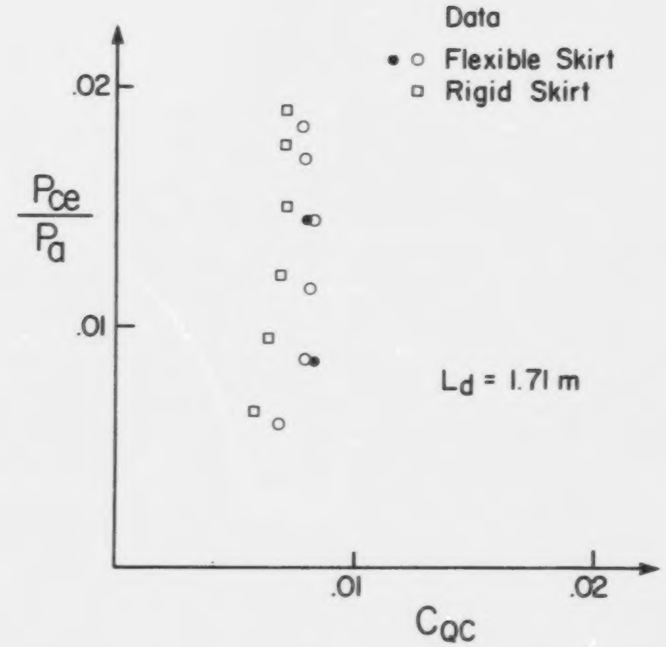

FIGURE 2.20 MEASURED STABILITY DATA FOR RIGID AND FLEXIBLE SKIRTS. SHORT DUCT CASE.

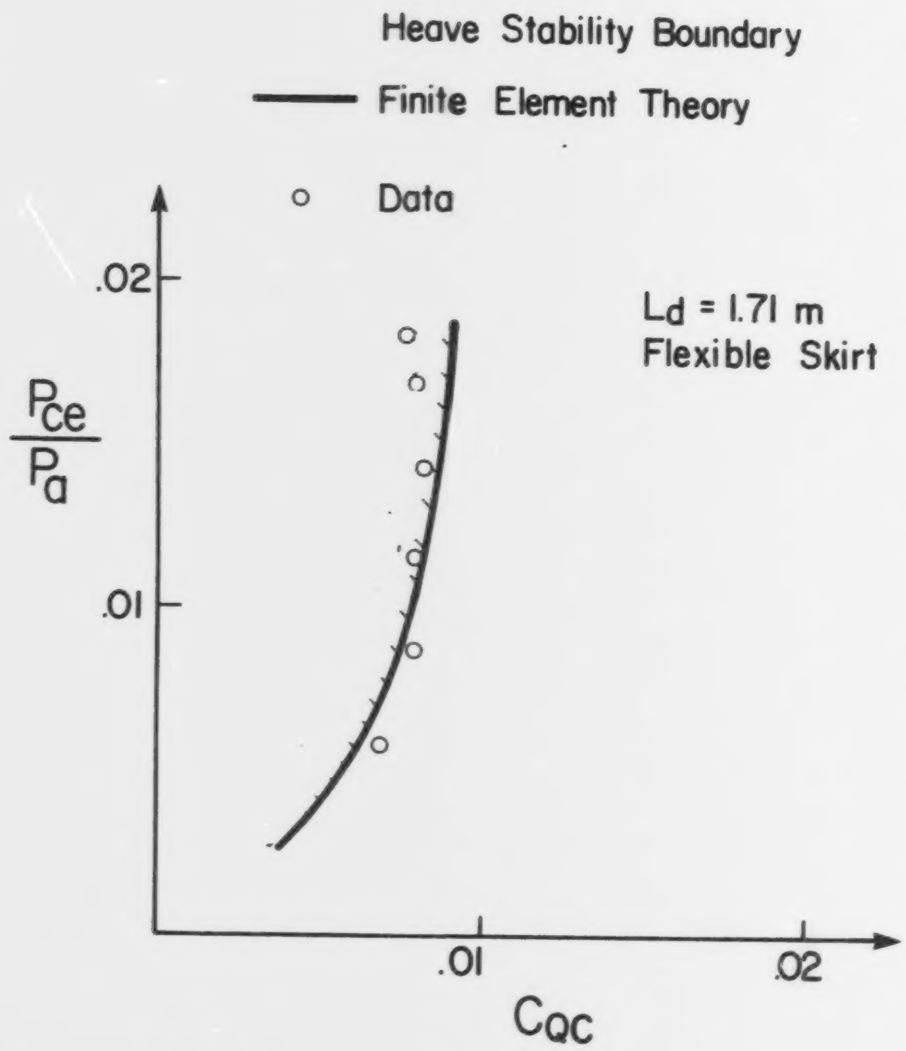

FIGURE 2.21 COMPARISON OF THEORY AND EXPERIMENT FOR SHORT DUCT FLEXIBLE SKIRT CASE

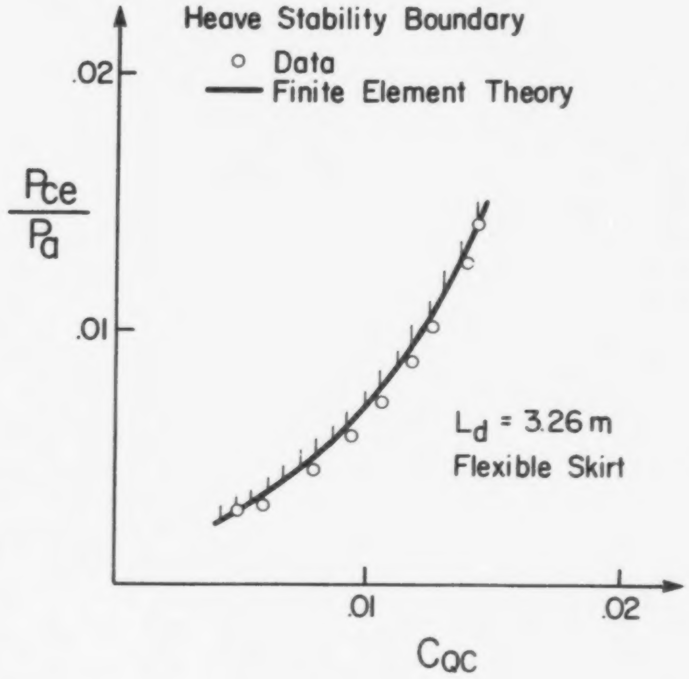

FIGURE 2.22 COMPARISON OF THEORY AND EXPERIMENT FOR THE LONG DUCT AND FLEXIBLE SKIRT CASE.

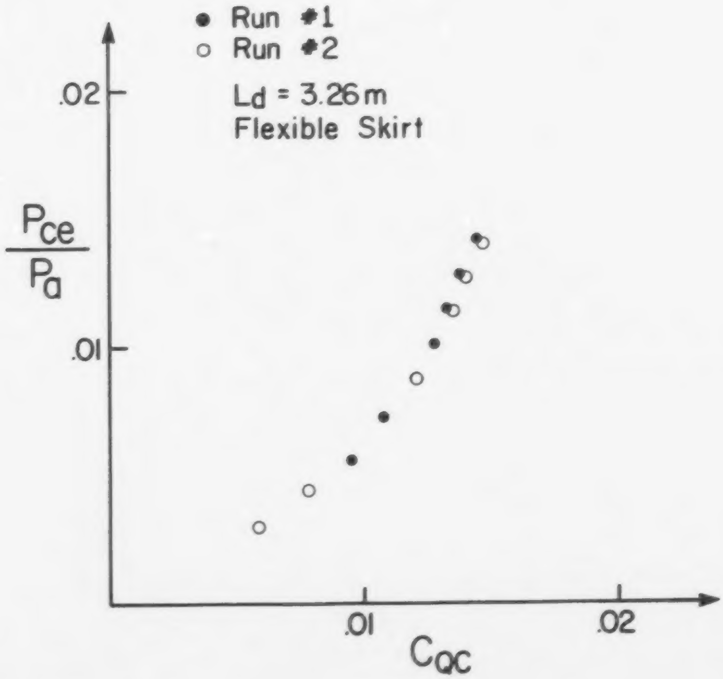

FIGURE 2.23 ILLUSTRATION OF REPEATABILITY OF THE EXPERIMENTAL DATA.

2.4.2) Comparison of Methods of Boundary Determination

Figure 2.24 compares the results obtained using the two boundary determination methods for a single data point for the short duct case. It is worth noting that this data was obtained some months later after the rig had been disassembled and used for another experiment. Also, both the theoretical results for the lumped inertance model and experimental results were obtained independently by G. Green [Ref. 2.19], who was not involved in the original experiments. This provides a good demonstration of the basic reproducibility of the results.

2.4.3) Internal Flow Effects

Experimental results showing an effect due to internal flow structure within the cushion volume as obtained using the sphere facility are given in Figure 2.25. They show that the long duct and centre feed hole arrangement without a baffle plate gives a smaller stable region than that obtained when a baffle plate is installed as indicated in Figure 2.6. For the short duct case, removal of the baffle plate resulted in a negligible change.

The results for both the long and short duct cases are qualitatively similar to those predicted by the radial wall-jet model discussed in Section 6 of [Ref. 2.1] (1978 Report) and Section 2.2.2.3 of the present report. Typical predictions made by this analysis for the present cushion geometry and duct system are given in Figure 2.26. They suggest that the quantity K_{jet} used in equation (16) of Section 2.2.2.3 is about 0.5 for these experiments.

2.5) Conclusions: Implications for Practical Stability Calculations

2.5.1) General

The Sphere Facility experiments clearly confirm the predictions of very large duct effects and modest or insignificant internal flow effects for cushion stability described in the 1978 report for the present Contract [Ref. 2.1]. But the experiments have a much broader significance than merely confirming the existence of significant duct effects. They represent the first time that we have been able to obtain a reasonably accurate experimental reproduction of the predictions of a linear stability analysis. This is an important milestone; it indicates a path for the systematic investigation of the effect that many other elements of a practical cushion system may have on cushion dynamics and stability. Some of the elements requiring urgent attention are: fan dynamics, viscoelastic skirt material properties and the valving effect of segmented skirt cushions; but there are many others.

It is also worth noting that the linear analysis used in this work definitely does not present the complete picture. For example, the internal flow effects observed at practical flow rates are apparently insignificant. However, at very high flow rates a large effect was observed when a baffle plate was not used. During a typical cycle of this instability, the skirt suddenly lost its shape and was sucked inwards and up. This was accompanied by a sudden loss of lift followed by a rapid motion of the model downwards with subsequent redeployment and rapid motion upwards. It may not be of any practical significance for amphibious air cushion systems but could be

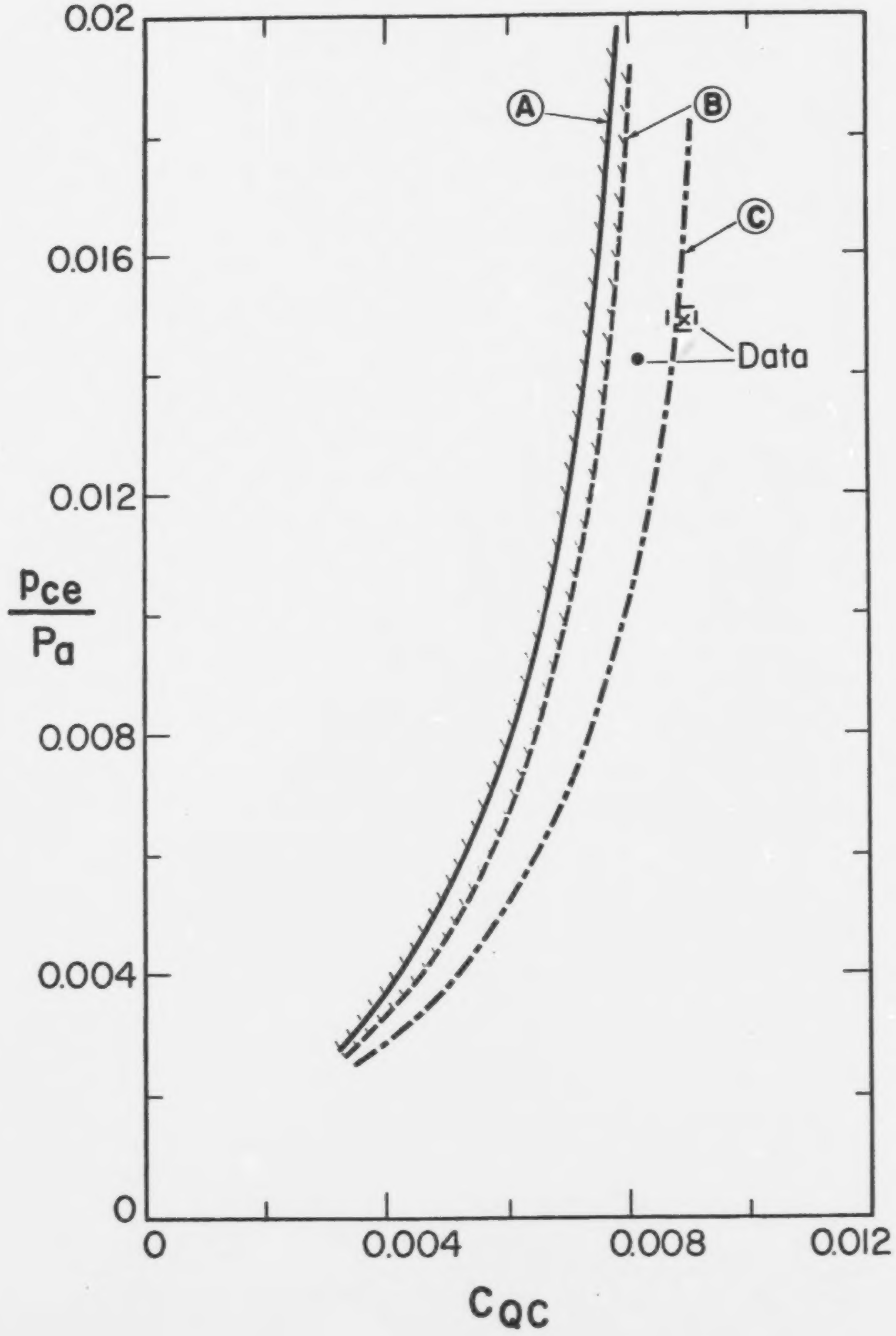

FIGURE 2.24. COMPARISON OF METHODS OF ASCERTAINING STABILITY BOUNDARIES WITH THEORETICAL PREDICTIONS FOR L_d = 1.71m. THEORY, LUMPED INERTANCE DUCT MODEL OF REF. 21, CURVE A; LUMPED INERTANCE MODEL OF REF. 1, CURVE B; FINITE ELEMENT MODEL OF REF. 1, CURVE C. DATA POINTS, EXTRAPOLATED DECREMENT METHOD INCLUDING ERROR BARS: ✕; OBSERVED MOTION METHOD: O.

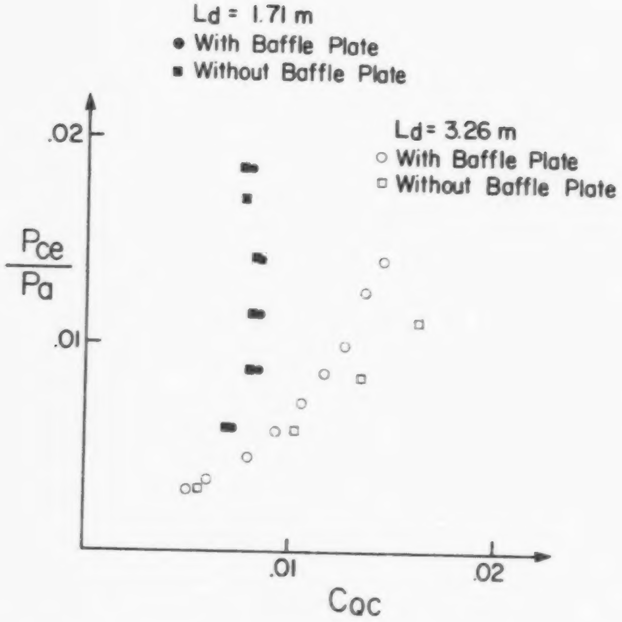

FIGURE 2.25 EXPERIMENTAL RESULTS OBTAINED IN SPHERE FACILITY SHOWING AN INTERNAL FLOW EFFECT.

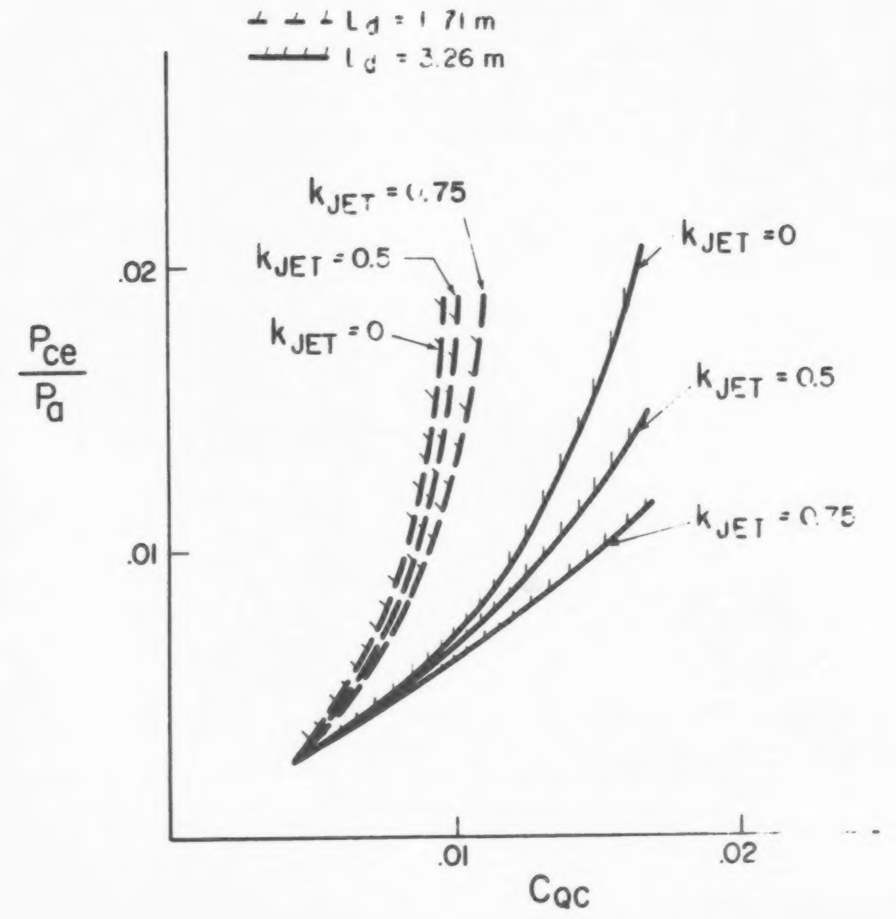

FIGURE 2.26 THEORETICAL RESULTS FOR RADIAL WALL-JET MODEL OF AN INTERNAL FLOW EFFECT FOR MODEL TESTED IN THE SPHERE FACILITY.

important for special designs. It is clearly outside the scope of the present theory.

2.5.2) Improved Modelling for Heave Table Facility

Figure 2.27 is a comparison of the test results obtained on the original heave table facility described in Section 2.3.1 with theoretical results based on a finite element supply duct model, a lumped capacitance tank model, and a constant pressure source fan model. Considering the complexity of this system,the agreement is quite remarkable. This suggests that linear stability analyses should be useful for design.

Finally the various results obtained here clearly indicate that, for practical systems, it is not possible to devise simple qualitative guidelines for the prediction of the onset of instabilities. It seems that each new design will require its own stability calculation; one will have to undertake the equivalent of a stress anslysis now widely used in the development of vehicle structures.

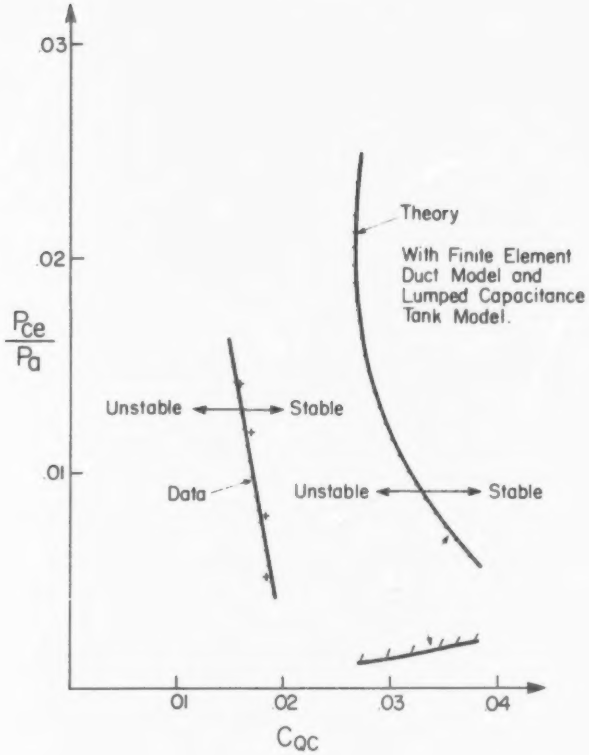

FIGURE 2.27 IMPROVED THEORETICAL PREDICTION OF STABILITY BOUNDARIES OBTAINED TEST FACILITY DEPICTED IN FIGURE 2.9 WHEN MODELLING OF THE SUPPLY DUCT IS INCLUDED.

3) STATIC PITCH AND ROLL STIFFNESS CHARACTERISTICS OF A SEGMENTED SKIRT CUSHION

3.1) Introduction

3.1.1) Background

As stated in the Introduction, one of the major objectives of the present Contract is the investigation of the static pitch and roll stiffness characteristics of a single plenum chamber segmented skirt cushion similar to the designs advocated in the first instance by Hovercraft Development Limited (HDL) of the U.K. As indicated in the work statement of the present Contract, particular emphasis is placed on a variant of that concept developed in Canada by Hoverlift Systems Limited of Calgary (HSL), but since a model of the HDL type is available at UTIAS, comparisons between the two systems are made where possible. The general approach adopted is the same as that described in the report on the investigation of the multicell type skirts undertaken under a previous contract with TDC [Ref. 3.1, "Flexicell" Contract, D500-201].

The British HDL skirt incorporates three distinctive features. In common with the British Hovercraft Corporation (BHC) skirt it uses a large number of segments or "fingers" to effect a partial cushion seal in the presence of obstacles. These have the capacity to restore the seal when one segment is seriously damaged or even completely torn off. When such an incident happens, the adjacent segments can expand to fill the gap. The second major feature is the distinctive mechanism by which it generates static stiffness in pitch and roll. The multicell skirts tested in Ref. 3.1 and the BHC skirt all – in principle at least – rely on compartmentation to generate the required spring effect. That is to say, the cushion is divided into a number of separate individual plenum chambers or cells, and the motion of the vehicle modulates the effective cushion flow exit area in such a way as to generate cushion pressure differentials between adjacent cells. This in turn generates the requisite restoring couples. In contrast, the HDL skirt has no compartmentation, but relies on contact of the skirt with the surface over which it is hovering to change the geometry of the inflated skirt so that the centre of the cushion "footprint" or pressure distribution on the ground or water surface is moved relative to the centre of mass of the vehicle, as is shown in Figure 3.1. A limitation of this concept is that, in contrast to multicell type cushions, in which roll and pitch stiffness can be increased by increasing the volume flow through the cells, the roll stiffness of the basic HDL cushion is limited by the geometry of the cushion. In particular, the segment angle Φ in Figures 3.1 and 3.2 is the dominant parameter controlling stiffness, and practical considerations may limit this angle to the range $35° \leq \Phi \leq 55°$. However, the effective stiffness may be increased by including the third distinctive feature, that is a loop as shown in Figure 3.1. This enables the entire skirt to be moved laterally relative to the vehicle by the control wires shown in Figure 3.1. This principle has been very effectively demonstrated by HDL on a small test vehicle [Ref. 3.2].

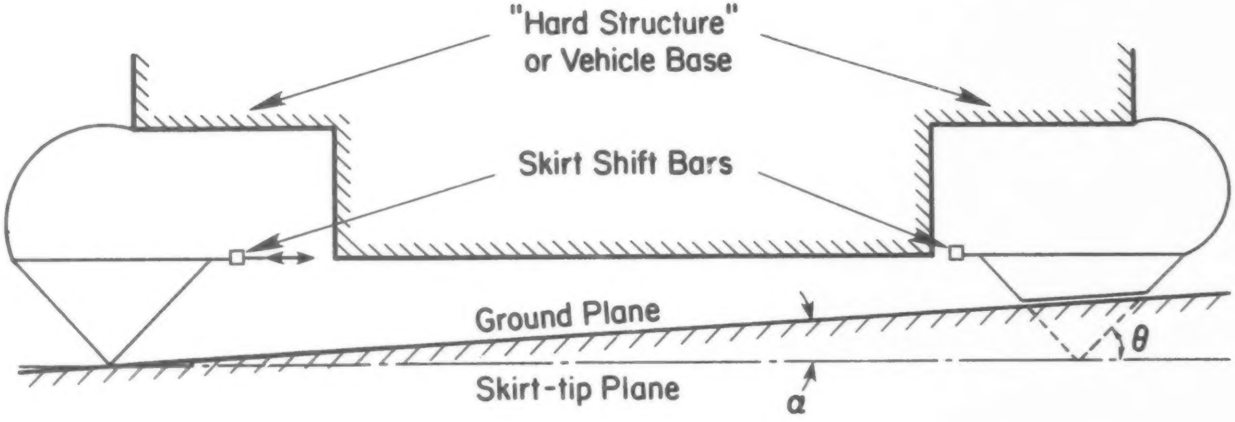
"Hard Structure" or Vehicle Base
Skirt Shift Bars
Ground Plane
Skirt-tip Plane
θ
α

FIG. 3.1 BASIC CONCEPT OF HOVERCRAFT DEVELOPMENT LIMITED (HDL) SKIRT.

For vehicles which move relatively slowly, the forces generated as a result of dynamic motion may be small enough to allow omission of the loop and skirt shift mechanism. This is the basic concept of the HSL skirt.

3.1.2) Details of HSL Skirts Built for UTIAS Facilities

The geometry of a typical segment for the skirt is shown in Figure 3.2. The loop is eliminated by altering the shape of the segment so that it can be attached to the vehicle base or "hard structure" at two points. In contrast to the HDT skirt, the segments are not free to rotate about the axis passing through the inner attachment points.

HSL skirts were constructed at UTIAS for both the Cushion Dynamics Facility and the Circular Track Test Vehicle, Vampire I. The segments were built to specifications supplied by H. S. Fowler [Ref. 3.3]. Details of the geometry are given in Table 3.1. It is noted that the segments for Vampire 1 are the same size and are made from the same material as those on the National Research Council's research vehicle HEX 4, which has base dimensions of 4.00 x 2.50m The segments for the cushion dynamics facility were constructed at a reduced size, and the scaling factor is approximately equal to the ratio of base widths. Segments for this model were fabricated from two materials; one is a urethane-coated nylon light weight tent fabric weighing 0.076 kg/m^2 and having a thickness of about 0.10 mm, and the second is 0.12 mm thick extruded polyethylene sheet which weighs 0.118 kg/m^2.

3.1.3) Detailed Objectives of the Work Described in This Section

A useful approximate value of the pitch and roll stiffness of this type of cushion can be obtained by simply assuming that the tips of the segments on one side remain touching the ground, and that the entire vehicle rotates about an axis passing through these tips. This is shown in Figure 3.1. However such an approach is not adequate for the present work.

Figure 3.3 is a photograph of the model on the Cushion Dynamics Facility hovering with an applied pitch moment, and for an appropriately scaled cushion air flow rate. It is clear that on smooth nonporous surfaces, the vehicle does not rotate about the tips of the segments on the high side. Furthermore, observation of the dynamic motion of the Circular Track Test Vehicle - Vampire 1 - in response to various types of disturbance shows that a relatively large and rapidly changing cushion air escape area, similar to that shown in Figure 3.3 can occur. Theoretical analysis of the vehicle dynamics requires the formulation of a cushion volume flow conservation equation which is the equivalent of Equation (8) in Section 2.2.1 of this report. This in turn requires development of reasonably accurate estimates of the history of the cushion air escape area. In addition, application of Newton's laws of mechanics to determine the dynamic

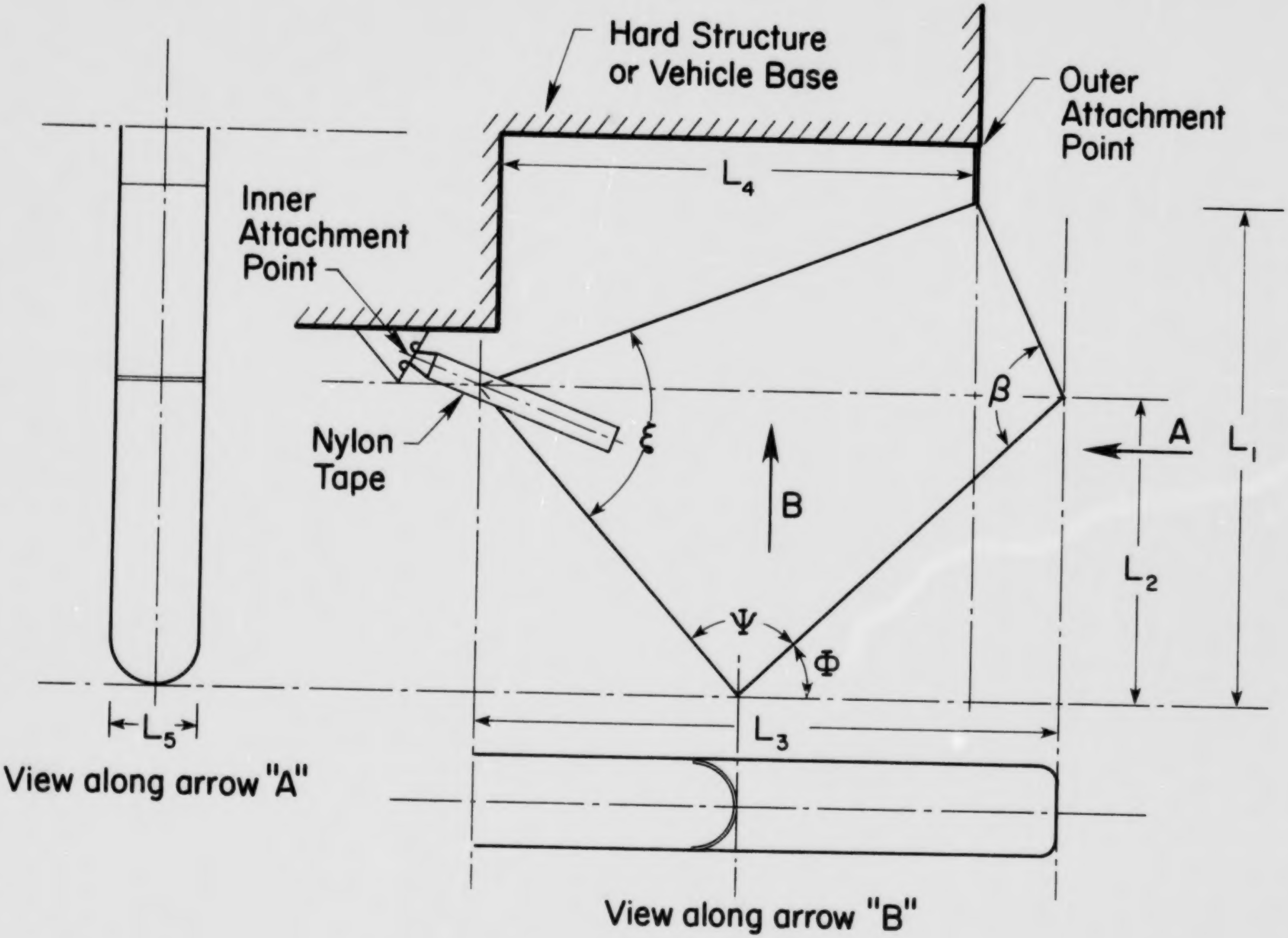
Hard Structure or Vehicle Base
Outer Attachment Point
L_4
Inner Attachment Point
Nylon Tape
ξ
B
β
A
L_1
L_2
Ψ
Φ
L_3
L_5
View along arrow "A"
View along arrow "B"

FIG. 3.2 DETAILS OF HOVERLIFT SYSTEMS LIMITED (HSL) SEGMENTS USED AT UTIAS.

(a)

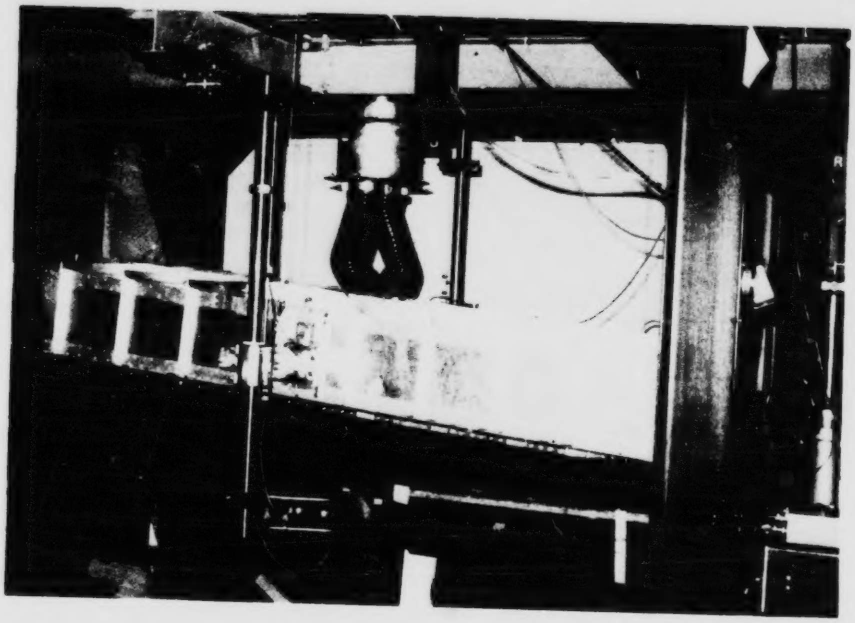

(b)

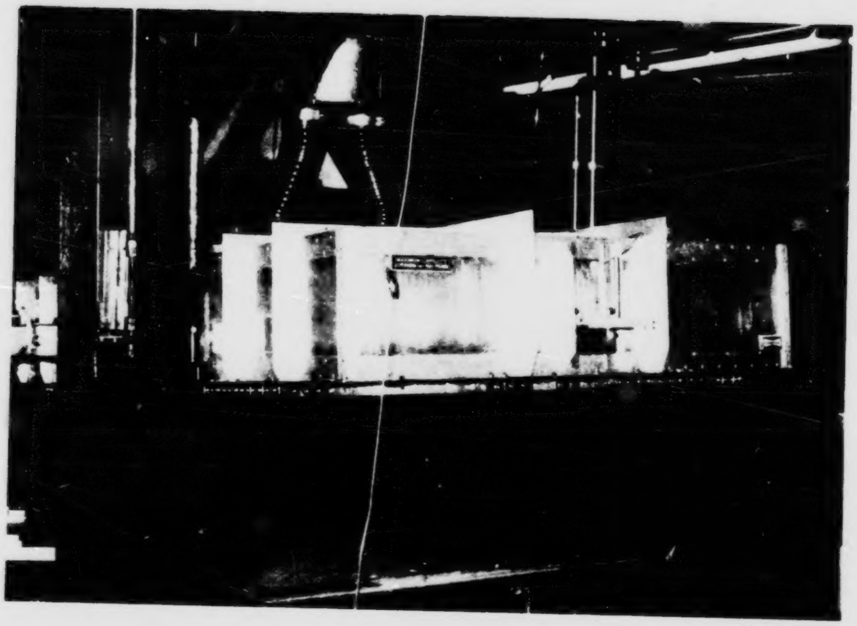

FIG. 3.3 PHOTOGRAPH OF HSL SKIRT MODEL ON CUSHION DYNAMIC TABLE HOVERING AT A SCALED VALUE OF CUSHION AIR FLOW RATE AND AT PITCH ANGLE.

(a) SIDE VIEW
(b) END VIEW

motions requires estimates of the histories such quantities as cushion pressure fluctuations and centre of mass motion. Even for the much simpler problem of interpreting experimental measurements of static stiffness characteristics, the availability of a theory which gives an accurate reproduction of the geometry of the motion as the vehicle pitches and rolls greatly improves the quality of the interpretation.

It is shown below that it is possible to set up a useful theory by using very simple ideas. The geometry of the cushion makes some of the algebraic manipulations involved tedious, but as the entire analysis is programmed for solution by a digital computer, this poses no difficulty.

3.2) Theoretical Development

3.2.1) Pitch and Roll Stiffness Theory

3.2.1.1) Basic Assumptions

The theory for the pitch and roll stiffness of the HSL cushion described below is based on the concepts used in a previous UTIAS investigation of multicell cushions [Ref. 3.1]. The basic ideas may be stated as follows. First, the cushion is supplied with air by a single fan for which the static pressure-volume flow relationship or "characteristic" is known. Second, the air in the cushion volumes contained by the skirt and vehicle hard structure is essentially at rest, so that the static pressure throughout these volumes is constant. That is to say, these volumes are reservoirs. Third, the cushion is in hover over a smooth flat horizontal surface. Fourth, the air escape process from the cushion is described by the one-dimensional orifice flow model, which is based on the Bernoulli principle and a suitable discharge coefficient. Fifth, the skirt material is an infinitesimally thin weightless inelastic membrane which is incapable of supporting any compression loads; this concept may be described as the "ideal-model" material. Sixth, when as a result of movement in roll or pitch parts of the skirt contact the ground, the skirt material buckles locally in such a way as to make a leak-free or perfect seal. Also, except in the immediate neighbourhood of the ground, the skirt maintains its fully deployed geometry. The last assumption is that no sliding friction forces are generated between the skirt and the ground when contact and relative motion occurs.

It follows from these assumptions that, since the skirt material is assumed to be incapable of taking any compression, the only forces supporting the vehicle are those arising from the cushion footprint on the ground generated by the cushion pressure. This is the so-called hover condition; it requires that the gross weight of the vehicle be equal to the integral of the cushion foot print pressure over the cushion foot print area.

Furthermore, the assumptions that the parts of the skirt in contact with the ground make a perfect seal, and that the air in the

Table 3.1

Geometric Details of HSL Skirt Segments Used on UTIAS Models

Model	Base Size (mxm)	Skirt Material				Segment Geometry								
		Brand Name	Composition	Weight (kg/m^2)	Thickness (mm)	Φ ( )°	β ( )°	ψ ( )°	ξ ( )°	L_1 mm	L_2 mm	L_3 mm	L_4 mm	L_5 mm
Vampire I	4.08x2.06	Uniroyal	Nylon weave coated on 2 sides with neoprene	0.543	0.483	40	110	90	70	406	244	495	419	106
Cushion Dynamics Facility	2.44x1.22	Beflex 40	Nylon weave coated on 1 side with polyurethane	0.076	0.102	40	110	90	70	241	142	290	275	49
		Polyethylene vapour barrier (Canadian Tire Corp.)	Polyethylene (extruded sheet)	0.118	0.117	40	110	90	70	241	142	290	275	49

plenum volume is at rest, imply that the cushion pressure is constant over almost all of the footprint. Hence the centre of pressure for the footprint, or the point on the ground through which a single force has to act in order to balance the cushion pressure forces, can be assumed to be located at the centroid of the footprint geometry. Therefore, the restoring moments generated by the cushion in pitch and roll are obtained in this analysis by calculating the movement of this centroid relative to a point on the base of the vehicle or experimental model.

The assumptions that skirt buckling is confined to the immediate neighbourhood of the parts that are in contact with the ground, and that the remainder of the skirt retains the shape of the fully deployed geometry corresponding to zero pitch or roll, imply that the part of the boundary of the cushion foot print in the region where skirt-ground contact occurs is defined by the curve of intersection of the fully deployed skirt and the ground plane.

It should be observed that the buckling assumptions used here must be consistent with all applicable structural stability requirements. In the context of the "ideal model" skirt concept, the combined loading arising from the internal cushion pressure, attachment points and other sources must be such that, at any point in the segment membrane, the lesser of the two principal membrane stresses does not become negative. If such a region of local compressive stresses occur, then sufficient local buckling must take place until this is relieved. As has been demonstrated in previous work for TDC [Refs. 3.1 and 3.4], such buckling phenomena may have large effects on cushion behaviour. For certain multicell geometries, local buckling leads to loss of the cushion seal. As is discussed below, buckling of the segments does occur at large enough roll or pitch angles for the HSL cushion, but this does not cause the loss of the cushion seal.

Finally, it is noted that not all of the simplifying assumptions discussed above may be accurate enough for engineering design purposes. To quote but one example, there is considerable evidence that the "ideal model skirt" assumption leads to serious oversimplifications in certain circumstances. That is, it precludes any prediction of the hysteretic damping effects encountered in previous work for TDC [Refs. 3.1 and 3.4]. Part of the present task is to assess the utility of these assumptions for the HSL skirt.

3.2.1.2) Measurement of Skirt Geometrical Parameters

The basic parameters defining the geometry of the skirt model are given in Figure 3.4. The skirt is attached to a plenum supply box having a length L and beam width B. The centre of mass of the system is located at a distance H_b above the base of the box. The other geometric parameters defined in Figure 3.4 were obtained for a particular test model and skirt system as follows. Owing to irregularities in construction of the individual segments, and because of the shape of the bottom parts of these segments, difficulties

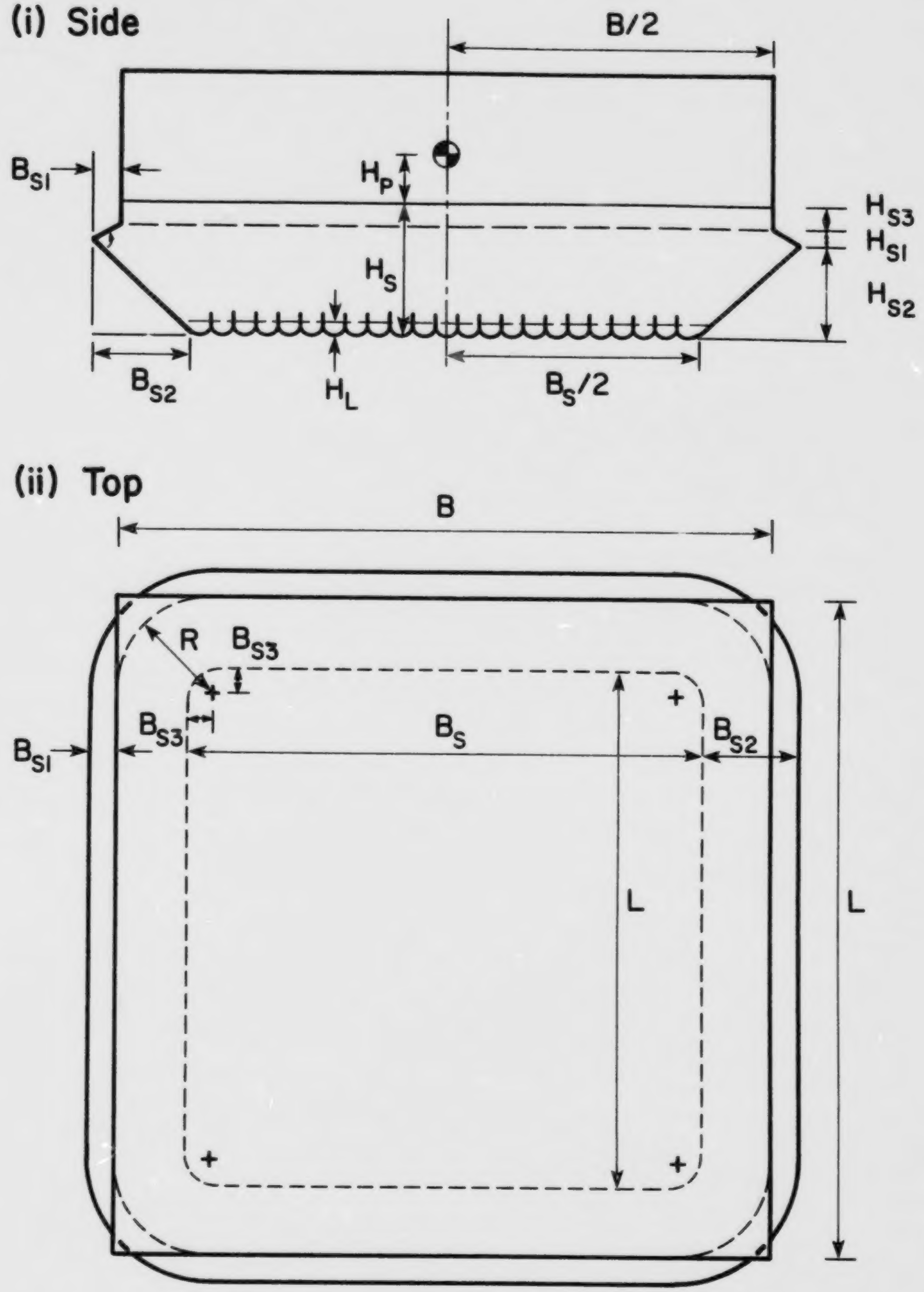

(i) Side

(ii) Top

B/2
B_{S1}
H_P
H_{S3}
H_{S1}
H_S
H_{S2}
B_{S2}
H_L
$B_S/2$
B
R
B_{S3}
B_{S3}
B_S
B_{S2}
B_{S1}
L
L

FIG. 3.4 BASIC PARAMETERS DEFINING THE GEOMETRY OF THE HSL SKIRT AT ZERO PITCH AND ROLL.

arise in defining a skirt height or a hovergap. It is noted in this respect that when this type of cushion is hovering at zero pitch or roll angle most of the segments are touching the ground.

To circumvent this problem, the following procedure was adopted. The cushion model was set parallel to the ground-board and at a height such that, with the air supply operating and the cushion fully inflated, almost all the segment tips were just touching the ground-board. This height was chosen as a reference height, and labelled H_s. As is depicted in Figures 3.4 and 3.5, this did not correspond to zero hovergap; indeed almost all of the cushion air was observed to escape through the approximately triangular or scallop-edged leakage areas between segment tips. Some air also escaped at points higher up, especially in the region where the segments were attached to the outer edge of the vehicle; however it was judged that this contributed only a very small fraction to the total leakage area. To account for this leakage, the model was locked at the reference height H_s and an "equivalent leak height" H_L was inferred from measurements of the cushion pressure p_c and cushion volume flow q_c. This height is marked in Figure 3.4, and the estimation proceeded as follows. According to the usual orifice flow model, for a mean leak height H_L, the quantity q_c is given by

$$q_c = 2C_D(\Phi, \mathrm{Re})(B_s + L_s)H_L\sqrt{\frac{2p_c}{\rho_a}} \qquad (1)$$

where C_D is the usual orifice discharge coefficient, which is a function of the segment angle Φ and the Reynolds Number Re based on the air exit velocity $V_j = \sqrt{2p_c/\rho_a}$. Here p_c and ρ_a are the cushion gauge pressure and atmospheric air density respectively. The total equivalent orifice area is $2(B_s + L_s)H_L$, where B_s and L_s are defined in Figure 3.3. Here, as in previous analyses of cushions [Ref. 3.1] it was assumed that Re was sufficiently large to cause C_D to be independent of it. However C_D depends on the angle Φ. Elsely and Devereux [Ref. 3.5] give the following expression for C_D for sharp edged orifices

$$C_D = 0.5 + (0.4 \times 10^{-3})\Phi + 0.109 \times 10^{-4}\,\Phi^2$$

$$- 0.494 \times 10^{-7}\,\Phi^3 + 0.345 \times 10^{-9}\,\Phi^4 \qquad (2)$$

where Φ, given in degrees, is measured from the free jet direction. That is, $\Phi = 0$ corresponds to the Borda orifice for which the inviscid value of $C_D = 0.5$. For the present skirt, $\Phi = 40°$, which gives $C_D = 0.5312$.

All other geometrical quantities required for the analysis and defined in Figure 3.4 were measured while the cushion was inflated

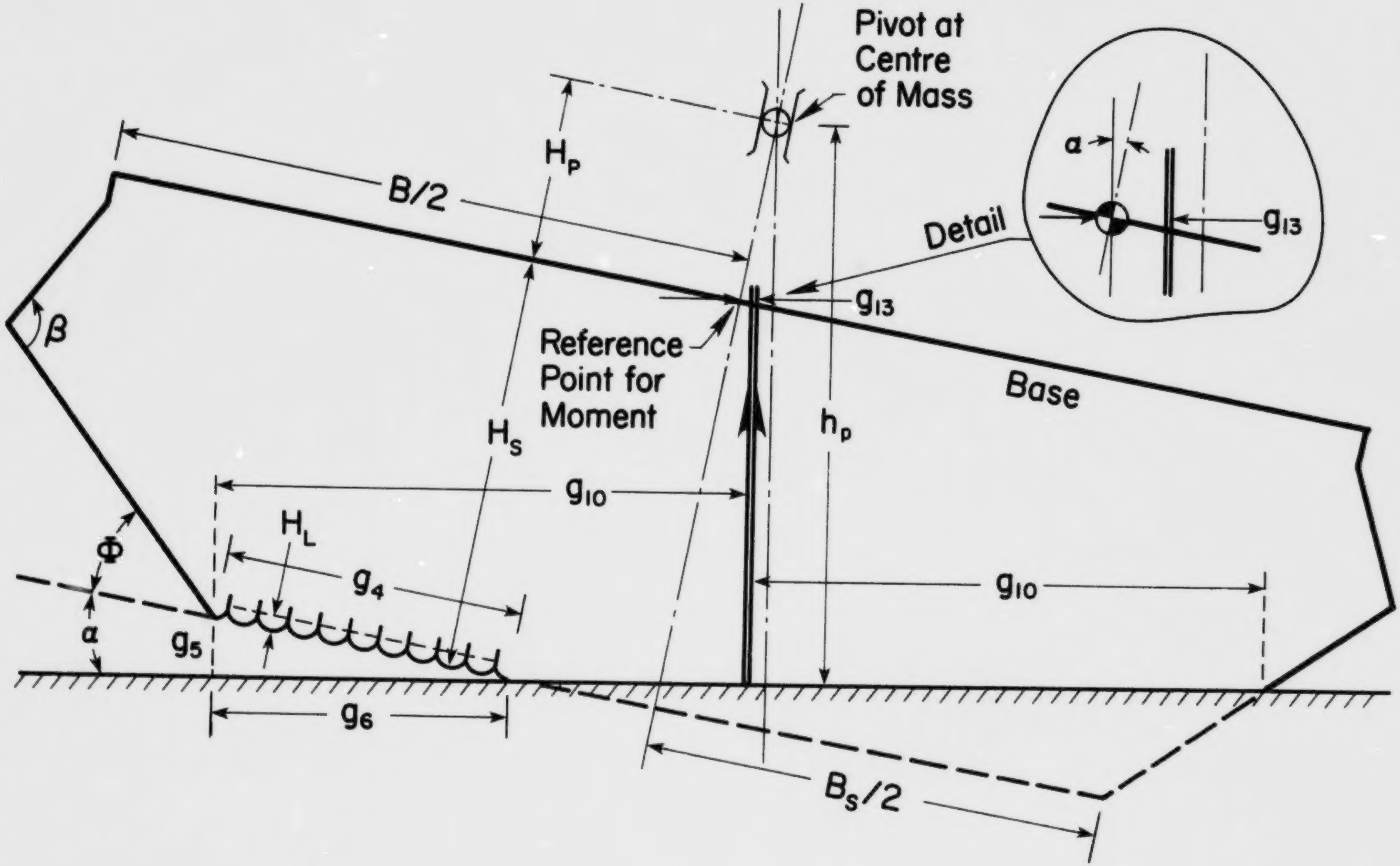
Pivot at Centre of Mass
H_p
$B/2$
Detail
g_{13}
α
g_{13}
β
Reference Point for Moment
Base
H_S
h_p
g_{10}
H_L
Φ
g_4
g_{10}
α
g_5
g_6
$B_s/2$

FIG. 3.5 DETAILS OF THE GEOMETRY OF THE HSL SKIRT ASSUMED FOR COMPUTING PITCH AND ROLL STIFFNESS. CASE I: BELOW THE KNEE REGION.

and locked at the reference height H_s. It is noted that, although the choice of H_s is to some extent arbitrary, as may be seen below, this poses no analytical problems, provided only that it is used consistently.

3.2.1.3) Formulation of the Roll Stiffness Equations

The formulation of the roll stiffness equations is now given. Figure 3.5 depicts the geometry of the cushion when rolled to an angle α. In the following analysis, fixed or known quantities are generally defined by upper case letters, while quantities which are variable and a function of the roll angle α are denoted by lower case letters. The model is assumed to be constrained to move vertically and to rotate about an axis passing through the centre of mass. This is called the pivot in Figure 3.5, and when the cushion is rolled, this pivot is located a distance h_p above the ground-board. If, when the cushion is rolled and inflated, its geometry is exactly the same as for zero roll - except of course for the dotted part shown in Figure 3.4 - then the geometrical parameters describing such quantities as the cushion air escape area and the location of the foot print centroid are functions of the two quantities α and h_p. It is a straightforward exercise in trigonometry to derive them. This is done in a sequence of steps and the quantity derived at each step is labelled in the sequence g_1, g_2, g_3... . The details of these derivations are given in Appendix E.

It is to be noted that, for sufficiently large values of α, it is possible for the "knee" of the segments on the rolled down side to contact the ground before α becomes large enough to force contact of the vehicle base with the ground, or hard structure contact (HSC). In the following analysis, it is assumed that for large enough α, it is possible for the geometry to take the form shown in Figure 3.6. It is not clear if this can occur in practice; and this point is addressed in the experiments.

In the following formulation it is assumed that the gross or all-up weight supported by the cushion W and the applied rolling moment M are given, and the task is to compute the four unknown quantities: α, h_p, q_c and p_c. Here q_c is the volume flow rate through the cushion and p_c is the cushion pressure. The first equation is the given fan pressure-volume flow characteristic. It is assumed that a cubic or other suitable functional relationship for the fan delivery pressure p_f and volume flux q_f is fitted to available design data. That is,

$$p_f = C_o + C_1 q_f + C_2 q_f^2 + C_3 q_f^3 + \dots \qquad (3)$$

where the coefficients C_o, C_1, C_2, C_3 are given. For this type of system, the fan outlet is usually connected directly to the plenum chamber so that $p_f = p_c$. Furthermore, in the absence of dynamic motion, the volume flux out of the cushion $q_c = q_f$. Hence equation

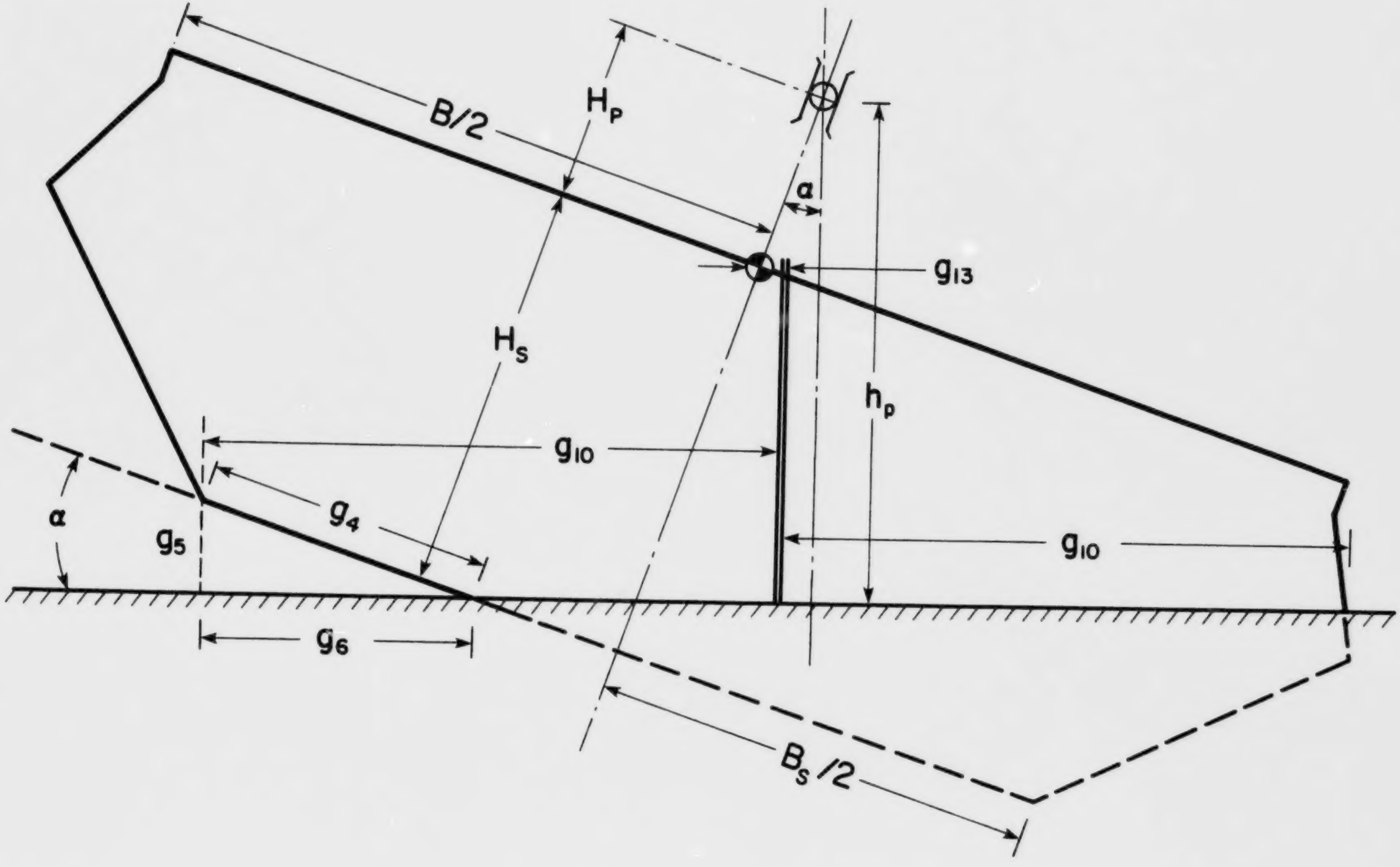
B/2
H_P
α
g_{13}
H_S
h_p
g_{10}
g_4
α
g_5
g_{10}
g_6
$B_S/2$

FIG. 3.6 DETAILS OF THE GEOMETRY OF THE HSL SKIRT ASSUMED FOR COMPUTING PITCH AND ROLL STIFFNESS. CASE II: ABOVE THE KNEE REGION.

(3) can be replaced by

$$p_c = C_o + C_1 q_f + C_2 q_f^2 + C_3 q_f^3 \tag{4}$$

The cushion air escape process is described by the one dimensional Bernoulli orifice flow law:

$$q_c = C_D \left(\sqrt{\frac{2p_c}{\rho_a}} \right) a_e(\alpha, h_p) \tag{5}$$

Here a_e is the cushion air escape area shown in Figure 3.3. The discharge coefficient C_D is assumed to be the same as that for $\alpha = 0$, since equation (2) shows that an increase in the effective orifice angle from Φ to $\Phi + \alpha$, with $\alpha = 10°$, increases C_D by about 2.2%. The escape area a_e is calculated as the sum of three parts:

(a) a rectangular component at the pitch or rolled up end, which for the roll case is $g_5(\alpha, L_p)L_s$;

(b) the two triangular areas at the ends or sides for roll and pitch respectively, for the roll case this contributes g_5, g_6;

(c) the addition associated with the leak height H_L.

To calculate the contribution (c), it is assumed that the leak height H_L only makes a contribution for that portion of the skirt perimeter in which the segment does not touch the ground. Inspection of the skirt when rolled or pitched has indicated that the fraction of the perimeter in which the segments contact the ground and for which significant leakage occurred through the triangular shaped regions between segment tips, is very small. Furthermore, for the smooth surface on which the experimental measurements were taken, the remainder of the segments formed an almost perfect seal. Figure 3.7 is a photograph of the segments on the pitched down side, the effectiveness of the seal is apparent. Hence the contribution by part (c) to the flow area is $(2g_4 + L_s)H_L$ for rolling motion. After some trigonometric manipulations, the expression for a_e is found to be, with $H_s + H_p \triangleq H$, and for the pure roll case

$$a_e(\alpha, h_p) = \left(\frac{B_s}{2} \sin\alpha - H\cos\alpha + h_p \right) \left(L_s + \frac{B_s}{2} \cos\alpha - H\cos\alpha \cot\alpha + h_p \cot\alpha \right)$$

$$+ H_L(B_s - 2H\cot\alpha + 2h_p \operatorname{cosec}\alpha + L_s) \tag{6}$$

Details of this development are given in Appendix D.

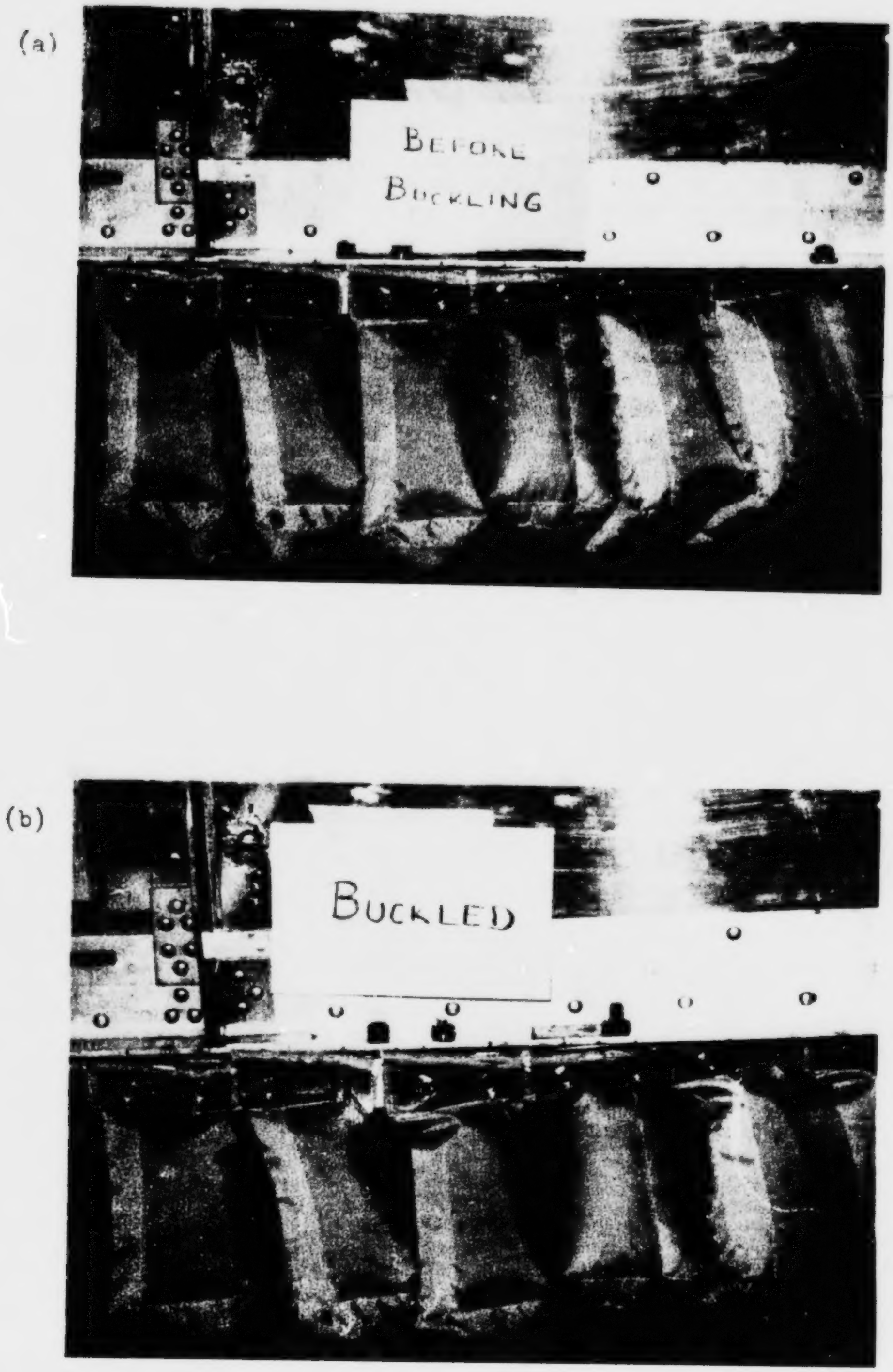
(a)
BEFORE BUCKLING
(b)
BUCKLED

FIG. 3.7 PHOTOGRAPH OF SKIRT SEGMENTS ON PITCH-DOWN SIDE SHOWING EFFECTIVE SEAL.

(a) BEFORE SEGMENT BUCKLING
(b) AFTER SEGMENT BUCKLING

The third and fourth equations for the set of unknowns (α, h_p, p_c, q_c) are derived respectively from the hover condition and the requirement that the location of the centroid be such as to sustain the applied moment. Both of these require consideration of the shape of the cushion footprint. The simplest possible approximation is to assume that it is a rectangle. For the roll case, this rectangle has an area $2L_s g_{10}(\alpha, h_p)$, where $g_{10}(\alpha, h_p)$ is defined as exactly half the distance between the rolled up and rolled down sides of the footprint. This is shown in Figure 3.5. The centre of pressure passes through the point which is midway between these sides of the footprint. The assumed shape of the footprint ultimately used in the calculations described below is given in Figure 3.8. The errors involved in assuming simpler shapes of footprint are discussed in Section 3.3.

The hover condition requires that the footprint area $a_f(\alpha, h_p)$ and cushion pressure be related through

$$W = p_c a_f(\alpha, h_p) \tag{7}$$

where for the rectangular approximation,

$$a_f(\alpha, h_p) = L_s\{[H \cos\alpha - h_p]\cot(\Phi - \alpha) + B_s[\cos\alpha + \sin\alpha \cot(\Phi - \alpha)]\} \tag{8}$$

The expression for $a_f(\alpha, h_p)$ corresponding to the footprint drawn in Figure 3.8 is given in Appendix C.

The moment equilibrium condition for a body acted upon external forces is simply that the sum of all couples about any reference point be zero (see Appendix D). For the present problem, the chosen reference is at the centre of the base as shown in Figure 3.5. The moment equilibrium condition then becomes

$$M = p_c a_f(\alpha, h_p) g_{13}(\alpha, h_p)$$

or just

$$M = W g_{13}(\alpha, h_p) \tag{9}$$

For a rectangular footprint, $g_{13}(\alpha, h_p)$ is given by

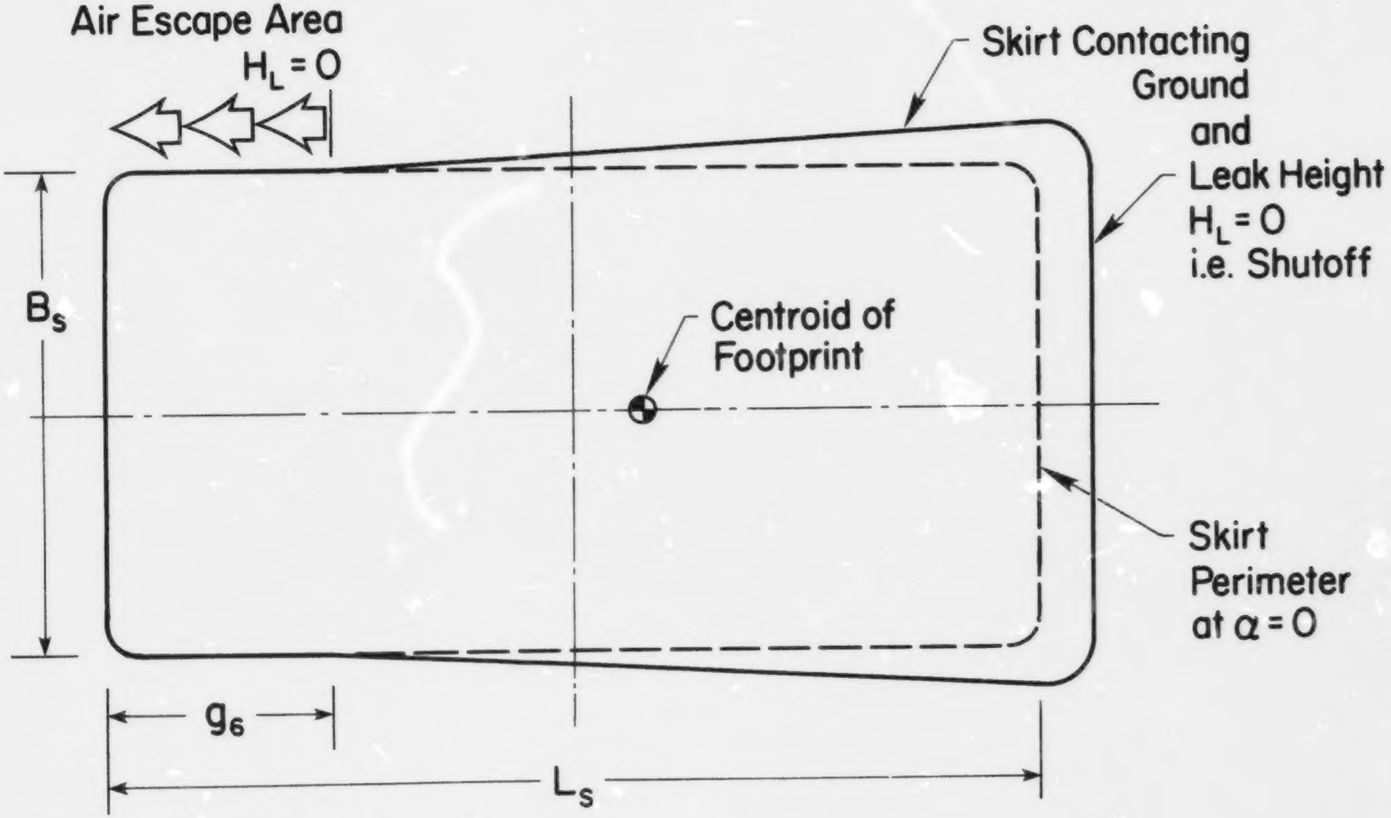
Air Escape Area
$H_L = 0$
Skirt Contacting Ground and Leak Height $H_L = 0$ i.e. Shutoff
B_s
Centroid of Footprint
Skirt Perimeter at $\alpha = 0$
g_6
L_s

FIG. 3.8 ASSUMED FOOTPRINT SHAPE FOR ROLL AND PITCH STIFFNESS CALCULATIONS.

$$g_{13}(\alpha, h_p) = H\left[\frac{1}{2}\cos\alpha\,\cot(\Phi - \alpha) - \sin\alpha\right] + H_p\sin\alpha$$
$$+ \frac{B_s}{4}\left[\sin\alpha\,\cot(\Phi - \alpha)\right] - \frac{h_p}{2}\cot(\Phi - \alpha) \qquad (10)$$

The expression for the footprint used here is given in Appendix D.

In summary, the formulation now has seven unknowns: the four mentioned above, namely (α, h_p, p_c, q_c), and three auxiliary unknowns (a_e, a_f, g_{13}) expressed in terms of the variables (α, h_p). The equations derived for this system use four physical principles; these are (i) the given fan characteristic, equation (4); (ii) the Bernoulli model of the cushion air escape process, equation (5); (iii) the hover condition, equation (7); the moment equilibrium condition, equation (9). The three additional equations required to complete the formulation are equations (6), (8), (10); they are derived purely from consideration of the geometry of the deployed skirt.

3.2.1.4) Formulation for Pitching Motion

The development of the analysis for pitching motion is identical to that for roll. The equations may be obtained directly by simply interchanging the symbols L_s and B_s.

3.2.1.5) Exact and Approximate Solution

The exact solution to the above system of equations can only be obtained by numerical methods.

One obvious way of simplifying the analysis is to exploit the fact that the value of α usually does not exceed 6° for pitch or 12° for roll. The small angle approximations

$$\sin\alpha \simeq \alpha[1 + O(\alpha^2)], \quad \cos\alpha \sim 1 + O(\alpha^2), \quad \operatorname{cosec}\alpha \sim \frac{1}{\alpha}[1 + O(\alpha^2)]$$

and others, are very accurate because they are correct to second order. Typically for $\alpha = 12°$, the approximation $\cos\alpha = 1$ commits only an error of 2.2%. Hence one might consider constructing formal asymptotic expansions to expressions such as equation (6). Therefore, since the quantities B_s, H, h_p, L_s and H_L all remain fixed in the limit $\alpha \rightarrow 0$, a first order approximation to $a_e(\alpha, h_p)$ is

$$a_e(\alpha, h_p) = \frac{1}{\alpha}\{(h_p - H)^2 + 2(h_p - H)H_L\} \qquad (11)$$

These are, however, problems incurred by such a simplification because, although the concepts of asymptotic sequences and series suggest that, for small enough α, it is possible to obtain an approximation which has acceptable accuracy, the requirement may be much more restrictive than for the approximations to the trigonometric function.

There are two reasons for this. First, the presence of both sine and cosine terms and other trigonometric combinations in equations such as (6) implies that the approximations are only correct to first order in α as $\alpha \rightarrow 0$. Second, the relative magnitudes of quantities which remain fixed in the limit may be such as to introduce large errors. For example it is evident from Figure 3.4 that h_p is very nearly equal $H = H_s + H_p$, so that the term $h_p - H\cos\alpha$ in equation (6) may be quite small and comparable to the term $B_s\sin\alpha/2$ even though the latter is formally of higher order in the limit $\alpha = 0$. The formulation contains several other examples where this type of error can occur, so that considerable care has to be exercised in developing a "small angle" approximation.

An alternative approach is to make approximations only to the trigonometric functions themselves, while retaining all of the terms in which they appear. With this approach, equation (6) for $a_e(\alpha, h_p)$ becomes

$$a_e(\alpha, h_p) = \alpha \left(\frac{B_s}{2} + \frac{1}{\alpha} (h_p - H) \right) \left(L_s + \frac{B_s}{2} + \frac{1}{\alpha} (h_p - H) \right) + H_L \left(B_s + \frac{2}{\alpha} (h_p - H) + L_s \right) \quad (12)$$

It is noted that the variable $\frac{1}{\alpha} (h_p - H)$ appears frequently in this and other approximations. Furthermore, even though $H_L \ll B_s$, in the above expression, terms such as $H_L B_s$ are added to terms such as $\frac{\alpha}{2} B_s L_s$.

In view of the exploratory nature of the present investigation, it was decided not to explore the possibilities offered by the small angle approximation, and to proceed directly to numerical solution of the equations. However, it is noted that for future work, especially in the application of the theory to full vehicle dynamics, exploitation of these types of approximation is desirable.

3.2.2) Dimensional Analysis

3.2.2.1) Analysis for the Ideal-Model Skirt Material

A dimensional analysis of the HSL skirt equations is developed along the lines of that described in Ref. 3.1. Since these equations assume that the skirt behaves like the "ideal-model" material, this analysis does not consider the question of correct scaling of the skirt material itself. The latter aspect is discussed briefly in the next section

Inspection of the equations given in Section 3.2.1.3 shows that the dependent quantities, α, h_p, p_c, and q_c are functions of:-

i) the coefficients describing the fan law (Equation r),

$$c_o, c_1, c_2, c_3 \ldots$$

ii) the principal geometric parameters (Equations 6, 8, 10),

B_s, L_s, H_s, H_p, H_L, Φ

iii) The all up weight W, the applied moment M, and atmospheric air density ρ_a

Consider a family of geometrically similar cushions. Then all geometric lengths are proportional to some suitable reference length, which may be taken as the overall base width B of the cushion for the investigation of roll stiffness characteristics, or the base length L for the investigation of pitch stiffness. For this family of cushions, one has, typically

$$\alpha,\ h_p,\ p_c,\ q_c \ =\ \text{fns}\ (W,\ M,\ B \text{ or } L,\ \rho,\ c_o,\ c_1,\ c_2,\ c_3) \qquad (13)$$

In Ref 3.1 it was shown for multicell cushions that, during a typical roll cycle, the fan pressure and volume flow moves along only a small segment of the fan characteristic, which in turn implies that the characteristic could be approximated by a straight line. It is assumed here that the same approximation can be made for the HSL skirt. This characteristic is perhaps most usefully specified in terms of the cushion air flow rate at zero roll or pitch angle $q_c\big|_{\alpha=0} \triangleq Q_{ce}$, and the slope of the curve dp_f/dq_f at $\alpha=0$. The quantity Q_{ce} is a parameter of direct design interest, it is usually determined partly by the nature of the surface over which the cushion operates. Also, by convention, the roll or pitch angle α is often considered to be an independent variable. Hence, equation (13) is replaced by

$$M,\ h_p,\ p_c,\ q_c \ =\ \text{fns}(\alpha,\ W,\ B \text{ or } L,\ \rho,\ Q_{ce},\ dp_c/dq_c\big|_{\alpha=0}) \qquad (14)$$

Application of the Buckingham II theorem using the variables W, B, and ρ as the dimensionally independent reference quantities gives, for roll

$$\underset{\pi_1}{\frac{M}{WB}}\ ,\ \underset{\pi_2}{\frac{h_p}{B}}\ ,\ \underset{\pi_3}{\frac{p_c B^2}{W}}\ ,\ \underset{\pi_4}{q_c\sqrt{\frac{\rho}{WB^2}}} = \text{fns}\left(\underset{\pi_5}{\alpha},\ \underset{\pi_6}{Q_{ce}\sqrt{\frac{\rho}{WB^2}}}\ ,\ \underset{\pi_7}{\frac{B^3}{\sqrt{\rho W}}\ \frac{dp_c}{dq_c}\bigg|_{\alpha=0}}\right) \qquad (15)$$

According to the principles of dimensional analysis, it is possible to replace any one of the seven dimensionless groups in equation (15) by products of any of them. For example π_7 can be replaced by

$$\pi_8 = \pi_6\ \pi_7 \ =\ \frac{Q_{ce}}{W}\ B^2\left(\frac{dp_c}{dq_c}\bigg|_{\alpha=0}\right) \qquad (16)$$

This idea may be used to rearrange them into forms which are more representative of the physics involved. For example, the hover condition requires $P_{ce} = h_f\ W/A_{ref}$, where Q_{ref} = BL is the base area of the vehicle and

$k_f \triangleq \pi_9 = f(\pi_6, \pi_7)$ is a dimensionless coefficient. For the HSL skirt, $k_f = 1$ approximately. Hence we replace $\pi_3 = p_c B^2/W$ by $p_c/p_{ce} = p_c A_{ref}/k_f W$ or $\pi_{10} = p_c A_{ref}/w \triangleq c_{pc}$. Also, the cushion air escape velocity at $\alpha=0$, v_{ce} is given by

$$v_{ce} = \sqrt{\frac{2p_{ce}}{\rho}} = \sqrt{\frac{2k_f W}{\rho A_{ref}}} \tag{17}$$

and it seems appropriate to express volume flows as fractions of the product $v_{ce}A_{ref}$. Hence π_3 and π_6 are replaced by

$$\pi_{11} = q_c \sqrt{\frac{\rho}{2WA_{ref}}}, \quad \pi_{12} \triangleq C_{QC} = Q_{ce}\sqrt{\frac{\rho}{2WA_{ref}}} \tag{18}$$

Also, it may be useful to replace the fan characteristic slope coefficient π_7 by a combination which contains only fan parameters, hence define

$$C_{SC} \triangleq \frac{Q_{ce}}{p_{ce}} \left(\left. \frac{dp_c}{dq_c} \right|_{\alpha=0} \right) = \frac{A_{ref}}{B^2 k_f} \pi_8 \tag{19}$$

To sum up, if the roll moment coefficient $C_{MR} \triangleq M/WB$ and the pitch moment coefficient $C_{MP} \triangleq M/WL$, the dimensional analysis yields

i) roll $C_{MR}, h_p/B, C_{pc}, \pi_{11} = f(\alpha, C_{QC}, C_{SC})$

ii) pitch $C_{MP}, h_p/B, C_{pc}, \pi_{11} = f(\sigma, C_{QC}, C_{SC})$

These forms are used in the data presentation to follow.

3.2.2.2) Scaling of Skirt Material

If the dimensional analysis given above is complete, that is, if it has not omitted any important variables affecting cushion performance, then roll or pitch stiffness curves obtained either from geometrically similar models of different size, or for a single test model operating at different gross weights W when plotted non-dimensionally should fall on the same curve, provided C_{QC} and C_{SC} are the same for all tests. Experimental results obtained at UTIAS for multicell skirts (Refs. 3.1 and 3.4) have indicated that failure to scale according the analysis given above usually indicates that the "ideal-model" skirt assumption does not hold. It was suggested, therefore, that the scaling failure may be related to the ability of the skirt material to sustain small but significant stresses caused by skirt-ground contact, the character of which are different in the roll-down and roll-up portions owing to the stress relaxation or viscoelastic character of some of the materials used in both model and full scale skirts. The most noticeable consequence of the presence of such stresses appears to be a static hysteresis in the roll and pitch stiffness curves. As is discussed in Section 4, this can have a significant effect on the dynamics of the vehicle motion.

Although previous UTIAS experiments have shown that this effect can be very significant on test models, for sufficiently thin skirt material it becomes negligible. A crucial question is: are such effects significant on full scale vehicles? The authors of this report are not aware of any documented evidence on the significance of such phenomena for full scale vehicles. Hence, work towards the elucidation of it has not been pursued until an assessment of its practical significance has become available.

The presence of such a phenomenon raises serious difficulties about the basis on which skirt material is scaled for model tests. For example, if significant viscoelastic phenomena occurred then the stress state inside the skirt structure might be characterized by its thickness "t", the storage modulus E_1, and a loss modulus* E_2. Hence to scale the skirt material according to the principles of dimensional analysis, one would require

$$C_{ST} \triangleq \left.\frac{t}{B}\right|_m = \left.\frac{t}{B}\right|_f \; ; \; \left.\frac{E_1 B^2}{W}\right|_m = \left.\frac{E_1 B^2}{W}\right|_f \; ; \; \left.\frac{E_2}{\sqrt{\rho W}}\right|_m = \left.\frac{E_2}{\sqrt{\rho W}}\right|_f$$

where the subscripts "m" and "f" indicate model and full scale, respectively. For a 1/10 size model, in which $W_m = W_f/100$, these rules require $E_{1m} = E_{1f}$, and since $\rho_m = \rho_f$, $E_{2n} = E_{2f}/10$. Thus one has to select a model material which has the same storage modulus as the full scale skirt, but has a strain rate modulus which is smaller by a factor of 10. An additional problem is that most full scale skirts are made of highly anisotropic elastomer-fabric composites, and these probably generate other constraints.

If the model is also to be used for vehicle dynamics experiments, then the inertial properties of the skirt material must also be scaled. Since skirt materials are very thin relative to characteristic dimensions of the skirt or vehicle this is best implemented through scaling of their weight per unit area w_s, that is, one must have

$$C_{SW} \triangleq \left.\frac{w_s A_{ref}}{W}\right|_m = \left.\frac{w_s A_{ref}}{W}\right|_f$$

These arguments demonstrate that development of rules for the scaling of skirt material based on dimensional considerations alone is extremely difficult since many contradictory constraints are introduced. It is therefore concluded that, for the present work, scaling the quantity C_{ST} or C_{SW} in model tests is an advance in ideas, and should provide additional information on the significance of skirt material properties for ACV dynamics. At the very least, it narrows the range of possibilities.

---

* The simplest model of a viscoelastic material relates the stress σ to the strain ε through $\sigma = E_1\varepsilon + E_2\dot{\varepsilon}$. Where E_1 and E_2 are functions of $\dot{\varepsilon}$ and temperature.

3.3) Results for Nylon-Urethane Skirt

3.3.1) General Comparison of Theory and Experiment

3.3.1.1) Roll Characteristics

Figure 3.9 compares the theoretically predicted rolling moment M in Newton-metres with experimentally measured values for $W_{EQ} = 872.1\text{N}$ (88.9 kg), $C_{QC} = 0.00714$ and a constant mass flow source ($C_{SC} = \infty$). As discussed in Section 3.2.1.3, the theory assumes that for large enough roll angle, the skirt assumes the geometry shown in Figures 3.5 and 3.6; and as shown in Figure 3.9, this results in a decrease in predicted rolling moment for α greater than 7.6°. Agreement between theory and experiment is very good for roll angles up to about 6°, but significant divergences occur for larger α, and the predicted drop in moment does not occur. This discrepancy is directly associated with segment buckling. For α less than 6° the curves show a small but distinct hysteresis, and beyond this angle the hysteresis is greatly increased.

Figures 3.10 and 3.11 compare the theoretically predicted and experimentally measured values of the motion of the centre of mass and changes in cushion pressure as a function of roll angle for a cushion weight of 507.0N (51.7 kg). The general agreement in both cases is very good; and in both cases the changes are large, which illustrates the importance of including correct accounting of both of these quantities in any description of the dynamics of vehicles equipped with this cushion. It is also important to note that the cushion pressure curve shows hysteresis which is small but quite distinct.

The effect of changing the fan slope coefficient is shown in figures 3.12 and 3.13. The experimental results in figure 3.12 exhibit only a small change in slope from the constant pressure source, $C_{SC}=0$ case, to the constant flow source, $C_{SC} = -\infty$ case. The theoretical curves of figure 3.13, however, predict large changes in slope for the smaller values of C_{SC}. The dashed curves illustrate the sensitivity of the theory to the footprint pressure distribution. In this case the assumed footprint pressure has been reduced for a distance L, equal to the gap, inside the skirt hemline to a value of 3/4 of the cushion pressure. This crudely approximates the pressure reduction resulting from the increase in fluid velocity which occurs near the exit. It indicates that the assumed pressure distribution is adequate for systems with larger values of C_{SC} but that a more detailed estimate would be required for very low values of C_{SC}. In most practical cases the added detail would not be necessary since C_{SC} is usually near -1.5 and the value for VAMPIRE 1 is -0.5.

3.3.1.2) Pitch Characteristics

Figures 3.14, 3.15 and 3.16 give typical results for pitching motions equivalent to those discussed in the previous Section. The pattern of agreement is the same as for the roll tests, however, the hysteresis in Figure 3.12 is much less than that displayed in the roll test data, it is, for all practical purposes, negligible. This is to be expected, since for pitching motion, a much smaller fraction of the total number of segments,

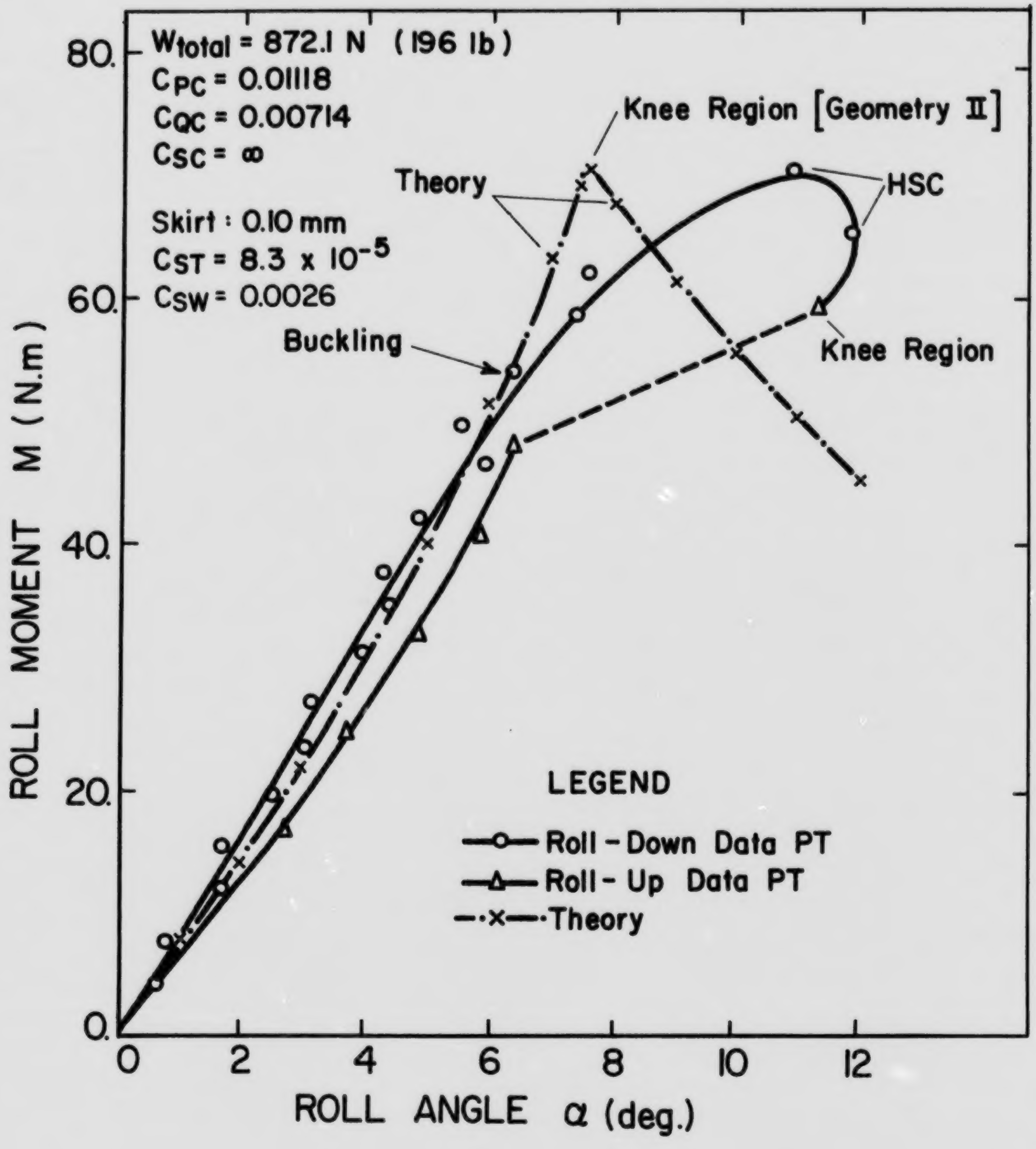

FIG. 3.9 COMPARISON OF TYPICAL ROLL STIFFNESS TEST RESULTS WITH THEORY FOR THE HSL SKIRT ON THE CUSHION DYNAMICS FACILITY. POLYURETHANE COATED NYLON IS THE SKIRT MATERIAL.

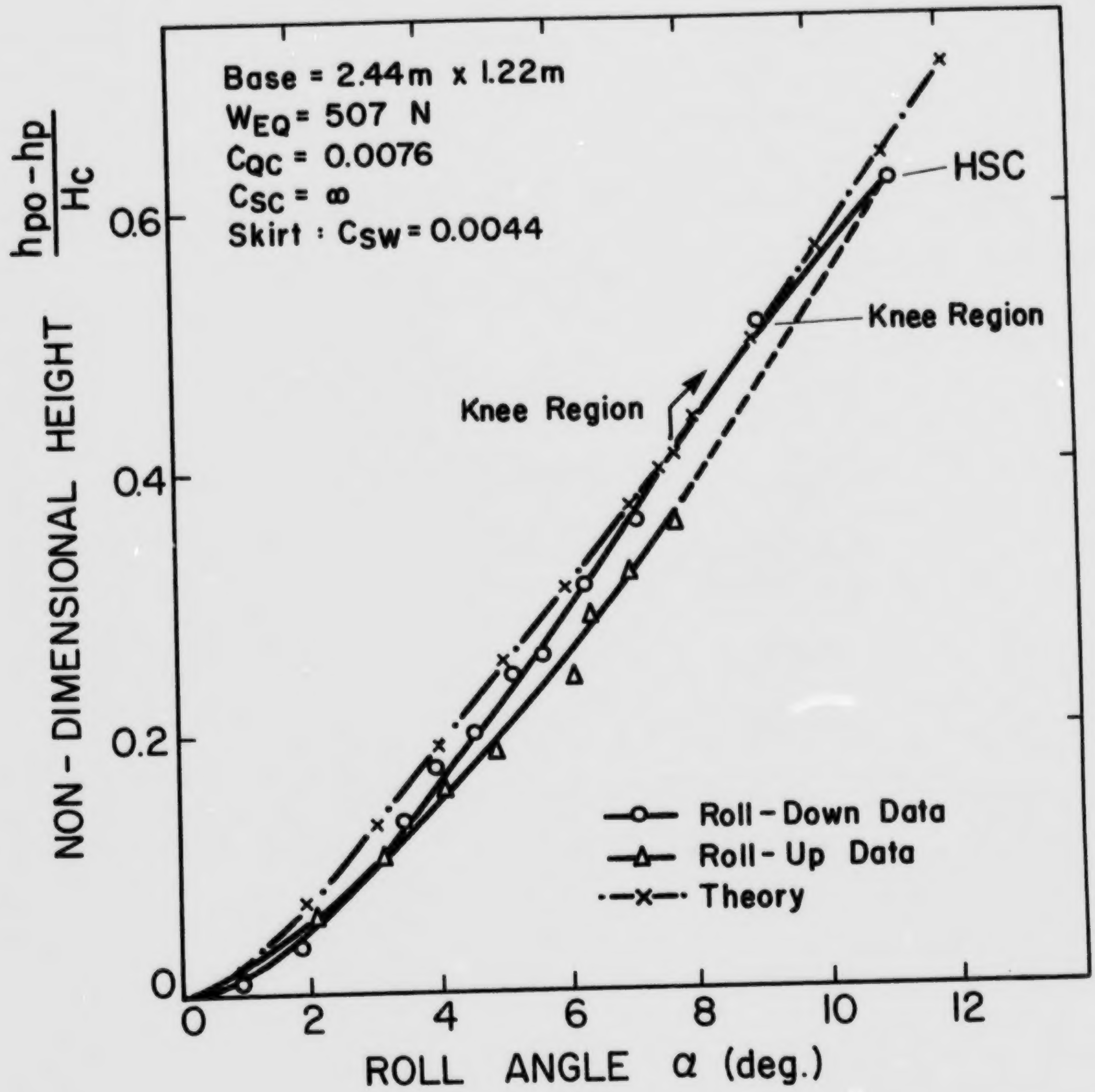

FIG. 3.10 COMPARISON OF PREDICTED AND MEASURED CENTRE OF MASS MOTION DURING ROLL FOR CUSHION DYNAMICS FACILITY WITH HSL SKIRT. SKIRT MATERIAL IS POLYURETHANE COATED NYLON.

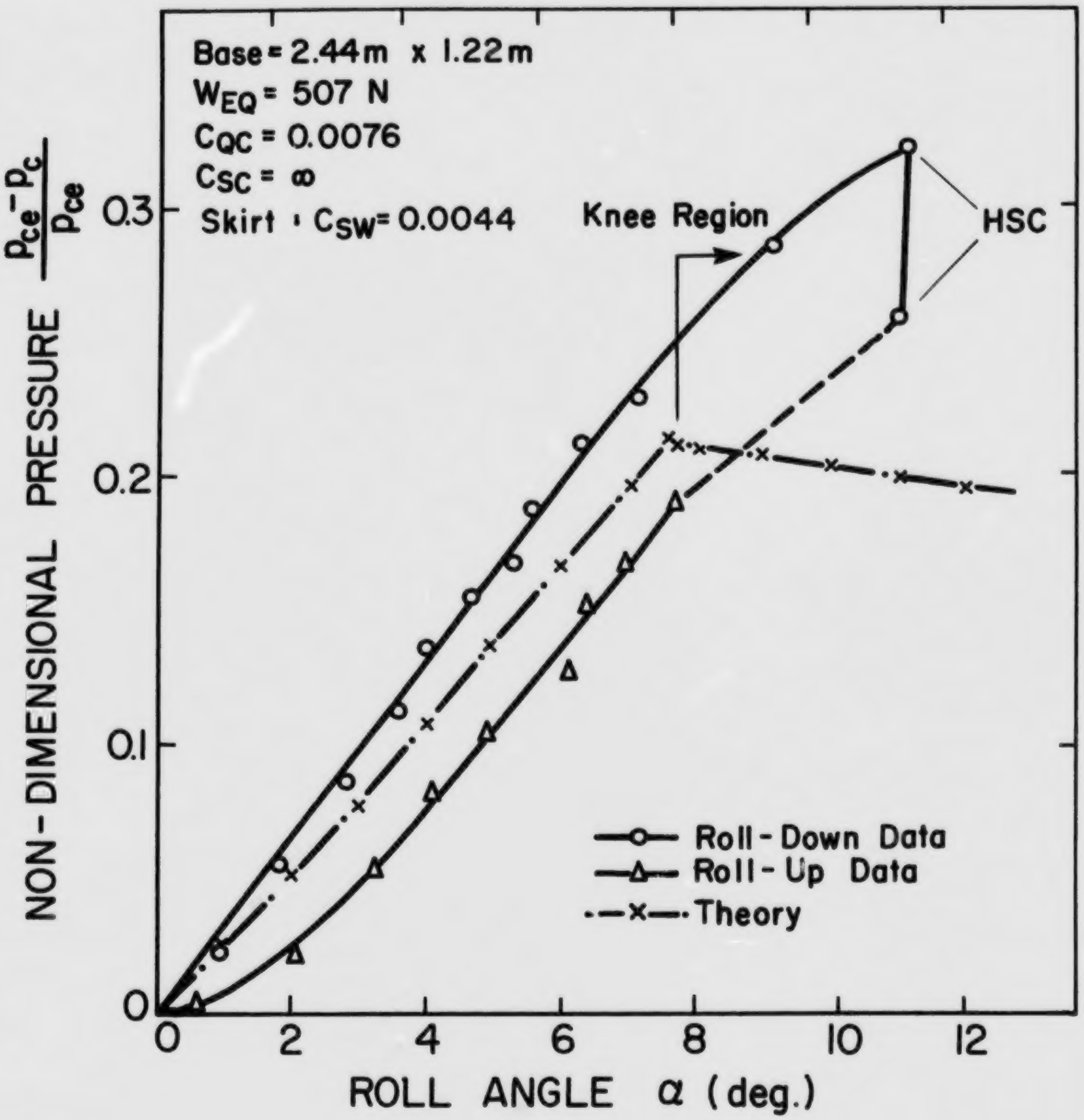

FIG. 3.11 COMPARISON OF PREDICTED AND MEASURED CUSHION PRESSURE DURING ROLL FOR CUSHION DYNAMICS FACILITY WITH HSL SKIRT. SKIRT MATERIAL IS POLYURETHANE COATED NYLON.

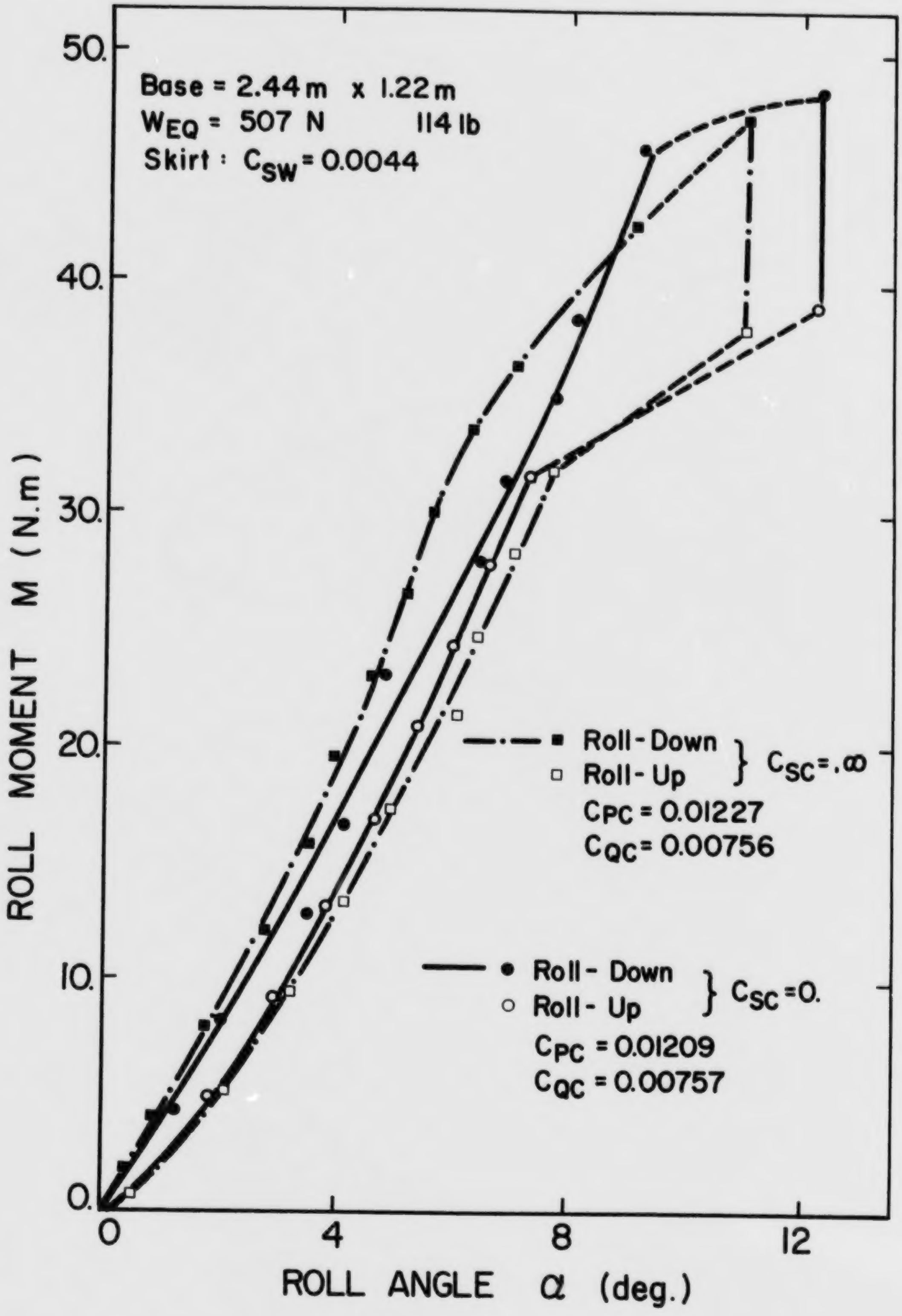

FIG. 3.12 EXPERIMENTAL RESULTS SHOWING THE EFFECT OF LIFT FAN SLOPE ON ROLL STIFFNESS OF CUSHION DYNAMICS FACILITY WITH HSL SKIRT. SKIRT MATERIAL IS POLYURETHANE COATED NYLON.

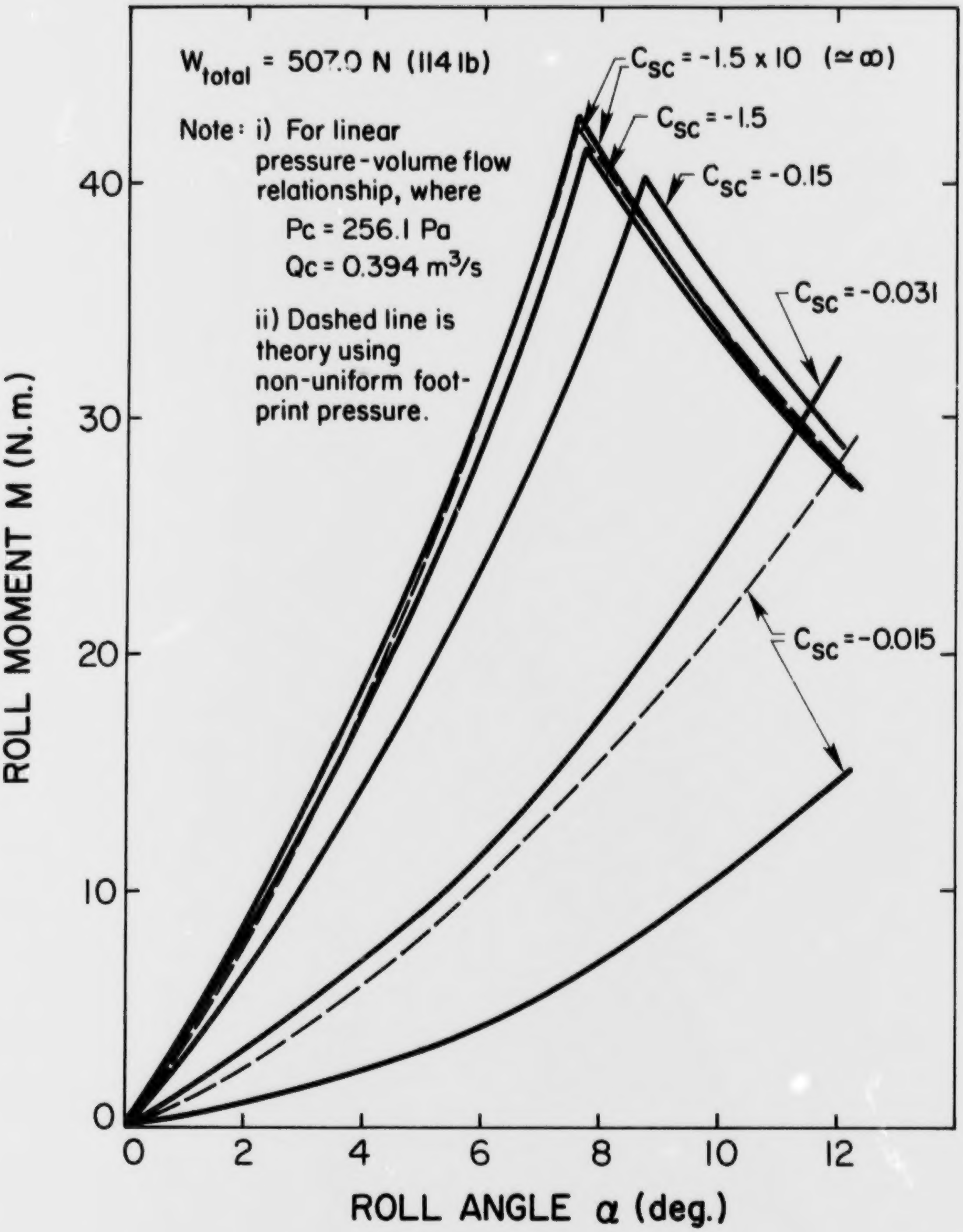

FIG. 3.13 THEORETICAL DEPENDENCE OF ROLL STIFFNESS CHARACTERISTIC ON FAN SLOPE COEFFICIENT (C_{SC}) FOR CUSHION DYNAMICS FACILITY WITH HSL SKIRT.

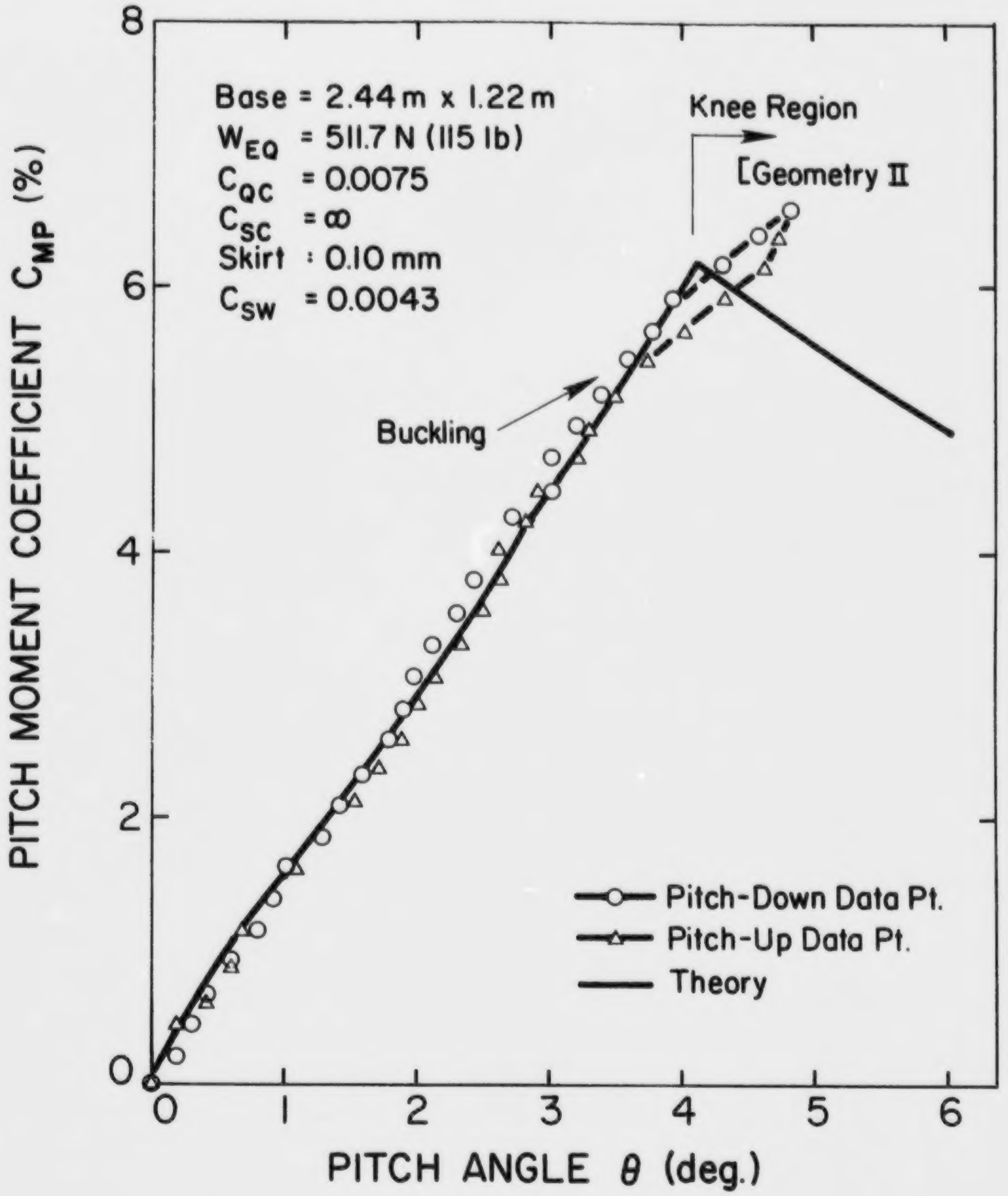

FIG. 3.14 THEORETICAL AND EXPERIMENTAL VALUES OF PITCH STIFFNESS OF CUSHION DYNAMICS FACILITY WITH HSL SKIRT. SKIRT MATERIAL IS POLYURETHANE COATED NYLON.

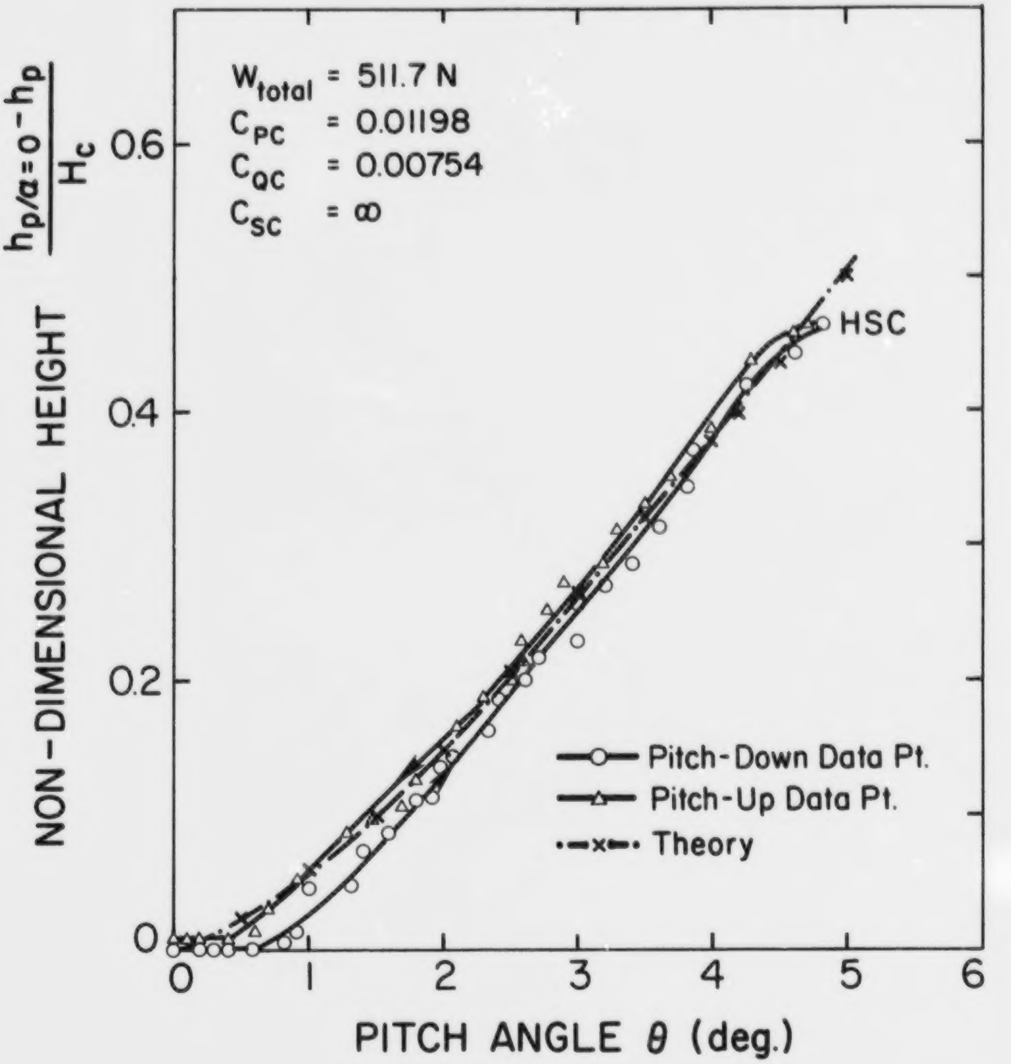

FIG. 3.15 THEORETICAL AND EXPERIMENTAL CURVES OF CENTRE OF MASS MOTION DURING PITCH CYCLE FOR CUSHION DYNAMICS FACILITY WITH HSL SKIRT. SKIRT MATERIAL IS POLYURETHANE COATED NYLON.

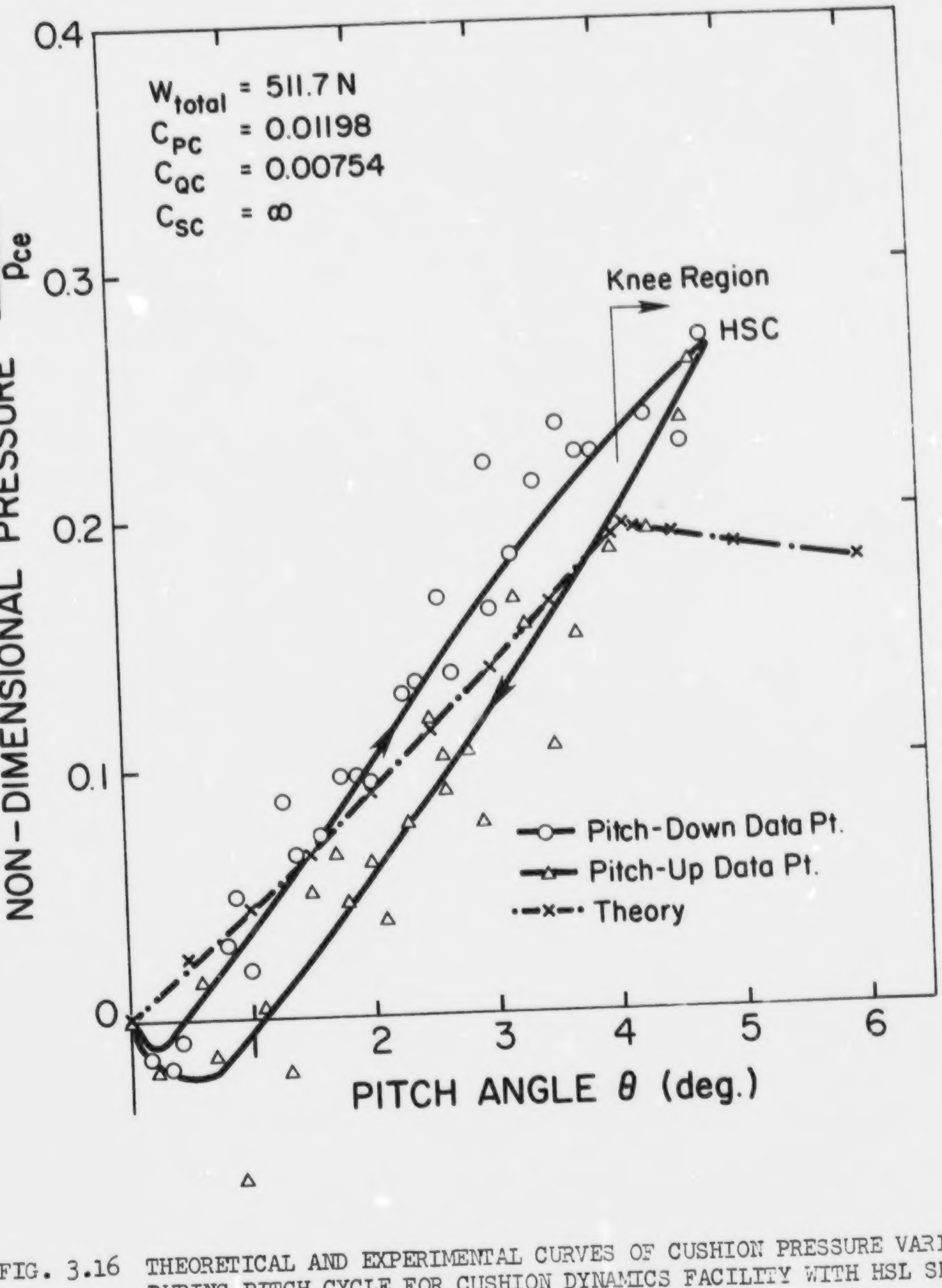

FIG. 3.16 THEORETICAL AND EXPERIMENTAL CURVES OF CUSHION PRESSURE VARIATION DURING PITCH CYCLE FOR CUSHION DYNAMICS FACILITY WITH HSL SKIRT. SKIRT MATERIAL IS POLYURETHANE COATED NYLON.

those at the pitched-down end, are forced into substantial contact with the ground. As for the roll tests, the segments buckle before the knee region is reached, however, the pitch angle at buckling is about 3.8°, considerably smaller than in the roll case. The cushion pressure results display an amount of scatter which is relatively large compared to that usually encountered in the series of tests described in this Report.

3.3.1.3) Effect of Approximations to Shape of Cushion Footprint

Figure 3.17 is a comparison of the mean of experimentally measured values of the roll characteristic given in Figure 3.10 with theoretical predictions based on three different assumptions about the shape of the footprint. It is clear that the rectangular approximation gives relatively poor results, especially at low values of α. The most detailed calculation, which includes estimates of the elliptical areas in the corners and the added length on the pitch down side shows very good agreement for roll angles up to about 5°. The added complexity of the geometry is seen to play a role in obtaining good agreement with experiment and any simplifications must be weighed against the poorer agreement.

3.3.2) Other Experimental Results

Several other parameters were varied experimentally to determine their importance and as a consistency check on the previous tests. Figure 3.18 shows the effect of partial roll on the roll stiffness characteristic. The half-roll curve follows the full-roll curve and the hysteresis is roughly the same.

Figure 3.19 illustrates the effect of vehicle weight on the roll stiffness characteristic. The curve for higher weight is seen to exhibit slightly less hysteresis than the lower weight curve and also displays a rounded curve in the region of hard surface contact (HSC).

The effect of skirt-ground friction on the rolling moment curve is illustrated in Figure 3.20. The two sets of data lie very close to one another showing that the effect is negligible for this material.

Four partial roll tests were performed at different weights to determine the effect on roll stiffness, that is centre of pressure, C.P., shift, at a constant roll angle. The results in Figure 3.21 show that the C.P. shift decreases with increasing weight.

Two roll tests were performed to confirm earlier findings that the roll characteristic of the HSL skirt is not affected by changes in the power coefficient. Figure 3.22 illustrates the two results.

The cushion pressure distribution was measured across the ground board to check cushion pressure variation with roll angle. The measurements, presented in Figure 3.23a & b, show a constant pressure value similar to that predicted by the theory of Appendix C. The theory is seen to underpredict the cushion pressure somewhat at the higher roll angle and slightly overpredict the pressure at 0° roll angle.

The sensitivity of roll measurements to step size in moment was investigated. This was done by transferring different size weights from

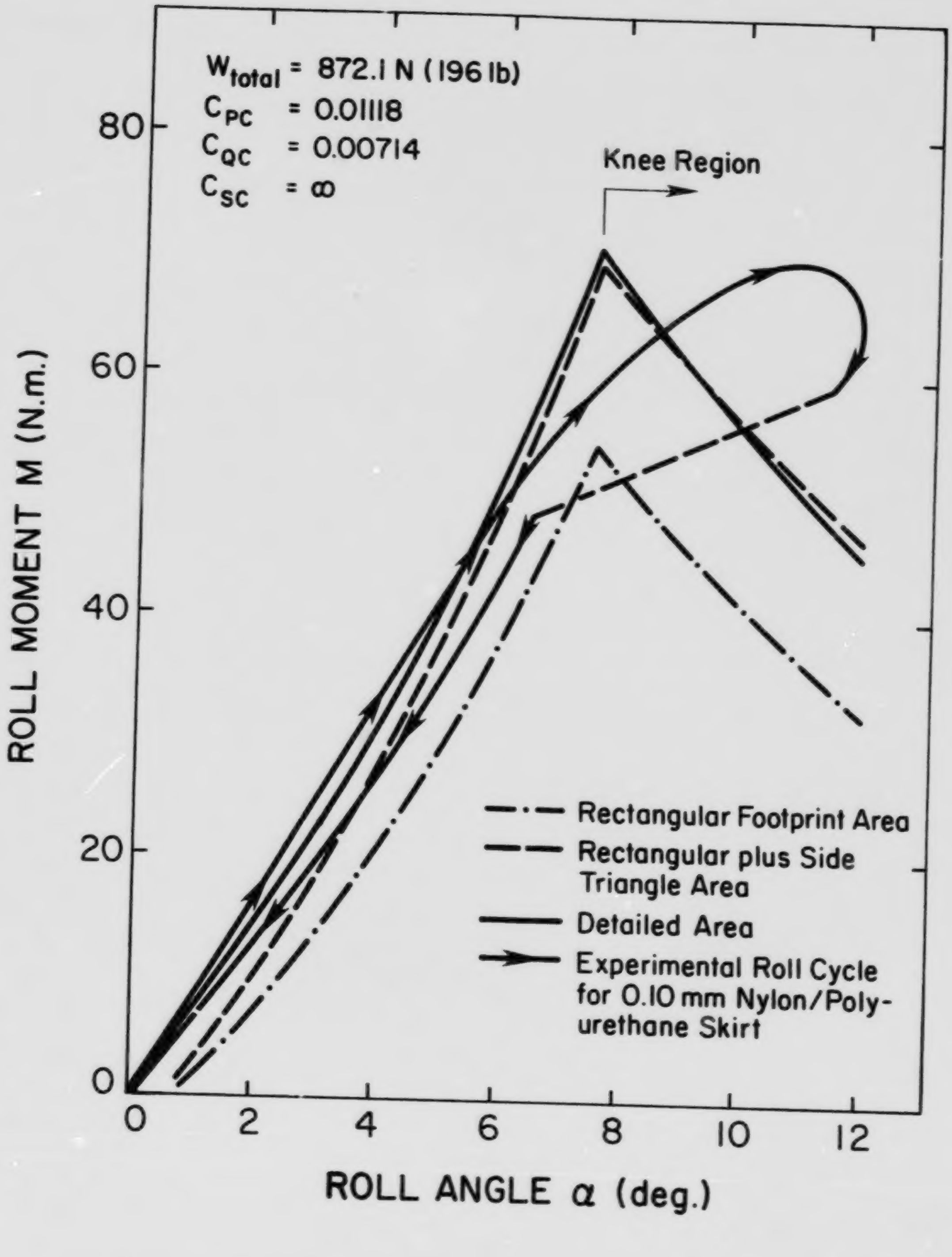

FIG. 3.17 COMPARISON OF AN EXPERIMENTAL ROLL STIFFNESS CHARACTERISTIC TO THEORETICAL PREDICTIONS BASED ON DIFFERENT ASSUMPTIONS ABOUT FOOTPRINT SHAPE.

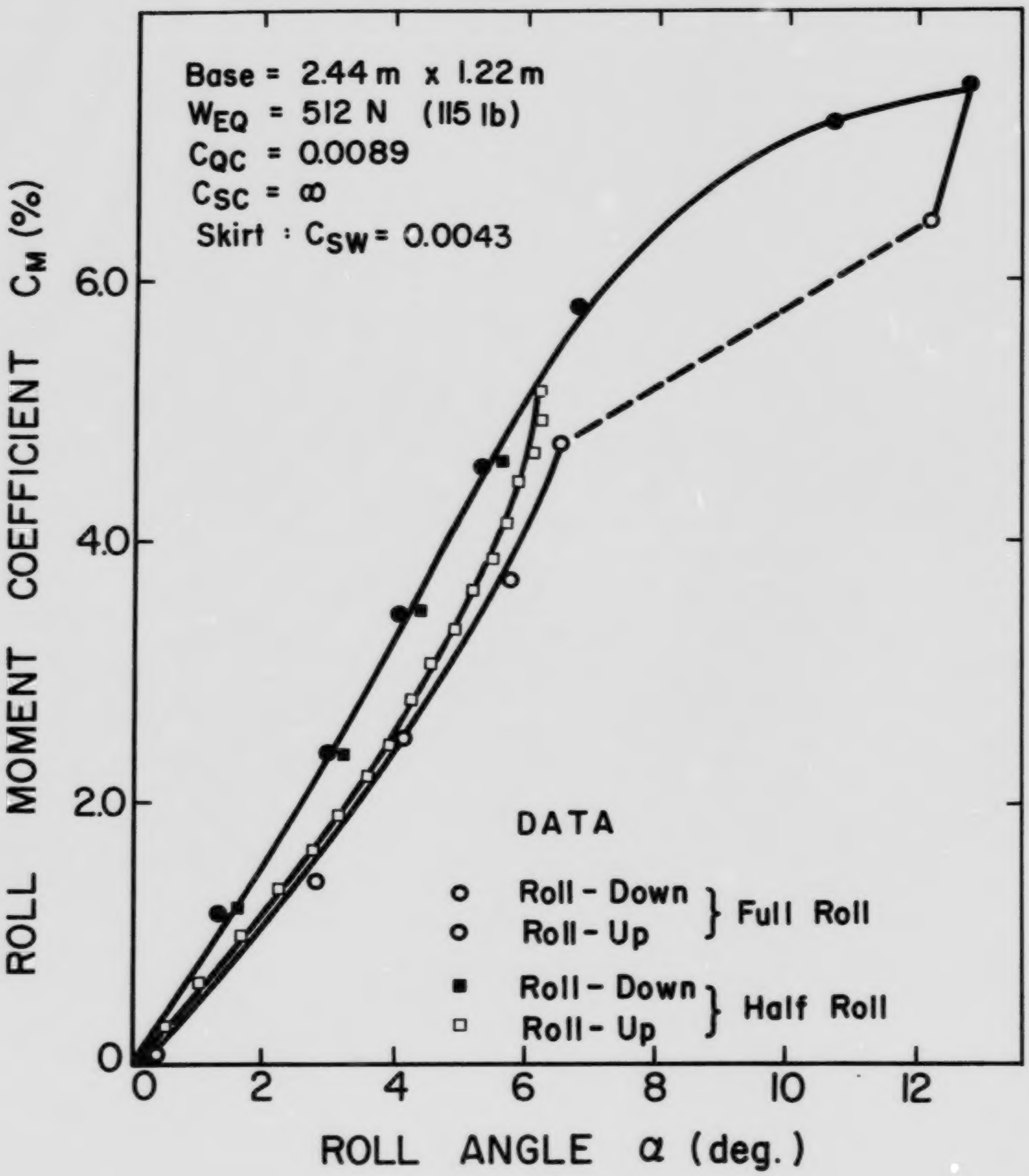

FIG. 3.18 EFFECT OF PARTIAL ROLL ON THE ROLL STIFFNESS CHARACTERISTIC OF THE CUSHION DYNAMICS FACILITY WITH THE HSL SKIRT. SKIRT MATERIAL IS POLYURETHANE COATED NYLON.

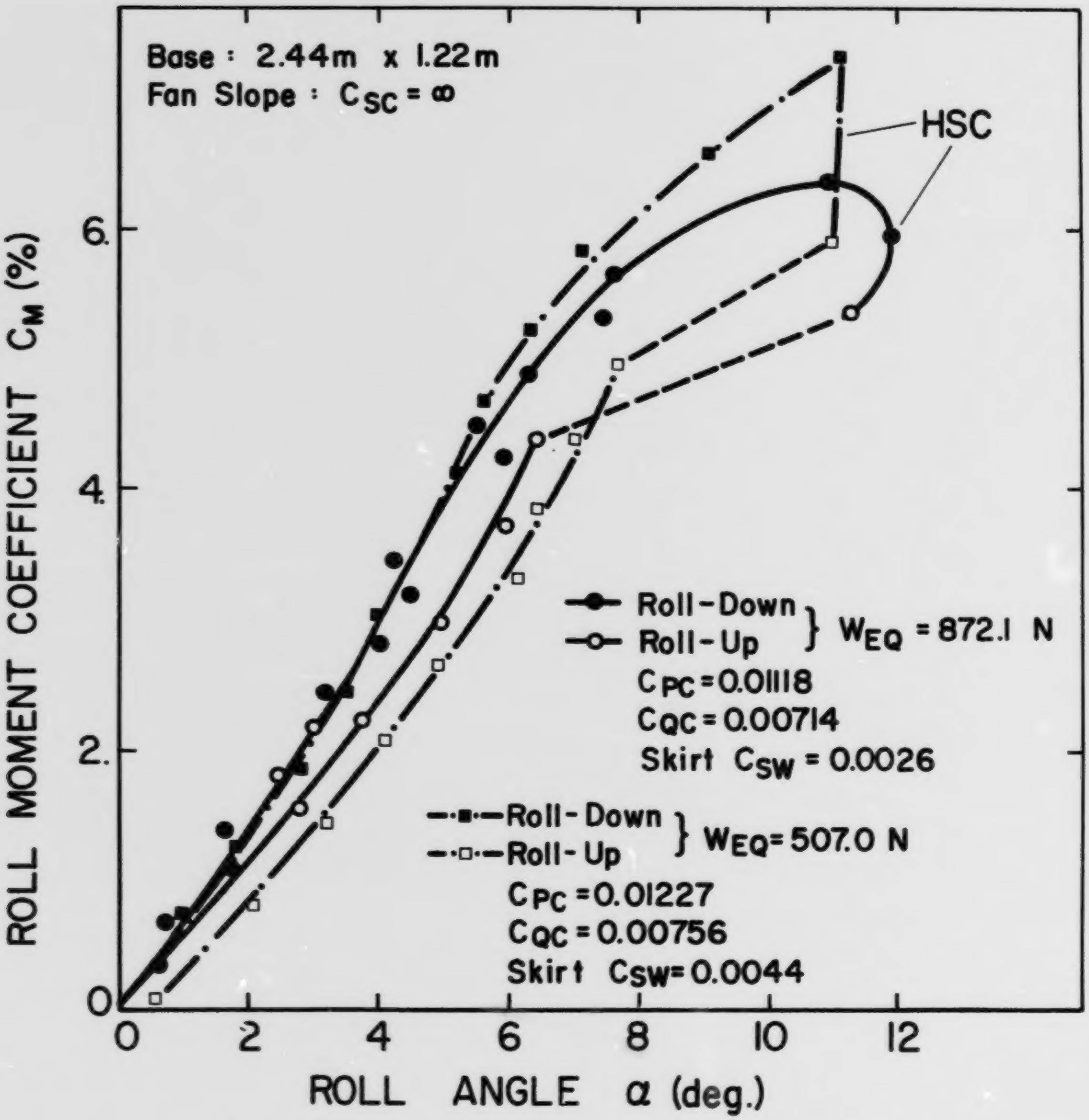

FIG. 3.19 EFFECT OF GROSS MODEL WEIGHT ON THE ROLL STIFFNESS CHARACTERISTIC OF THE CUSHION DYNAMICS FACILITY WITH HSL SKIRT. SKIRT MATERIAL IS POLYURETHANE COATED NYLON.

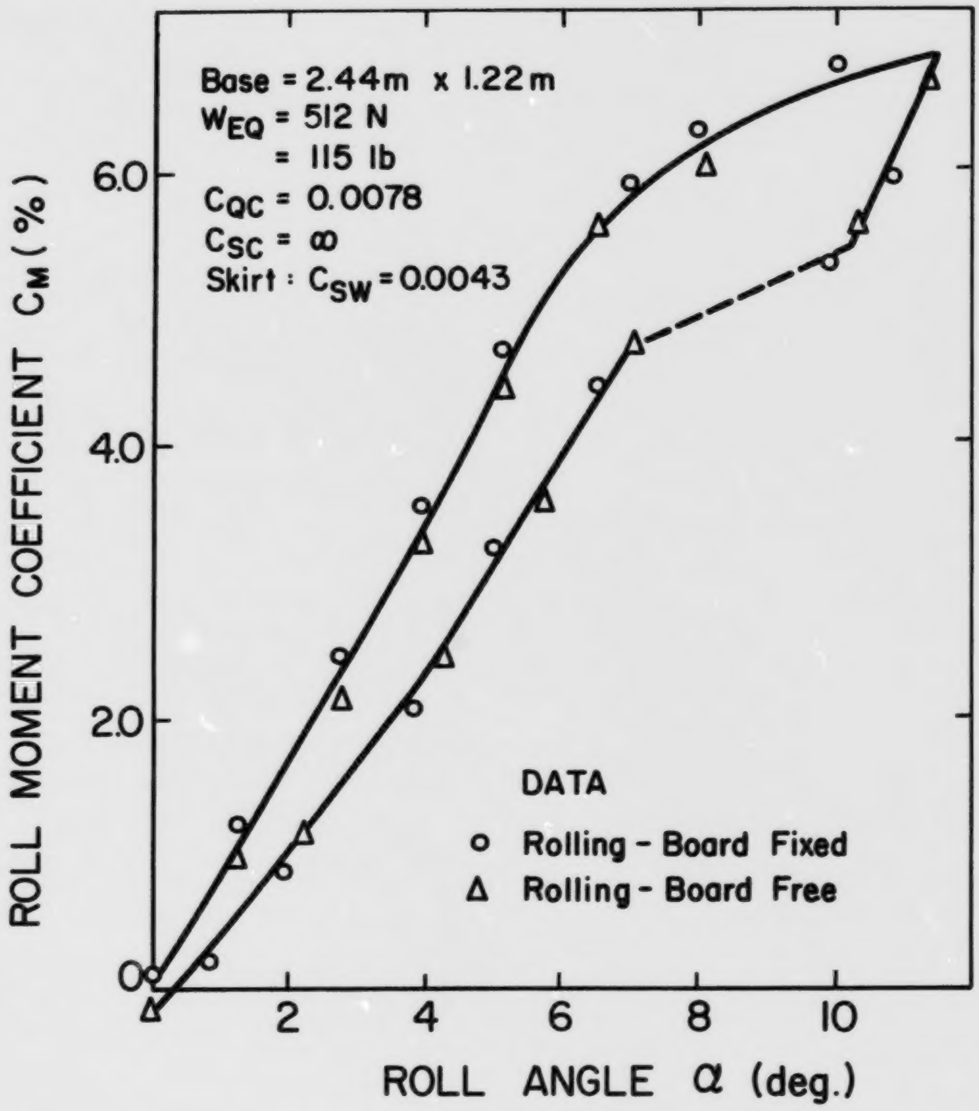

FIG. 3.20 EFFECT OF SKIRT GROUND FRICTION ON THE ROLL STIFFNESS CHARACTERISTIC OF THE CUSHION DYNAMICS FACILITY WITH THE HSL SKIRT. SKIRT MATERIAL IS POLYURETHANE COATED NYLON.

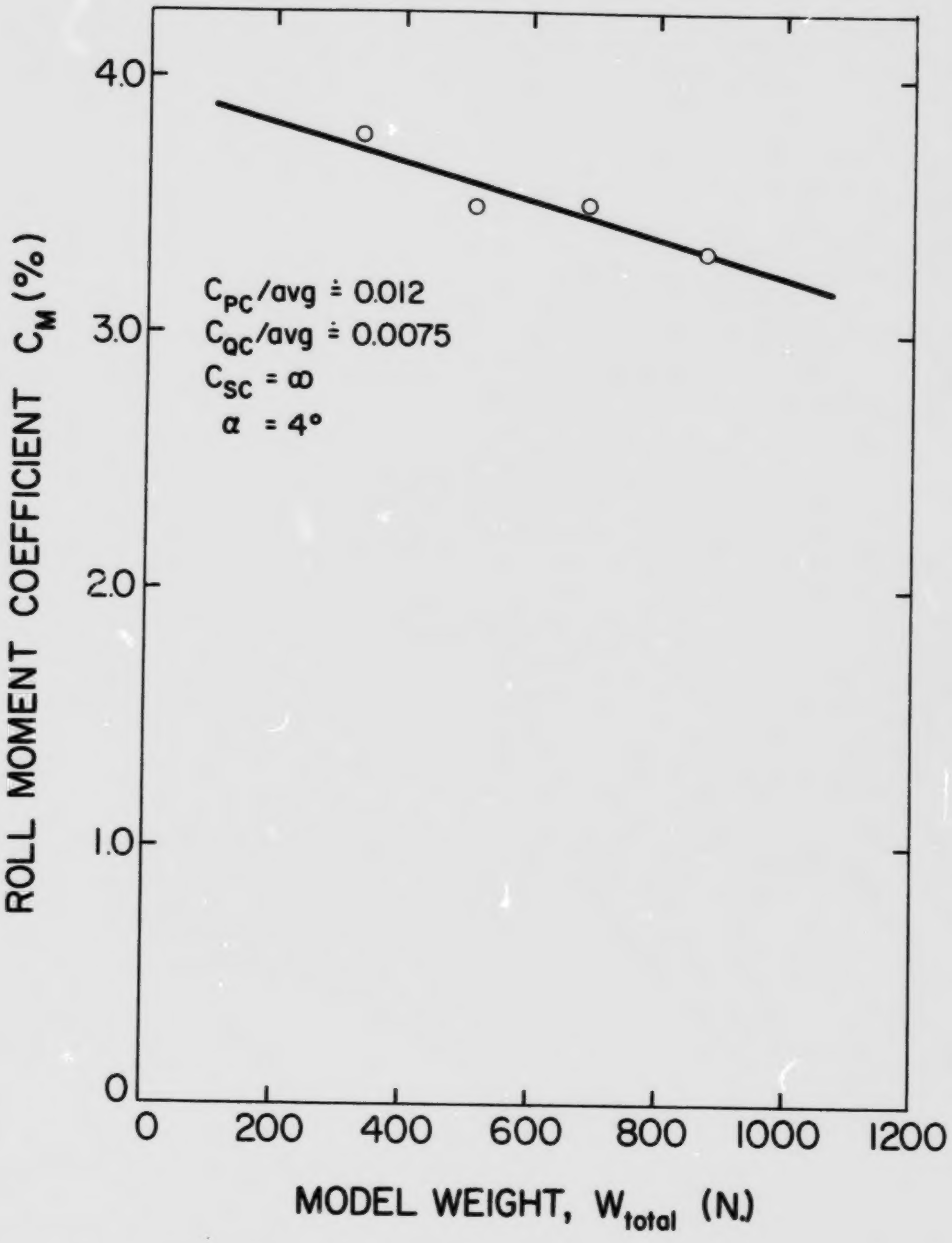

FIG. 3.21 EFFECT OF GROSS MODEL WEIGHT ON ROLL STIFFNESS CHARACTERISTIC OF CUSHION DYNAMICS MODEL WHEN HELD AT CONSTANT ROLL ANGLE. MATERIAL FOR HSL SKIRT IS POLYURETHANE COATED NYLON.

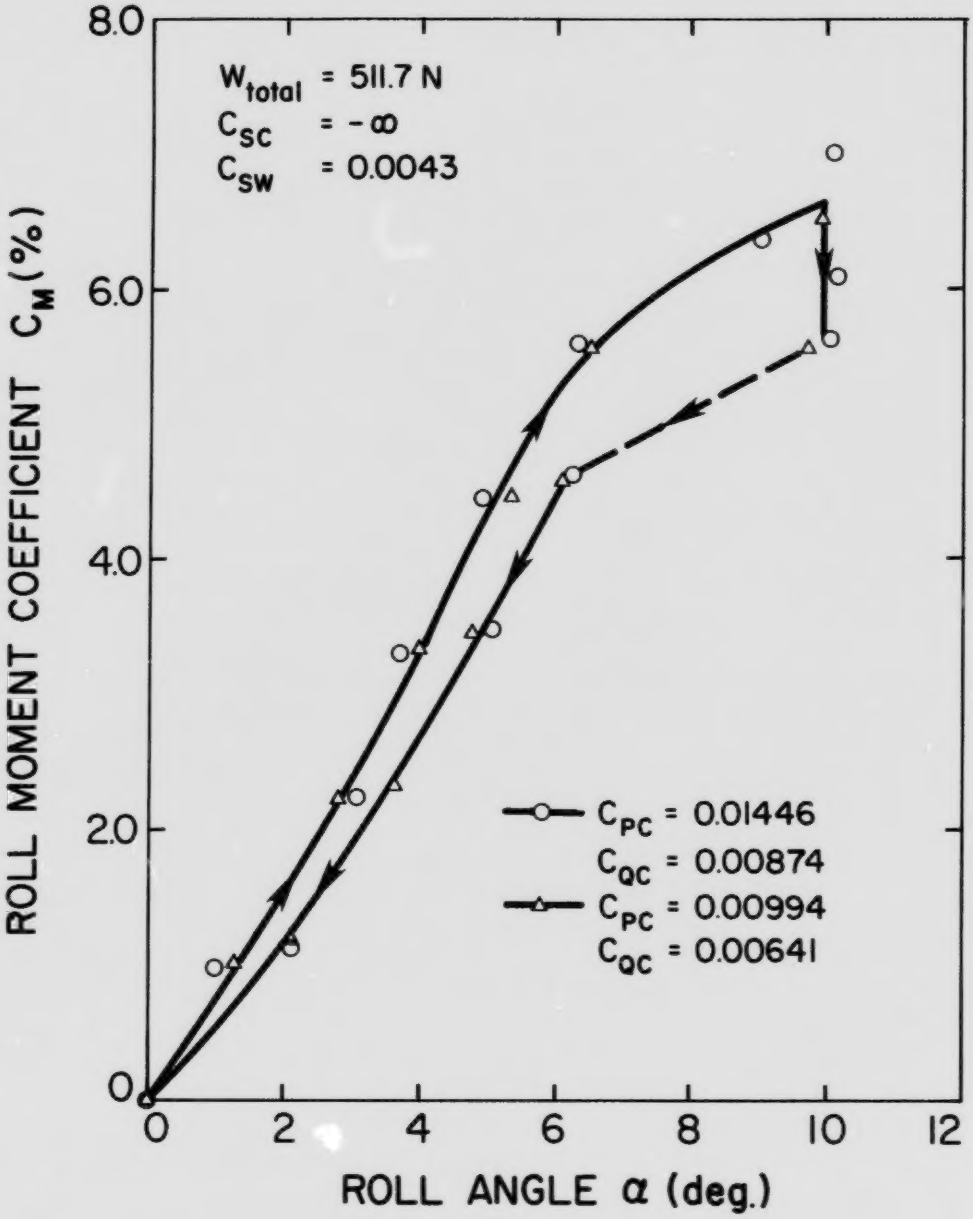

FIG. 3.22 EFFECT OF CUSHION PRESSURE COEFFICIENT (C_{PC}) ON ROLL STIFFNESS CHARACTERISTIC OF CUSHION DYNAMICS MODEL EQUIPPED WITH HSL SKIRT. SKIRT MATERIAL IS POLYURETHANE COATED NYLON.

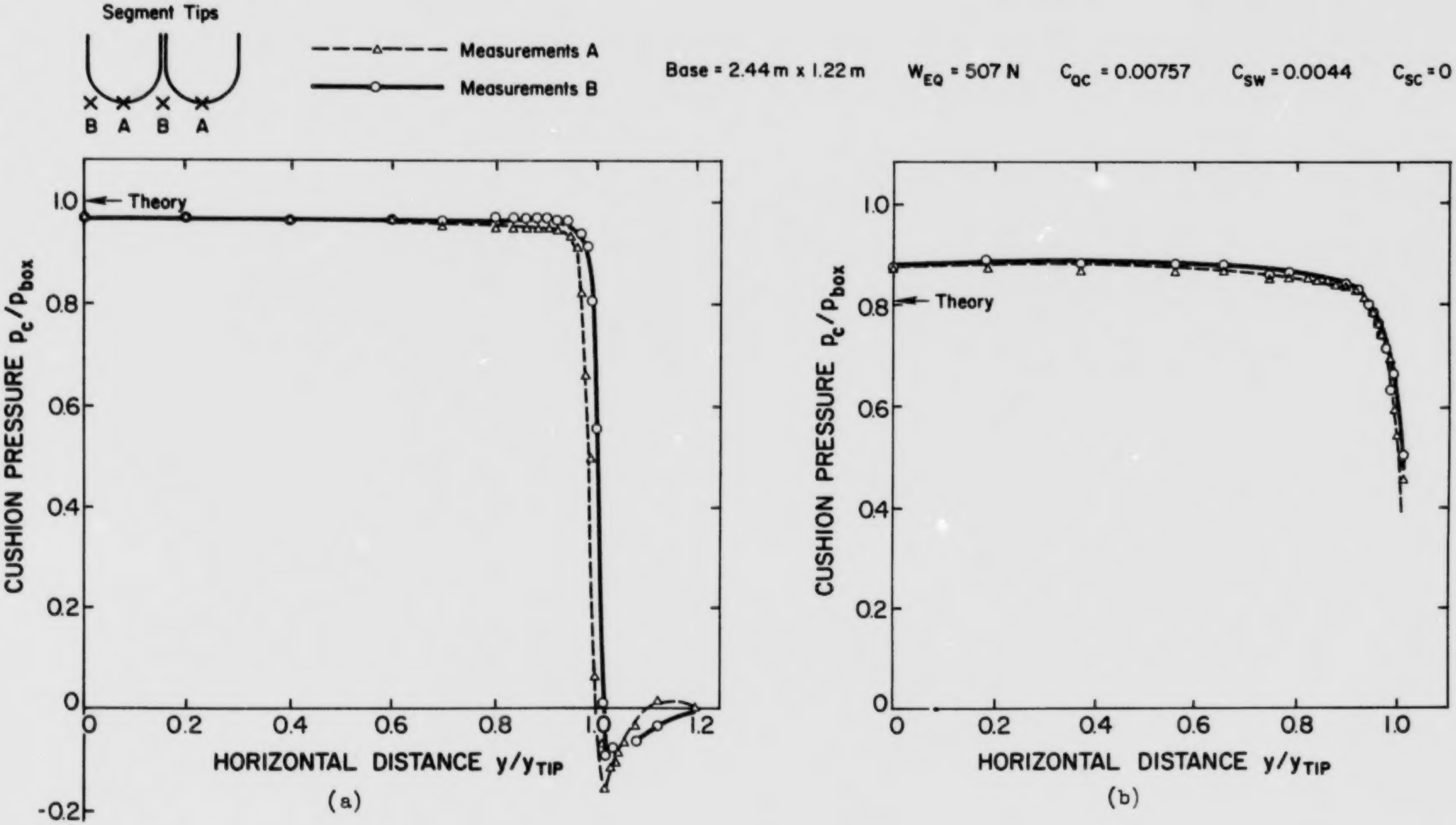

(a)

(b)

FIG. 3.23 CUSHION PRESSURE DISTRIBUTION ACROSS GROUNDBOARD DIRECTLY UNDER TIPS OF SEGMENTS (A), AND AT MIDPOINT (B).

(a) ROLL ANGLE, $\alpha = 0°$
(b) ROLL ANGLE, $\alpha = 7.2°$

one side of the model to the other. Figure 3.24 shows that some variation in the curve does occur although it is small. The result that hard structure contact is reached earlier, at lower roll angle and lower C.P. shift, is of note as it implies that the hard structure and consequently, the centre of gravity of the test rig is closer to the ground board in the small increment case. No explanation for this has been determined, however, it is associated with segment buckling.

The fan slope coefficients were determined using a polynomial least squares fit to the pressure-flow data. The slope was then calculated at the operating point. A sample of the data and the least squares fit curve are shown in Figure 3.25. For this case the fan characteristic is approximately linear through most of its range.

3.4) Experimental Results for Polyethylene Skirt Material

3.4.1) Roll Characteristics

The roll stiffness of the polyethylene HSL skirt was measured for the cases of fixed ground board and moving ground board. The slope of the curves, Figure 3.26, is different in each case, being larger with friction than without. There is also a greater amount of hysteresis with the fixed ground board. Results for the nylon-polyurethane skirt are shown as a cross-hatched area. The slope of the polyethylene curve is, in the case of the moving ground board, very close to that obtained with the nylon-polyurethane, "red", skirt. The amount of hysteresis is also much greater with the polyethylene skirt than with the "red" skirt.

3.4.2) Pitch Characteristics

Figures 3.27, 3.28 and 3.29 present the results of pitch tests with the polyethylene skirt. Large hysteresis is found for the non-dimensional pressure and pitch stiffness curves. Hysteresis is much smaller for the non-dimensional height curve. Comparable results for the nylon-urethane skirt are shown in figures 3.14, 3.15 and 3.16; in all cases the polyethylene exhibits more hysteresis. The pitch stiffness and non-dimensional pressure curves also have a larger mean slope. This is due to the skirt ground friction as shown in figure 3.26.

The sudden change in the amount of hysteresis in the pitch stiffness curve, Figure 3.27, corresponds to the pitched down end segments going from a point where part of each segment is deformed by ground contact with the outside of the segments to the point where the only contact occurs at the lowest points of the segments, the tips, indicated in Fig. 3.23 by the letter A.

3.5) Experimental Results for Loop-Segment Skirt

Roll stiffness measurement for a loop and segment skirt system are shown in figure 3.30. Again, the effect of friction with the ground board is to increase the amount of hysteresis and also to increase the stiffness at small roll angles. The material used in this test was a "blue", 0.229 mm thick, 0.238 kg/m^2 weight, elastomer coated fabric; it's detailed composition is unknown. Test results from a previous installation

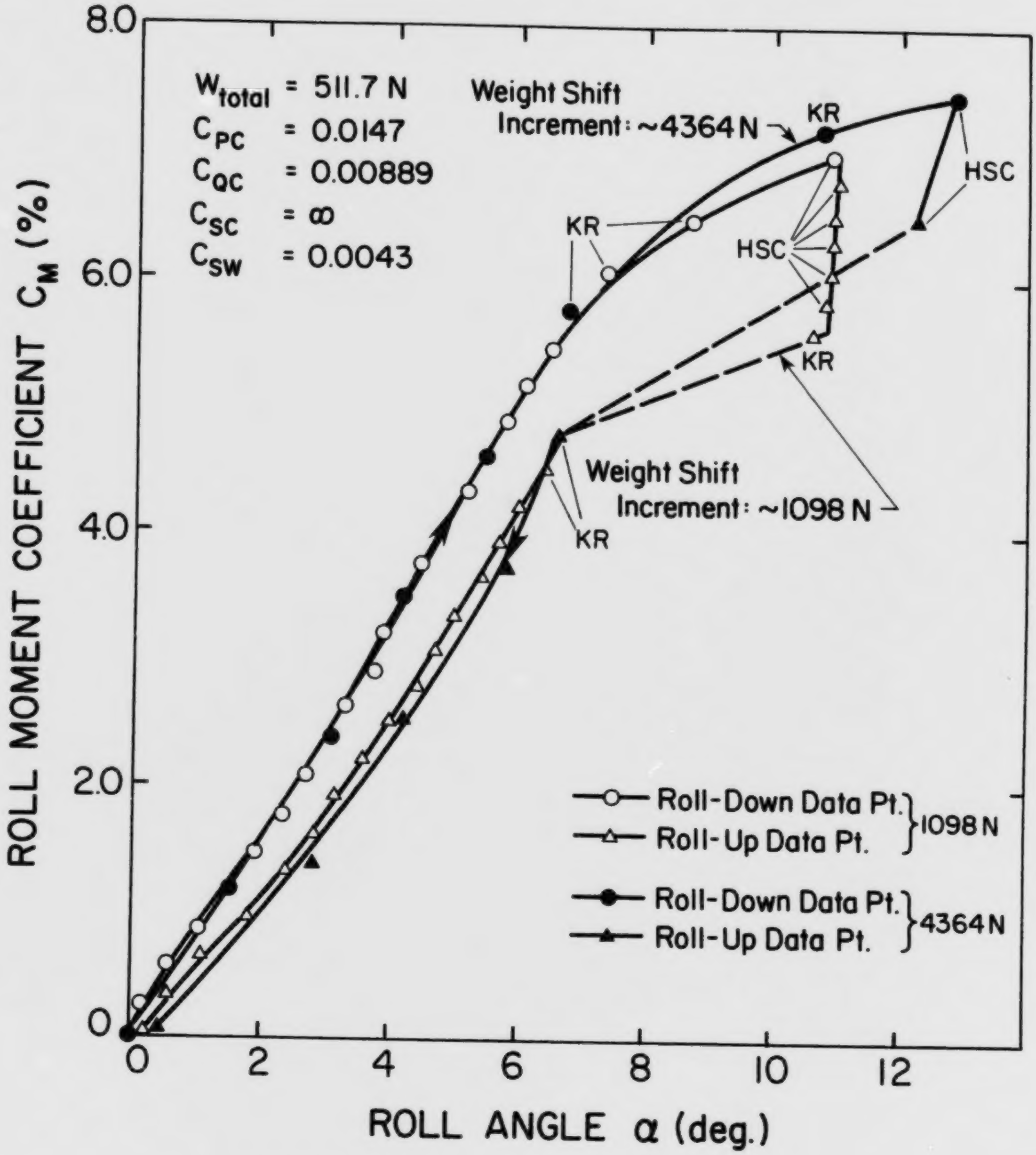

FIG. 3.24 EFFECT OF MOMENT INCREMENT SIZE ON ROLL STIFFNESS CHARACTERISTIC OF CUSHION DYNAMICS MODEL EQUIPPED WITH HSL SKIRT. SKIRT MATERIAL IS POLYURETHANE COATED NYLON.

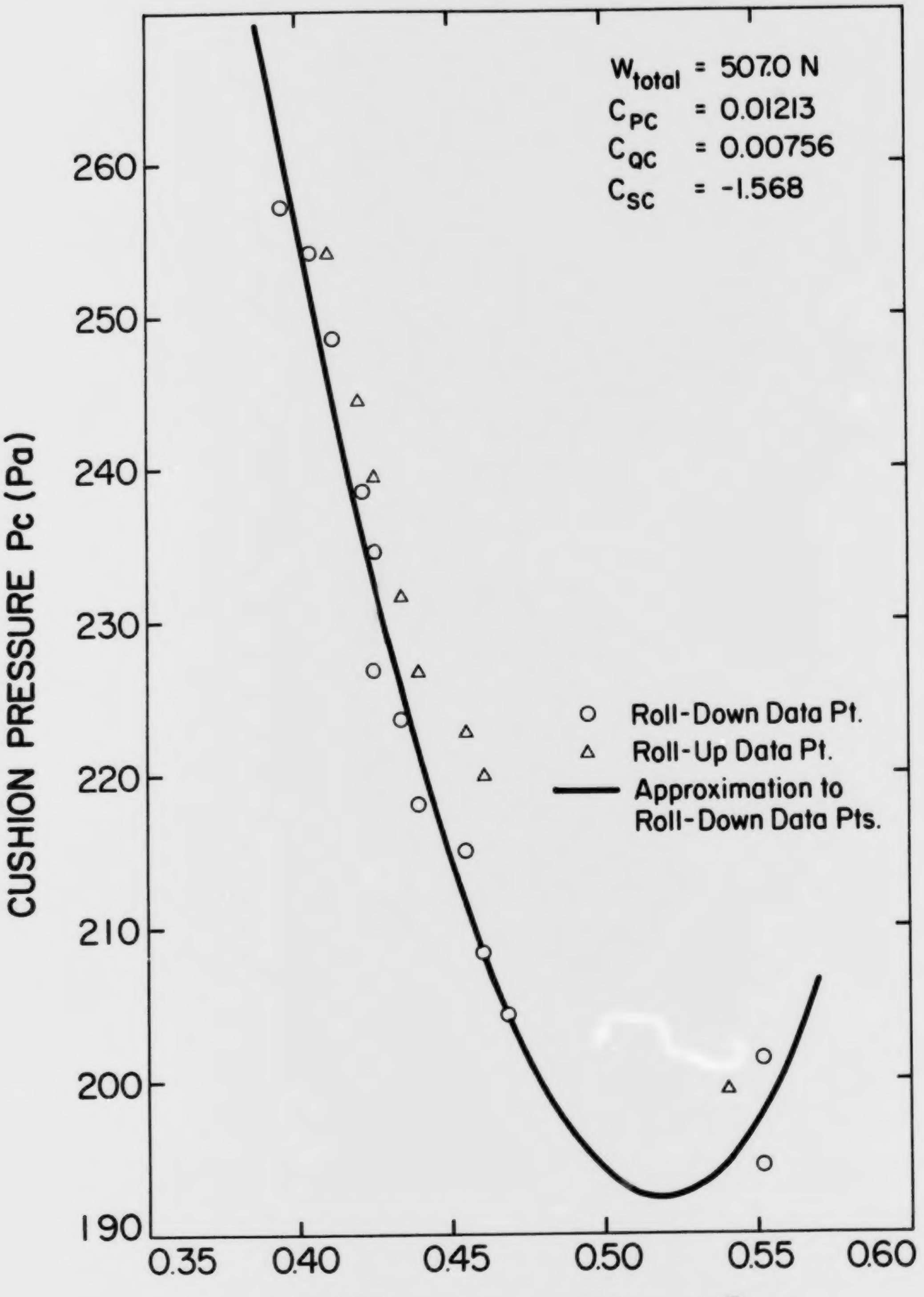

FIG. 3.25 TYPICAL CUSHION PRESSURE VERSUS VOLUME FLOW CURVE FOR CUSHION DYNAMICS FACILITY EQUIPPED WITH HSL SKIRT.

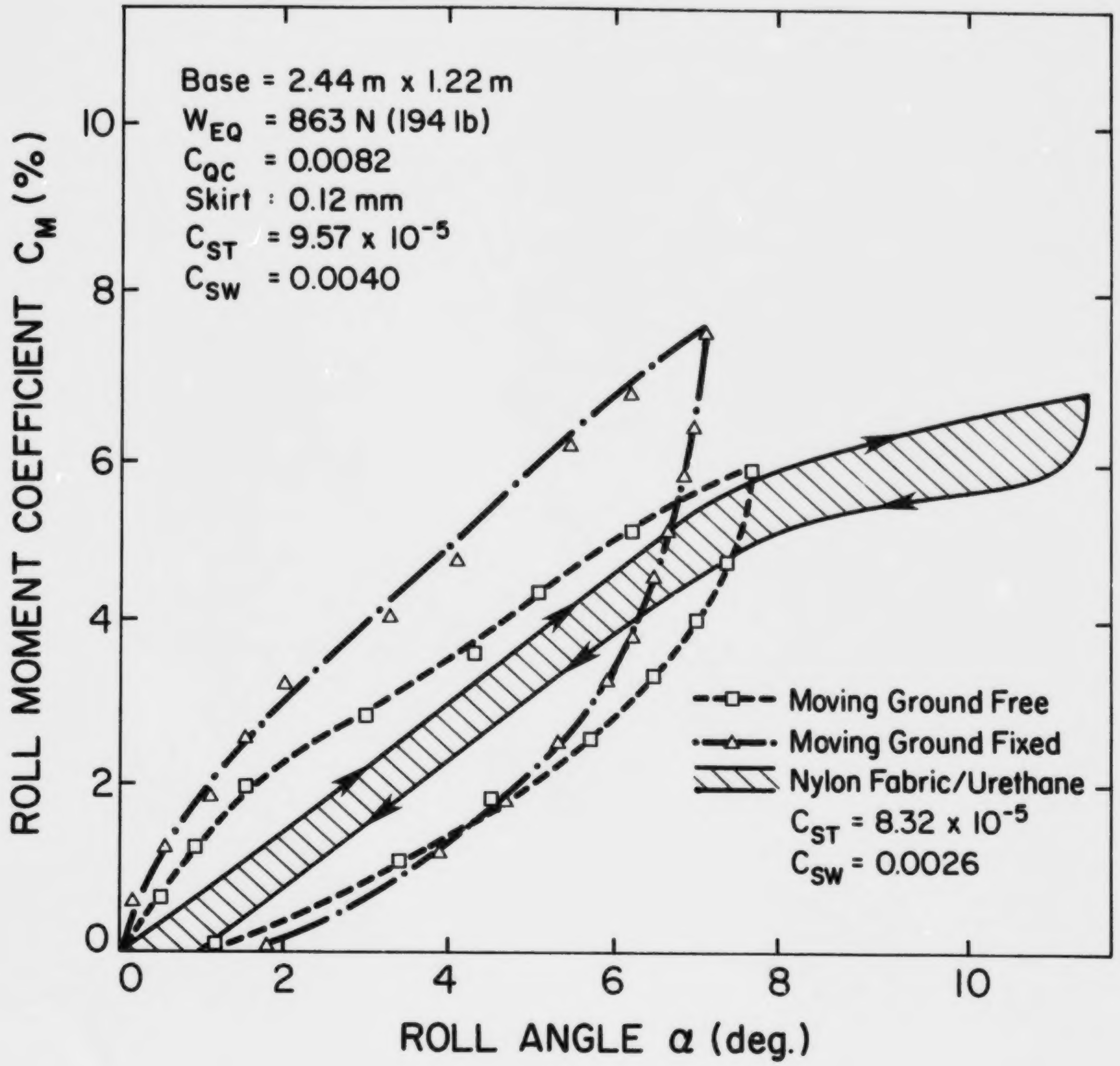

FIG. 3.26 ROLL STIFFNESS CHARACTERISTIC OF CUSHION DYNAMICS MODEL EQUIPPED WITH HSL SKIRT INCLUDING THE EFFECT OF SKIRT-GROUND FRICTION. SKIRT MATERIAL IS POLYETHYLENE FILM.

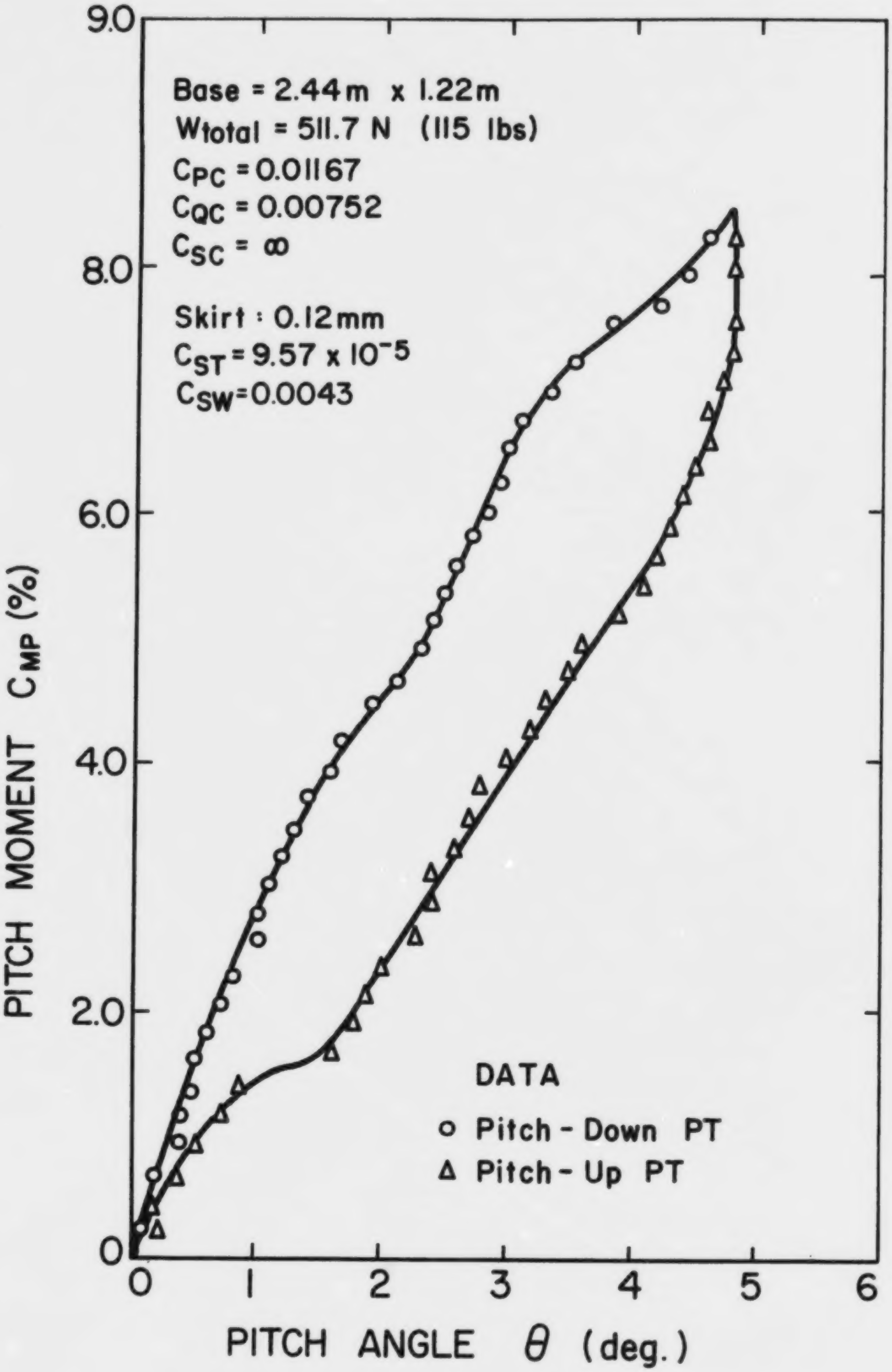

FIG. 3.27 EXPERIMENTAL PITCH STIFFNESS MEASUREMENTS FOR THE CUSHION DYNAMICS MODEL EQUIPPED WITH THE POLYETHYLENE HSL SKIRT.

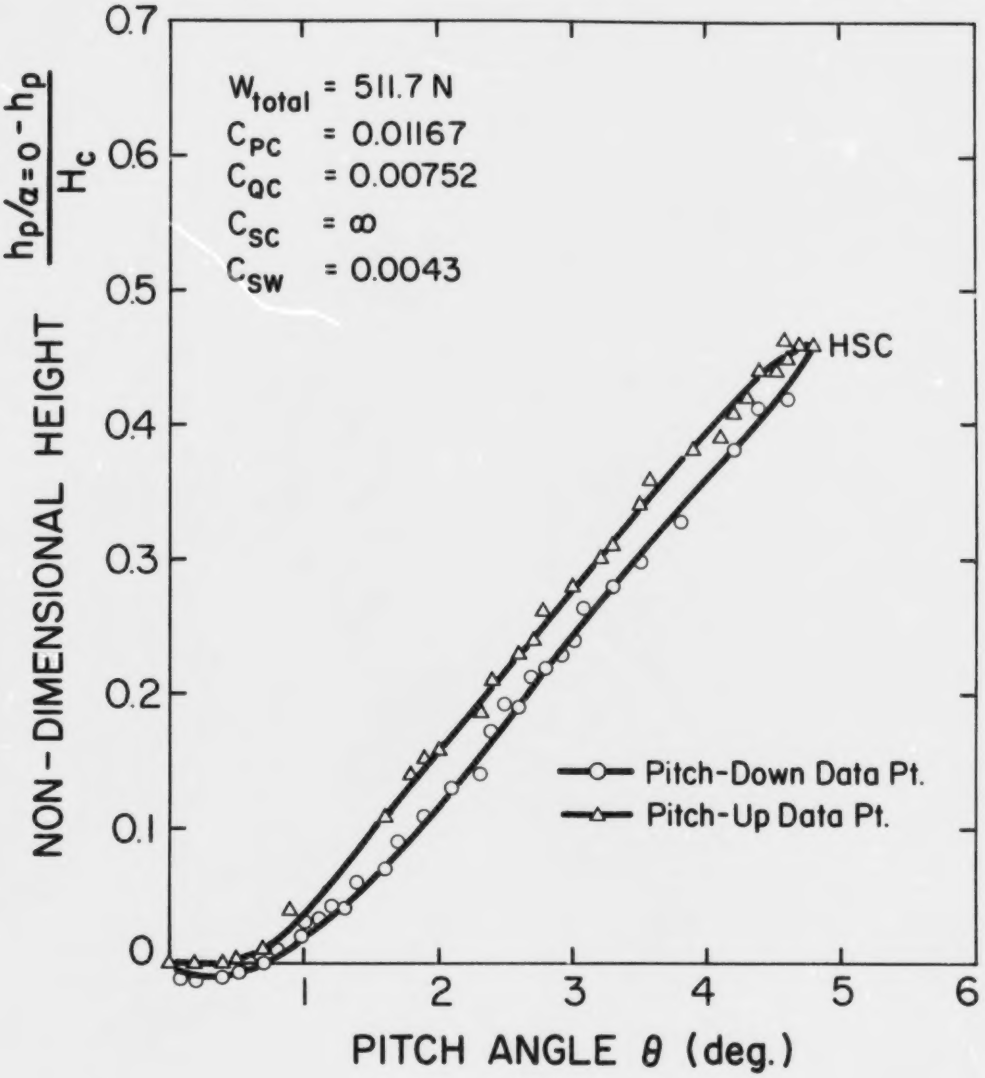

FIG. 3.28 NONDIMENSIONAL HEIGHT VERSUS PITCH ANGLE, θ, FOR THE CUSHION DYNAMICS MODEL EQUIPPED WITH THE POLYETHYLENE HSL SKIRT.

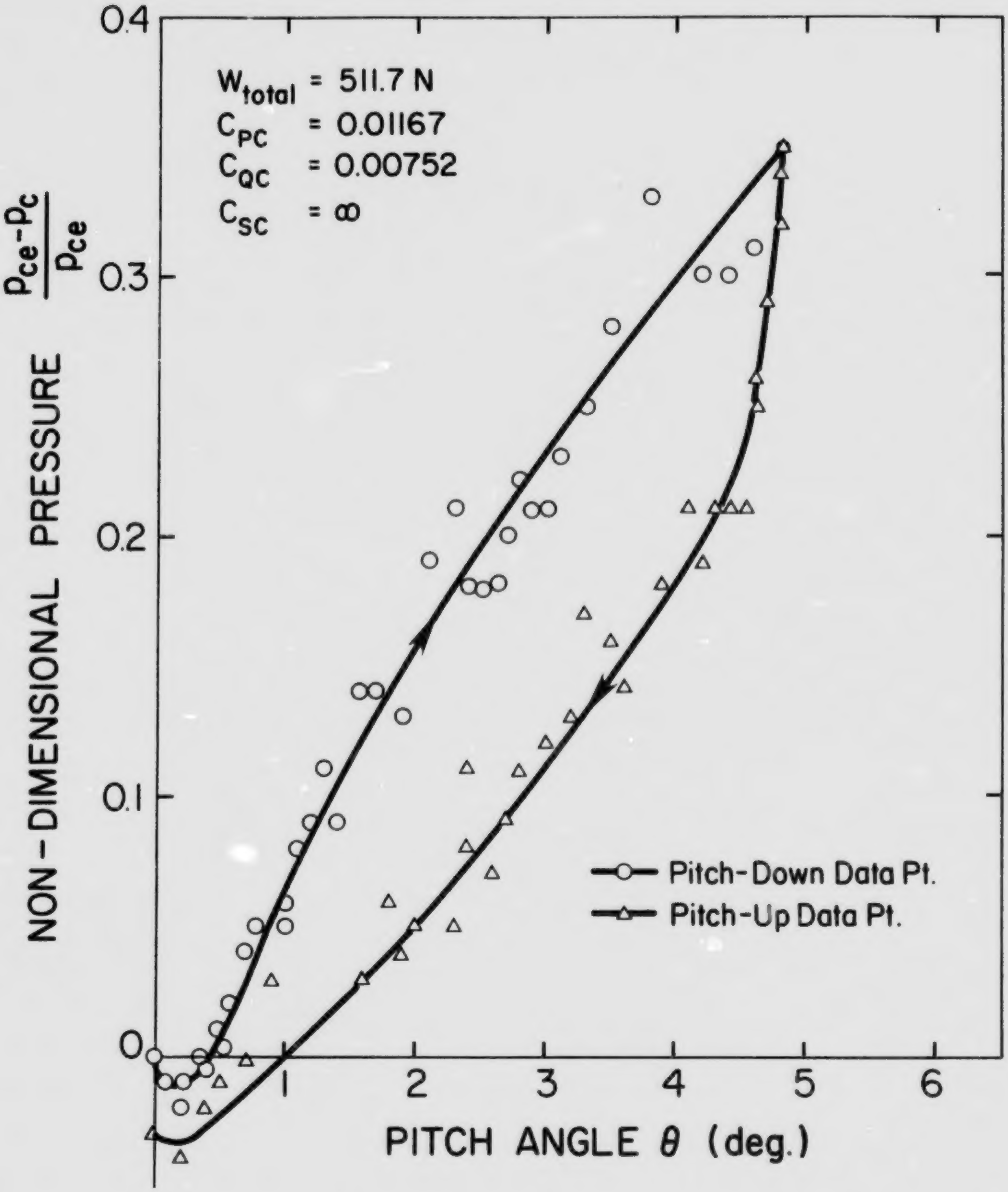

FIG. 3.29 NONDIMENSIONAL PRESSURE VERSUS PITCH ANGLE, θ, FOR THE CUSHION DYNAMICS MODEL EQUIPPED WITH THE POLYETHYLENE HSL SKIRT.

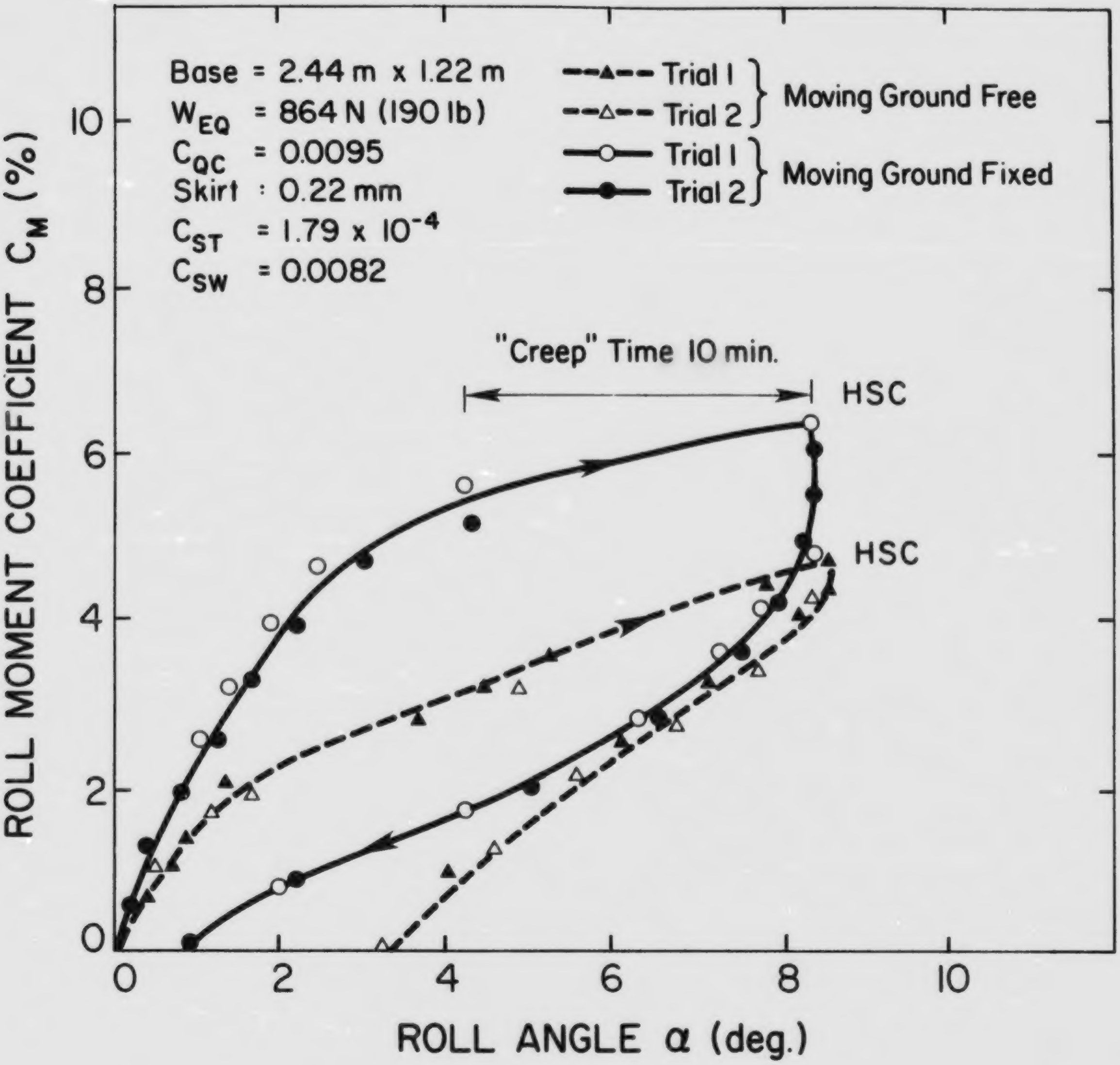

FIG. 3.30 ROLL STIFFNESS CHARACTERISTICS OF CUSHION DYNAMICS MODEL EQUIPPED WITH A SINGLE PLENUM CHAMBER LOOP AND SEGMENT SKIRT INCLUDING THE EFFECT OF SKIRT-GROUND FRICTION. SKIRT MATERIAL IS AN ELASTOMER COATED FABRIC.

of the loop and segment skirt on the 2.44 x 1.22 m model are shown in figures 3.31 and 3.32. The former shows the comparable roll stiffness moving/fixed ground board measurements and confirms the present results. The latter gives the effect of weight change which is to reduce the roll moment coefficient required for a given angle of roll, as was noted with the HSL skirt, and to decrease the amount of hysteresis in the curve.

3.6) Conclusions

An accurate representation of the static behaviour of the HSL skirt is now available. It includes footprint centre of pressure movement and the cushion leakage area. It is necessary, even for this simple geometry, to derive complicated geometric models to obtain this agreement. The inclusion of geometry for the knee region adds little to the agreement of theory and experiment as buckling of the segments always occurs before reaching the knee region.

Buckling of the skirt results in a reduction in stiffness, however, the loss is not catastrophic. This is in contrast to the multicell cushion studied under previous contracts as buckling of the cones results in loss of seal, venting and subsequent loss of pressure for support.

No detailed explanation of the static hysteresis phenomenon has been obtained. It is, however, sensitive to the type of material used for the skirt and appears to be associated with the ability of the material to sustain small compressive loads.

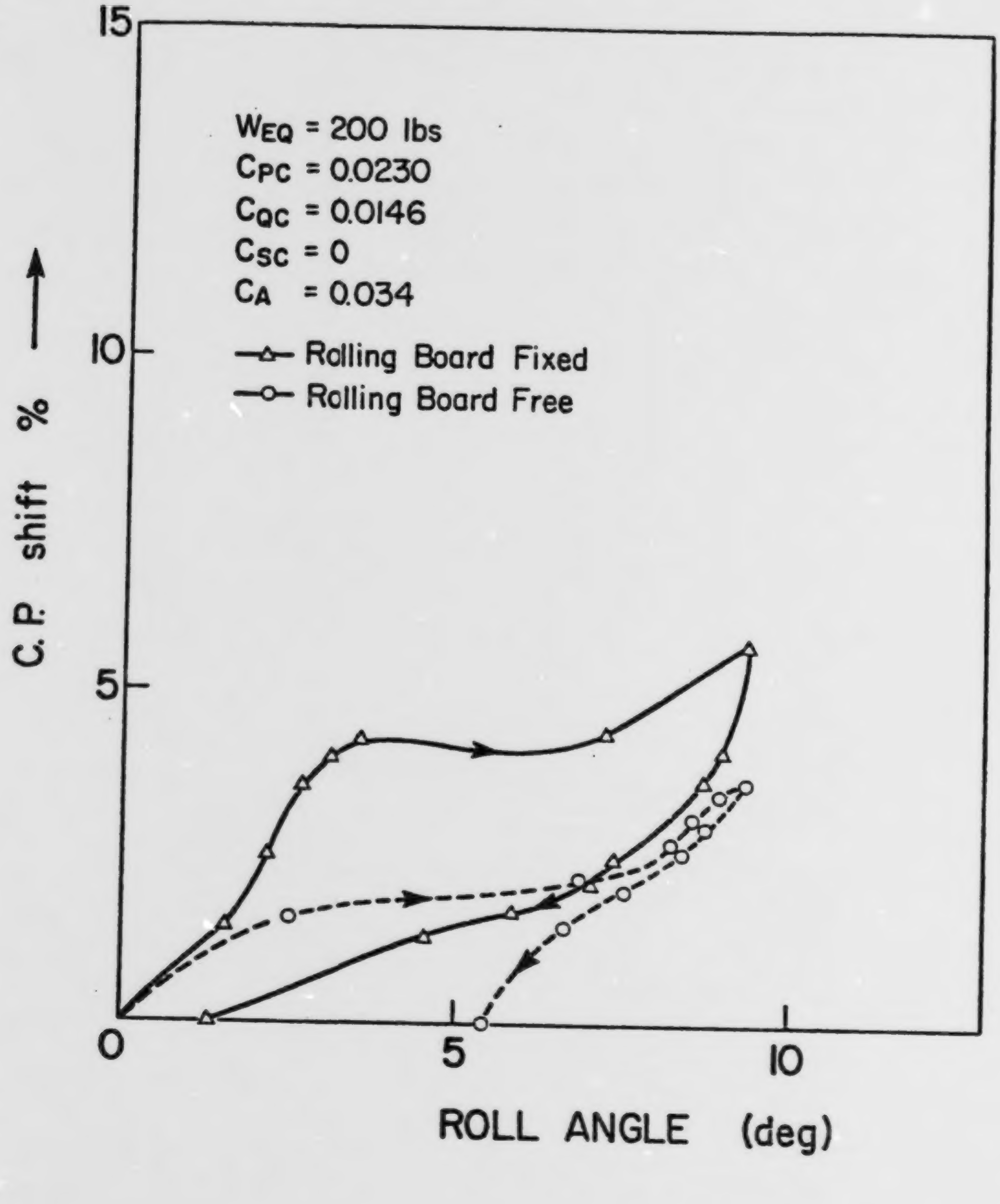

FIG. 3.31 ROLL STIFFNESS CHARACTERISTICS OF CUSHION DYNAMICS MODEL EQUIPPED WITH A SINGLE PLENUM CHAMBER LOOP AND SEGMENT SKIRT, INCLUDING THE EFFECT OF SKIRT-GROUND FRICTION. ELASTOMER COATED FABRIC IS USED FOR THE SKIRT MATERIAL.

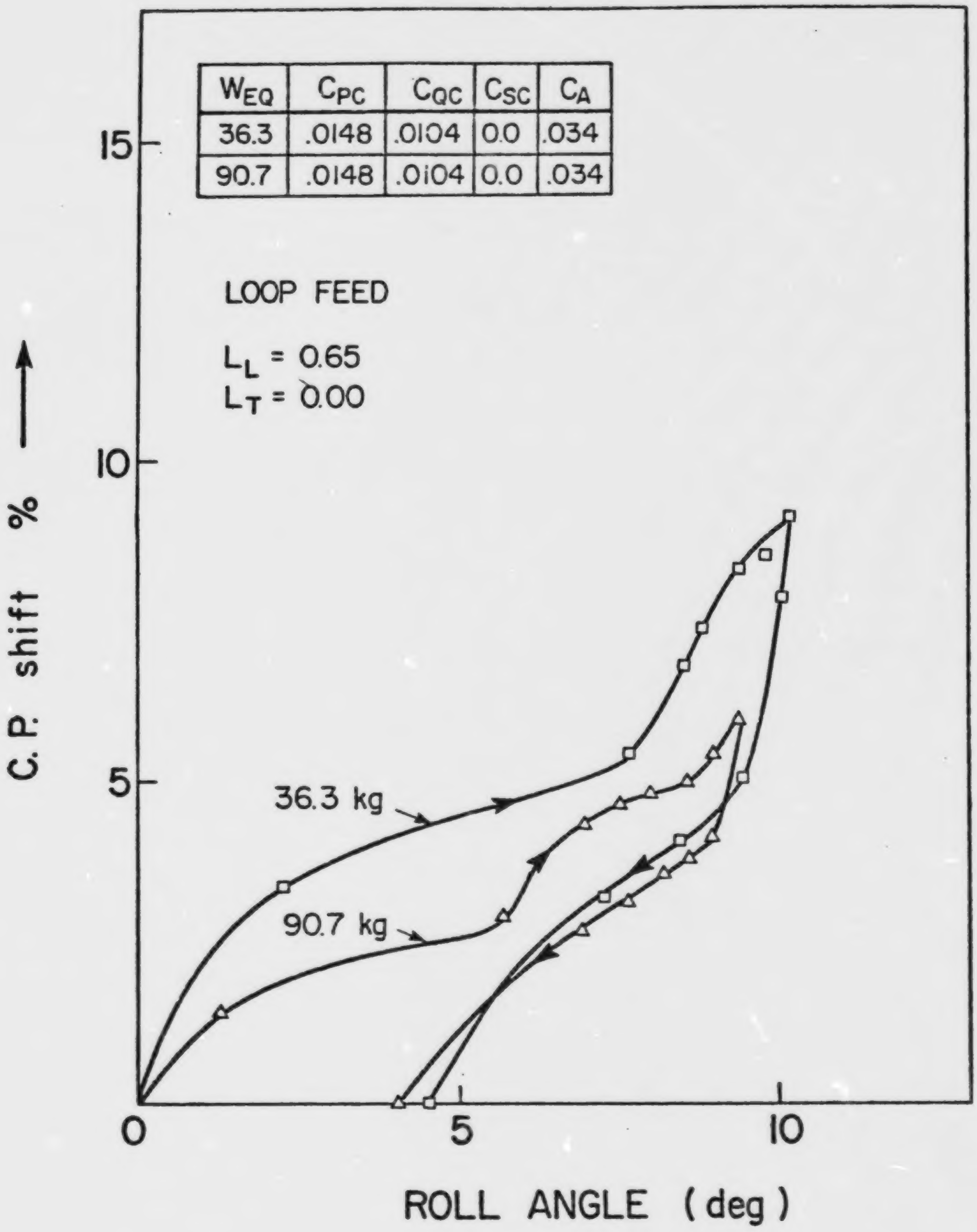

FIG. 3.32 EFFECT OF MODEL WEIGHT ON THE MEASURED ROLL STIFFNESS OF THE CUSHION DYNAMICS MODEL EQUIPPED WITH THE ELASTOMER COATED FABRIC LOOP AND SEGMENT SKIRT SYSTEM.

4) PITCH-HEAVE DYNAMICS OF THE SEGMENTED SKIRT CUSHION

4.1) Introduction

4.1.1) General Objective

As discussed in the Introduction, a major objective of the present contract is the theoretical and experimental investigation of the dynamics of the HSL Cushion. A theory for the static pitch and roll stiffness of this cushion is a fundamental prerequisite for the development of a theory for the dynamics; this has been achieved, and is described in Section 3 of this report, along with some experimental pitch and roll stiffness measurements obtained on the 2.44 x 1.22m model. The project described here is based on the VAMPIRE 1 test vehicle used in the UTIAS 43m diameter circular track facility. The facility is equipped with a sophisticated instrumentation package for data acquisition, described by Ribner (4.1), and is sized to facilitate scaling of skirt systems on a material weight basis. The geometry of the HSL skirt segments used is given in section 3.1.2, figure 3.2 and table 3.1.

In addition to the general objective of developing mathematical models for the dynamics of representative cushion systems for engineering prediction purposes, a much more specific objective has emerged in the course of the present contract. This is the investigation of the material properties of the elastomer fabric composites used for ACV skirts on the dynamics of the vehicle.

As documented in previous contract reports (4.2)(4.3), hysteresis has been observed in the static roll and pitch stiffness curves of several types of cushion systems. Static hysteresis represents a form of damping in the dynamic case. Figure 4.1 shows the predicted effect on oscillations following a roll disturbance, if the hysteresis in the static roll stiffness curve, figure 4.2, is interpreted as an equivalent damping. Tests on the 1.22 x 2.44m air cushion using the dynamics table in the UTIAS ACV lab have illustrated this predicted effect. If the pitch stiffness curves for the HSL skirt, presented in section 3, for polyethylene, Fig. 3.27, and for the "red", nylon-urethane, material, Fig. 3.13, are examined it is easily seen that the polyethylene skirt exhibits more hysteresis. The effect on vehicle damping is shown in figures 4.3 and 4.4 which are raw voltage traces of pitch responses to heave and pitch angle, initial conditions type of disturbances. In addition to lower damping, the air cushion will, under certain pressure and flow conditions, exhibit a limit cycle behaviour in pitch and heave at large initial disturbance amplitude when equipped with the "red" nylon-urethane skirt. In this section an attempt is made to correlate the static hysteresis with a measured dynamic damping for the VAMPIRE 1 test vehicle.

4.1.2) Choice of Skirt Material

The type of skirt material used has been shown to be a factor in the dynamics of model scale vehicles. The choice of skirt material is important if the model dynamics are expected to be similar to full scale. Scaling of skirt material is, however, quite difficult, and as discussed in section 3.2.2.2, probably not fully achievable. Also, at the time of the tests, skirt material property information was limited. Consequently, material was chosen on the basis of weight per unit area and availability. The relevant parameter when comparing skirt weights is the skirt weight coefficient which

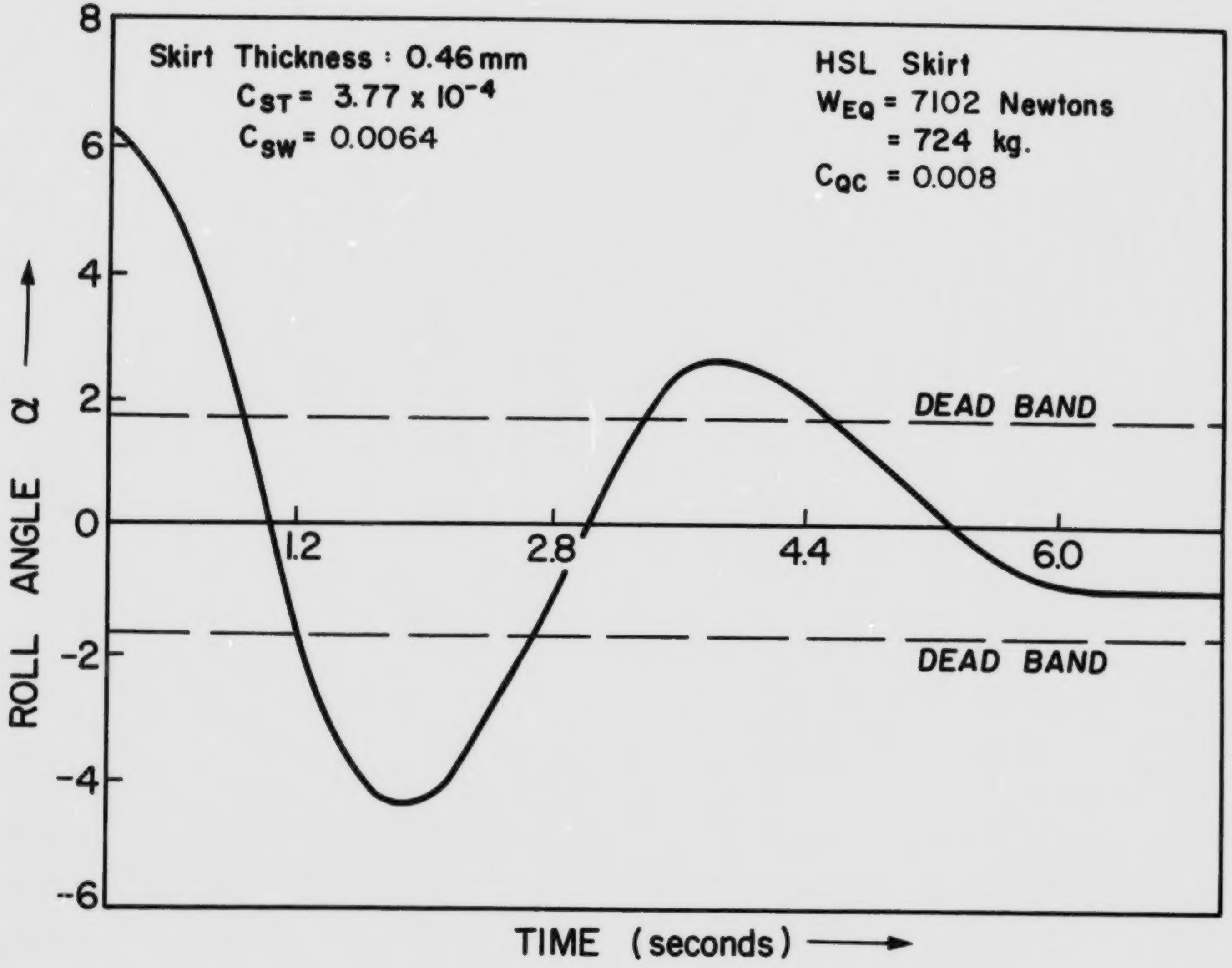

FIG. 4.1 THEORETICAL ROLL RESPONSE WHEN STATIC HYSTERESIS IS INTERPRETED AS A VISCOUS LOSS.

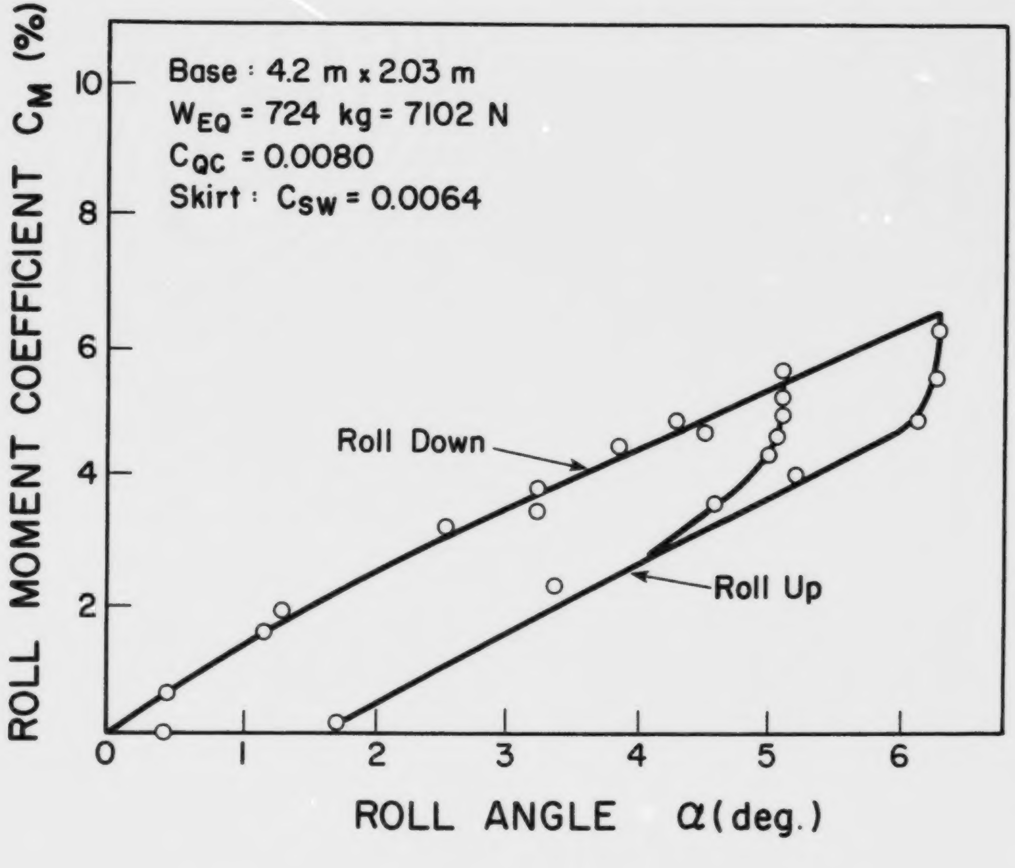

FIG. 4.2 TYPICAL STATIC ROLL STIFFNESS CURVE SHOWING HYSTERESIS WITH THE HSL SKIRT.

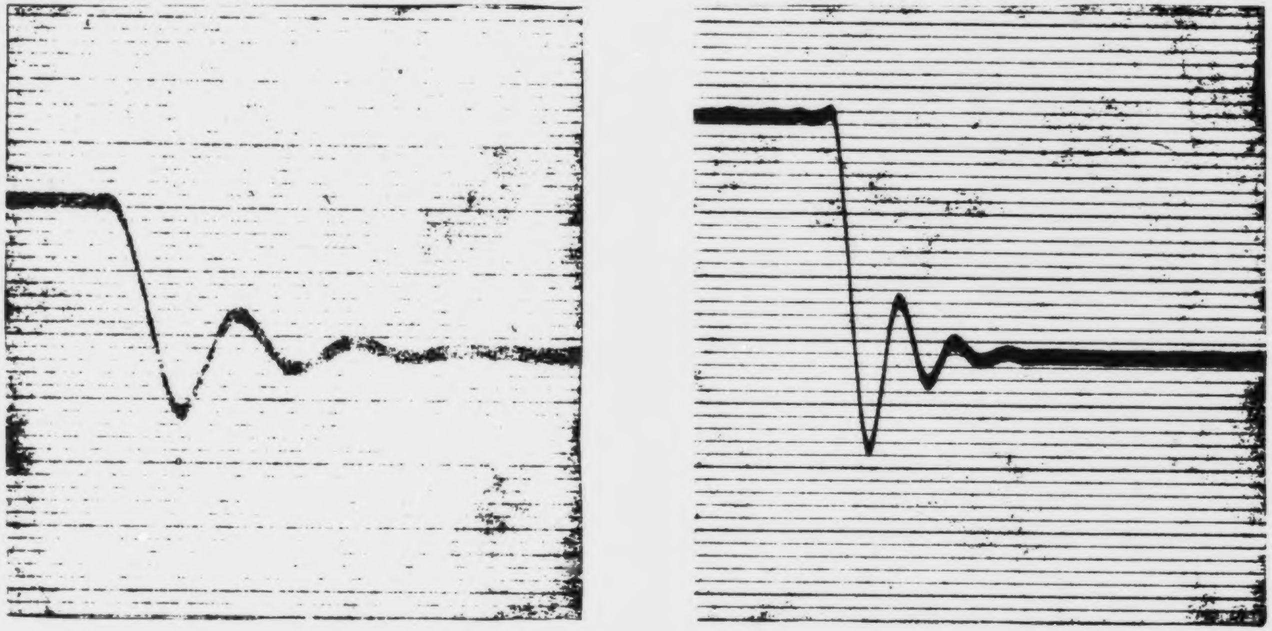

(a) RVDT OUTPUT

$C_{QC} = 0.01335$

$W = 416N$

$\theta_o = 2.6°$

$\theta_{eq} = 0.0°$

Paper speed = 1000 mm/min

(b) RVDT OUTPUT

$C_{QC} = 0.01164$

$W = 416N$

$\theta_o = 4.0°$

$\theta_{eq} = 0.0°$

Paper speed = 500 mm/min

FIG. 4.3 PITCH RESPONSE TO DISTURBANCE FOR POLYETHYLENE SKIRT.

(a) $\theta_o = 2.6°$
(b) $\theta_o = 4.0°$

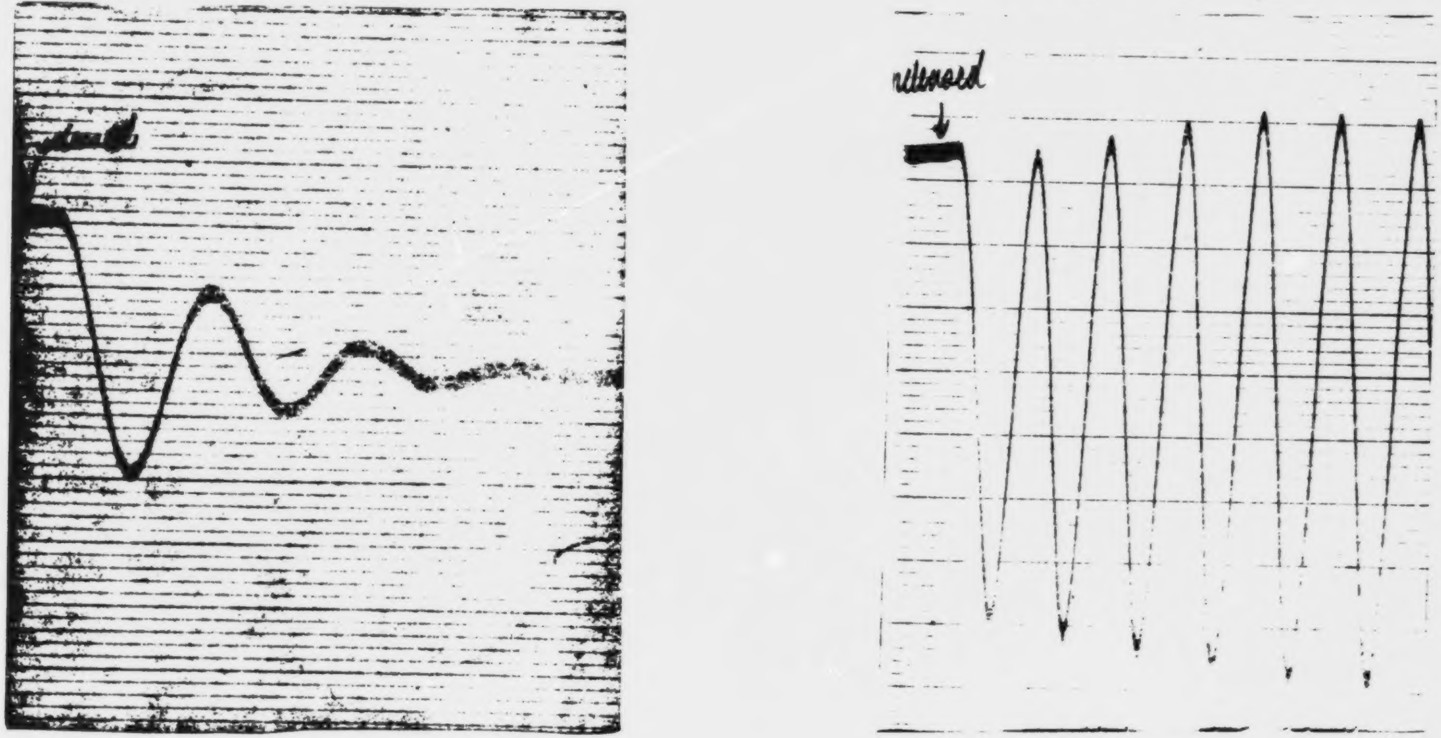

(a) RVDT OUTPUT
$C_{QC} = 0.01335$
$W = 416N$
$\theta_o = 2.6°$
$\theta_{eq} = 0.0°$
Paper speed = 1000 mm/min

(b) RVDT OUTPUT
$C_{QC} = 0.01164$
$W = 416N$
$\theta_o = 4.0°$
$\theta_{eq} = 0.0°$
Paper speed = 500 mm/min

FIG. 4.4 PITCH RESPONSE TO DISTURBANCE FOR NYLON URETHANE SKIRT.

(a) $\theta_o = 2.6°$
(b) $\theta_o = 4.0°$

is closely given by the ratio of skirt weight per unit area to the equilibrium cushion pressure. For the La Crete Ferry, a full scale ACV using the HSL skirt system, the value is 0.004, and for VAMPIRE 1 equipped with a Neoprene Nylon HSL skirt the value is 0.0064. Thus, the skirt system on the VAMPIRE 1, although not a close match for the full scale vehicle, is acceptably close for the purposes of this section.

4.2) Static Pitch and Heave Stiffness Measurements

4.2.1) Description of the Experiment

The experimental setup for static pitch-heave measurements is shown in Fig. 4.5. A 15.2 x 7.6cm steel I-beam with bearing assemblies at both ends is bolted to the main structural frame of the vehicle so that its axis passes through the centre of gravity of the vehicle. Each bearing assembly, shown in Fig. 4.6, incorporates one radial and one linear bearing giving the vehicle freedom to pitch and heave and, at the same time, prevents any lateral or longitudinal movement. The linear bearings slide along 50mm dia. solid steel rods, one of which is attached to a structural column of the Circular Track model bay (Fig. 4.6). The other steel rod rests on a 12mm dia. roller and is restrained at both ends by guides to move laterally only, approximately 15mm each side of its normal position. This arrangement prevents buckling forces in the I-beam which would result from misalignment if both rods were fixed and not exactly parallel. The vehicle itself has two 12mm dia. rods installed on its longitudinal centerline, one at each end as shown in Fig. 4.5. The steel plates used in the experiment to vary the pitching movement have a hole in their geometrical centre and are stacked on these rods, one on top of the other as required.

To measure pitch angle and heave height, four triangular tabs were attached to the corners of the vehicle as shown in Fig. 4.5, and during an experiment, their height above the floor was measured with a Vernier height gauge. The heave height and pitch angles were calculated from this data. A manometer was used to measure the cushion pressure at three different locations, and the average of these was used in subsequent calculation. Cushion flow rates were inferred from the non-dimensional fan characteristic determined in a separate experiment (see Appendix F), the measured cushion pressure and fan speed, together with the computed atmospheric density.

Results were obtained for a number of fan speeds N and total vehicle weight combinations. At the beginning of each experiment the fan speed was adjusted to the desired value and then periodically checked using a calibrated stroboscope. The vehicle was loaded with steel plates, each weighing approximately 89N, distributed between the front and aft ends of the vehicle in such a way that, at the desired total weight, the vehicle was pitched nose down with the front wheels almost touching the ground. The plates were then transferred one by one from the front end to the aft end and the measurements were taken after each transfer. This process was repeated until a full cycle - from nose down attitude to tail down and back to nose down - was completed.

4.2.2) Static Experiment Results

The results of the static pitch-heave experiments are presented in figures 4.7, 4.8, 4.9. These show pitching moment, heave, roll angle and air mass flow rate versus pitch angle for fan speeds of 1800rpm, 2000rpm and 2200 rpm respectively. In the case of the pitching moment curves, the data is plotted along with "eyeball" fit lines for both the increasing and decreasing

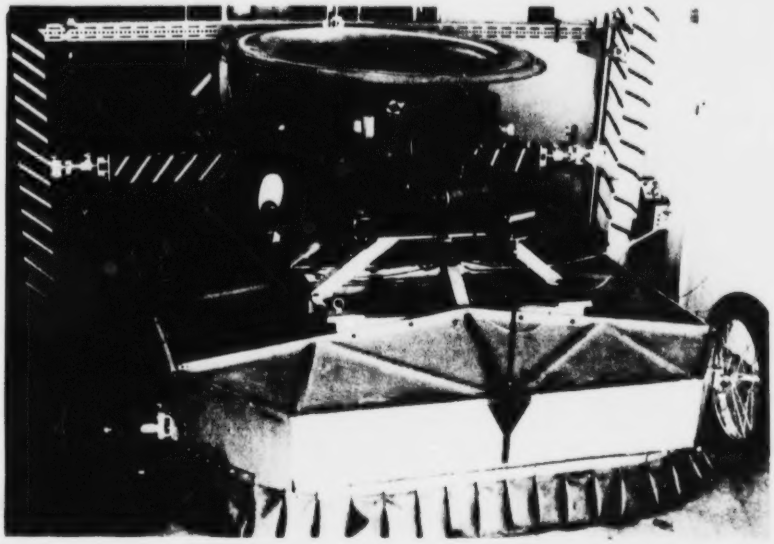

FIG. 4.5 EXPERIMENTAL SETUP FOR STATIC PITCH-HEAVE MEASUREMENTS - VAMPIRE I.

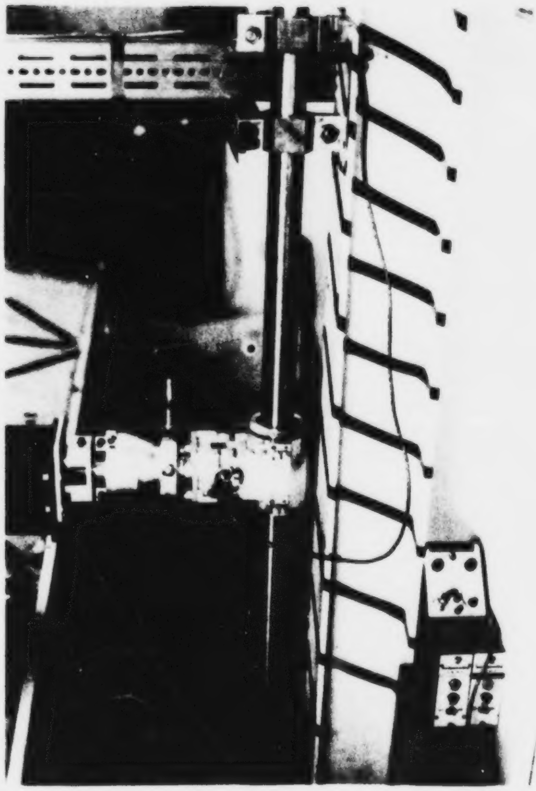

FIG. 4.6 BEARING ASSEMBLY FOR STATIC PITCH-HEAVE EXPERIMENT.

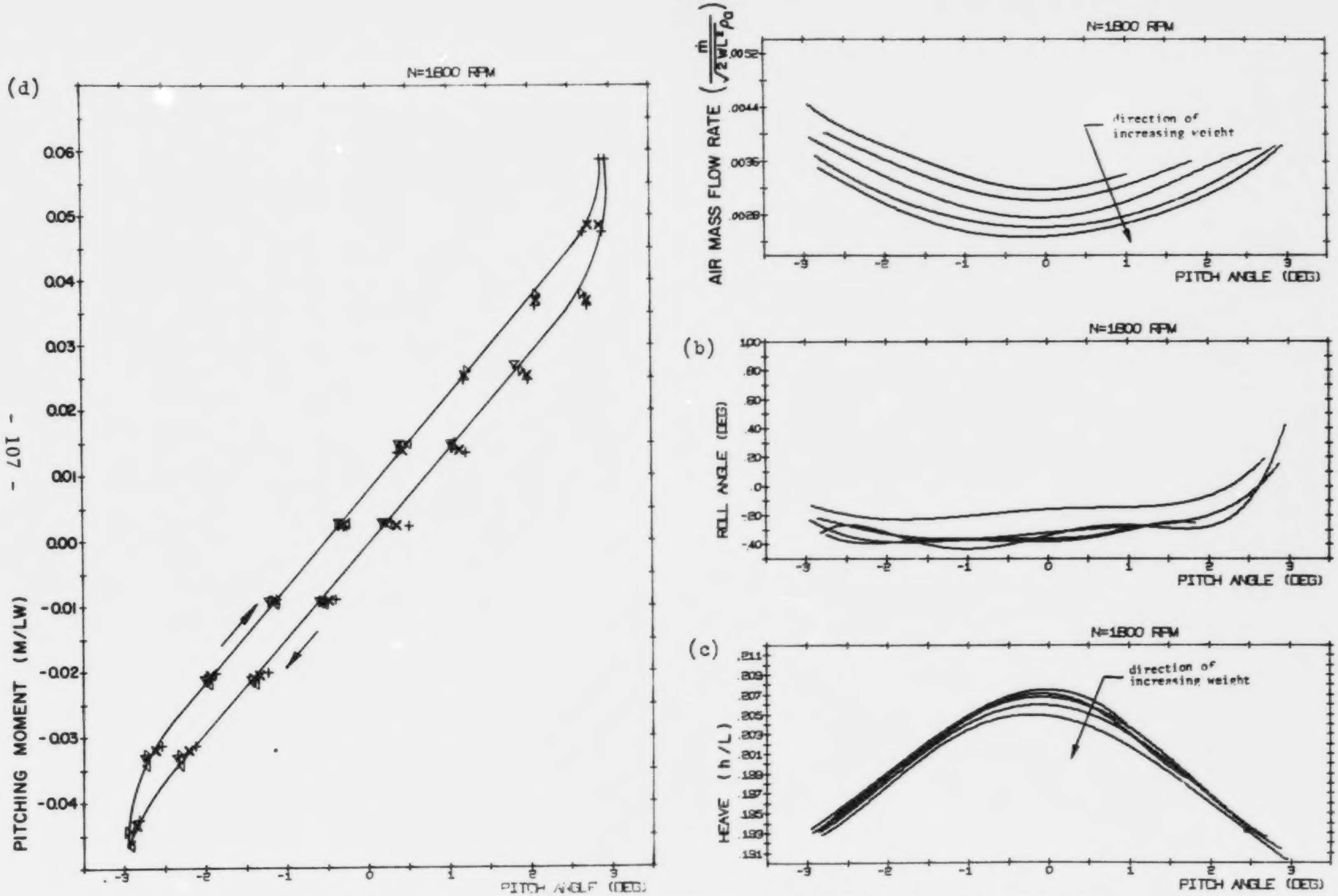

FIG. 4.7 STATIC PITCH-HEAVE EXPERIMENTAL RESULTS FOR 1800 RPM FAN SPEED.

(a) AIR MASS FLOW RATE vs θ-SINGLE LINE FIT TO DATA.
(b) ROLL ANGLE vs θ-SINGLE LINE FIT TO DATA.
(c) HEAVE HEIGHT vs θ-SINGLE LINE FIT TO DATA.
(d) PITCH STIFFNESS CURVE.

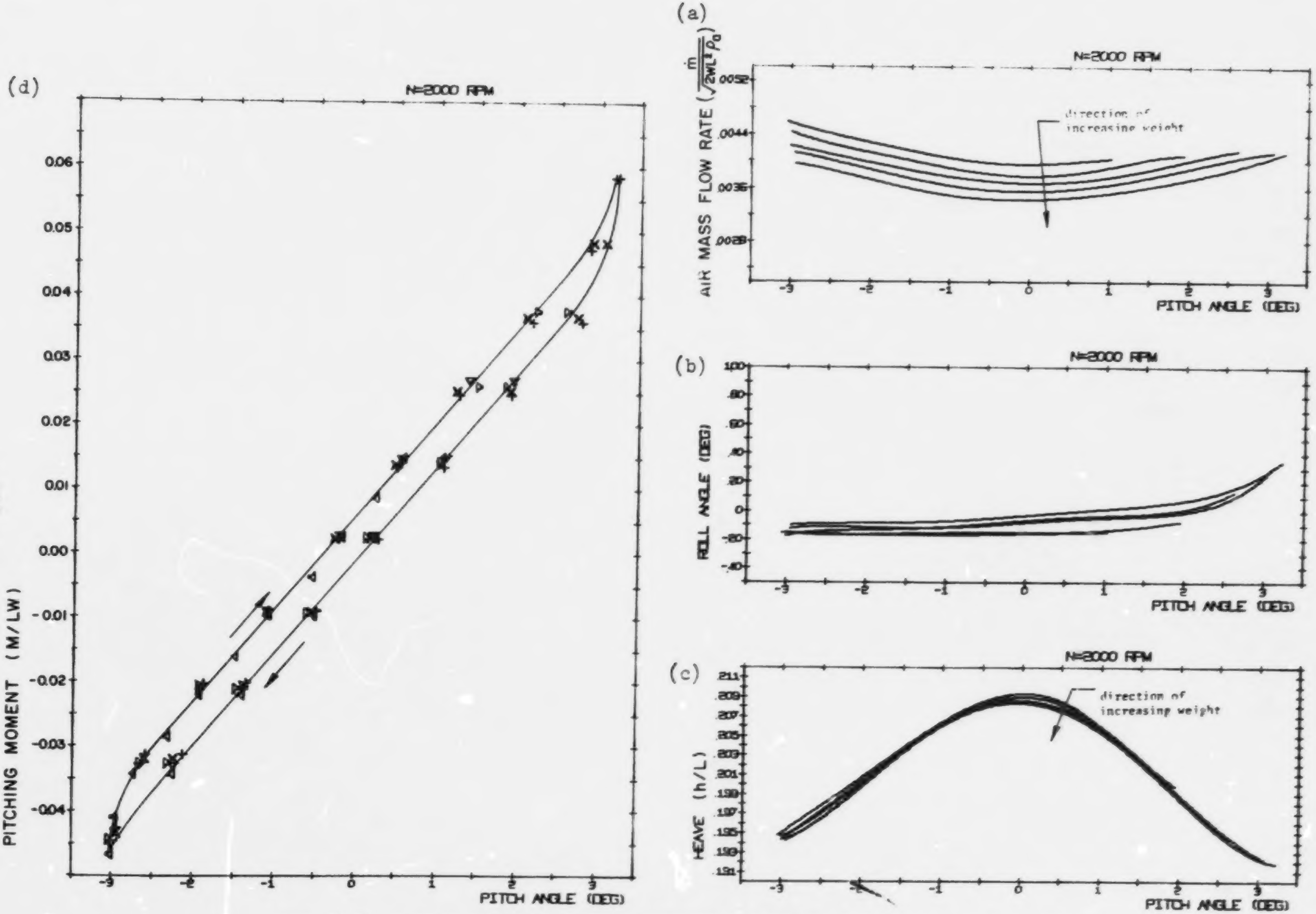

FIG. 4.8 STATIC PITCH-HEAVE EXPERIMENTAL RESULTS FOR 2000 RPM FAN SPEED.

(a) AIR MASS FLOW RATE vs θ-SINGLE LINE FIT TO DATA.
(b) ROLL ANGLE vs θ-SINGLE LINE FIT TO DATA.
(c) HEAVE HEIGHT vs θ-SINGLE LINE FIT TO DATA.
(d) PITCH STIFFNESS CURVE.

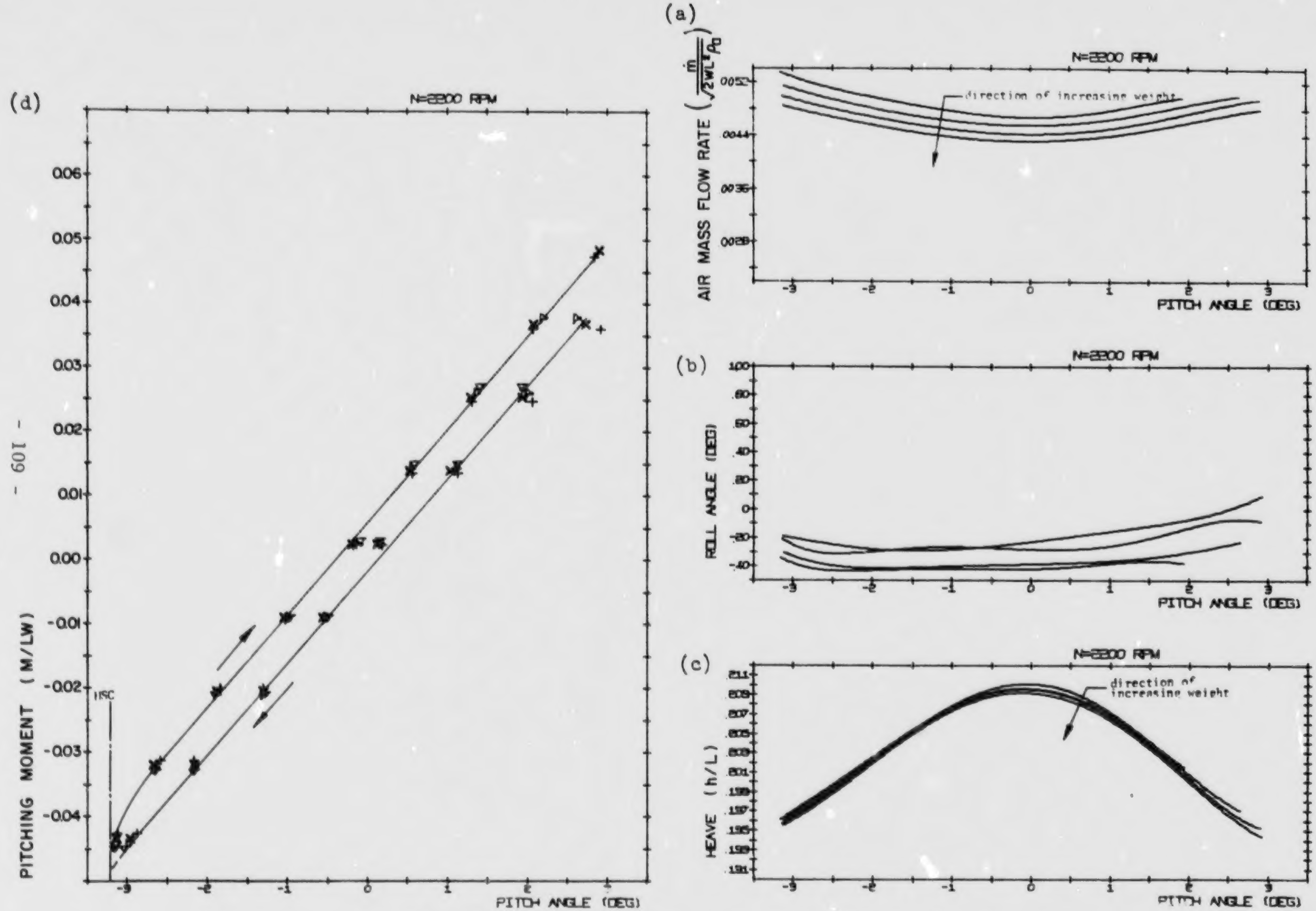

FIG. 4.9 STATIC PITCH-HEAVE EXPERIMENTAL RESULTS FOR 2200 RPM FAN SPEED.

(a) AIR MASS FLOW RATE vs θ-SINGLE LINE FIT TO DATA.
(b) ROLL ANGLE vs θ-SINGLE LINE FIT TO DATA.
(c) HEAVE HEIGHT vs θ-SINGLE LINE FIT TO DATA.
(d) PITCH STIFFNESS CURVE.

moment cases. The other plots are a single-line least squares fit to the data using 5th order Chebyshev polynomials. The single-line fits enable a better illustration of the effects of weight changes on the individual characteristics.

The most notable feature of the pitching moment curve is the hysteresis, similar to that described in section 3.5 and the preliminary roll stiffness data discussed in section 4.1. Hysteresis is present in the other curves as well, however, it is weaker, as may be seen in figure 4.10 which also illustrates the consistent form of these plots at different fan speeds.

The individual characteristics are discussed separately below:

i) Pitching moment

Generally, the plots show either full or partial loop characteristics. The extent of this loop was in most cases limited; this was due to one or both of the following reasons:

a) the vehicle in its normal configuration requires three steel plates (~278N) as a ballast at the front end to balance it (i.e. pitch $\theta=0$). These plates could be used in addition to the other steel plates to vary the pitching moment, thus increasing the range of tail-down moments. This proved to be valuable at low-weight experiments, when the total number of steel plates was low, giving a smaller total range of moments. As a result, while the range of nose-down moments was limited, it was possible to obtain full required tail-down range of moments.

b) the hard structure contact (HSC), in the case of the VAMPIRE 1 when one of the wheels touches the ground, is a function of both the pitch angle and heave height. These, in turn, are functions of weight and cushion pressure (or lift fan RPM). As shown in the plots, the HSC occurred at several weight-fan RPM combinations before the lower end of the loop was reached.

The pitching moment vs. pitch angle loops are characterized by two straight-line parallel sides, with the slope as well as the loop area being independent of the vehicle weight or the lift fan RPM. The deviations from this hysteresis loop (non-parallel sides, scatter of data points) appear to be related to the variations in roll angle.

ii) Heave

At constant weight and lift fan RPM, the heave height generally decreases with pitch angle symmetrically in both directions. The hysteresis is much weaker and the hysteresis loop is in the form of a very narrow, banana-shaped figure 8. Because of this the data can be fitted with a single line. Comparison of heave plots shows that the heave height is, as could be expected, proportional to the lift fan RPM and inversely proportional to the vehicle weight.

iii) Roll Angle

Since only the pitching moment is being varied, the roll angle should remain unchanged and equal to zero. The vehicle, however, exhibited a noticeable tendency to roll when at nose-down attitude. Because of the consistency in this phenomena it can be attributed to the skirt asymmetry, probably due to the manufacturing or assembly tolerances. The hysteresis in roll was found to be largest at the maximum vehicle weight. No consistent trends in the mean roll angle curves were observed with either vehicle weight or fan RPM.

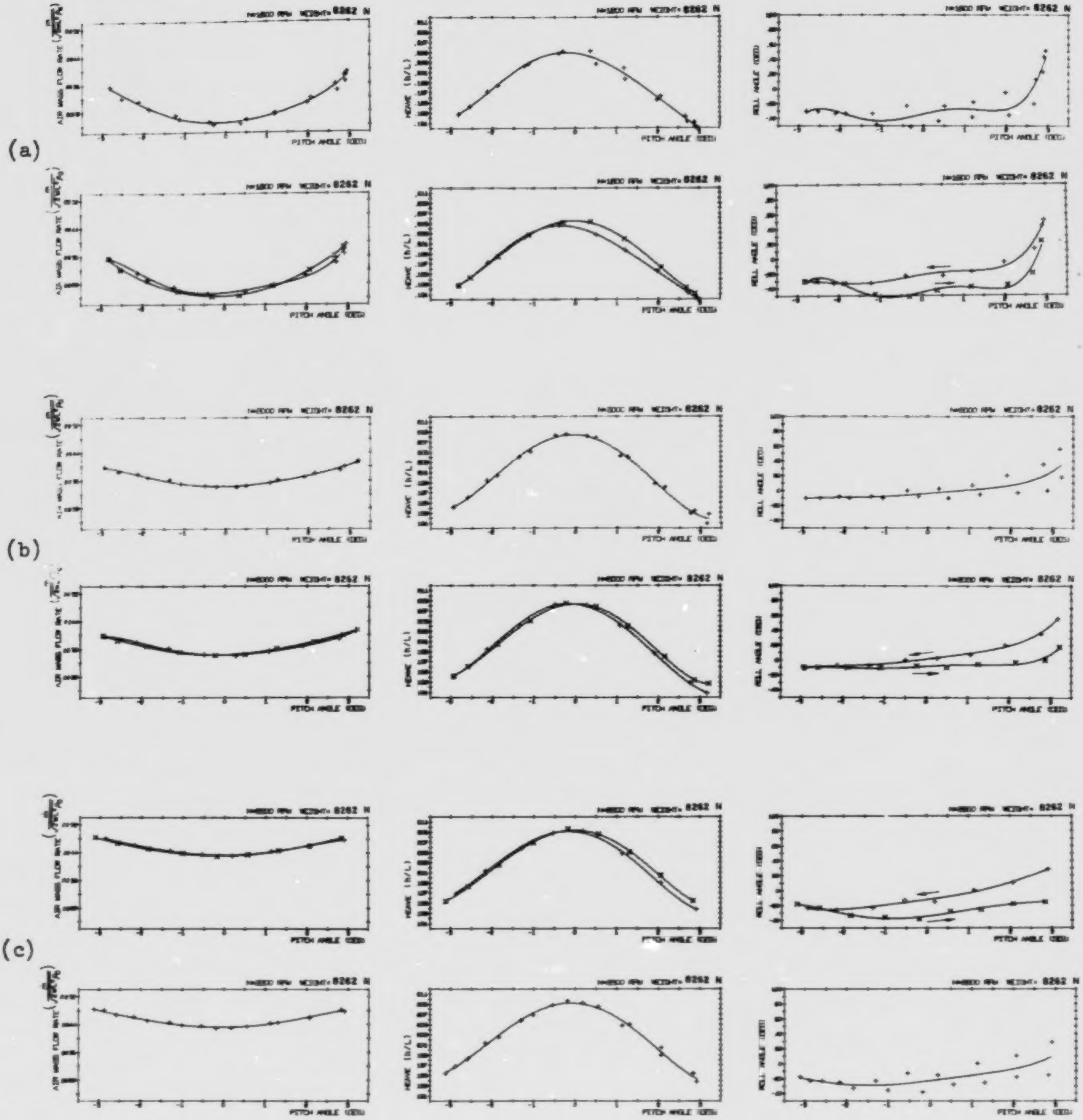

FIG. 4.10 COMPARISON OF SINGLE LINE AND HYSTERESIS LINE FITS TO AIR FLOW, ROLL ANGLE AND HEAVE DATA FOR VARIOUS FAN SPEEDS.

(a) N = 1800 RPM
(b) N = 2000 RPM
(c) N = 2200 RPM

iv) Air mass flow rate

The hysteresis in air mass flow rate is a direct result of, and proportional to the hysteresis in heave. This hysteresis is also very weak and the data can be adequately represented by a single line.

4.3) Theoretical Model of Pitch-Heave Dynamics

4.3.1) Assumptions

The theoretical model of the dynamical response of VAMPIRE 1 to a ramp type disturbance is developed using the following assumptions:

i) the vehicle moves at constant forward speed and is disturbed in pitch and heave only;
ii) gyroscopic effects of the rotating parts of the vehicle such as the fan and propeller are ignored;
iii) the dynamic effects associated with the basic motion of the vehicle on a circular path around the track are negligible;
iv) the assumptions used in Section 3.2.1.1 for the development of a static stiffness theory apply;
v) the fan behaviour in the presence of variations of cushion pressure and cushion volume flow associated with the dynamics follows the static characteristic given in Appendix F, that is, the fan behaves quasisteadily;
vi) the assumptions described in Section 2.2 for the basic cushion dynamics apply, so that the cushion air compressibility can be modelled as a lumped pneumatic capacitance, and all air flow processes are incompressible and quasisteady;
vii) additional damping from the pitch from the skirt material hysteretic damping is modelled as an equivalent viscous damping.

4.3.2) Equations

The first part of the formulation follows closely the development given in Section 3.2.1.3. The fan law is the same as equations (3) and (4) of that section:

$$P_c = P_{c_0} + C_1 q_f + C_2 q_f^2 + C_3 q_f^3 + \dots \qquad (1)$$

The cushion air escape law is given by equation (5) of Section 3;

$$q_c = C_D \sqrt{\frac{2P_c}{\rho_a}}\; a_e\,(h,\theta) \qquad (2)$$

Here, $a_e(h,\theta)$ is the cushion air escape area defined by equation (6) of Section 3, and the height h of the centre of mass of the vehicle replaces h_p and the pitch angle θ replaces α. Note that here, in contrast to the static stiffness theory of Section 3, owing to vehicle motion $q_c \neq q_f$ in general. The lift force F generated at any instant by the cushion is given by equation (7) of Section 3.

$$F = P_c\, a_f\,(h,\theta) \qquad (3)$$

Also, owing to vehicle motion $F \neq W$, the vehicle weight. The moment M generated by the cushion has to be computed with respect to the centre of mass of the vehicle, and not the base as is done in Section 3. Hence equation 9, Section 3, is replaced by

$$M = P_c \, a_f \, (h,\theta) \; g13 \; (h,\theta) \tag{4}$$

where the expression for the footprint centroid location, g13 (h,θ) is given in Appendix C.

The equations for the dynamics of the vehicle and cushion volume can now be specified. First, the cushion conservation law has the same general form as in Section 2. If $V_c = V_c \, (\theta,h)$ is the volume enclosed by the cushion, then

$$\frac{d}{dt} V_c + C_c \frac{dP_c}{dt} = q_f - q_c \tag{5}$$

The quantity C_c is the cushion capacitance given by

$$C_c = V_c/\rho a^2 \tag{6}$$

In Section 2, the capacitance is computed by using the equilibrium cushion volume, $V_c = V_{ce}$, but here, because large variations in V_c occur as a result of the vehicle motion the capacitance is a variable. Newton's law for the vehicle heaving motion is

$$\frac{W}{g} \ddot{h} = F - W - \xi_h \dot{h} \; ; \; \dot{h} \equiv \frac{d}{d+} h \tag{7}$$

and Euler's equation for the pitching motion is

$$I\ddot{\theta} = M - \xi_\theta \dot{\theta} \; ; \; \dot{\theta} = \frac{d}{dt} \theta \tag{8}$$

Here, ξ_h and ξ_θ are equivalent linear viscous damping terms used to account for skirt material effects, and W and I are the vehicle weight and pitch moment of inertia, determined from separate experiments.

4.3.3) Nondimensionalization

The quantities chosen to have reference dimensions are the vehicle weight W, atmospheric density ρ_a, and vehicle hard structure length L. In the following, a bar $(^{-})$ is used to denote dimensionless quantities. With

$$P_c = \frac{W}{L^2} \bar{P}_c \tag{9}$$

$$q_f = \sqrt{\frac{WL^2}{\rho_a}} \, \bar{q}_f ; \quad q_c = \sqrt{\frac{WL^2}{\rho_a}} \, \bar{q}_c \tag{10}$$

$$h = L\bar{h} \tag{11}$$

$$a_e(h,\theta) = L^2\bar{a}_e(\bar{h},\theta); \quad a_f(h,\theta) = L^2\bar{a}_f(\bar{h},\theta) \qquad (12)$$

$$g13(h,\theta) = L\bar{g}13(\bar{h},\theta) \qquad (13)$$

$$V_c(h,\theta) = L^3\bar{V}_c(\bar{h},\theta) \qquad (14)$$

$$F = W\bar{F}; \quad M = LW\bar{M}; \quad I = \rho_a L^5\bar{I} \qquad (15)$$

$$t = L^2\sqrt{\frac{\rho_a}{W}}\ \bar{t}; \quad g = \frac{W}{L^3\rho_a}\ \bar{g}; \quad C_c = \frac{L^5}{W}\ \bar{C}_c \qquad (16)$$

$$\rho = \rho_a\ \bar{\rho} \qquad (17)$$

the system differential equations are

$$\bar{P}_c = \bar{P}_{co} + \bar{C}_1\bar{q}_f + \bar{C}_2 q_f^2 \qquad (18)$$

$$\bar{q}_c = \sqrt{2}C_D\ \bar{P}_c^{\frac{1}{2}}\ \bar{a}_e\ (\bar{h},\theta) \qquad (19)$$

$$\ddot{\bar{h}} = \bar{g}\left[\bar{P}_c\bar{a}_f(\bar{h},\theta) - 1 - \bar{\xi}_{\bar{h}}\ \dot{\bar{h}}\right] \qquad (20)$$

$$\bar{q}_f - \bar{q}_c = \frac{1}{\sqrt{2}}\left[\frac{d}{d\bar{t}}\ (\bar{V}_c(\bar{h},\theta)) + \bar{C}_c\ \dot{\bar{P}}_c\right] \qquad (21)$$

$$\bar{I}\ddot{\theta} = \bar{P}_c\bar{a}_f(\bar{h},\theta)\ \bar{g}_{13}(\bar{h},\theta) - \bar{\xi}_\theta\dot{\theta} \qquad (22)$$

Here, $\bar{P}_{co}$, $\bar{C}_1$, $\bar{C}_2$, $\bar{\xi}_h$, $\bar{\xi}_\theta$ are nondimensional equivalents of the respective dimensional quantities.

4.3.4) Linearized Equations

The above system of equations is now linearized about the equilibrium point corresponding to $\dot{h} = \dot{\theta} = 0$ and $h = h_e$, $\theta = 0$.

From equations 3,8,9, and 12 this implies that

$$\bar{P}_{ce}\bar{a}_f\ (\bar{h}_e,0) = 1 \qquad (23)$$

$$\bar{M} = 0 \qquad (24)$$

at the equilibrium point.

About the equilibrium point:

$$\bar{P}_c = \bar{P}_{ce}(1 + \tilde{p}) \tag{25}$$

$$\bar{q}_c = \bar{q}_{ce}(1 + \tilde{q}_c) \tag{26}$$

$$\bar{h} = \bar{h}_e(1 + \tilde{q}_f) \tag{27}$$

$$\bar{q}_f = \bar{q}_{ce}(1 + \tilde{q}_f) \tag{28}$$

$$\theta = \tilde{\theta} \tag{29}$$

where $\tilde{(\ )}$ means small variations so that products of these quantities are are negligible.

The following linearized non-dimensional equations are obtained.

First the fan law becomes

$$\tilde{p} = \bar{C}_{sc}\tilde{P}_f \tag{30}$$

where

$$\bar{C}_{sc} = \left\{(\bar{C}_1\,\bar{Q}_c + 2\bar{C}_2\,(\bar{Q}_c)^2)/\bar{P}_c\right\}_e$$

and the notation {}e indicates that all quantities are evaluated at the equilibrium conditions. The cushion air escape law becomes

$$\tilde{q}_c = \frac{\tilde{p}}{2} + A_1\tilde{h} + A_2\tilde{\theta} \tag{31}$$

where the constants A_1 and A_2 are given by

$$A_1 = \left\{\frac{\bar{h}}{\bar{a}_e}\left(\frac{\partial\bar{a}_e}{\partial\bar{h}}\right)\right\}_e, \quad A_2 = \left\{\frac{1}{\bar{a}_e}\left(\frac{\partial\bar{a}_e}{\partial\theta}\right)\right\}_e \tag{32}$$

Newton's law for the vertical motion becomes

$$\ddot{\tilde{h}} = B_1\tilde{p} + B_2\tilde{h} + B_3\tilde{\theta} - B_4\dot{\tilde{h}} \tag{33}$$

where

$$B_1 = \{\bar{g}/\bar{h}\}_e, \quad B_2 = \left|\bar{g}\,\frac{\partial \bar{a}_f}{\partial \bar{h}}\right|_e, \quad B_3 = \left|\frac{\bar{g}}{\bar{h}}\,\frac{\partial \bar{a}_f}{\partial \theta}\right|_e, \quad B_4 = \xi_{\bar{h}}\,\bar{g}$$

Euler's equation for the pitching motion becomes

$$\ddot{\tilde{\theta}} = C_1\tilde{h} + C_2\tilde{\theta} - C_3\dot{\tilde{\theta}} \tag{34}$$

where

$$C_1 = \left|\frac{\bar{h}}{\bar{I}}\,\frac{\partial \bar{g}_{13}}{\partial \bar{h}}\right|_e, \quad C_2 = \left|\frac{1}{\bar{I}}\,\frac{\partial \bar{g}_{13}}{\partial \theta}\right|_e, \quad C_3 = \frac{\bar{\xi}_\theta}{\bar{I}}$$

Finally, the cushion conservation law becomes

$$\tilde{q}_f - \tilde{q}_c = D_1\dot{\tilde{h}} + D_2\dot{\tilde{p}} \tag{35}$$

where

$$D_1 = \left|\frac{\bar{h}}{\bar{p}_c\bar{Q}_c}\right|_e, \quad D_2 = \left|\frac{\bar{C}_c\bar{p}_c}{\bar{Q}_c}\right|_e,$$

To cast this into matrix form $\dot{\underset{\sim}{x}} = \underset{\sim}{A}\,\underset{\sim}{x}$ substitute Eqs. (27) and (28) into (32) to obtain

$$\dot{\tilde{p}} = E_1\tilde{p} - E_2\tilde{h} - E_3\tilde{\theta} - E_4\dot{\tilde{h}} \tag{36}$$

where

$$E_1 = \left(\bar{C}_{sc}^{-1} - \frac{1}{2}\right)\left|\frac{\bar{Q}_c}{\bar{C}_c\bar{p}_c}\right|_e, \quad E_2 = \left|\frac{\bar{h}}{\bar{C}_p}\,\frac{\partial \bar{a}_e}{\partial \bar{h}}\right|_e$$

$$E_3 = \frac{1}{\bar{C}_p}\left|\frac{\partial \bar{a}_e}{\partial \theta}\right|_e, \quad E_4 = \left|\frac{\bar{h}}{\bar{C}_c\bar{p}_c^{\,2}}\right|_e,$$

$$\bar{C}_p = \frac{\bar{C}_c}{C_D}\left(\frac{\bar{p}_{ce}}{2}\right)^{1/2}$$

Now, for simplicity, dropping the (~) symbol, define

$$\underset{\sim}{x} = \begin{bmatrix} \dot{h} \\ \dot{\theta} \\ h \\ \theta \\ p_c \end{bmatrix}, \qquad \dot{\underset{\sim}{x}} = \begin{bmatrix} \ddot{h} \\ \ddot{\theta} \\ \dot{h} \\ \dot{\theta} \\ \dot{p}_c \end{bmatrix} \tag{37}$$

to give the required form

$$\dot{\underset{\sim}{x}} = \underset{\sim}{A}\,\underset{\sim}{x} \tag{38}$$

where the (5x5) system matrix $\underset{\sim}{A}$ has the following non-zero elements:

$$\underset{\sim}{A} = [a_{ij}] = \begin{bmatrix} a_{11} & 0 & a_{13} & a_{14} & a_{15} \\ 0 & a_{22} & a_{23} & a_{24} & 0 \\ 1 & 0 & 0 & 0 & 0 \\ 0 & 1 & 0 & 0 & 0 \\ a_{51} & 0 & a_{53} & a_{54} & a_{55} \end{bmatrix} \tag{39}$$

$a_{11} = -B_4; \quad a_{13} = B_1; \quad a_{14} = B_3; \quad a_{15} = B_1$

$a_{22} = -C_3; \quad a_{23} = C_1; \quad a_{24} = C_2$

$a_{51} = -E_4; \quad a_{53} = -E_2; \quad a_{54} = -E_3; \quad a_{55} = E_1$

This is the normal form for uncontrolled ACB pitch-heave motion. Recall that the first subscript denotes the row number, and the second, that of the column.

4.4) Dynamic Experiments and Results

4.4.1) Experiments

The dynamic experiments used the 43m diameter circular track (Fig. 4.11); this facility is described briefly in Appendix G. Figure 4.12 is a photograph of the test vehicle, VAMPIRE 1 equipped with the HSL cushion and in flight over the test ramp. The underside of the cushion is shown in Fig. 4.13, a photograph taken while the location of the centre of gravity was being determined.

The experiments used 9 channels of data, these being, 3 Trailing Air Sensors (TAS), 3 accelerometers and 3 rate gyros. These give respectively;

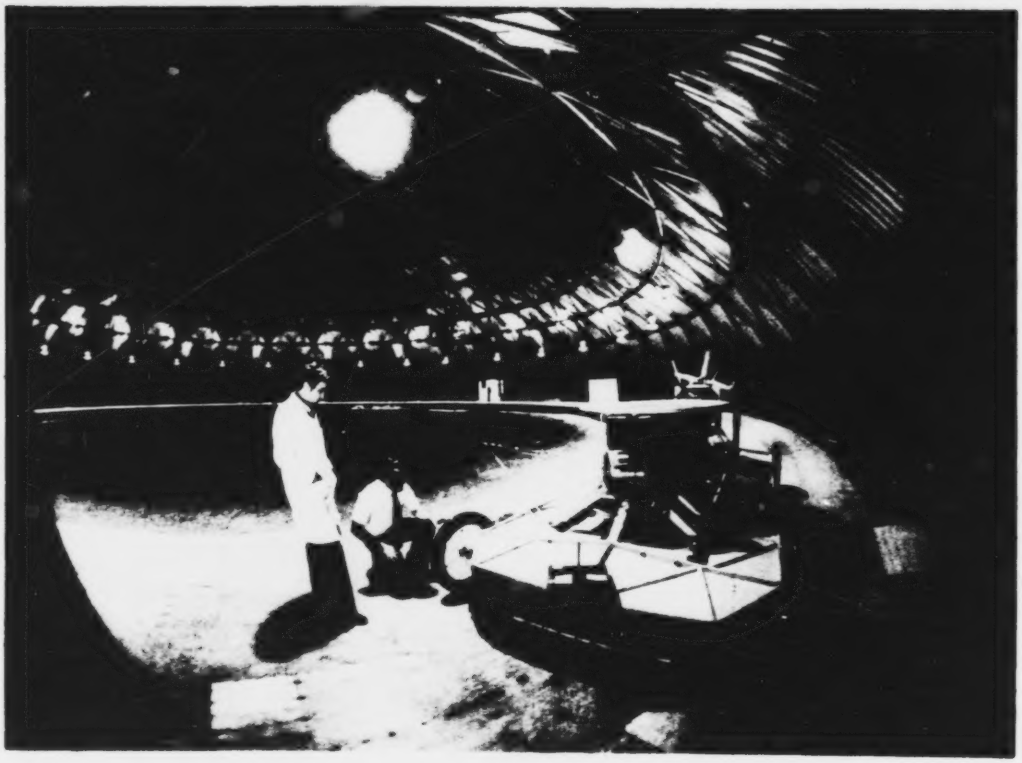

FIG. 4.11 UTIAS CIRCULAR TRACK VIEW.

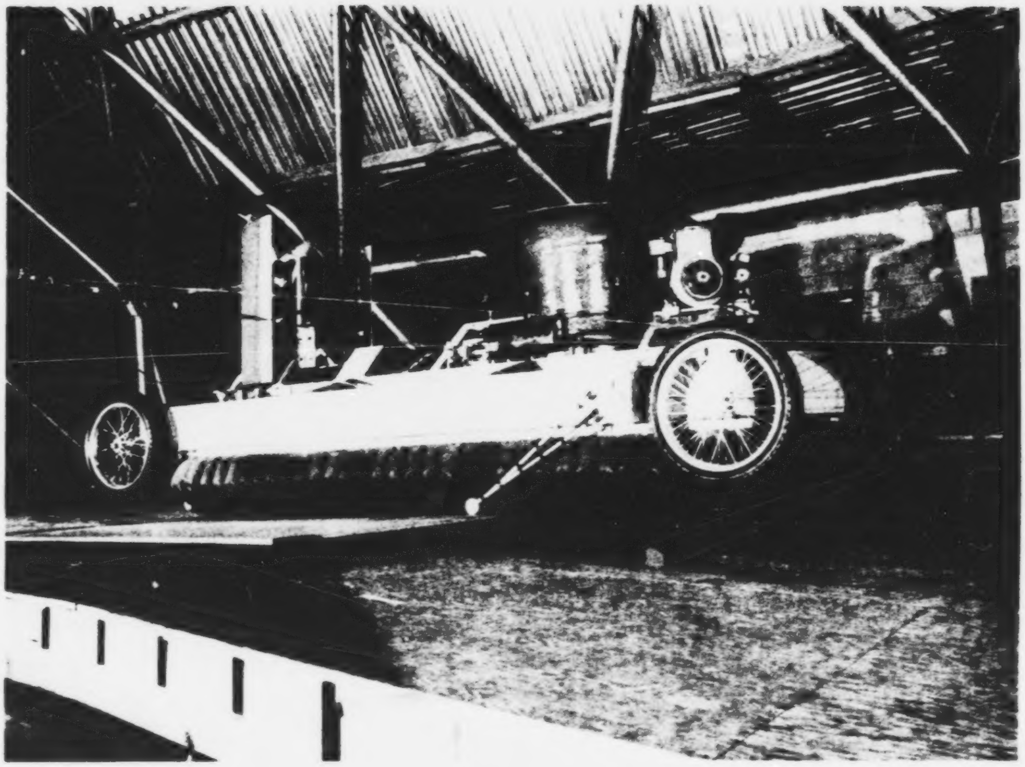

FIG. 4.12 TEST VEHICLE IN FLIGHT OVER RAMP.

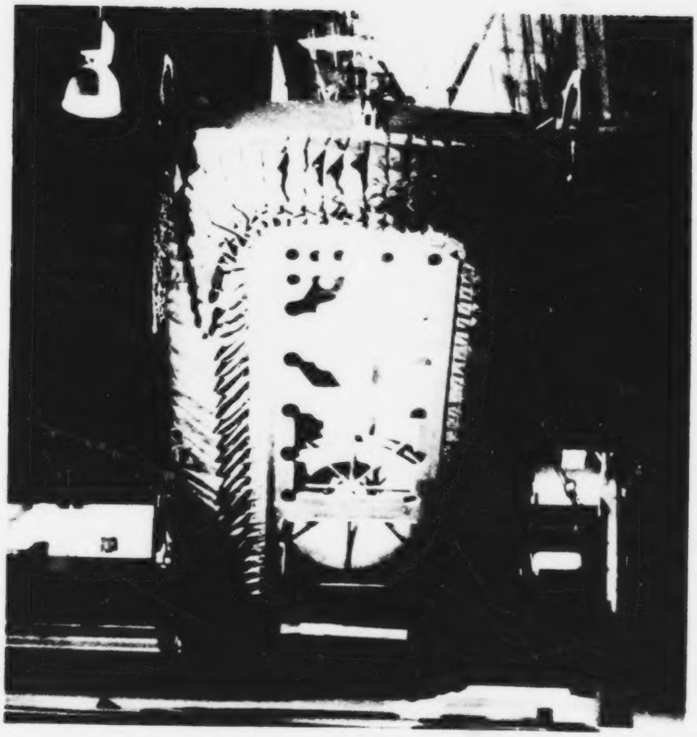

FIG. 4.13 UNDERSIDE OF TEST VEHICLE TAKEN DURING CENTRE OF GRAVITY MEASUREMENTS.

pitch, heave and roll position; x, y and z accelerations; and pitch, roll and yaw rates. The digitized data is recorded on magnetic tape in a form compatible with the University of Toronto IBM 370 computer.

The experiment consists of starting the vehicle and running it around the track until the desired forward speed has been reached. The vehicle is then subjected to a disturbance by raising the hydraulic ramps. In the tests described here the two ramps were operated in unison to provide a pitch-heave disturbance without roll. To eliminate gyroscopic effects from the propulsion fan, it was switched off and stopped just before the vehicle reached the ramp. Data was transmitted and recorded from a time just prior to the ramp disturbance and for several seconds after until the resulting oscillations had stopped.

4.4.2) Dynamic Test Results

Examination of the TAS voltage plots, Fig. 4.14, clearly indicates the time when the arms have all dropped off the ramp. Time point No. 110 (1.1s) was selected to define the initial conditions and the preceding data was discarded. Time histories of the measured variables following this point were used for parameter estimation.

Typical time histories of the vehicle response to a ramp disturbance are shown in Fig. 4.15. Of the measured variables, only heave acceleration $\ddot{h}$, pitch rate $\dot{\theta}$, heave height h, and pitch angle θ were used in the parameter identification (SPI). The other measured parameters, roll angle, yaw rate, roll rate, x-acceleration and y-acceleration are used only as aids to understanding, since they are not included in the previously derived dynamics model. The measured responses are non-dimensionalized for use in the parameter identification program. The values used in the program are then

$$\bar{h} = \frac{h}{L} \text{ (meas)} \tag{40}$$

$$\theta = \theta \text{ (meas)} \tag{41}$$

$$\Delta\bar{t} = \frac{1}{L^2}\sqrt{\frac{W}{\rho_a}}\ \Delta t\text{(meas)} \tag{42}$$

$$\ddot{\bar{h}} = \frac{L^3\rho_a}{W}\ \ddot{h} \text{ (meas)} \tag{43}$$

$$\dot{\theta} = L^2\sqrt{\frac{\rho_a}{W}}\ \dot{\theta} \text{ (meas)} \tag{44}$$

where (meas) = measured value

$L = 4.08\text{m}$

$W = 6895\text{N}$

$\rho_a \approx 1.227$ kg/m (standard atmosphere)

$\Delta t = 0.01\text{s}$

The SPI program was used to estimate the stiffness and damping coefficients in pitch and heave from the data. Difficulty was encountered in obtaining program convergence. This was thought to be due to the large

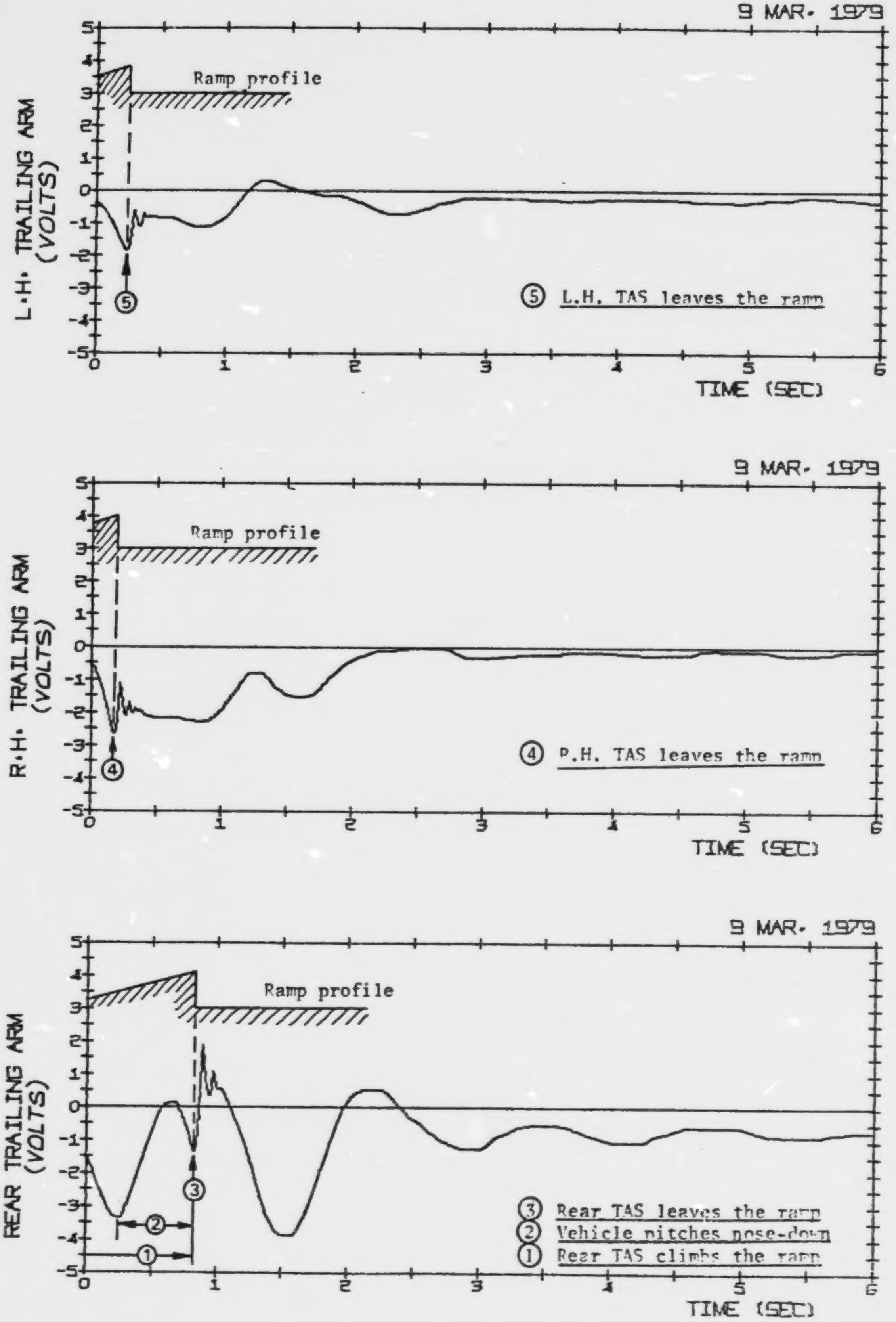

FIG. 4.14 TRAILING ARM SENSOR RESPONSE TO RAMP DISTURBANCE.

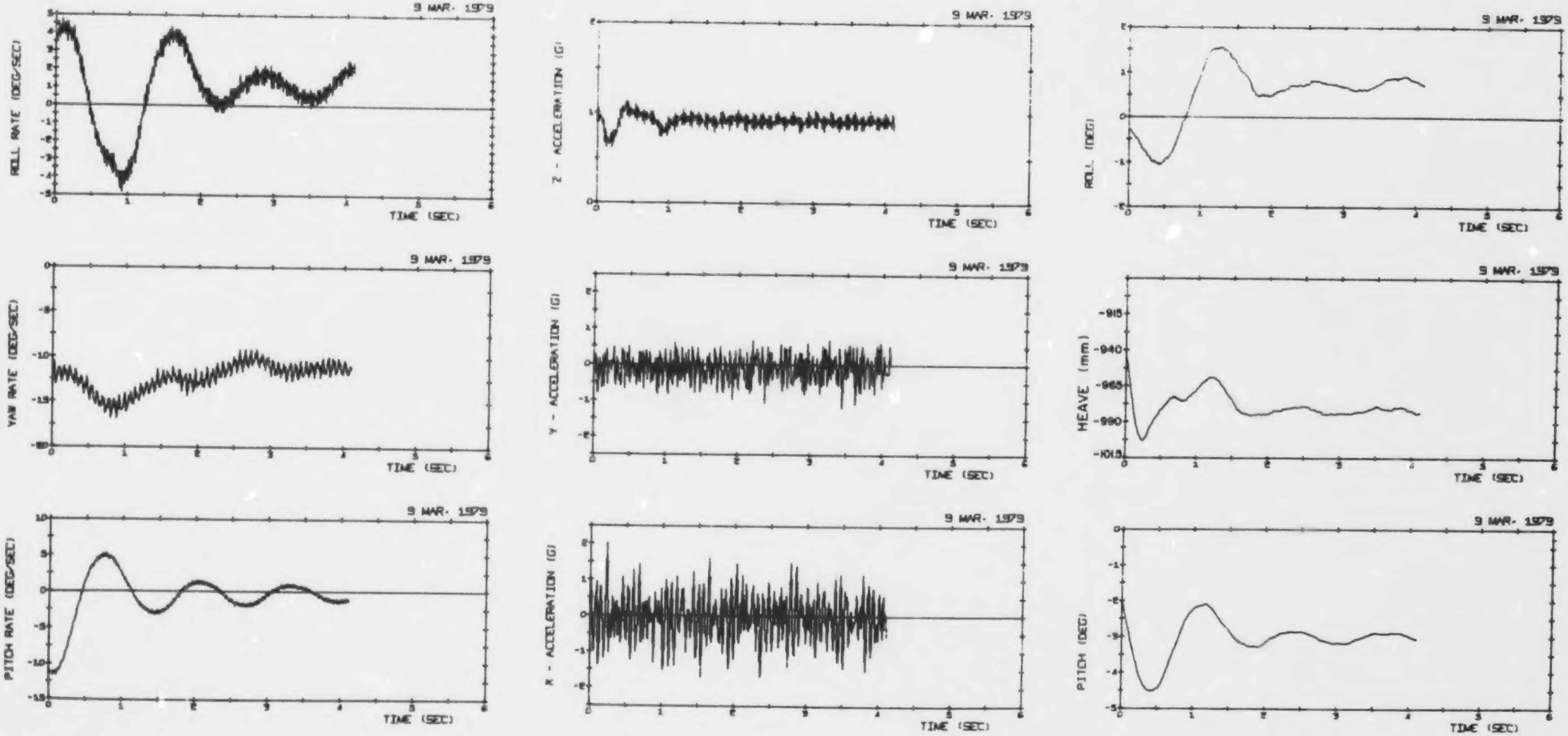

FIG. 4.15 VEHICLE RESPONSE TO RAMP DISTURBANCE – TIME HISTORIES FROM POINT WHERE LAST TRAILING ARM HAS LEFT RAMP.

number of parameters being estimated and the existence of local minima. Attempts were made to achieve results by uncoupling the pitch from the heave dynamics to achieve a global minimum position as the starting point for iterations on the coupled system. Other parameters were estimated from the steady state data and from theoretical considerations. The development of the theoretical estimates, based on simpler models than those presented in section 3 of this report, is given in section 3.4 of [4.2]. The results are presented here in table 1.

Time histories of SPI predicted vehicle motion and measured vehicle motion are shown in figure 4.16. Good agreement is obtained in the pitch and pitch rate curves, and the trends shown in heave are predicted.

4.5) Correlation of Dynamic and Static Measurements

4.5.1) Estimation of Dynamic Coefficients from Static Data

A test of consistency for the dynamic and static models is in the comparison of various parameter values obtained by the two tests. Since the dynamic data was determined at a fan speed of 2200 RPM and a vehicle weight of 6895N, the static data for this fan speed can be extrapolated to this weight and the following estimations made.

i) Damping coefficients ξ_h and ξ_θ:

In the linearized model of an ACV which is derived in section 4.3, the damping effects from all the possible sources were lumped together in the viscous damping coefficients ξ_h and ξ_θ, respectively. However, it is expected that the major source of damping will be the hysteresis in both the pitching and heaving modes, in which case the damping will be proportional to the amplitude of displacement rather than proportional to the velocity as assumed in the model equations. Since both types of damping result in a loss of energy, it is possible to estimate a viscous damping coefficient corresponding to the damping due to the hysteresis. Because the hysteresis damping is proportional to the displacement, the damping coefficient has to be estimated for a specific amplitude of motion. Also, due to the weak hysteresis in the heaving mode, only the damping coefficient in pitch was estimated.

The work done by torque is given by

$$E = \int_{\theta_1}^{\theta_2} \tau d\theta \qquad (45)$$

and the torque τ is related to the pitching moment arm function $\bar{g}_{13}(\bar{h},\theta)$ by

$$\tau = WL\bar{g}_{13}(\bar{h},\theta) \qquad (46)$$

So,

$$E = WL\int \bar{g}_{13}(\bar{h},\theta)d\theta \qquad (47)$$

If the vehicle undergoes one pitch cycle from θ_1 to θ_2 and back to θ_1, the work done by the torque τ is:

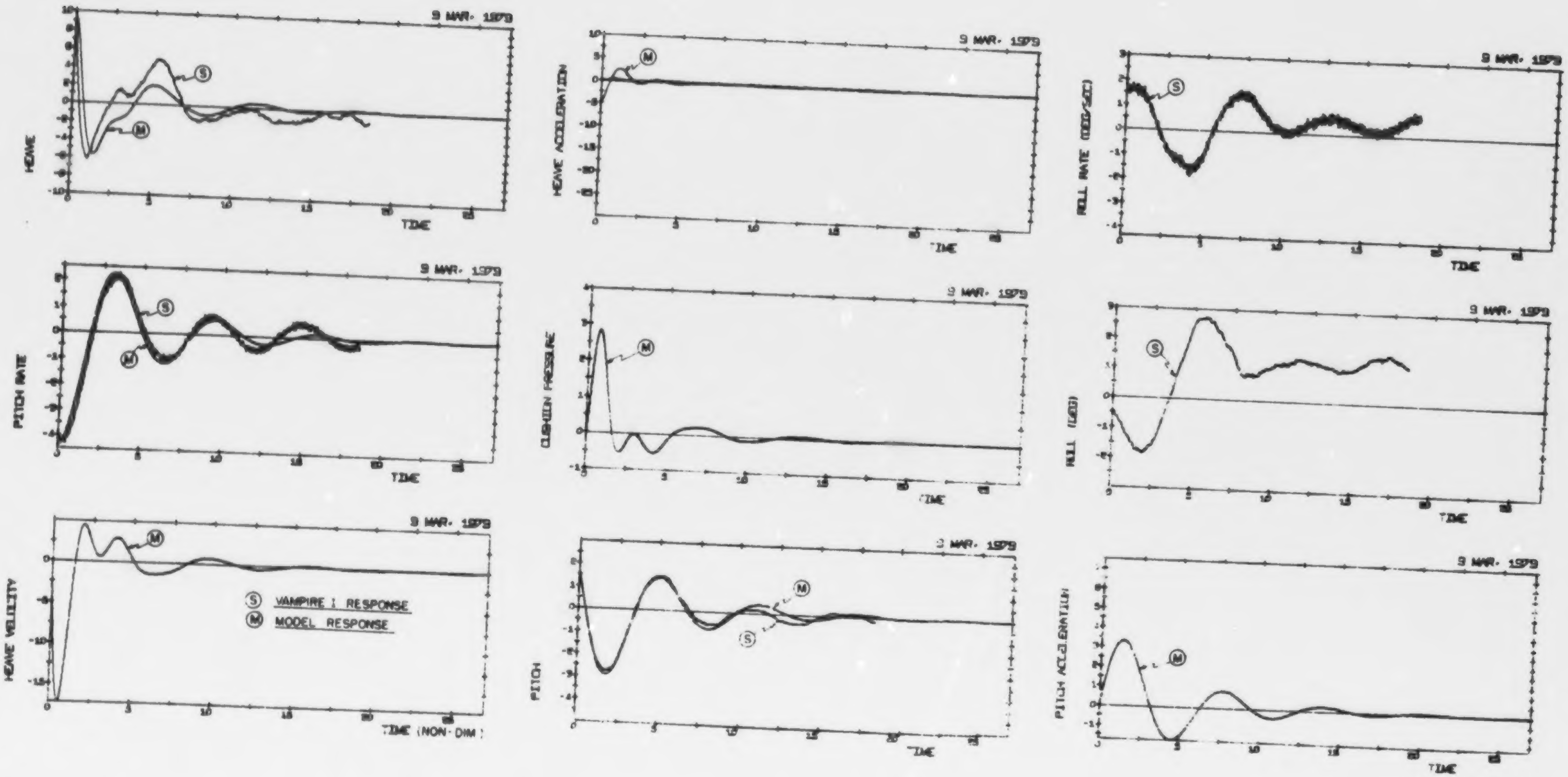

FIG. 4.16 COMPARISON OF SPI PREDICTED RESPONSE AND MEASURED VEHICLE RESPONSE.

$$E = WL\left\{\int_{\theta_1}^{\theta_2} \bar{g}_{13}d\theta - \int_{\theta_2}^{\theta_1} \bar{g}_{13}d\theta\right\} \tag{48}$$

The difference of the two integrals is the hysteresis loop area bounded by the pitch angles θ_1 and θ_2. Defining this area as

$$A_L = \int_{\theta_1}^{\theta_2} \bar{g}_{13}d\theta - \int_{\theta_2}^{\theta_1} g_{13}d\theta \approx \Theta\Delta\, C_{mp} \tag{49}$$

where

Θ = amplitude of the pitching oscillations

ΔC_{mp} = vertical distance between the two parallel sides of the hysteresis loop.

Hence

$$E = WLA_L \tag{50}$$

which is the system energy lost due to the hysteresis in one pitch cycle.

From the system eqns. (3.125) the pitch equation is (assuming $\frac{d\bar{g}_{13}}{2\bar{n}} = 0$)

$$WL(\bar{I}\ddot{\theta} + \bar{\xi}_\theta\dot{\theta} - \bar{g}_{13\theta}\theta) = 0 \tag{51}$$

In the above equation all three terms have dimensions of torque, however, only the second term is non-conservative, i.e. only the $\bar{\xi}_\theta\dot{\theta}$ term is associated with the system energy loss.

Assuming

$$\theta = \Theta \sin\omega t \tag{52}$$

the torque due to the viscous damping is

$$\tau = WL\bar{\xi}_\theta\dot{\theta} = WL\bar{\xi}_\theta\omega\Theta\cos\omega t \tag{53}$$

and the work done by this torque

$$dE = WL\bar{\xi}_\theta\dot{\theta}d\theta = WL\bar{\xi}_\theta\omega^2\cdot\Theta^2\cos^2\omega t\ dt \tag{54}$$

Thus the energy lost in one pitch cycle due to the viscous damping

$$E = WL\bar{\xi}_\theta\omega^2\cdot\Theta^2\int_0^T \cos^2\omega t\ dt \tag{55}$$

$$E = WL\bar{\xi}_\theta\omega^2\ \Theta^2\pi \tag{56}$$

On comparing the two expressions for energy lost in one pitch cycle we get

$$WLA_L = WL\bar{\xi}_\theta\omega^2\ \Theta^2\pi \tag{57}$$

$$\bar{\xi}_\theta = \frac{A_L}{\omega^2\ \Theta^2\pi} = \frac{2\Delta C_{mp}}{\omega^2\ \Theta\pi} \tag{58}$$

The amplitude of pitching oscillations in the first period of data used for SPI estimation measured response is approximately 0.78° and the period $T = 5.8$ (non-dim.), i.e. $\omega \approx 1.1$. From the static plots of pitching moments $\Delta C_{mp} \approx 0.0075$. Thus $\bar{\xi}_\theta \approx 0.192$ and the matrix coefficient $\bar{\xi}_\theta/\bar{I} = 0.214$.

The viscous damping is proportional to the square of the oscillation amplitude and the hysteretic damping is proportional to the amplitude. Thus if the amplitude of the oscillation were smaller and the major component of the damping was hysteretic, with a loop width independent of amplitude, a larger equivalent viscous coefficient would be estimated. For this case the estimates given above would represent a lower bound on the SPI estimate, since the amplitude chosen was that of the first oscillation after the ramp disturbance and the other data used for estimation was at the ensuing smaller amplitudes. If, instead, the average amplitude of the data used for SPI estimation is obtained from the pitch trace in figure 4.15, the values for $\bar{\xi}_\theta$ and $\bar{\xi}_\theta/\bar{I}$ become 0.422 and 0.470 respectively.

ii) Pitch Stiffness Coefficient, $\bar{g}_{13\theta}/\bar{I}$

From the static pitching moment curves for a fan speed of 2200RPM we have

$$\frac{d}{d\theta}(\bar{g}13(\bar{h},\theta) \approx \frac{\Delta\bar{g}13(\bar{h},\theta)}{\Delta\theta} \tag{59}$$

$$\bar{g}13_\theta \approx 0.83$$

so that the matrix coefficient

$$\bar{g}13_\theta/\bar{I} \approx 0.893$$

iii) Heave Stiffness Coefficient, $\bar{g}\frac{\partial}{\partial\bar{h}}\bar{a}_f$

From the nondimensional definitions

$$\bar{g}\frac{\partial\bar{a}_f}{\partial\bar{h}} = \frac{L^2\rho_a}{w}g\frac{\partial}{\partial h}\left(\frac{w}{P_{ce}}\right) \tag{60}$$

The static data at 2200 RPM and $\theta = 0$ are:

$w_1 = 8255N$, $P_{ce1} = 1435$ Pa, $h_1 = 0.854$ m

$w_2 = 7697N$, $P_{ce2} = 1365$ Pa, $h_2 = 0.857$ m

enabling the estimation of

$$\frac{\partial}{\partial h}(w/P_{ce}) \approx \frac{\Delta(w/P_{ce})}{\Delta h} \approx -37.93\,\frac{m^2}{m} \tag{61}$$

$$\bar{g}\frac{\partial\bar{a}_f}{\partial\bar{h}} = \underline{\underline{-1.10}}$$

iv) Heave Stiffness from Pitch Coefficient, $\frac{\bar{g}}{\bar{h}_e}\frac{\partial\bar{a}_f}{\partial\theta}$

From the nondimensional definitions

$$\frac{\bar{g}}{\bar{h}_e}\frac{\partial \bar{a}_f}{\partial\theta} = \left(\frac{L^4\rho_a}{w}\right)\left(\frac{g}{h_e}\right)\frac{\partial}{\partial\theta}a_f \qquad (62)$$

where a_f is determined from

$$a_f = \frac{w}{P_{ce}} \qquad (63)$$

The function $P_{ce} = f(\theta)$ is determined by a least squares fit to the pressure data at the minimum weight measured, and gives

$$w\frac{\partial}{\partial\theta}\frac{1}{P_{ce}} = 1.103$$

so that $\dfrac{\bar{g}}{\bar{h}_e}\dfrac{\partial}{\partial\theta}\bar{a}_f = 0.033$

From the symmetry of the cushion, the foot print area will also be symmetric about zero angle. The derivative $\bar{a}_{f\theta}$ would then be zero. The existence of a non-zero value for this term is probably due to a slight offset in the vehicle trim during the static tests or the coupling of leave motion with the pitch.

v) Pitch Stiffness from Heave Coefficient, $\left\{\frac{\bar{h}}{\bar{I}}\right\}_e \frac{\partial g_{13}}{\partial \bar{h}}$

Static measurements were not taken to determine this coefficient since at $\theta = 0$, $g_{12} = 0$ and the skirt footprint area is symmetrical. This coefficient would be expected to be small, since contributions could come only from structural differences in the skirt fore and aft.

vi) $-\left\{\frac{\bar{h}}{\bar{C}_c\bar{P}_c{}^2}\right\}_e$

At equilibrium with a fan speed of 2200 RPM, extrapolation to a vehicle weight of 6895N gives P_{ce} = 1263 Pa, so that

$$\bar{P}_{ce}{}^2 = 9.298$$

As before $\bar{h}_e = 0.241$ and

$$\bar{C}_c = \frac{W}{L^5}\frac{V_{ce}}{\rho A^2} = \frac{W\,V_{ce}}{L^5\gamma(P_{ce}+P_{atm})} \qquad (64)$$

where V_{ce} is determined from the skirt vehicle geometry, P_{atm} = atmospheric pressure and γ is the ratio of specific heats for air.

$$\bar{C}_c = 0.000186$$

so that

$$-\left\{\frac{\bar{h}}{\bar{C}_c\bar{P}_c{}^2}\right\}_e = -139.4$$

vii) Air Escape Area Coefficient for Heave, $\left\{\frac{\bar{h}}{\bar{C}_p}\,\frac{\partial \bar{a}_e}{\partial \bar{h}}\right\}_e$

Using the mass flow data as follows

$h_1 = 0.854\text{m}, \qquad \bar{m}_1 = 0.00430, \qquad P_{ce} = 1435 \text{ Pa}$

$h_2 = 0.857\text{m}, \qquad \bar{m}_2 = 0.00466, \qquad P_{ce} = 1365 \text{ Pa}$

and approximating $\bar{a}_{e\bar{h}}\big|_e$ as

$$\frac{\Delta \bar{a}_e}{\Delta \bar{h}} = \frac{L}{\sqrt{2}C_D}\left(\frac{\bar{m}_2}{\sqrt{P_{c2}}} - \frac{\bar{m}_1}{\sqrt{P_{c1}}}\right) \tag{65}$$

If a value of 0.62 is assumed for C_D then $\frac{\partial a_e}{\partial \bar{h}} \simeq 0.268$

$\bar{C}_p$ is given by

$$\bar{C}_p = \frac{\bar{C}_c\sqrt{P_{ce}}}{\sqrt{2}\;C_D} \tag{66}$$

which for the vehicle equilibrium pressure of 1263 Pa is

$$\bar{C}_p = 0.000370$$

and the coefficient

$$-\left\{\frac{\bar{h}}{\bar{C}_p}\,\frac{\partial a_e}{\partial \bar{h}}\right\}_e \simeq -174.6$$

viii) Air Escape Coefficient for Pitch, $-\frac{I}{\bar{C}}\frac{\partial a_e}{\partial \theta}$

Examination of the air mass flow rate plots for pitch angle variation shows that a minimum is reached at $\theta = 0$. Since the equilibrium cushion pressure is determined from $W = a_f P_c$, and since it is previously shown that $W\frac{\partial}{\partial\theta}(1/P_c) \neq 0$, the variation of air escape area with pitch

$$\left\{\frac{\partial a_e}{\partial \theta}\right\}_e = 0 \quad .$$

This parameter is then estimated as zero.

ix) $\frac{\bar{q}_{ce}}{\bar{C}_c \bar{P}_{ce}}\left(\frac{1}{\bar{C}_{sc}} - \frac{1}{2}\right)$

The cushion flow at equilibrium is obtained by extrapolating the data for different weights at $\theta = 0$ to the vehicle weight of 6895N.

$$\bar{q}_{ce} = \bar{m}_{ce} = 0.00517$$

The far slope coefficient may be estimated from the slope of the fan calibration at 2200 RPM or from the mass flow data at $\theta = 0$. Noting that $\tilde{p} = \bar{C}_{sc}\,\tilde{q}_f$ where $\tilde{p}$ and $\tilde{q}_f$ are small changes

$$\bar{C}_{sc} = \frac{\Delta\bar{P}_{ce}}{\Delta\bar{q}_{fe}} = \frac{\Delta\bar{P}_{ce}}{\Delta\bar{q}_{ce}} \qquad (67)$$

$$= \frac{4.08^2\ (1365-1435)}{6895(0.00466-0.00430)}$$

$$= -469.4$$

Thus

$$\frac{\bar{q}_{ce}}{\bar{C}_c \bar{P}_{ce}}\left(\frac{1}{\bar{C}_{sc}} - \frac{1}{2}\right) = -4.58$$

4.5.2) Discussion of Dynamic and Static Results

The estimates of the unknown parameters in the system matric $\underset{\sim}{A}$ of equation 37 obtained from both the static and dynamic experiments, as well as from the geometry of the vehicle, are summarized in Table 4.1. The relatively large degree of uncertainty in the parameter estimates, as indicated by the spread of the estimated values, is due to several factors; these are briefly discussed below.

i) Static Experimental Factors

Because of the method employed in the static experiments, in which steel plates were used to vary the pitching moment, the results were obtained at a weight anywhere between 12% and 20% higher than the vehicle weight during the dynamic experiments. As a consequence, errors were introduced into the parameter estimates by the extrapolation of data to lower vehicle weights. One exception appears to be the estimate of the pitching moment stiffness function $\bar{g}_{12}$ (equivalent to the nondimensional pitching moment coefficient $\bar{C}_m$ used in the previous reports), or rather its derivative $\partial\bar{g}_{12}/\partial\theta$ which is the slope of the hysteresis loop. As shown in the static data plots, the pitching moment hysteresis loop - its area as well as its slope - is independent of the weight, which also implies independence on the heave height. Hence, the

TABLE 4.1

Table of Estimated and Calculated Parameters

Matrix Element	Parameter	Static Experiment	SPI	Notes
a_{11}	$-\bar{\xi}_h \bar{g}$	X	-0.636	Heave Damping
a_{13}	$\bar{a}_{fh} \bar{g}$	-1.10	-6.745	Heave Stiffness
a_{14}	$\bar{a}_{f\theta} \bar{g}/\bar{h}_e$	0.033	0.742	
a_{15}	$\bar{g}/\bar{h}_e$	0.494	0.037	
a_{22}	$-\bar{\xi}_\theta/\bar{I}$	-0.470	-0.423	Pitch Damping
a_{24}	$\bar{g}_{12\theta}/\bar{I}$	0.893	1.040	Pitch Stiffness
a_{51}	$-\bar{h}_e/(\bar{C}_c x \bar{P}_{ce}^2)$	-139.4	-179.9	
a_{53}	$-\bar{a}_{eh}/C_p$	-174.6	-30.0	
a_{54}	$-\bar{a}_{e\theta}/C_p$	0.0	- 3.2	
a_{55}	$\frac{\bar{q}_{ce}}{\bar{C}_c \bar{P}_{ce}} \left(\frac{1}{\bar{C}_{sc}} - \frac{1}{2}\right)$	- 4.58	-10.5	

$\bar{g}_{12\theta}/\bar{I}$ parameter estimate should not be affected by different vehicle weights in static and dynamic experiments. This is supported by a close agreement with the value of the same parameter obtained by the SPI method.

Also, the static estimates are all made from data about the 0^o pitch and 0^o roll angle equilibrium points. The data obtained from the dynamic experiment, however, indicates that the vehicle oscillations decayed to an equilibrium pitch angle of about -3^o and a roll angle of about 0.75^o. This means that parameters, such as the footprint area, the air escape area, and their derivatives, that were derived from static data would give poor estimates for the dynamic program coefficients.

ii) System Input and Measured Variables

The SPI program used for dynamic parameter identification is more suited to a controlled forced-input type of disturbance. This method of disturbance can provide longer time duration data than the decaying oscillations resulting from an initial conditions (IC) type of disturbance. In addition, significant improvements could be made by measuring more of the state variables. For example, the cushion pressure could be measured. Also, the heave velocity could be estimated from suitable integration of the heave acceleration, and/or, differentiation of the heave data.

iii) Non-linear System

The system is modelled as linear and it has been shown (section 3) that the footprint and flow area functions are highly non-linear in the range of pitch angles encountered in the dynamic experiments. These factors contribute to poor parameter estimation when these functions are part of the linear dynamic coefficients. Examination of Table 1 shows poor correlation between the static and dynamic estimates for most of these values.

The static pitching moment measurements show a hysteresis which is modelled as a viscous dissipation in the linear dynamic model. The limiting problems for this type of approximation have been described in section 4.5.1 i). Another factor is the increase in stiffness of the skirt material in the dynamic over the static case. It is known from section 3 that the type of material chosen has a large effect on the amount of hysteresis in the pitch stiffness measurements. Since the skirt undergoes bending and buckling during the pitch down cycle and a removal of the associated moment forces during the return to equilibrium, it is reasonable to assume that the magnitude of the forces generated is proportional to the bending stiffness of the material. Thus, one might expect larger hysteresis in the dynamic case than in the static. In view of these problems the agreement obtained between the static and dynamic estimates of pitch damping factor is quite good.

iv) Gyroscopic Effects

During the dynamic experiments, it was observed that a significant roll was induced by the ramp disturbance. After all possible sources of this roll, such as yaw of the vehicle or the tether suspension not being located at the CG, were checked, the order of magnitude of the gyroscopic effects was evaluated as follows. If the lift fan is modelled by a solid, 10mm thick aluminum disk of the same diameter, which is conservative (lower), considering the high solidity ratio of the fan plus inertia of all the flanges, shaft, etc., and if the roll moment of inertia of the vehicle is estimated on the assumption of a uniform mass distribution which is very conservative (higher) because most of the vehicle mass is concentrated close to the centre line, we may estimate the amount of precession induced roll:

The fan's moment of inertia

$$I_F \approx \frac{1}{2} M_F R^2 = \underline{\pi R^4 \rho t} \qquad (68)$$

where $R = 0.37\mathrm{m}^3$= fan radius

$\rho = 2710\mathrm{kg/m}$ = specific weight of aluminium

$t = 10\mathrm{mm}$ = thickness of the disk

The moment of inertia of the vehicle in roll

$$I_v \doteq \frac{1}{12} M_v b^2 \qquad (69)$$

where $M_v = 703$ kg = mass of the vehicle

$b = 2.057\mathrm{m}$ = width of the vehicle

If the disk rotates at $\omega_F = \frac{RPM}{60} 2\pi$ rad/sec, the precession torque due to the pitch rate $\dot\theta$ is

$$\tau = \dot\theta I_F \omega_F \qquad (70)$$

Assuming the vehicle is freely suspended, i.e. neglecting the skirt damping and stiffness, the precession torque τ induced roll would be given by

$$\tau = I_v \ddot\Phi \qquad (71)$$

where $\ddot\Phi$ is the angular acceleration in roll.

The maximum measured amplitude of the pitch rate was approximately 12 deg/sec, and the corresponding roll rate was approximately 4 deg/sec at a frequency of slightly less than 1 Hz. Thus assuming the pitch rate to be

$$\dot\theta = -12 \sin \omega t \qquad (72)$$

and substituting the appropriate numerical values we obtain

$$\ddot\Phi_{max} = \frac{I_F}{I_v} \omega_F \theta = -8.89 \text{ deg/sec}^2 \qquad (73)$$

Assuming $f \approx 0.8$ Hz, i.e. $\omega_p = 5.03$ rad/sec, we get

$$\ddot\Phi = -A\omega_p^2 \sin \omega_p t = -8.89 \sin \omega_p t \quad (\text{deg/sec}^2) \qquad (74)$$

$$\dot\Phi = +A\omega_p \cos \omega_p t = -1.76 \cos \omega_p t \quad (\text{deg/sec}) \qquad (75)$$

$$\Phi = +A \sin \omega_p t = 0.35 \sin \omega_p t \quad (\text{deg})$$

which are of the same order as, and about ½ the value of the measured roll angle and roll rate. This indicates that the lift fan gyroscopic effect was most probably the major contributing factor causing the vehicle to roll and should be considered in the analysis of the ACV dynamics. A similar gyroscopic effect could be expected from the propeller, however, since the prop engine was stopped just before the vehicle reached the ramp, the small yaw variations seem to be the result of the induced roll and the differential skirt drag.

4.6) Conclusions

The static and dynamic pitch-heave characteristics of a segmented skirt on the VAMPIRE I vehicle have been examined experimentally. In the dynamic case a linear dynamic model was used to aid in the understanding and interpreting of the data as fitted through the use of the SPI program. Attempts to correlate the results of the static and dynamic experiments have only been moderately successful, however, the notable exceptions of the pitch damping and stiffness. A number of problem areas have been identified as possible causes for the discrepancies. These include the small number of parameters measured for input to the SPI program, the use of an IC type of disturbance, and the non-linearities present in the system area functions and damping mechanisms. Other possible causes are the non-zero pitch and roll equilibrium positions found in the dynamic case, the higher weights used in the static case with the resulting extrapolation error, and interaction of pitch and roll motions through gyroscopic action resulting from the lift fan.

The static measurements have confirmed the presence of significant hysteresis in the pitch stiffness characteristic. This corresponds to hysteresis observed with similar skirt systems in the dynamics lab showing that the former are not rig effects. Hysteresis was also found in other vehicle characteristics although it is less well defined.

The results presented for the VAMPIRE I vehicle represent an important step towards the understanding of ACV dynamics. Many questions have arisen regarding the importance of the factors mentioned earlier and several have been checked through order of magnitude type estimates. For the others, a systematic investigation is necessary to determine their importance.

5) BUCKLING OF SKIRT MATERIAL

5.1) Introduction

5.1.1) Preamble

One important requirement for the successful operation of an air cushion vehicle (ACV) is the structural stability of the particular flexible skirt system used. The stability requirement is important, because if, while a vehicle is in forward motion, a series of cells or segments collapse due to adverse loading conditions, the forward motion can be greatly reduced or stopped abruptly causing extensive damage due to hard structure contact with the ground.

The first skirt system to be studied at UTIAS was the tapered conical cell used on the basic Bertin/multicell cushion. Although this geometry is perhaps not particularly practical for Canadian applications, it provided a starting point for the study of the behaviour and stability of pressure stabilized flexible structures under loads typical of the ACV environment. When structural stability problems were encountered, it was noticed that extensive wrinkled regions may appear before final collapse of the cell. Wrinkled regions were also observed on other skirt systems such as the loop and segment system.

This behaviour suggested that we could use some wrinkling theory which was developed in the late 1950's and early 1960's to study large area low mass pressurized membrane structures for space applications. These included the analysis reported by Stein and Hedgepeth [Ref. 5.1] in 1961, and Jahsman [Ref. 5.5] in 1965 which established a suitable theory for ideal membranes. Good experimental verification was reported for some simple geometries and load cases.

A complete investigation of the buckling failure of the conical cells used in the multicell cushion requires (a) analysis of the stresses in the pre-wrinkling stage, (b) a suitable description of the wrinkling behaviour, and (c) application of an appropriate buckling criterion. Thus a rigorous description of the phenomenon is quite involved. The problem is made even more complex by the widespread use of elastomer-coated fabrics as skirt materials. These materials are not isotropic as their elastic properties depend on the local orientation of the weft and warp of the fabric. Another complication is that the wrinkled region varies in size over the length of the conical cell whereas in cylinders this is not so. Also, skirt-ground contact may induce a transverse shear load in the skirt segment causing secondary wrinkled regions. In addition, it may be shown that a small uniform shear load applied at the bottom of the conical cell drastically changes the wrinkling pattern.

Because of the above complications, it becomes evident that a complete solution to the conical cell problem and more complicated segmented skirts requires a numerical solution. The present report demonstrates that a numerical solution can be obtained for a cylinder with wrinkling. The approach is very general and should be applicable to the more complex conical case.

A thin pressurized cylinder subjected to an applied bending moment is considered. Isotropic, orthotropic and anisotropic materials cases are investigated. A 24 degree of freedom curvilinear finite element is developed to study the wrinkling behaviour. The analysis is more general than the Stein and Hedgepeth model, mainly because we do not discard the bending stiffness of the material and we do allow small compressive stresses before part of the cylinder wrinkles.

5.1.2) Definitions of Stability and Analytical Approaches

The investigation of the stability of equilibrium states or of motion must proceed with considerable care, since criteria for stability or instability depend on the problem under investigation. For the present problem there are three methods of approach [Ref. 5.10] that reflect these concepts. They are:

(i) The Adjacent Equilibrium Approach

This is the classical Euler method of analysis. A small deflection static analysis is used to determine the conditions for which additional equilibrium states exist, which are close (adjacent) to the original equilibrium state. The applied load which yields this multiplicity of equilibrium states is defined as the critical load. A large deflection analysis (nonlinear) in this case shows a "bifurcation" of equilibrium at the critical load (Figure 5.1). The magnitude of the deflection is undefined in the linear analysis, but is determinate in the nonlinear analysis.

(ii) The Nonadjacent Equilibrium Approach

A large deflection analysis is used to determine the critical load for which a nonadjacent equilibrium configuration may exist, which is not close to the original unbuckled equilibrium configuration. The mode of buckling in this case is commonly known as "snap-through buckling". At the critical load, the structure becomes unstable and a small disturbance causes the structure to jump to a nonadjacent (static) stable equilibrium configuration (Figure 5.2).

(iii) The Dynamic Approach

Instability in this case is a dynamic state of motion and is not a static equilibrium state. The original unbuckled configuration is the only equilibrium state, but at the critical load it is an unstable equilibrium configuration. At the critical load, a small disturbance causes the structure to assume a state of unbounded motion. A static equilibrium approach cannot detect this mode of instability, but a small deflection dynamic formulation can and does. A dynamic solution can also detect the static equilibrium states (i) and (ii) above. An example of this kind of a problem is a column with a "follower load", a load that remains tangent to the column at its point of application as the column deforms.

Once the critical load is reached, a small disturbance can cause the structure to jump to a new stable configuration, as in Figure 5.2, or continue to go unstable, as in Figure 5.3. If this is the case, we say that the structure has "collapsed" since it will not reach a new stable equilibrium.

In the Stein and Hedgepeth [Ref. 5.1] and finite element analysis the collapse load is approached asymptotically as the curvature approaches infinity. This is not physically viable. One could always define collapse when a small

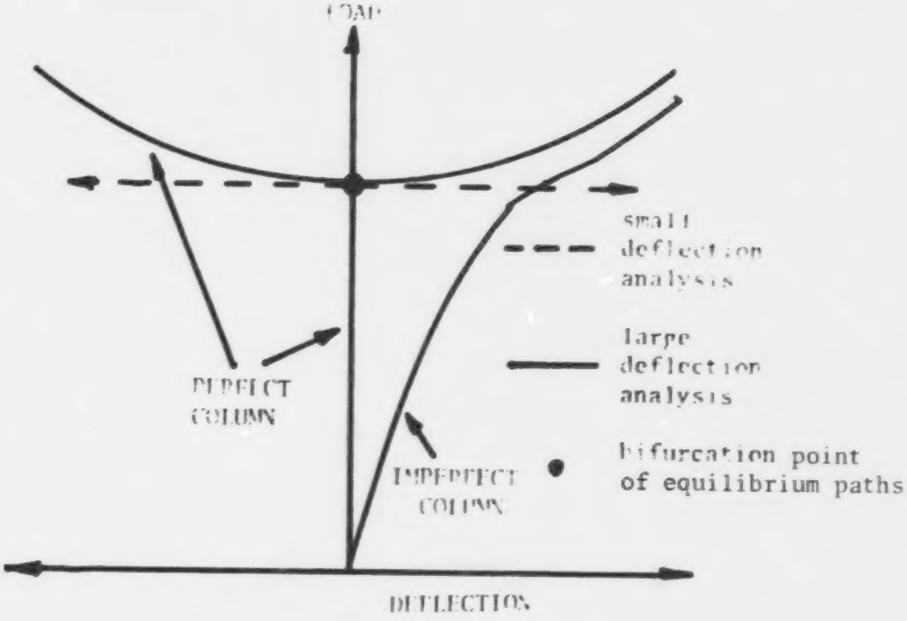

FIG. 5.1 ADJACENT EQUILIBRIUM BUCKLED STATE.

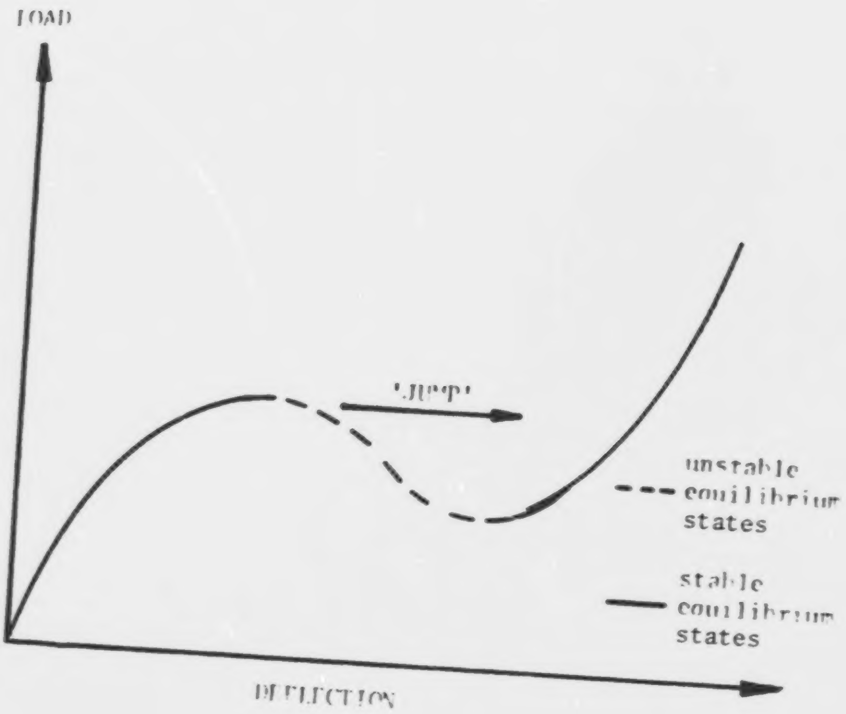

FIG. 5.2 NON-ADJACENT EQUILIBRIUM BUCKLED STATE.

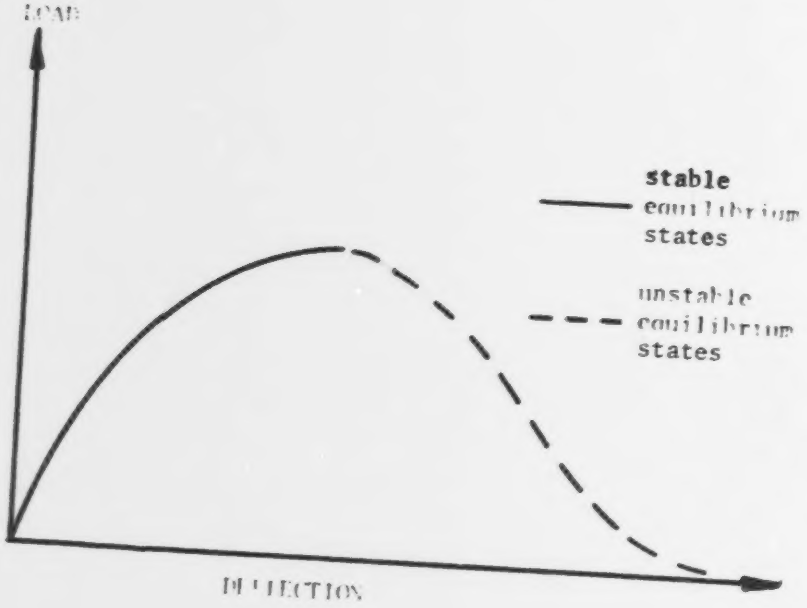

FIG. 5.3 COLLAPSE OF A STRUCTURE.

increase in the load causes a large increase in the curvature. If this definition is used, the collapse of the pressurized cylindrical membrane would occur when, approximately, over 66% of its circumference has wrinkled (Figure 5.5).

5.2) Previous Work

5.2.1) Historical Review of Wrinkling Theory

A theory for partially wrinkled membranes was developed in the early 1960's by Stein and Hedgepeth [Ref. 5.1] for light-weight inflatable space structures. The membrane was considered elastic, isotropic, had no bending stiffness and could carry little or no compressive stress. Therefore, when the stress became negative in a particular region wrinkling would occur.

The principal stresses for two-dimensional solids are

$$\sigma_1 = \frac{\sigma_x + \sigma_y}{2} + \sqrt{\left(\frac{\sigma_x - \sigma_y}{2}\right)^2 + \tau_{xy}^2} \qquad (1a)$$

$$\sigma_2 = \frac{\sigma_x + \sigma_y}{2} - \sqrt{\left(\frac{\sigma_x - \sigma_y}{2}\right)^2 + \tau_{xy}^2} \qquad (1b)$$

If the principal stresses are positive, the membrane is in tension and will not wrinkle. The transition from unwrinkled to wrinkled will occur when one principal stress becomes zero and the other is positive or both principal stresses become zero at a particular point in the domain.

The condition for a principal stress to vanish is, from equation (1b),

$$\sigma_x \sigma_y = \tau_{xy}^2; \qquad \sigma_x, \sigma_y \geq 0 \qquad (2)$$

This equation must hold at the boundary of a wrinkled region. The equations of equilibrium are:

$$\frac{\partial \sigma_x}{\partial x} + \frac{\partial \tau_{xy}}{\partial y} = 0 \qquad (3a)$$

$$\frac{\partial \sigma_y}{\partial y} + \frac{\partial \tau_{xy}}{\partial x} = 0 \qquad (3b)$$

which together with equation (2) constitute three equations in three unknowns. They permit the determination of the stresses on the boundary of a wrinkled region independent of strain compatibility. If no shear is present, equation (2) becomes

$$\sigma_x = 0 \qquad (\text{or } \sigma_y = 0) \qquad (4)$$

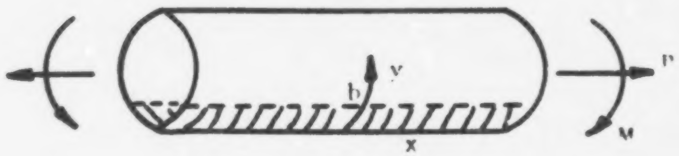

FIG. 5.4 LOADS FOR PRESSURIZED CYLINDER.

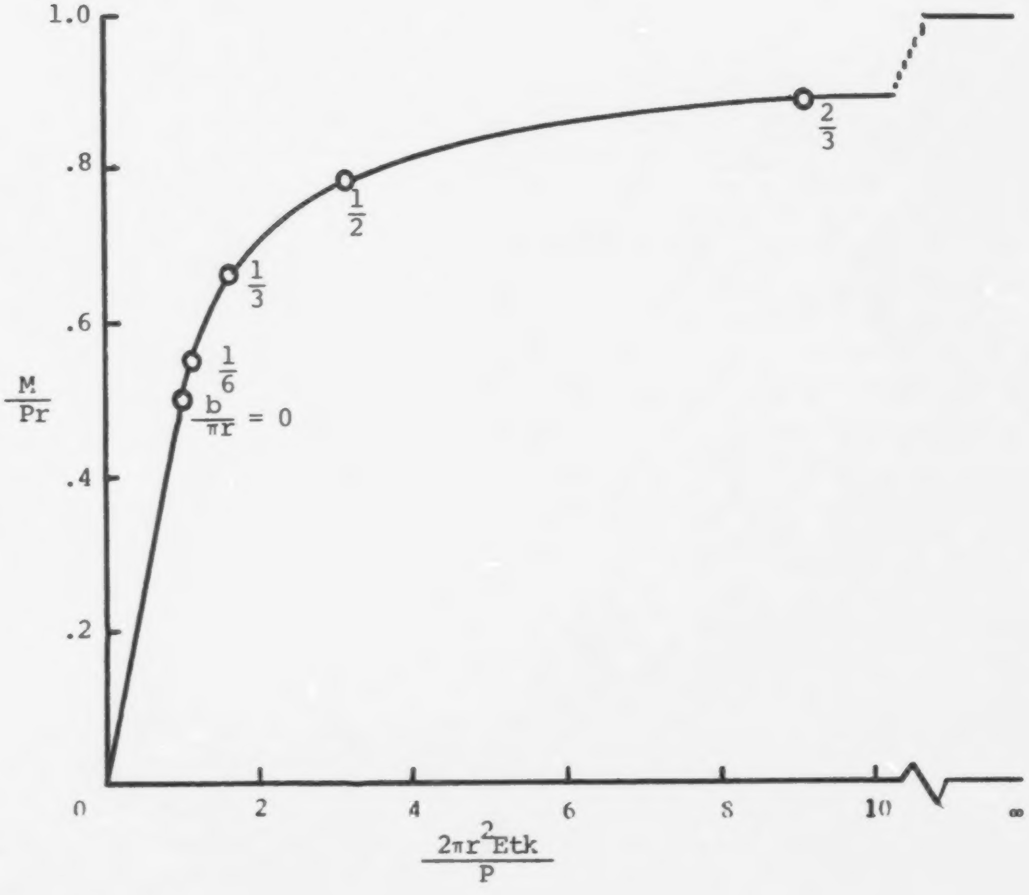

FIG. 5.5 MOMENT-CURVATURE RELATIONSHIP FOR THE BENDING OF A PRESSURIZED CYLINDER.

Stein and Hedgepeth developed the analysis for a pressurized membrane cylinder subjected to combined bending and axial loads shown in Figure 5.4. They determined the expressions for the applied axial load P (which has no moment about the neutral axis) and applied bending moment M in terms of the extent of the wrinkled region, b, and the curvature k as

$$P = 2Etr^2k \left[\sin\frac{b}{r} + \left(\pi - \frac{b}{r} \right) \cos\frac{b}{r} \right] \tag{5a}$$

$$M = Etr^2k \left[\pi - \frac{b}{r} + \frac{1}{2}\sin\frac{2b}{r} \right] \tag{5b}$$

where $P = p\pi r^2 - P_{ax}$. Their results were presented in the form of moment-curvature plots and are shown in Figure 5.5. The analysis of the membrane cylinder showed that: (i) For moments satisfying $M/Pr < 1/2$, the cylinder bends like an elastic beam and the response is linear. (ii) At $M/Pr = 1/2$ wrinkling begins along one generator of the cylinder and as the moment is increased further, the extent of the wrinkled region increases in a circumferential direction. (iii) The moment-curvature relationship becomes non-linear after wrinkling begins, and its slope (representing the bending stiffness of the cylinder) decreases as the moment increases. (iv) Only when the wrinkled region has progressed all the way around the cylinder does the slope become zero which (theoretically) implies a loss of stability (collapse). The collapse moment $M/Pr = 1$ is approached asymptotically. Notice that the theoretical collapse moment for this membrane cylinder is precisely twice the moment for the initiation of wrinkling.

In Figure 5.6 the extent of the wrinkled region is compared with the extent of the compression region in a cylindrical shell subject to the same loading assuming no wrinkling occurs. It is to be noted that, except for a small region near the wrinkled load, the extent of the regions are very different. That is, the membrane is completely wrinkled at its (finite) maximum moment, whereas the shell is in compression for only half its circumference as the moment approaches infinity.

McComb et al [Ref. 5.2] did experiments on a Mylar cylinder to verify the Stein and Hedgepeth theory. Since the theory of Stein and Hedgepeth assumed that moments due to externally applied axial load were negligible, McComb et al had to shorten the test specimens until such moments were negligible. Their results, for Mylar cylinders having length-radius ratio of about unity, 0.0762 m (3 in) radius and radius-to-thickness ratio of 6000 are shown in Figure 5.7. When McComb et al modified the Stein-Hedgepeth theory by assuming that over the wrinkled portion of the cylinder the skin could carry a small compressive stress normal to the wrinkles, the dash-dot curves shown in Figure 5.7 were obtained. These curves can be seen to agree well with the experimental results. The test results are above the solid curve due to bending stiffness (which was assumed nonexistent) and the curves show a dependence on the magnitude of the axial load.

Peery [Ref. 5.3] derived equations similar to those of Stein and Hedgepeth. However, he added a uniform critical wrinkling load N_c to the loading. In this case, the bending moment is resisted by a load that varies from zero at an angle θ to a maximum of N per unit length. As in the Stein

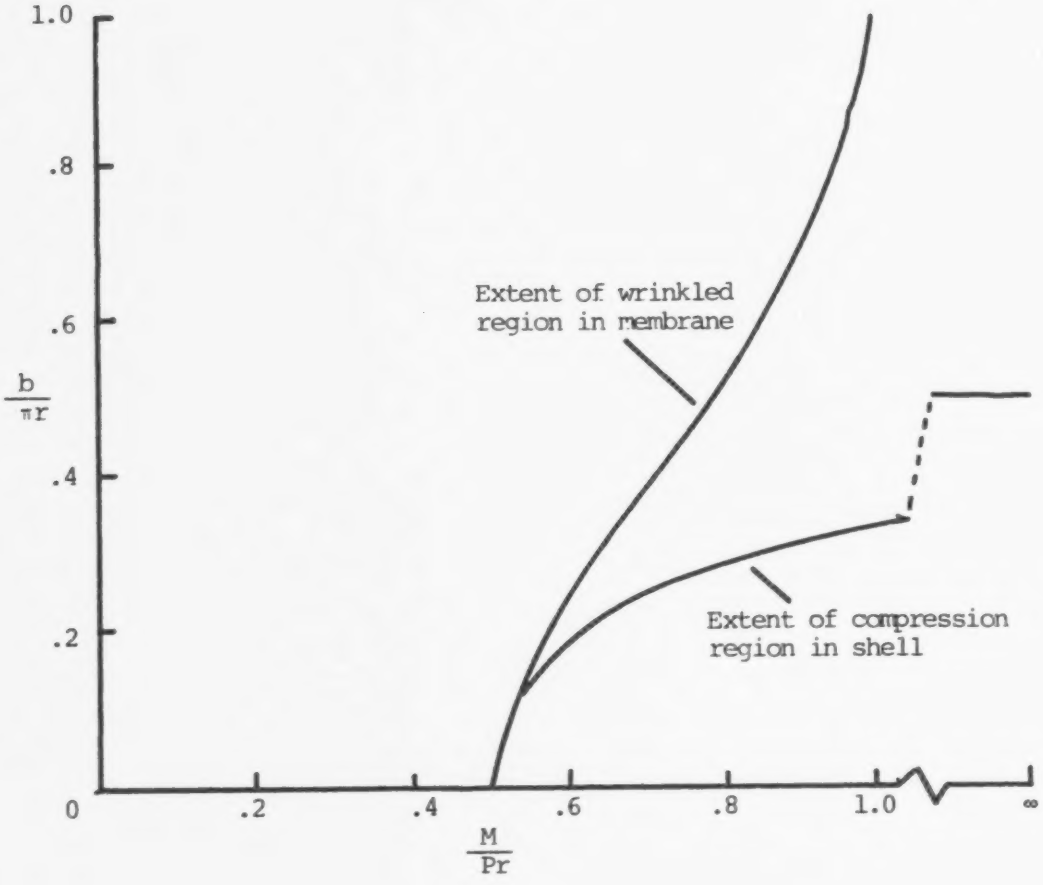

FIG. 5.6 COMPARISON OF WRINKLED REGION IN PRESSURIZED CYLINDRICAL MEMBRANE IN BENDING WITH COMPRESSION REGION IN CYLINDRICAL SHELL WITH SAME LOADING (REF. 5.2).

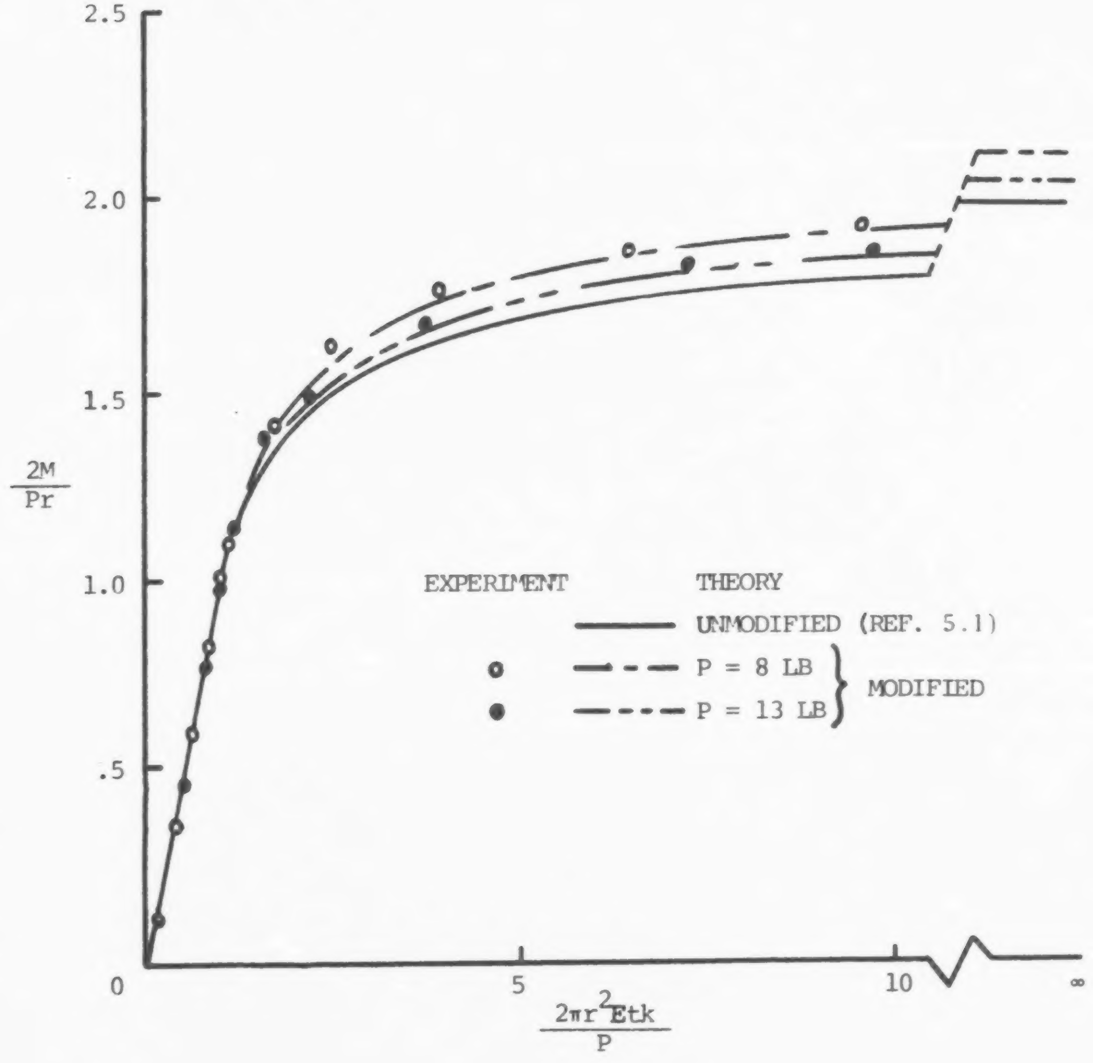

FIG. 5.7 MOMENT CURVATURE RELATIONSHIP FOR MYLAR CYLINDERS IN BENDING (REF. 5.2).

and Hedgepeth theory, the pressure, axial load and uniform load N_c have no moment about the neutral axis. The critical wrinkling load, N_c, was assumed to be that given by the classical theory for buckling of a thin wall unpressurized cylinder:

$$N_c = \frac{1}{\sqrt{3(1 - \nu^2)}} \left(\frac{Et^2}{r} \right) \tag{6a}$$

The total axial tensile load is now expressed as

$$P = p \, \pi \, r^2 - P_{AX} + 2\pi \, r \, N_c \tag{6b}$$

The effect of adding N_c, when $\nu = 0.3$, $N_c = 0.6Et^2/r$ which was used by McComb et al [Ref. 5.2], can be seen in Figure 5.7 as the dash-dot curves. The cylinder bends through an angle ϕ' per unit length given by

$$\phi' = \frac{N}{Etr(1 - \cos\theta)} \tag{7}$$

If this is substituted in the expressions for P and M obtained by Peery, we obtain expressions similar to those of Stein and Hedgepeth. For $N_c = 0$ the analysis is the same as Stein and Hedgepeth.

Jahsman [Ref. 5.5] modified Stein and Hedgepeth's analysis to take into account the bending due to the axial load P_{AX}. That is, the total moment is now given by

$$M = M_e + P_{AX} z \tag{8}$$

where z is the lateral deflection of the centreline of the cylinder from its undeformed position, Figure 5.8. Letting $\alpha = \pi - b/r)$ in equation (5), and dividing (5b) by (5a) yields

$$\bar{M} = \frac{2M}{Pr} = \frac{\alpha - \sin\alpha \cos\alpha}{\sin\alpha - \alpha\cos\alpha} \quad (0 \leq \alpha \leq \pi) \tag{9}$$

and from equation (5a)

$$\bar{k} = \frac{2\pi \, Er^2 \, tk}{P} = \begin{cases} \dfrac{\pi}{\sin\alpha - \alpha\cos\alpha}, & \begin{pmatrix} 0 \leq \alpha \leq \pi \\ 1 < \bar{M} \leq 2 \end{pmatrix} \\ \bar{M}, & \begin{pmatrix} \alpha = \pi \\ 0 \leq \bar{M} \leq 1 \end{pmatrix} \end{cases} \tag{10}$$

where, as before,

$$P = p \, \pi \, r^2 - P_{AX} \geq 0 \tag{11}$$

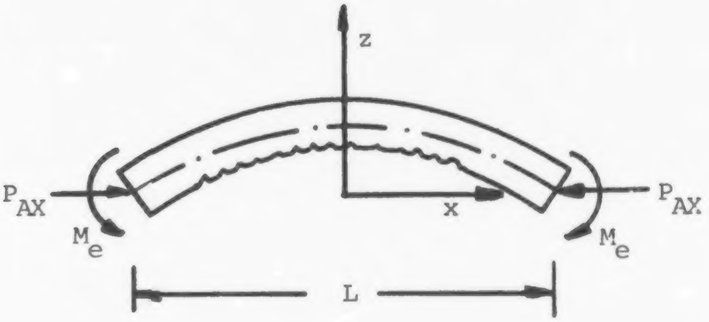
z
P_{AX}
P_{AX}
x
M_e
M_e
L

FIG. 5.8 LOADS AND DEFORMATIONS FOR PRESSURIZED CYLINDER.

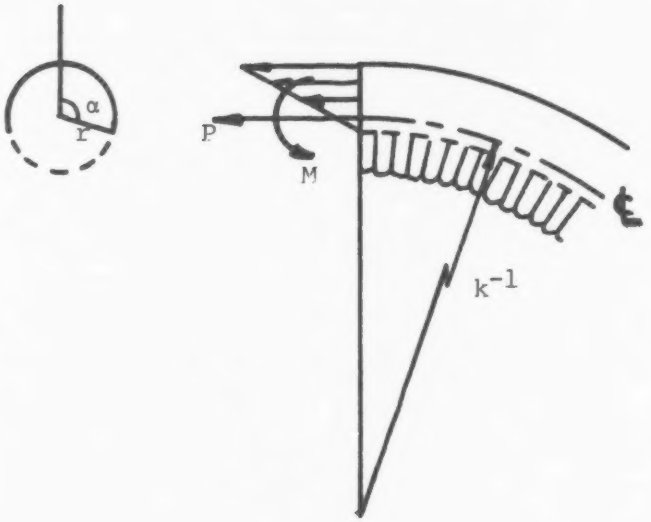

FIG. 5.9 CURVATURE AND LONGITUDINAL STRESS DISTRIBUTION IN CYLINDER.

See Figure 5.9. Equations (9) and (10) were derived originally for constant M, but also holds when M varies along the cylinder. The curvature is related to z through the usual small-deflection formula

$$k = -\frac{d^2z}{dx^2} \tag{12}$$

Equations (8) and (12) may be combined with equation (10) to yield

$$\frac{d^2\bar{M}}{d\bar{x}^2} = -\bar{k} \tag{13}$$

where

$$\bar{x} = \pi \bar{P}_{AX}^{1/2} \frac{x}{L}, \qquad \bar{P}_{AX} = \frac{P_{AX}}{P_E}, \qquad P_E = \frac{\pi^3 E r^3 t}{L^2}$$

and P_E is the Euler load. For a simply supported cylinder, the boundary conditions are, zero slope at midlength and zero deflection at the end. With these boundary conditions and equation (13) together with equations (9) and (10), the problem is completely defined.

His analysis breaks down into three phases:

(1) No wrinkling, i.e., smooth cylinder,

(2) wrinkles appearing along part of its length, and

(3) when wrinkles appear over the entire length of the cylinder.

His results were presented in the form of load-deflection curves at the midlength of the cylinder. The deflection $\bar{z}_D$ is a function of $\bar{P}_{AX}$, $\bar{M}_e$ and $\bar{p}$, where $\bar{P}_{AX}$, $\bar{M}_e$ and $\bar{p}$ are dimensionless axial compressive load, end moment equation (9) and internal pressure $[\bar{p} = (p\pi r^2/P_E)]$ respectively; $\bar{z}_o$ is obtained by an iterative procedure depending on the extent of wrinkling. The ratio $[(z_o 8\pi^2/\bar{p}\,\bar{M}_e)]$ is chosen for the abscissa so that all curves begin at unity when $\bar{P}_{AX} = 0$, see Figure 5.10. As the load is increased from zero, the deflection increases according to the beam-column formula until wrinkling begins at the midlength of the column. At this point, the curve departs from the beam-column curve which continues to increase toward $\bar{P}_{AX} = 1$. The departing curve rises slightly but reaches a maximum value of $\bar{P}_{AX}$ rapidly. After this point is reached, the curves fall slowly toward $\bar{P}_{AX} = 0$ as $\bar{z}_o \to \infty$. Jahsman noted that at point D in Figure 5.10 for $\bar{M}_e = 0.338$, most of the column is straight and a pronounced kink has started to develop at the centre.

Leaumont [Ref. 5.6] did combined compression and bending experiments with cylinders made of thin polyester film of constant length-to-radius ratio of 3 and radius-to-thickness ratios of 3000, 6000 and 12000. He also varied the pressure for each series of tests. With constant axial force, the bending moment was increased from zero in small increments until the deflection would not stabilize but continued to grow without application of additional bending moment. This point was defined as collapse. He noted that for cylinders of greater length-to-radius ratio than those tested, one would expect the column bending effect mentioned by Jahsman [Ref. 5.5]. He also noted that deep

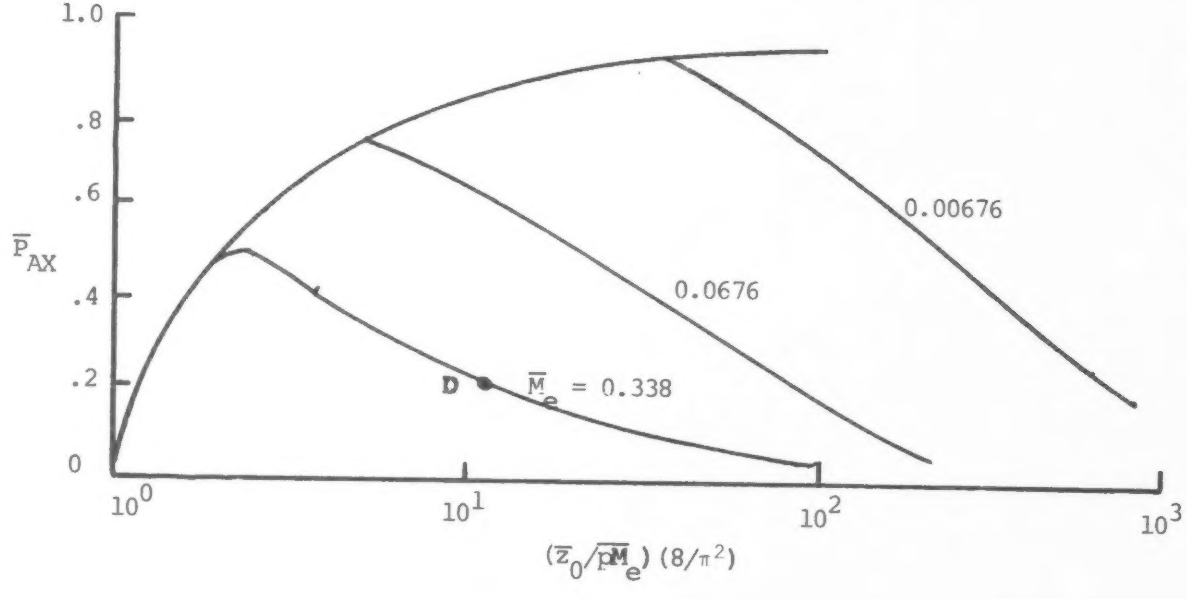

FIG. 5.10 LOAD-DEFLECTION CURVE FOR $\bar{p}$ = 1.20 (REF. 5.5).

wrinkling encompassing approximately 75% of the circumference and centreline deflections approaching 0.0127m (0.5 in) were not uncommon before collapse occurred.

Miller [Ref. 5.7] conducted three bending-strength tests on a full-scale production-type Atlas booster to satisfy three general objectives: (1) to verify the existence of post-wrinkling bending strength as indicated by theory and model tests, (2) to determine the bending capability of the basic tank structure, and (3) to establish a bending envelope for the entire Atlas booster. Only the third case will be discussed in this report.

A constant bending moment was induced over the entire length of the tank by differential loading of two longitudinal cables. The tank pressure was set at the flight pressure of 196,000 Pa gauge (28.5 psig), and the axial load was maintained at the simulated flight axial load of 559,000 N (126,000 lbs). The tank had a diameter of 3.042m (120 in). A moment in excess of 1.02×10^6 m-N (9×10^6 in-lbs) was placed over the entire Atlas. Figure 5.11 shows the load distribution around the tank circumference at about 1/5 of the length of the Atlas vehicle. As the moment was increased from 0.71×10^6 to 0.78×10^6 m-N (6.3×10^6 to 6.9×10^6 in-lbs) wrinkling of the skin began; this is indicated by the flat portions of each load curve in Figure 5.11. The length of the flat portion describes the extent of wrinkling around the circumference. The curves indicate that the wrinkle angle progresses from about 52° at 0.78×10^6 m-N (6.9×10^6 in-lbs) to 152° at 1.085×10^6 m-N (9.6×10^6 in-lbs). The predicted curves in Figure 5.11 are from Peery [Ref. 5.3]. As can be seen there is good agreement with experimental results.

Peery also derived an effective moment of inertia as a function of the extent of skin wrinkling. The expression is

$$I_{eff} = tr^3(\theta - \sin\theta \cos\theta)$$

where θ is the angle encompassing the tensile region. That is, when wrinkling first occurs ($\theta = \pi$), $I_{eff} = tr^3\pi$. This equation for moment of inertia can be used for deflection computations for pressure stabilized vehicles in the nonlinear (wrinkled) range.

Webb [Ref. 5.8] conducted theoretical and experimental studies of inflated "mattress" type beams with nonlinear material properties. His analysis assumed that the strain distribution across the beam cross-section was linear, the stress-strain law of the material was specified by a cubic relationship and wrinkling of the material occurred when a compressive stress existed. His theory predicted initial wrinkling of the cylinder when M/Pr = 0.6589 whereas the linear stress-strain law of Stein and Hedgepeth [Ref. 5.1] produced initial wrinkling when $M/P_r = 0.5$ which is half the collapse moment. Thus it appears that the onset of wrinkling may be delayed if a nonlinear stress-strain material is being used.

Mikulas [Ref. 5.9] gave a generalization of Stein and Hedgepeth's results [Ref. 5.1] for the rotation of a hub attached to a finite, stretched, circular membrane. In his case, the membrane was stretched by a uniform stress T, and the attached hub was rotated through an angle ϕ, by a torque M.

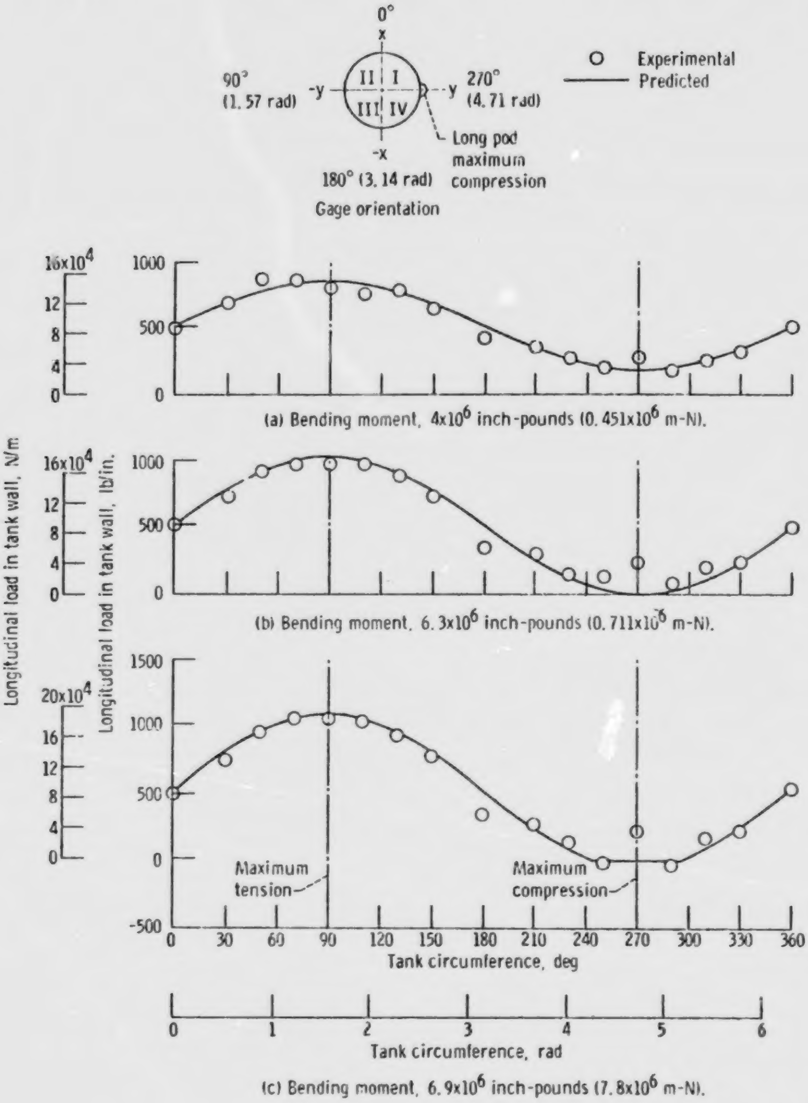

FIG. 5.11 MEASURED LOAD DISTRIBUTION AROUND CIRCUMFERENCE OF ATLAS AT STATION S84 COMPARED WITH PREDICTED-TEST 3 (FLAT PORTION OF CURVES INDICATES PORTION OF TANK SKIN THAT HAS WRINKLED) (REF. 5.7).

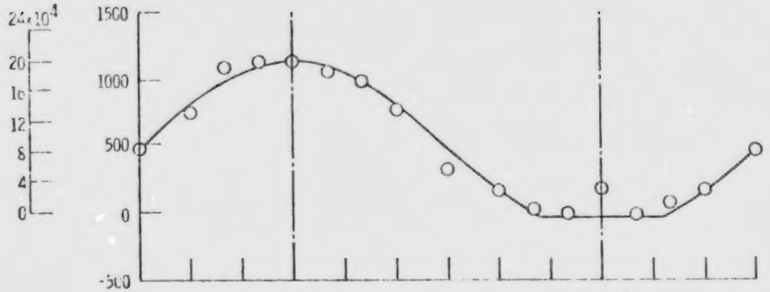

(d) Bending moment, 7.4x10^6 inch-pounds (0.835x10^6 m-N).

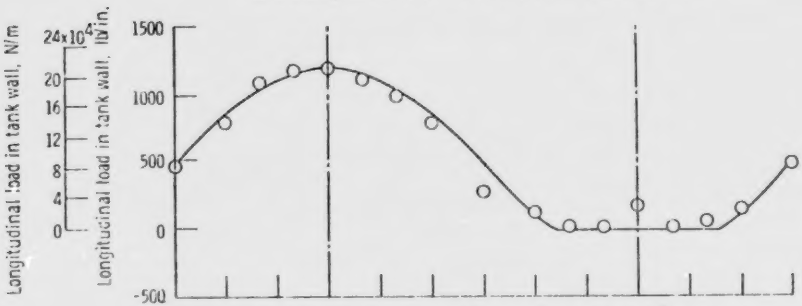

(e) Bending moment, 7.9x10^6 inch-pounds (0.891x10^6 m-N).

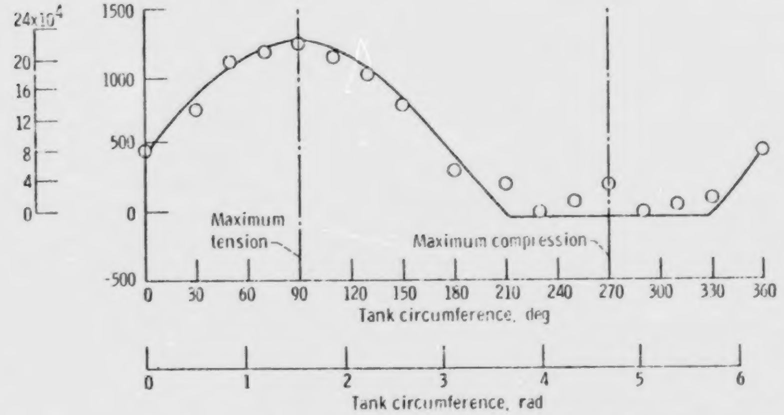

(f) Bending moment, 8.5x10^6 inch-pounds (0.96x10^6 m-N).

FIG. 5.11 (CONTINUED)

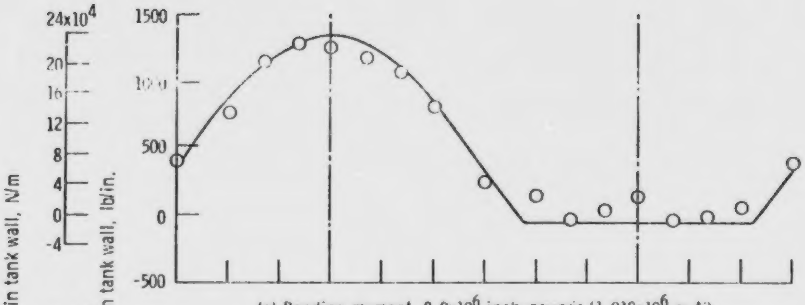

(g) Bending moment, 9.0x10^6 inch-pounds (1.019x10^6 m-N).

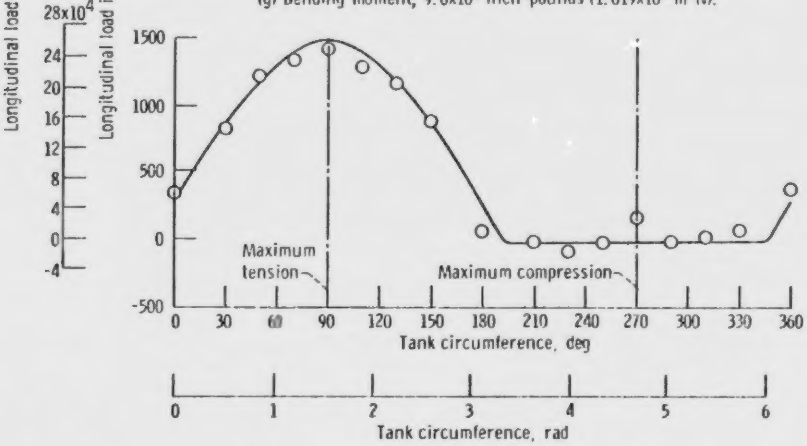

(h) Bending moment, 9.6x10^6 inch-pounds (1.084x10^6 m-N).

FIG. 5.11 (CONCLUDED)

After a certain value of torque, wrinkles began to form around the hub out to some radius R. He obtained closed-form solutions for several different boundary conditions; typical results are given in Figure 5.12 in the form of torque-rotation plots. The experimental results lie slightly above the theoretical results since the theory is for a perfect membrane with zero bending stiffness, while in fact, the plastic film used in the tests had a finite, though small bending stiffness.

The flat stretched membrane behaved like an elastic plate until wrinkling occurred at a value of dimensionless torque $M/2\pi a^2 Tt = 1$. At this value of torque, a region around the hub in an elastic plate would go into compression, but since a membrane can carry no compressive stress, wrinkling occurred in the membrane. As the torque was increased, the stiffness of the wrinkled stretched membrane decreased in a nonlinear fashion. There was no sharp reduction in stiffness, in contrast to the cylindrical membrane, and the torque could be increased until failure of the material occurred.

5.2.2) Wrinkling of Skirt Systems on ACV's

One of the first skirt systems used on air cushion vehicles was developed by Bertin/SEDAM in France. It consisted of a series of conical cells fed by a common air supply. These have evolved into segmented skirts, finger loop type skirts and other types.

One of these cells was tested at UTIAS to determine under what conditions it would collapse. The experimental setup consisted of a pressurized conical membrane attached to a box or an air supply reservoir. The box was constrained by a bearing assembly to roll about a horizontal axis as indicated in Figure 5.13. Typical dimensions of the conical cell were: thickness of 1.27×10^{-4}m (0.005 in), top diameter of 0.508m (20 in), height of 0.3048m (12 in) and a half taper angle of 6° ($\alpha^* = 84°$).

During the initial experiments [Ref. 5.11], it was found that, when the roll angle had been increased to a certain critical value, a single wrinkle would appear, and while the roll angle, the load, and cushion flow were held nominally constant, this wrinkle would spread slowly in the hoop direction. Eventually the wrinkle would become so long that the cell would buckle sideways, vent and cause the system to drop either to HSC (hard structure contact) or to a new equilibrium height.

This is a classic demonstration of the different modes of instability that are mentioned in Section 5.1.2. In the experiments there were also creep instabilities since the time between first appearance of the wrinkle and eventual failure would often be as long as twenty minutes.

For the materials used in the initial experiments only one wrinkle would occur. This is not, however, typical of all materials used in ACV skirt systems. Figures 5.14 and 5.15 show wrinkling patterns obtained for a different material. As can be seen, there is a complex nonuniform wrinkled region, and the structure has not yet collapsed. Figure 5.16 shows the wrinkles in a multi-segmented skirt system on the experimental hovercraft "Vampire 1", under pressure load only.

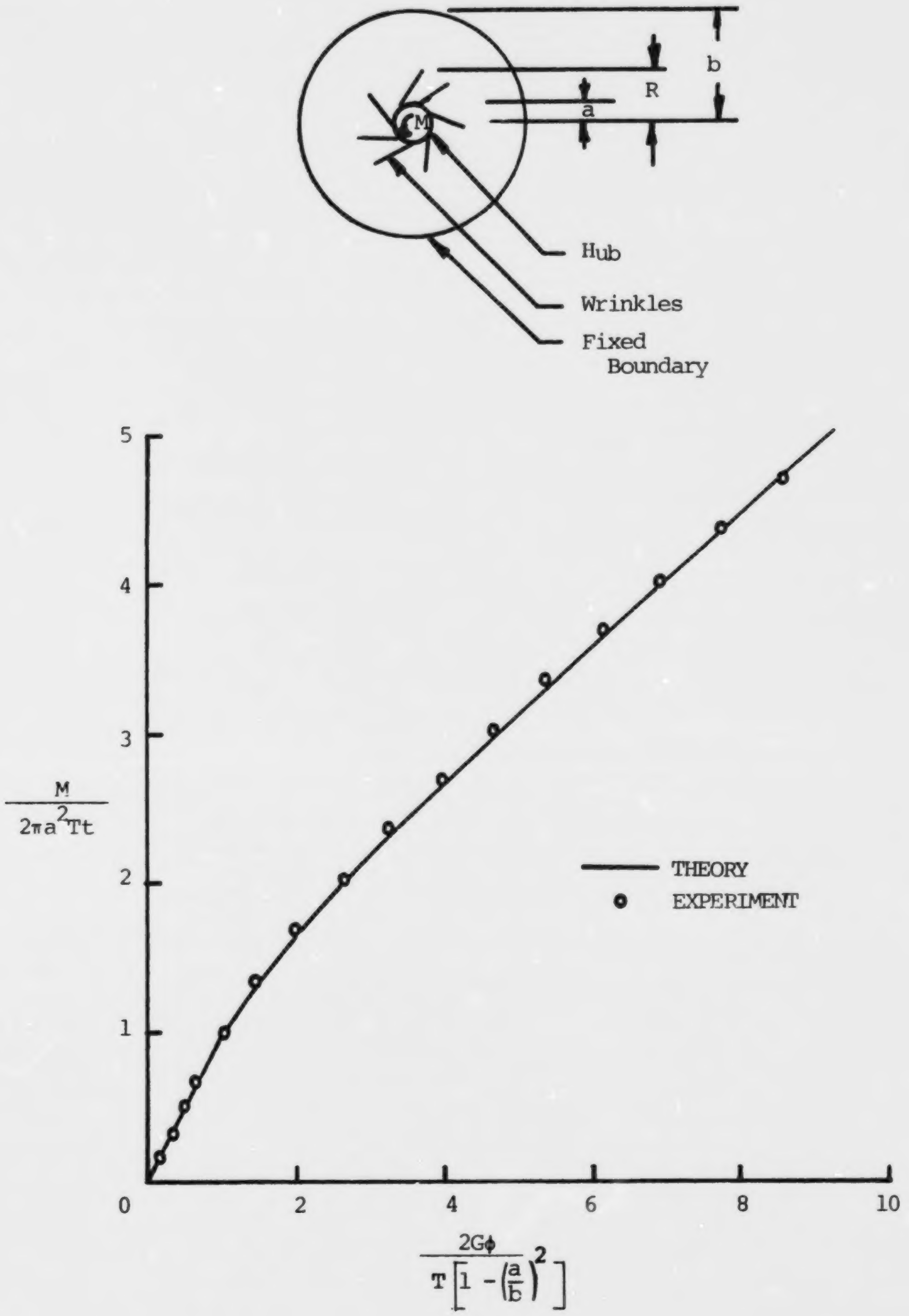

FIG. 5.12 TORQUE-ROTATION RESULTS FOR WRINKLING OF A CIRCULAR MEMBRANE BY ROTATION OF ATTACHED HUB (REF. 5.9).

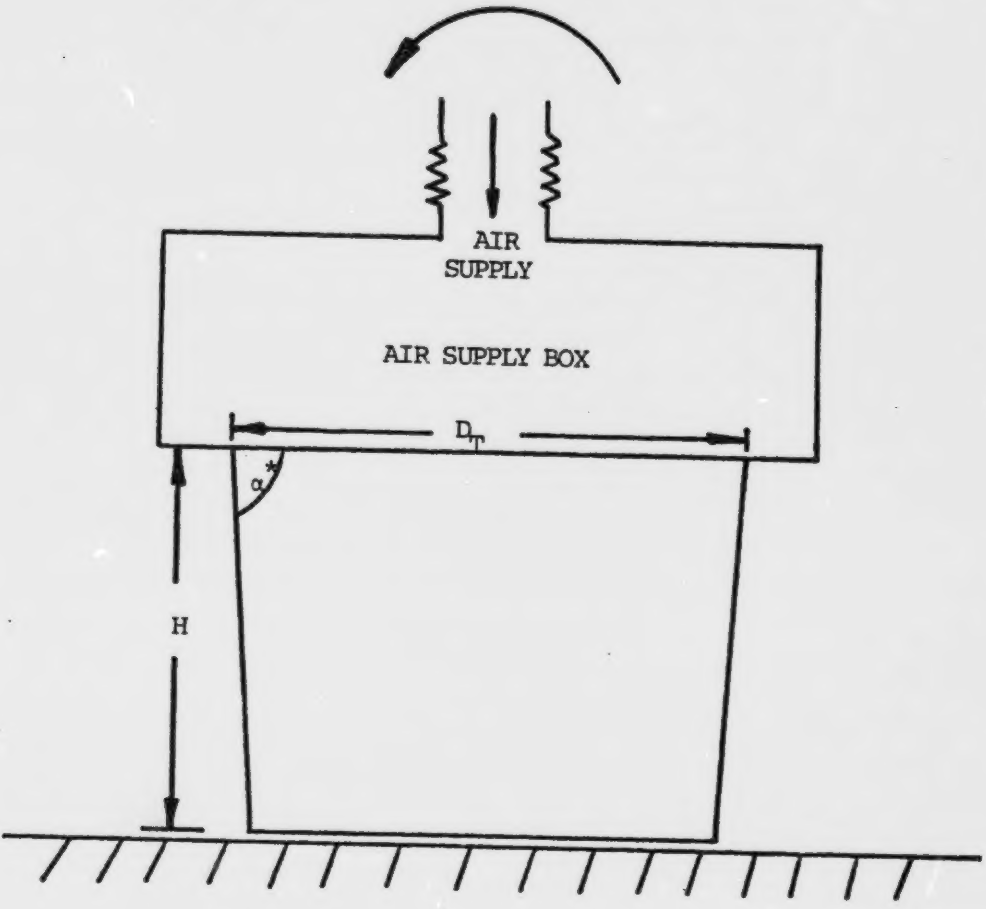
AIR
SUPPLY
AIR SUPPLY BOX
D_T
α^*
H

FIG. 5.13 SCHEMATIC OF ROLL INSTABILITY EXPERIMENT.

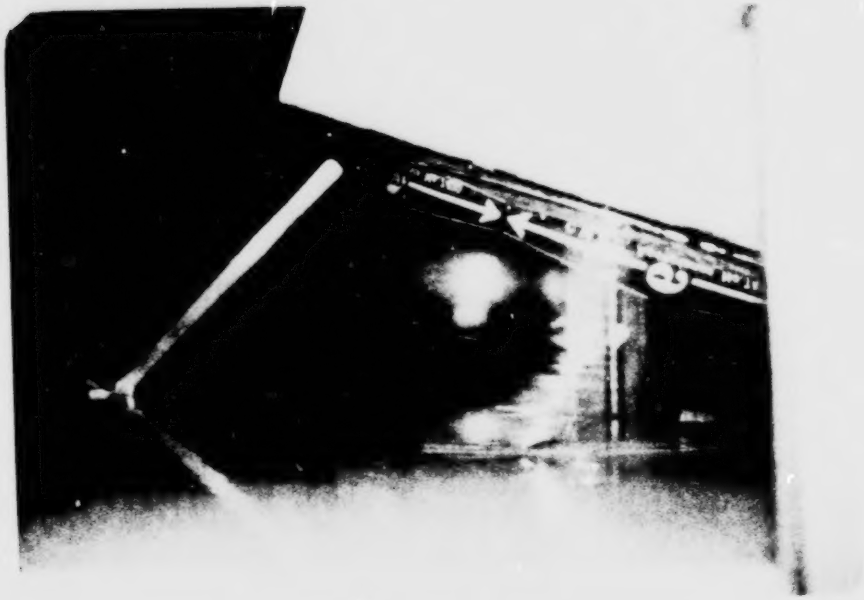

FIG. 5.14

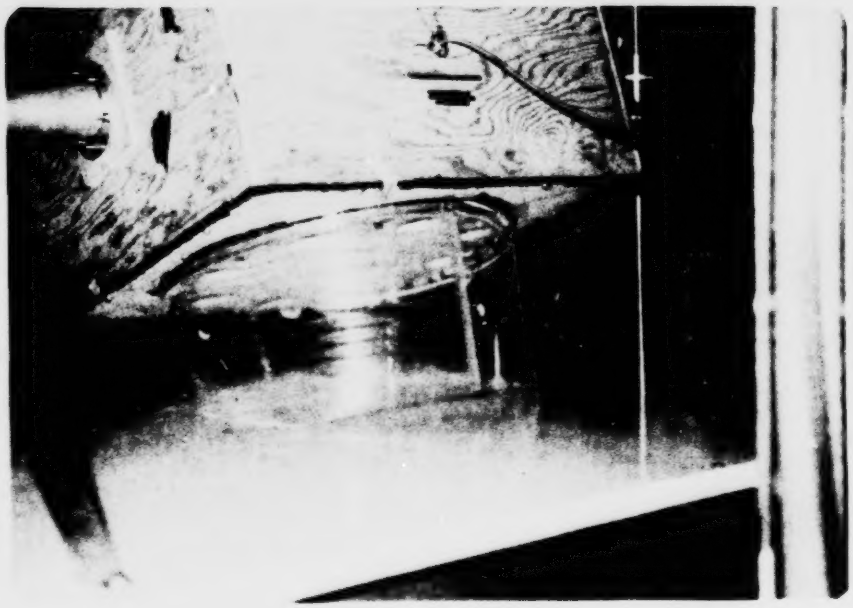

FIG. 5.15

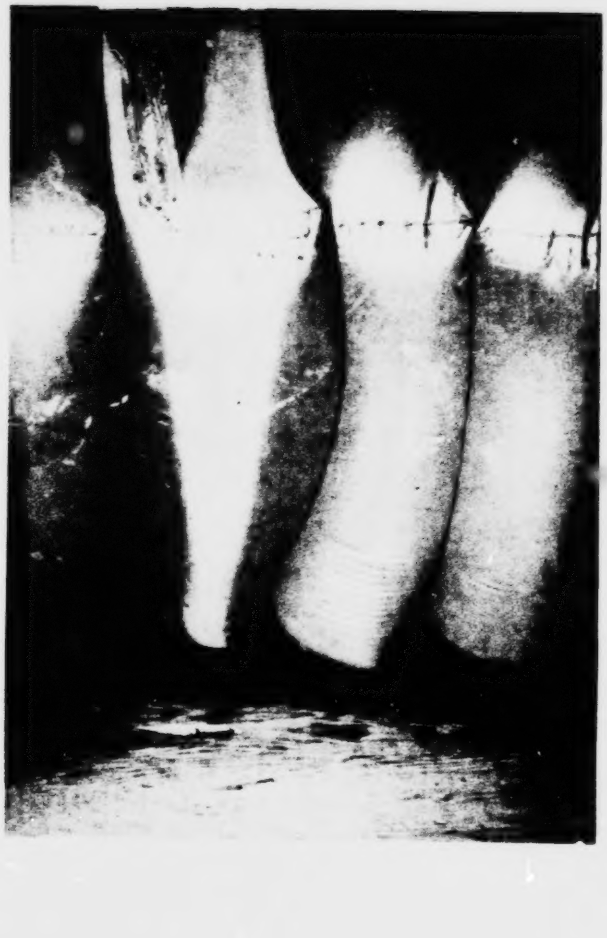

FIG. 5.16 WRINKLED REGION ON SEGMENTED SKIRT.

As with the cylinder, the first appearance of wrinkles does not imply that the structure will collapse. It is able to take more load and the wrinkling region continues to grow until failure occurs as shown in Figure 5.17.

5.3) Finite Element Formulation of Wrinkled Region

5.3.1) Finite Element Formulation

Due to the nonuniformity of the wrinkled region for the conical membrane, an analytical solution would be very difficult to obtain. The major difficulty is in applying the condition that the principal stress normal to the wrinkles be zero. Therefore, before attacking the cone problem numerically, it was decided to investigate the cylinder problem numerically and compare the results with the closed-form solutions in the literature.

Also, the analysis was expanded to take into account the bending stiffness of the material and rotations, however small, which had been neglected in previous work.

A four node, six degree of freedom per node, curvilinear coordinate rectangular, thin shell finite element was derived to model the cylinder for isotropic, orthotropic and anisotropic materials. The derivation can be found in Appendix C.

5.3.2) Formulation of Stress Resultant

We assume a stress resultant of the following form acting on the cylinder,

$$N_x = N_{AX} - N'r(\cos\phi - \cos\phi_o) \tag{14}$$

The total end load and moment acting on the cylinder due to the assumed stress resultant distribution is given by

$$P = \frac{1}{t} \iint_A N_x \, dA \tag{15}$$

$$M = \frac{1}{t} \iint_A N_x \, y \, dA \tag{16}$$

where A is the cross-sectional area of the cylinder (Figure 5.18). Rewriting equations (15) and (16) in polar coordinates, it follows that

$$P = \frac{2}{t} \int_{r - \frac{t}{2}}^{r + \frac{t}{2}} \int_{o}^{\pi} N_x \, r dr \, d\phi \tag{17}$$

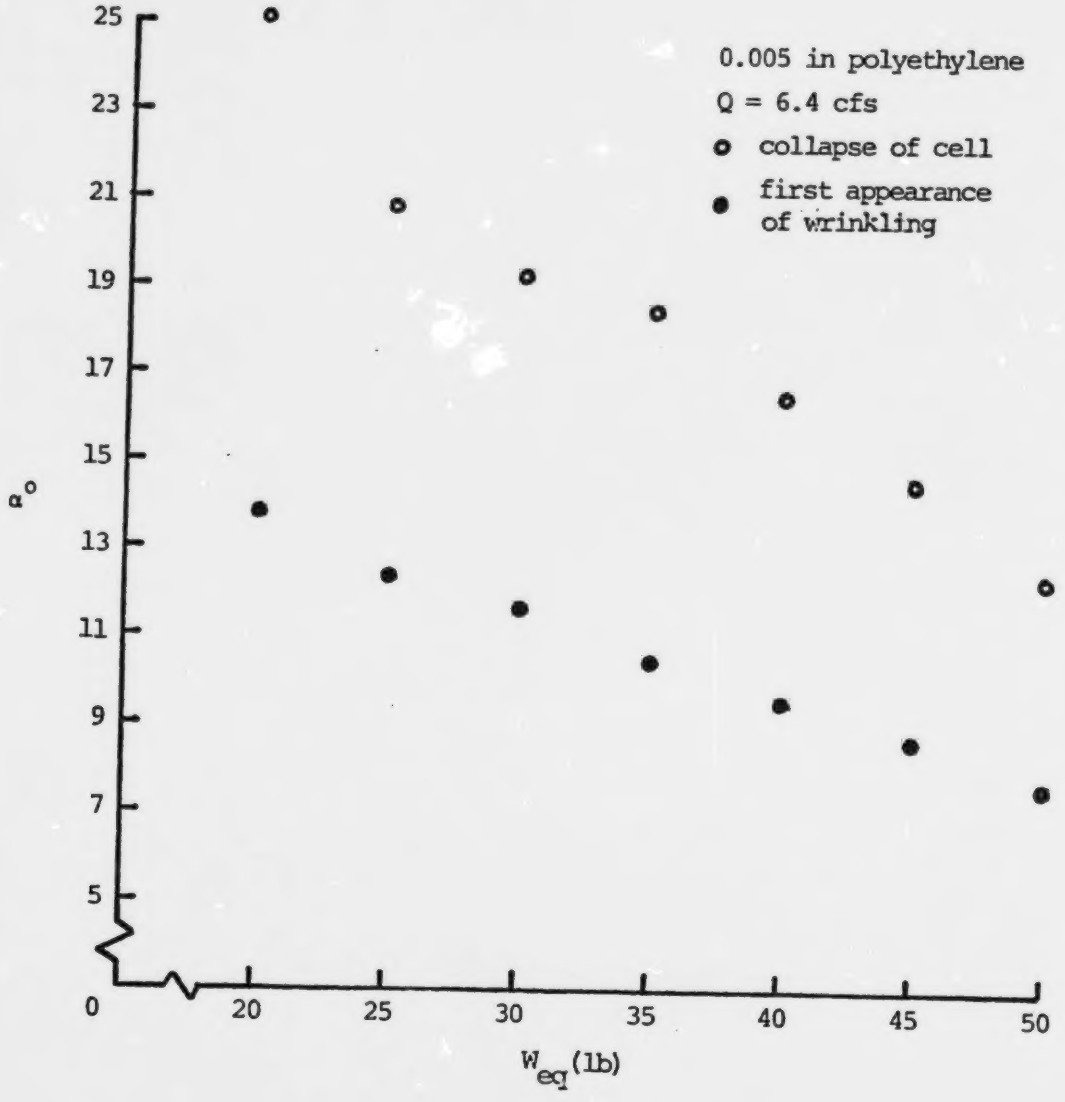

FIG. 5.17 WRINKLING AND COLLAPSE ANGLE FOR CONICAL CELL OVER A SMOOTH SURFACE.

$$M = -\frac{2}{t}\int_{r-\frac{t}{2}}^{r+\frac{t}{2}}\int_{0}^{\pi} N_x r^2 \cos\phi \, dr d\phi \tag{18}$$

If we postulate that wrinkling of the cylinder occurs uniformly up to an angle α (see Fig. 5.19), the above two equations are evaluated from α to π when integrated on ϕ. Substituting the assumed stress resultant N_x from equation (14) in equations (17) and (18), and performing the integration through the thickness on r and from α to π on ϕ, we obtain

$$P = 2N_{AX}r(\pi - \alpha) + 2N'r^2[-\sin\alpha + (\alpha - \pi)\cos\phi_o] \tag{19}$$

$$M = 2N_{AX}r^2\sin\alpha + N'r^3\left[\left(\pi - \alpha - \frac{1}{2}\sin 2\alpha\right) + 2\cos\phi_o\sin\alpha\right] \tag{20}$$

where t/r was assumed to be much smaller than one.

Since

$$P = p\pi r^2 - P_{AX} \geq 0 \tag{21}$$

and M, the applied external bending moment, are known we have two equations, (19) and (20), and three unknowns, N_{AX}, N', and $\cos\phi_o$. As P is kept constant throughout the loading of the cylinder, and the applied moment M is varied, assuming pure bending, it follows from equation (19) that

$$N_{AX} = \frac{P}{2r(\pi - \alpha)} \tag{22}$$

and

$$\cos\phi_o = \frac{-\sin\alpha}{(\pi - \alpha)} \tag{23}$$

Multiplying equation (23) by -r, we obtain

$$\bar{y} = -r\cos\phi_o = \frac{r\sin\alpha}{(\pi - \alpha)} \tag{24}$$

which is the effective centroid of the unwrinkled region of the cylinder. Substituting equations (22) and (23) in (20) and solving for N', it follows that

$$N' = \frac{M(\pi - \alpha) - P\,r\sin\alpha}{r^3\left[(\pi - \alpha)\left(\pi - \alpha - \frac{1}{2}\sin 2\alpha\right) - 2\sin^2\alpha\right]} \tag{25}$$

When all of the cylinder is in tension, we obtain the usual expressions

$$N_{AX} = \frac{P}{2\pi r} \tag{26}$$

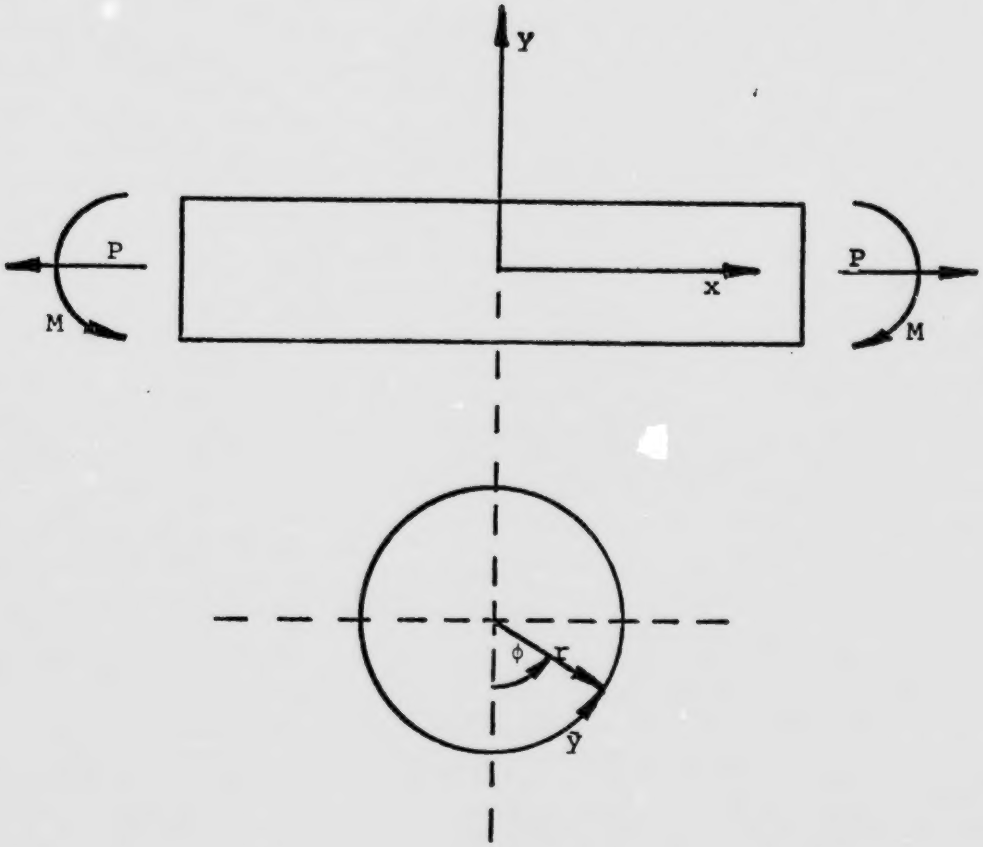

FIG. 5.18 LOADING AND COORDINATE SYSTEM FOR FINITE ELEMENT ANALYSIS.

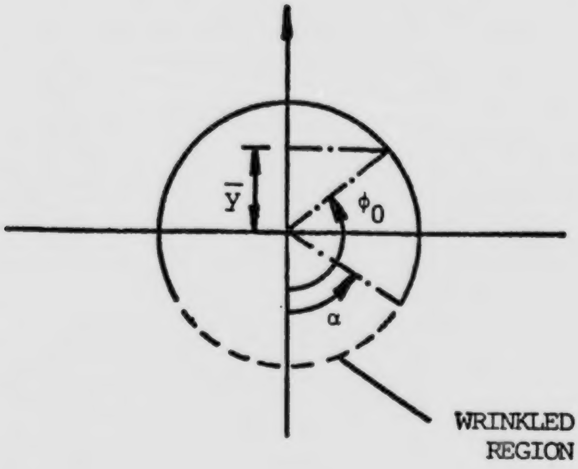

$\bar{y}$
ϕ_0
α
WRINKLED REGION

FIG. 5.19 CROSS-SECTIONAL VIEW OF WRINKLED REGION.

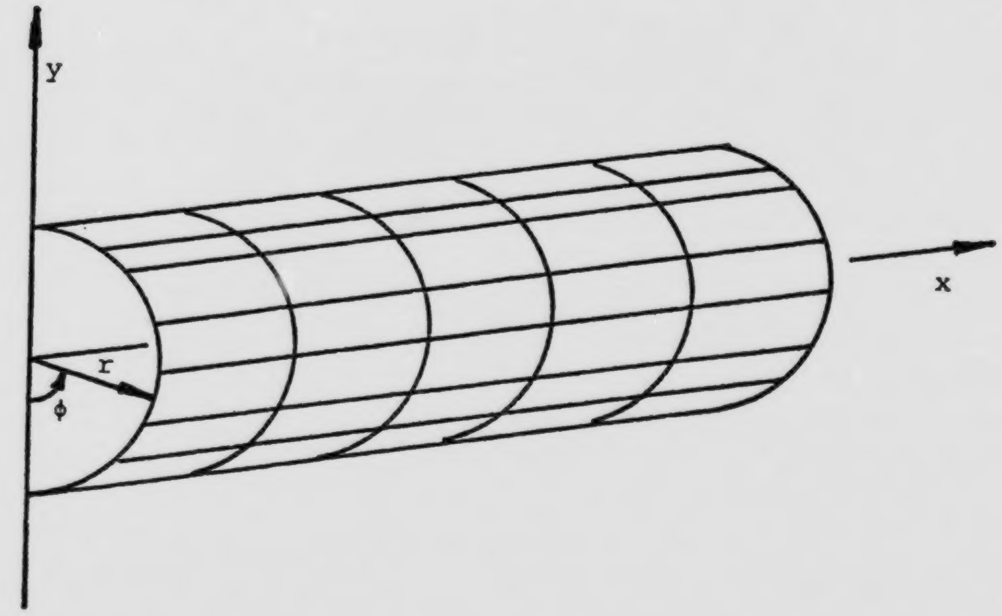

FIG. 5.20 FINITE ELEMENT REPRESENTATION OF CYLINDER WITH CURVED RECTANGULAR ELEMENTS.

$$N' = \frac{M}{\pi r^3} \qquad (27)$$

$$\cos\phi_o = 0 \qquad (28)$$

Since the wrinkled angle varies from 0 to π the following bounds on ϕ_o are imposed:

$$\frac{\pi}{2} \leq \phi_o \leq \pi \qquad (29)$$

or

$$0 \leq \bar{y} \leq r \qquad (30)$$

Since the wrinkled region cannot take any compressive loads by definition, the applied bending moment is redistributed over the unwrinkled part of the cylinder through equation (25), and $\cos\phi_o$ acts as a shift of the neutral surface of the cylinder.

5.3.3) Wrinkling Criterion for Finite Element Cylinder

In this section we will deal only with the isotropic and orthotropic cylinders. The anisotropic case will be treated in Section 5.5.

Due to the symmetry of loading, only one quarter of the cylindrical shell needs to be analyzed if appropriate boundary conditions are used. The cylinder is subdivided into curved finite elements, as shown in Figure 5.20. It is internally pressurized and it has an axial load and a bending moment applied at the end.

We first apply the pressure and an axial load at the end of the cylinder. Since no wrinkling occurs under this loading the stress resultant is given by equation (25) (see Figure 5.21a; the figures in 5.21 are all plotted in the $\tilde{y}$ coordinate system, $\tilde{y} = r\phi$). We then superimpose a bending moment as per equation (14):

$$N_B = -N'r\cos\phi \qquad (31)$$

where N' is calculated from equation (27) since no wrinkling has occurred (see Figure 5.21b; the diagonal lines show the compression region). If we superimpose N_{ax} and N_B we obtain

$$N_x = N_{AX} - N'r\cos\phi \qquad (32)$$

and the result is shown in Figure 5.21c. Now at a certain value of the bending moment M, the bottom row of elements of the cylinder will be in compression as shown in Figure 5.21d. Since a membrane cannot take compression, we redistribute the bending moment through equation (25), calculate $\cos\phi_o$ through

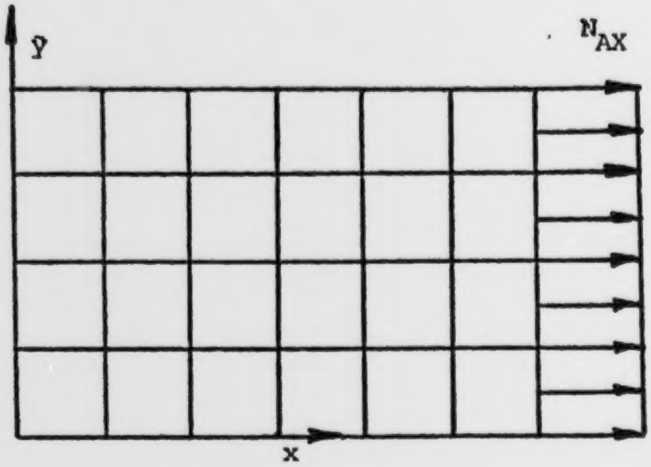

(a) AXIAL LOAD DUE TO INTERNAL PRESSURE

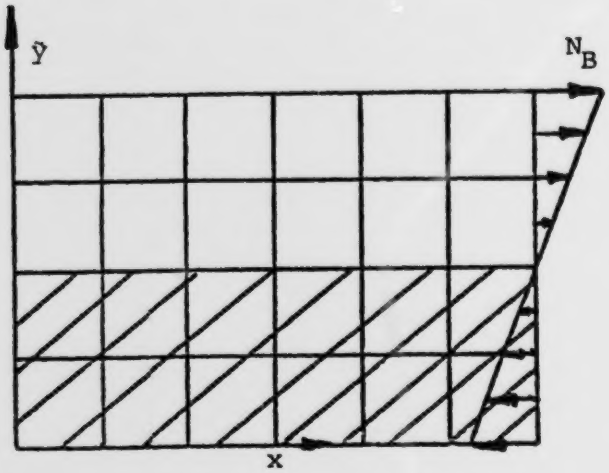

(b) BENDING MOMENT APPLIED ONLY

FIG. 5.21 LOADS FOR PRESSURIZED CYLINDER.

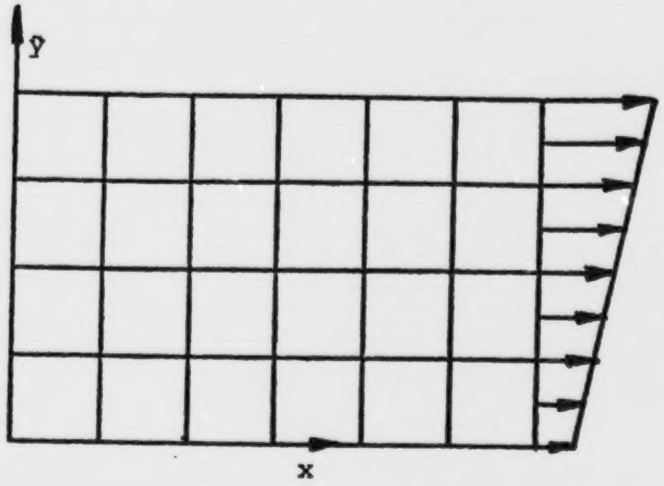

(c) SUPERIMPOSED BENDING MOMENT AND AXIAL LOAD

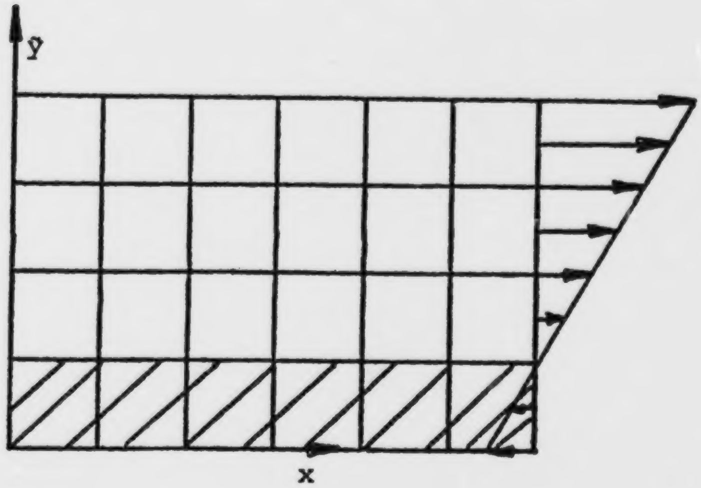

(d) BOTTOM ROW OF ELEMENTS IN COMPRESSION

FIG. 5.21 (CONTINUED)

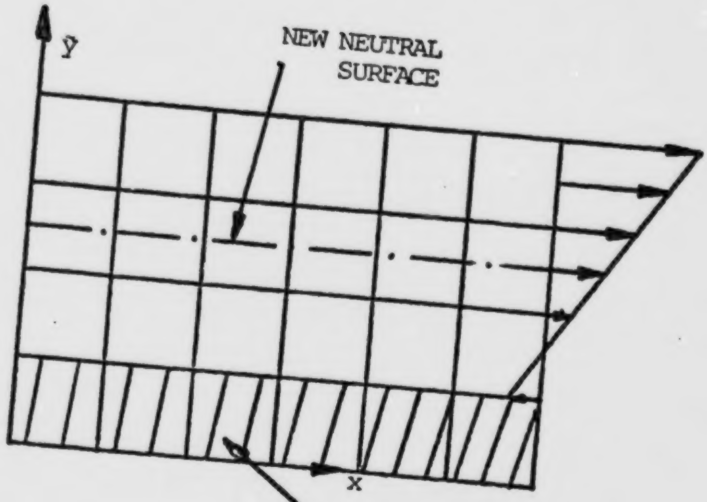
ȳ
NEW NEUTRAL SURFACE
x
WRINKLED REGION

(e) REDISTRIBUTION OF BENDING MOMENT AND BOTTOM ROW OF ELEMENTS IS WRINKLED

FIG. 5.21 (CONCLUDED)

equation (23) thereby determining the new neutral surface and re-apply the new loading pattern as given by equation (14) (see Figure 5.21e. There are no forces applied over the wrinkled region. We continue to increase the bending moment M, calculate N' with equation (25), in conjunction with (26) and (14) until the second row of elements goes in compression, and redistribute using the new wrinkling angle α. We continue in this fashion until most of the cylinder is wrinkled.

At each stage of loading we calculate the curvature of the cylinder along the top row of elements. For more details the reader is referred to Appendix C. Also, we define an element to be in compression when the longitudinal axial stress resultant is negative at the centre of the element.

The stress-strain relationship for an orthotropic and isotropic materials are given by equation (C-1) of Appendix C when $\psi = 0$. They are

$$\begin{aligned}\sigma_x &= Q_{11}\epsilon_x + Q_{12}\epsilon_y \\ \sigma_y &= Q_{12}\epsilon_x + Q_{22}\epsilon_y \\ \tau_{xy} &= Q_{66}\gamma_{xy}\end{aligned} \tag{33}$$

where

$$Q_{11} = \frac{E_{11}}{(1 - \nu_{12}\nu_{21})}, \qquad Q_{22} = \frac{E_{22}}{(1 - \nu_{12}\nu_{21})}$$
$$Q_{12} = \frac{\nu_{21}E_{11}}{(1 - \nu_{12}\nu_{21})} = \frac{\nu_{12}E_{22}}{(1 - \nu_{21}\nu_{12})}, \quad Q_{66} = G_{12} \tag{34}$$

for the orthotropic case, and the isotropic case follows if we let

$$E = E_{11} = E_{22}; \qquad \nu = \nu_{12} = \nu_{21} \text{ and } G_{12} = \frac{E}{2(1 + \nu)} \tag{35}$$

The elements can be imagined as a configuration of springs as shown in Figure 5.22 (plotted in the $\tilde{y}$ system) with different stiffness, where E_{11}, E_{22} and G_{12} represent the stiffness of the springs in the x-direction, $\tilde{y}$-direction and on the diagonal respectively. If the loading at the end of the cylinder is such that the bottom row of elements is in compression, then by definition, a wrinkled region loses its stiffness in the x-direction. Therefore, we would expect the stiffness in the x-direction (E_{11}) to become zero and by equation (36), ν_{12} would also be zero. The wrinkled region cannot take shear stresses and therefore the shear stiffness (G_{12}) would also be zero. But since the wrinkled region is generated by the longitudinal loading, the wrinkled region can still support hoop stress from the internal pressure and therefore (E_{22}) is not affected. In summary, in the wrinkled region,

$$E_{11} = \nu_{12} = G_{12} = 0 \tag{36}$$

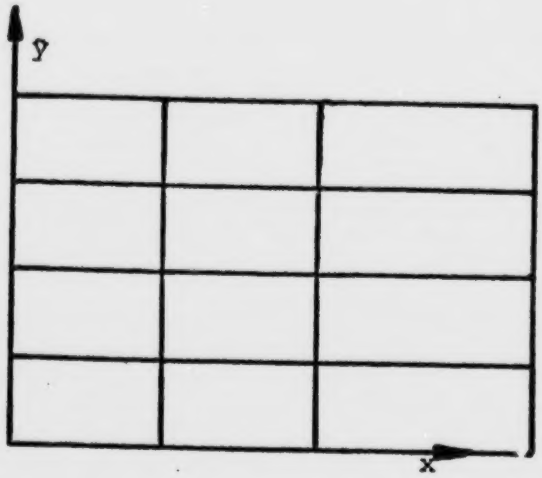

(a) FINITE ELEMENT GRID

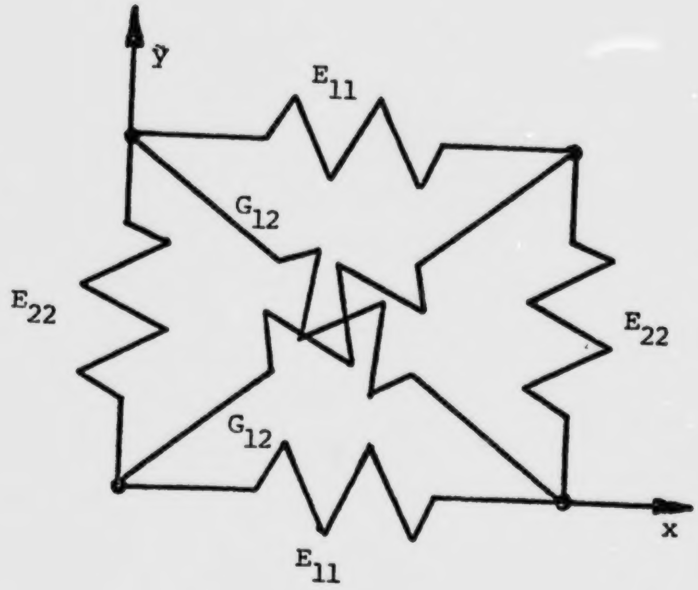
ȳ
E_{11}
G_{12}
E_{22}
E_{22}
G_{12}
x
E_{11}

(b) SPRING CONFIGURATION OF ELEMENT

FIG. 5.22 SPRING ANALOGY OF ELEMENTS.

and the stress-strain relationship (33) becomes

$$\sigma_x = 0$$

$$\sigma_y = E_{22}\epsilon_y \tag{37}$$

$$\sigma_{xy} = 0$$

If the conditions of equations (36) are applied in the derivation of the elemental stiffness matrix, this matrix becomes singular. To prevent this from occurring, one modification to equations (36) must be applied. Instead of letting the shear stiffness G_{12} to be zero, we set it to a small positive number less than one. The modified conditions are now read as

$$E_{11} = \nu_{12} = 0, \quad G_{12} = 0.001 \text{ say} \tag{38}$$

which implies that the last of equation (37) is now

$$\tau_{xy} = 0.001\ \gamma_{xy} \tag{39}$$

Since no shear loads are applied to the cylinder, the final result is still $\tau_{xy} = 0$ and the condition for a wrinkled region

$$\sigma_x\sigma_y - \tau_{xy}^2 = 0 \tag{40}$$

is still appropriate.

In conclusion, when a row of elements goes into compression, we find a new neutral surface, redistribute the applied bending moment, enforce the conditions of equation (38) in the wrinkled region and the process is repeated for the remaining rows of elements until most of the cylinder is wrinkled.

5.4) Performance Tests

In this section, we will present the verification of the present finite element results with known analytical results, for the isotropic and orthotropic cases. These include tests for the flat plate, quarter cylinder and half cylinder under different loading and boundary conditions. Convergence will also be examined by increasing the number of elements. The computer code was originally developed by Heppler [Ref. 5.14] for the isotropic case. The present work included modifying the code to include orthotropic and rectilinear anisotropic material behaviour. Further, the modified code also provided the possibility of including wrinkling in the analysis.

5.4.1) Curvilinear Shell Element Test

Several different models were used to test the features of the finite element formulation.

The first test case, which was performed by Heppler [Ref. 5.14] consisted of an isotropic cylinder with a uniform symmetric radial load applied around its middle as described by Timoshenko [Ref. 5.16]. Extremely rapid convergence was observed and an indication of the overall error can be obtained from Figure 5.23. As can be seen the agreement with theory is excellent. In all the models tested for the radial applied load, excellent symmetry agreement was displayed at every node.

The second test case consisted of a cylinder with capped ends under a uniform pressure load for isotropic and orthotropic materials. The exact solution for this case can be found in Krauss [Ref. 5.17]. The stresses were also verified for this case. The results for the isotropic and orthotropic cases are found in Tables 1 and 2 respectively. The results are in terms of maximum relative percentage error as follows:

$$\text{Error} = \left| \frac{(\ )_{\text{exact}} - (\ )_{\text{fin. ele.}}}{(\ )_{\text{exact}}} \right| \times 100 \qquad (41)$$

The agreement with the exact solution is excellent. It should be noticed that the results are better for the case where there are fewer elements. The reason for this discrepancy is due to the round-off error when solving the global stiffness matrix.

For the next series of tests, a small bending moment was applied at the end of a pressurized capped cylinder. The longitudinal stress acting on the cylinder is of the following form:

$$N_x = \frac{pr}{2} - \frac{\rho' r^2}{2} \cos\phi \qquad (42)$$

An exact solution for this form of loading can be found in Krauss [Ref. 5.17]. The results are repeated here for convenience in Table 3. Again, the tests were performed for the isotropic and orthotropic case, with the same number of nodes and elements. The results are shown in the same form mentioned previously. Overall, the displacement and stresses agree well with the exact solution. The stresses at the nodes are worse than those evaluated at the centre of the element due to the discontinuities in the u and v derivatives from element to element. This is explained further in Appendix C where the stresses are derived from the displacements.

All the results in this section were performed on a quarter of the cylinder. The program was also tested on the half and full cylinder in the course of the research. In these tests, excellent symmetry was displayed in the results where it was expected.

As a further test, a linear relationship was expected in the moment-curvature plots. That is, if the cylinder is kept at constant pressure, and

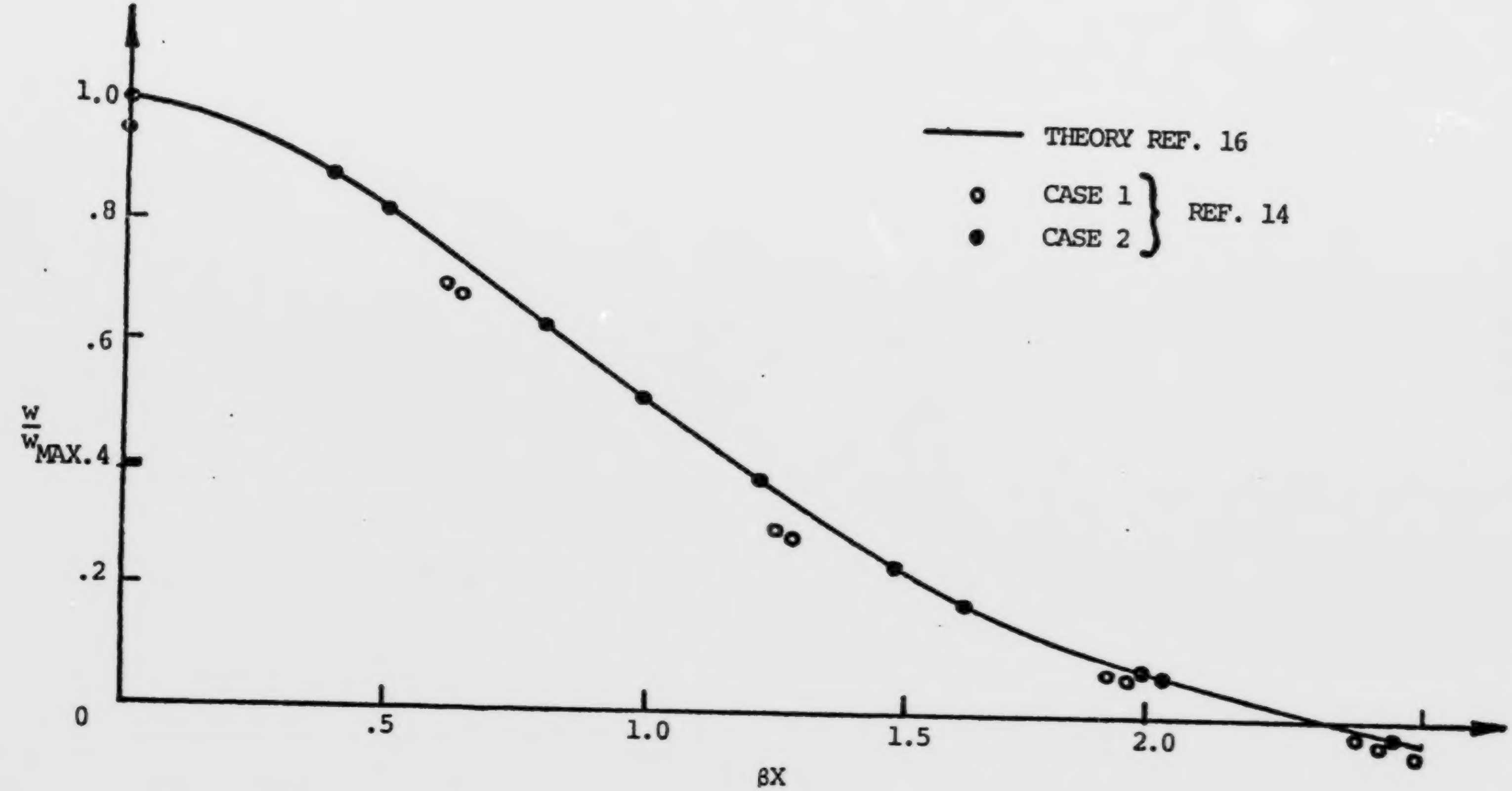

FIG. 5.23 COMPARISON OF FINITE ELEMENT ANALYSIS WITH EXACT SOLUTION FOR A CYLINDER WITH A UNIFORM CIRCUMFERENTIAL LOAD APPLIED AT MIDLENGTH.

Table 5.1

CURVILINEAR TEST FOR ISOTROPIC CASE

The cylinder tested had the following properties

$E = 2.275(10^{10})$ Pa $(3.3(10^{6})$ lbf/in^2)

$\nu = 0.3$

$p = 6.894(10^{4})$ Pa (10 lbf/in^2)

$t = 0.3556$ mm (0.014 in)

$l = 3.81$ m (150 in)

$r = 1.524$ m (60 in)

MAXIMUM RELATIVE PERCENTAGE ERROR

AT THE NODES

CASE	u	w	N_x	N_θ	# of elements	# of nodes in x-direction	# of nodes in y-direction
1	0.001	0.005	0.008	0.010	6	4	3
2	0.002	0.004	0.003	0.007	4	2	5
3	0.010	0.080	0.020	0.040	40	6	9
4	0.030	0.030	0.020	0.030	50	6	11

AT CENTRE OF ELEMENT

CASE	u	w	N_x	N_θ	# of elements	# of nodes in x-direction	# of nodes in y-direction
1	.0004	0.002	0.002	0.003	6	4	3
2	0.002	0.003	0.002	0.003	4	2	5
3	0.020	0.020	0.010	0.007	40	6	9
4	0.020	0.030	0.020	0.010	50	6	11

Table 5.2

CURVILINEAR TEST FOR ORTHOTROPIC CASE

The cylinder tested had the following properties

$E_{11} = 2.137(10^{10})$ Pa $(3.1(10^6)$ lbf/in$^2)$
$E_{22} = 1.379(10^{10})$ Pa $(2.0(10^6)$ lbf/in$^2)$
$\nu_{21} = 0.3$
$\nu_{12} = 0.465$
$G_{12} = 6.249(10^9)$ Pa $(9.1(10^5)$ lbf/in$^2)$
$p = 6.895(10^4)$ Pa (10 lbf/in^2)
$t = 0.3556$ mm (0.014 in)
$l = 3.81$ m (150 in)
$r = 1.524$ m (60 in)

MAXIMUM RELATIVE PERCENTAGE ERROR

AT THE NODES

CASE	u	w	N_x	N_θ	# of elements	# of nodes in x-direction	# of nodes in y-direction
1	0.006	0.004	0.020	0.020	6	4	3
2	0.006	0.003	0.006	0.006	4	2	5
3	0.070	0.080	0.040	0.080	40	6	9
4	0.060	0.030	0.030	0.030	50	6	11

AT CENTRE OF ELEMENT

CASE	u	w	N_x	N_θ	# of elements	# of nodes in x-direction	# of nodes in y-direction
1	0.007	0.003	0.003	0.003	6	4	3
2	0.009	0.004	0.004	0.004	4	2	5
3	0.050	0.010	0.009	0.008	40	6	9
4	0.090	0.020	0.020	0.020	50	6	11

Table 5.3

CURVILINEAR TEST WITH SMALL BENDING MOMENT APPLIED

The solution for the loading of equation (41) is

$$u = \frac{x}{E_{11}t}\left[pr\left(\frac{1}{2} - \nu_{12}\right) - \rho' \frac{r^2}{4} \cos\phi \right]$$

$$v = \frac{-1}{E_{11}t} \frac{(\ell^2 - 4x^2)}{32} \rho' r \sin\phi$$

$$w = \frac{1}{E_{22}t}\left[pr^2\left(1 - \frac{\nu_{21}}{2}\right) - \nu_{21} \frac{\rho' r^3}{4} \cos\phi \right] + \frac{r}{E_{11}t}\left[\frac{\ell^2 - 4x^2}{32} \right] \rho' \cos\phi$$

$$N_x = \frac{pr}{2} - \frac{\rho' r^2}{2} \cos\phi$$

$$N_\theta = pr$$

$$N_{x\theta} = 0.0$$

ISOTROPIC CASE

The cylinder tested had the following properties

$E = 2.275(10^9)$ Pa ($3.3(10^5)$ lbf/in^2)
$\nu = 0.3$
$\rho = 9.799(10^3)$ Pa/m (0.0361 lbf/in^3)
$p = 1.103(10^5)$ Pa (16 lbf/in^2)
$t = 0.3556$ mm (0.014 in)
$l = 3.81$ m (150 in)
$r = 1.524$ m (60 in)

MAXIMUM RELATIVE PERCENTAGE ERROR (63 nodes, 48 elements)

AT THE NODES	AT CENTRE OF ELEMENT
u - 0.22	u - 1.2
v - 1.03	v - 3.6
w - 0.08	w - 0.02
N_x - 0.40	N_x - 0.13
N_θ - 0.30	N_θ - 0.03

.....continued

Table 5.3 - Continued

ORTHOTROPIC CASE

The cylinder tested had the following properties

$E_{11} = 2.275(10^9)$ Pa $(3.3(10^5)$ lbf/in$^2)$

$E_{22} = 1.138(10^9)$ Pa $(1.65(10^5)$ lbf/in$^2)$

$G_{12} = 5.648(10^8)$ Pa $(8.19(10^4)$ lbf/in$^2)$

$\nu_{21} = 0.3 \qquad \nu_{12} = 0.6$

$\rho = 9.799(10^3)$ Pa/m (0.0361 lbf/in^3)

$p = 1.103(10^5)$ Pa (16 lbf/in^2)

$t = 0.3556$ mm (0.014 in)

$l = 3.81$ m (150 in)

$r = 1.524$ m (60 in)

MAXIMUM RELATIVE PERCENTAGE ERROR (63 nodes, 48 elements)

AT THE NODES		AT CENTRE OF ELEMENT	
u	0.22	u	1.2
v	1.03	v	3.6
w	0.08	w	0.02
N_x	0.4	N_x	0.13
N_θ	0.3	N_θ	0.03

the applied bending moment is increased in small increments, the curvature of the cylinder should increase linearly. This feature was observed in all moment-curvature plots when the cylinder had not yet wrinkled, as for example in Figure 5.27.

In summary, we can conclude with confidence that the finite element analysis and the computer program perform very well under different loading conditions. In the next section, we will present the results for the cases where the cylinder wrinkles.

5.5) Numerical Results and Discussions

All the results are given in dimensionless moment-curvature plots. The applied bending moment is nondimensionalized by the non-negative total end load P [equation (21)] multiplied by the radius of the cylinder,

$$Pr = (p \pi r^2 - P_{AX})r \tag{43}$$

The curvature, $\rho = -\omega_{,xx}$ is nondimensionalized, as in Stein and Hedgepeth [Ref. 5.1], by multiplying it by

$$\frac{2\pi r^2 E_{11} t}{P} \tag{44}$$

It should be noticed that we utilize the orthotropic modulus in the principal direction in equation (44). In this manner, we can also compare the results for the orthotropic material with Stein and Hedgepeth. For the isotropic material, equation (44) is the same as Stein and Hedgepeth, since $E_{11} = E_{22} = E$. The displacement results in the wrinkled region do not give the actual wrinkling configuration of the cylinder, but do give average displacements.

Typically the behaviour as predicted by the numerical results is the same as was mentioned before. There is a linear relationship in the dimensionless form of the moment and curvature and when wrinkling occurs the curve continues in a nonlinear fashion.

5.5.1) Isotropic Case

A series of tests were performed for the isotropic material using different l/r ratios and for different values of the total end load by varying P_{AX} in equation (43).

The first test case was for a cylinder with 40 elements (8 elements in the y-direction and 5 elements in the x-direction). The l/r ratio was 2.5 and the results are shown in Figure 5.24. As can be seen, very good agreement is achieved between the present and Stein and Hedgepeth's results. Since we defined earlier that a row of elements is in compression when the longitudinal stress is negative at the centre of the element, wrinkling starts at a value of M/Pr greater than 1/2. This does not affect the general behaviour of the moment-curvature plot.

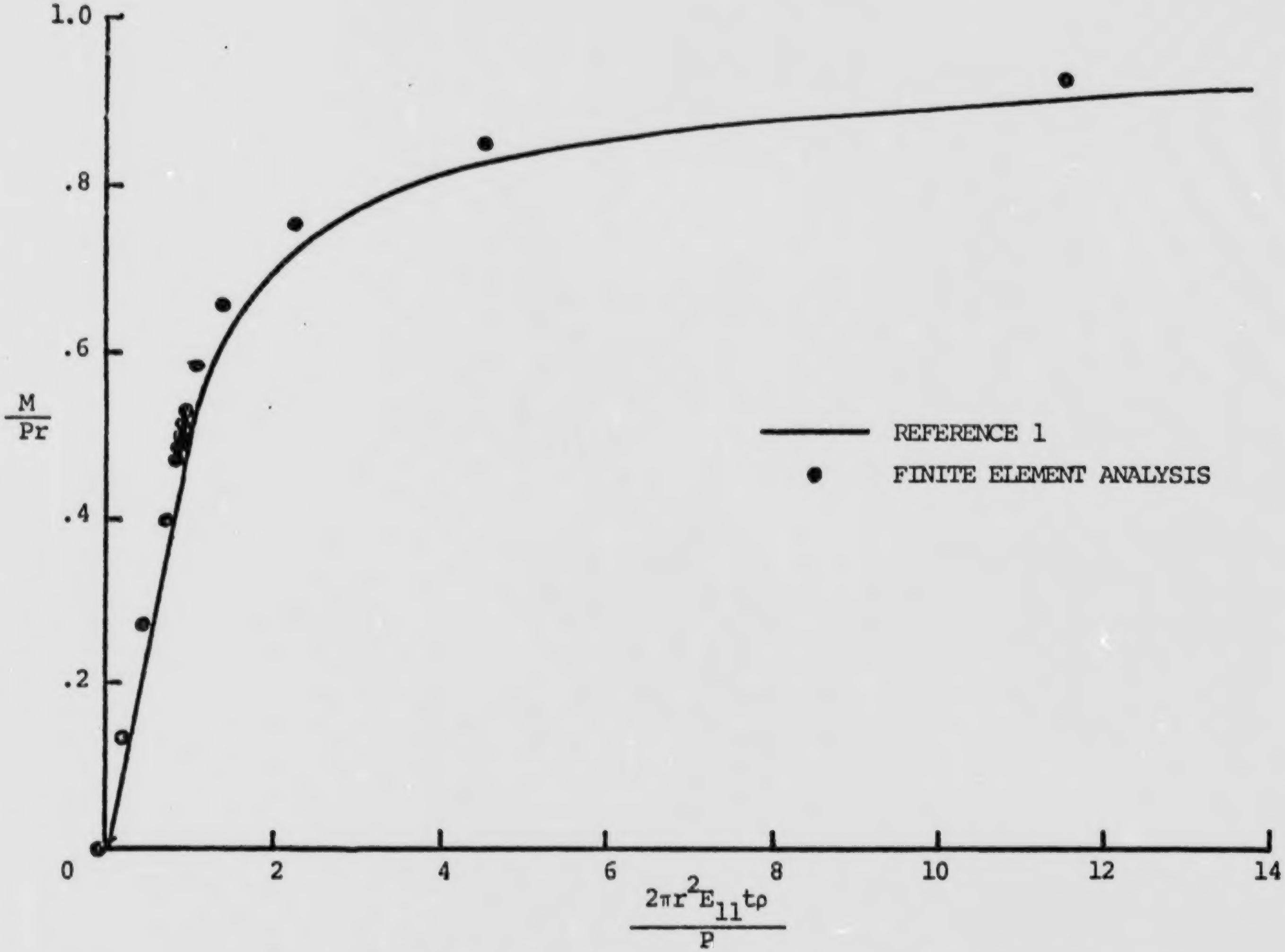

FIG. 5.24 COMPARISON OF FINITE ELEMENT ANALYSIS WITH STEIN AND HEDGEPETH'S THEORY (40 ELEMENTS).

MATERIAL PROPERTIES: $E_{11} = E_{22} = 2.28\ (10^9)$ Pa; $t = 0.3556$ mm;
$\nu_{12} = \nu_{21} = 0.3$.

DIMENSIONS: $p = 3.5\ (10^4)$ Pa; $P_{ax} = 1.8\ (10^5)$ N; $r = 1.524$m;
$L/r = 2.5$.

To verify the convergence, the next plot (Figure 5.25) shows the results for the same data as Figure 5.24, but when the number of elements was doubled by increasing the number of elements in the circumferential direction. The increased number of elements also gives us more numerical points in the wrinkled region. There is excellent agreement in the unwrinkled region and the numerical results lie slightly above the Stein and Hedgepeth curve in the wrinkled region. This discrepancy may be due to the bending stiffness of the material which was neglected in the Stein and Hedgepeth analysis and the fact that we do allow individual elements to go in compression before wrinkling occurs. This effect was also noticed in experimental results done by McComb et al [Ref. 5.2] for the cylinder and Mikulas [Ref. 5.9] for a flat stretched membrane. This behaviour was noticed in all numerical results for the isotropic and orthotropic material.

Figure 5.26 compares the effect of increasing the total end load P, by letting $P_{AX} = 0.0$ in equation (43) with the same data of Figure 5.24. The curves show a small dependence on the magnitude of the axial load. For ratios of $l/r \leq 3$, Leaumont [Ref. 5.6] and McComb et al [Ref. 5.2] also noticed this dependence experimentally and classify it as negligible.

The next plot is for a cylinder of ratio $l/r = 5$ (see Figure 5.27). The internal pressure was increased while the material properties were as before. The numerical points lie slightly higher than the previous cases where lower l/r ratios were used. This is due to the magnitude of the axial load which starts to add an extra moment in addition to the applied external bending moment as mentioned in Jahsman [Ref. 5.5]. If the l/r ratio was further increased, the numerical points would shift even higher and the wrinkled region would be nonuniform. The finite element analysis does not take into account this extra moment due to the axial load.

Figure 5.28 shows the normal displacement at the top of the cylinder versus the nodal position along the cylinder at different stages of loading for Figure 5.24. The top curve is for the last data point of Figure 5.24 when most of the cylinder is wrinkled.

For the last case, typical values of the material and dimensions of a slightly tapered HJ-15 conical cell were utilized. The dimensions of the HJ-15 cell [Ref. 5.19] are: average diameter of 1.83m (6 feet); height of 0.915m (3 feet). Typically, it operates at an internal pressure of about 896.4 Pa (0.13 psi). The material utilized is polyethylene (classified as isotropic) with the following properties: thickness of 1.27×10^{-4}m (0.005 in); Young's modulus of 2.21×10^{8} Pa (32000 psi) and a Poisson's ratio of 0.4. The l/r ratio for this cylinder is one and we would expect good agreement as seen in Figure 5.29. The stress resultants acting on this cell are quite small due to the low internal pressure. For example, the hoop stress resultant is 819.5 N/m (4.68 lbs/in) and the longitudinal stress resultant is half this value under pressure load only.

5.5.2) Orthotropic Case

For the orthotropic cylinder, a few tests were done by varying the orthotropic moduli E_{11} and E_{22}. Figure 5.30 compares the cases for

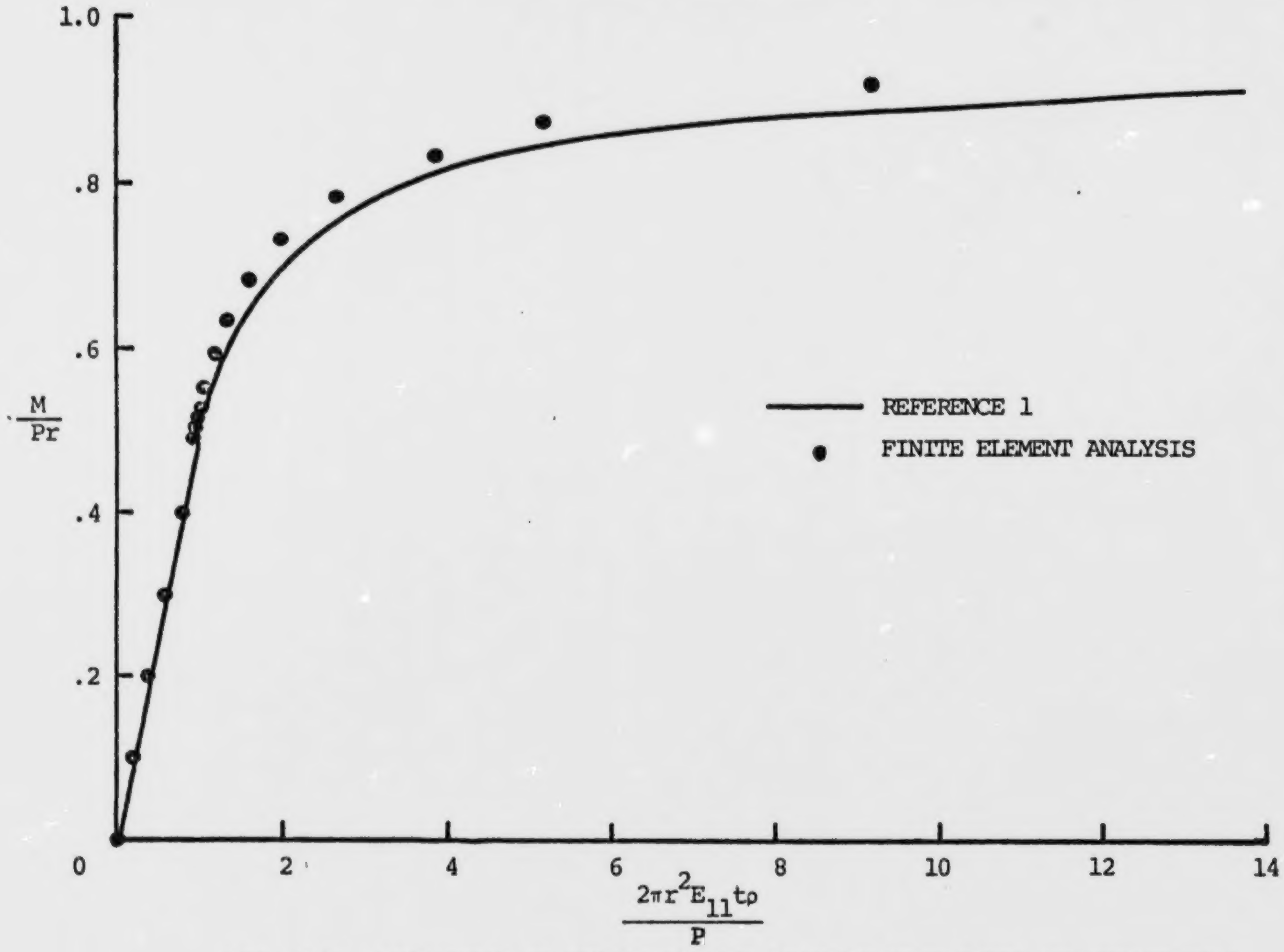

FIG. 5.25 COMPARISON OF FINITE ELEMENT ANALYSIS WITH STEIN AND HEDGEPETH'S THEORY (80 ELEMENTS).

MATERIAL PROPERTIES: $E_{11} = E_{22} = 2.28\ (10^9)$ Pa; $t = 0.3556$ mm;

$\nu_{12} = \nu_{21} = 0.3$.

DIMENSIONS: $p = 3.5\ (10^4)$ Pa; $P_{ax} = 1.8\ (10^5)$ N; $r = 1.524$m;

$L/r = 2.5$.

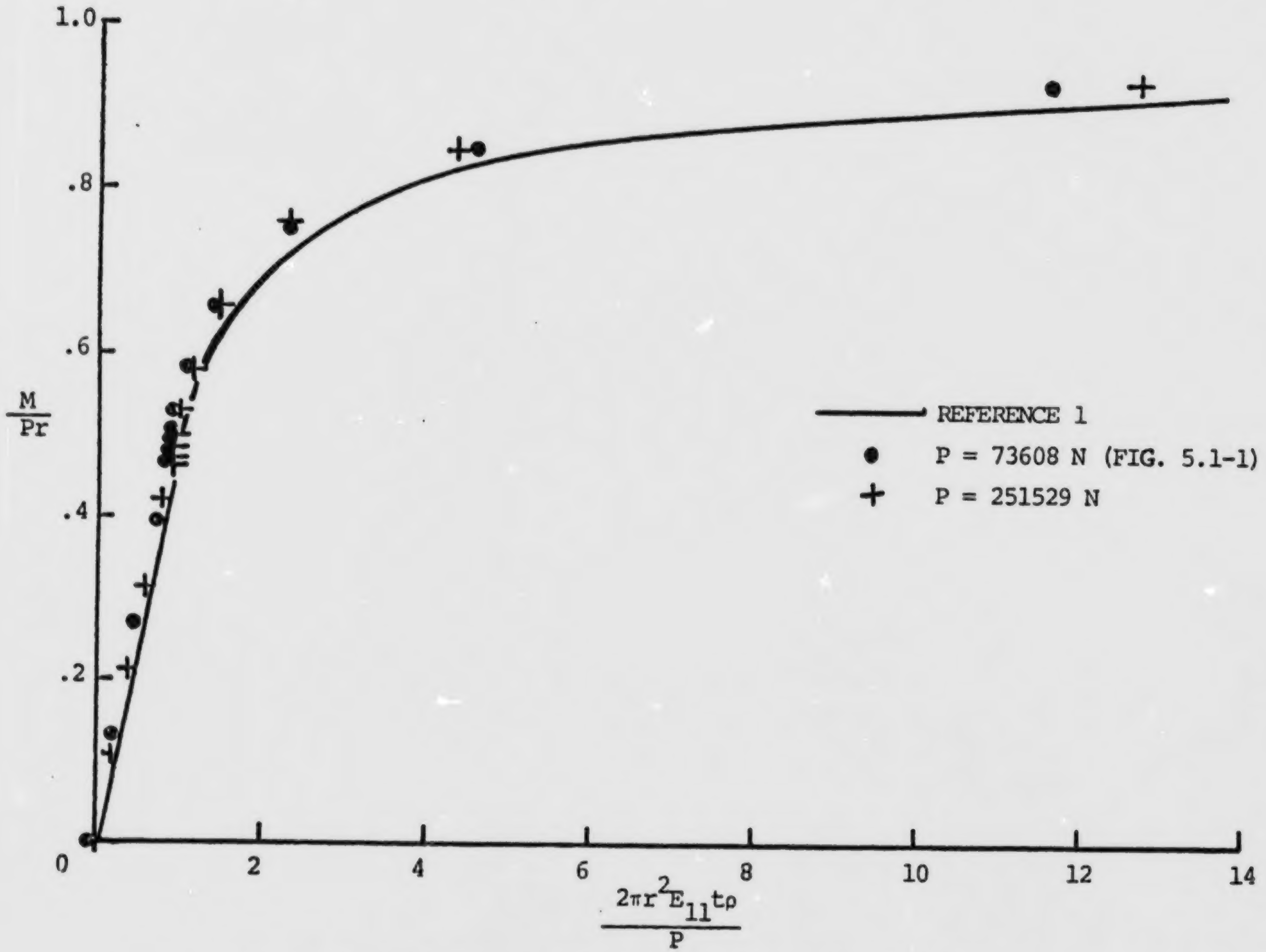

FIG. 5.26 COMPARISON FOR INCREASE OF TOTAL APPLIED AXIAL LOAD.

MATERIAL PROPERTIES: $E_{11} = E_{22} = 2.28\ (10^9)$ Pa; $t = 0.3556$ mm;
$\nu_{12} = \nu_{21} = 0.3$.

DIMENSIONS: $p = 3.5\ (10^4)$ Pa; $P_{ax} = 0.0\ (10^5)$ N; $r = 1.524$m;
$L/r = 2.5$.

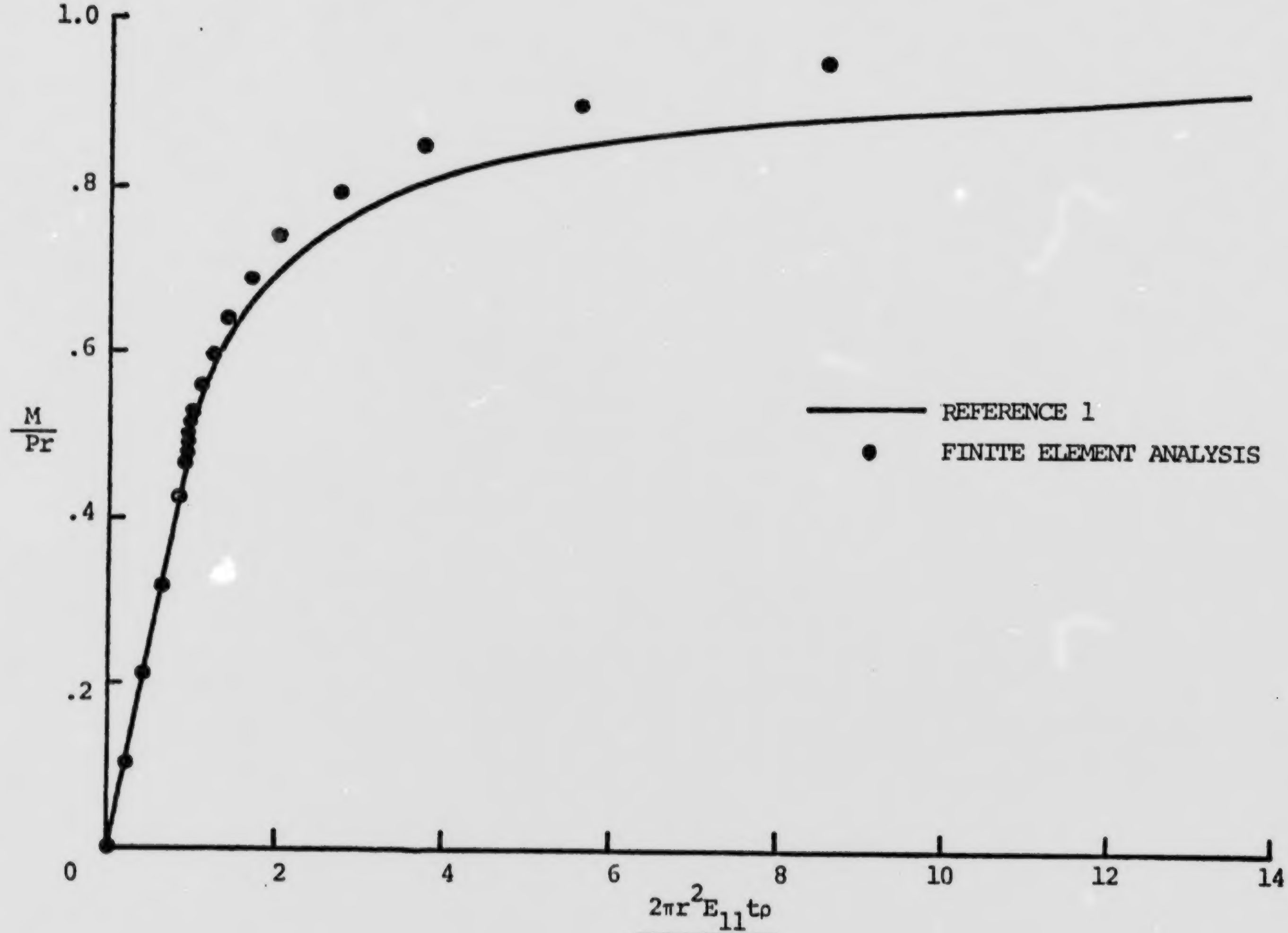

FIG. 5.27 COMPARISON FOR L/r = 5.

MATERIAL PROPERTIES: $E_{11} = E_{22} = 2.28\ (10^9)$ Pa; t = 0.3556 mm;
$\nu_{12} = \nu_{21} = 0.3$.

DIMENSIONS: p = 6.9 (10^4) Pa; P_{ax} = 88960 N; r = 0.762m.

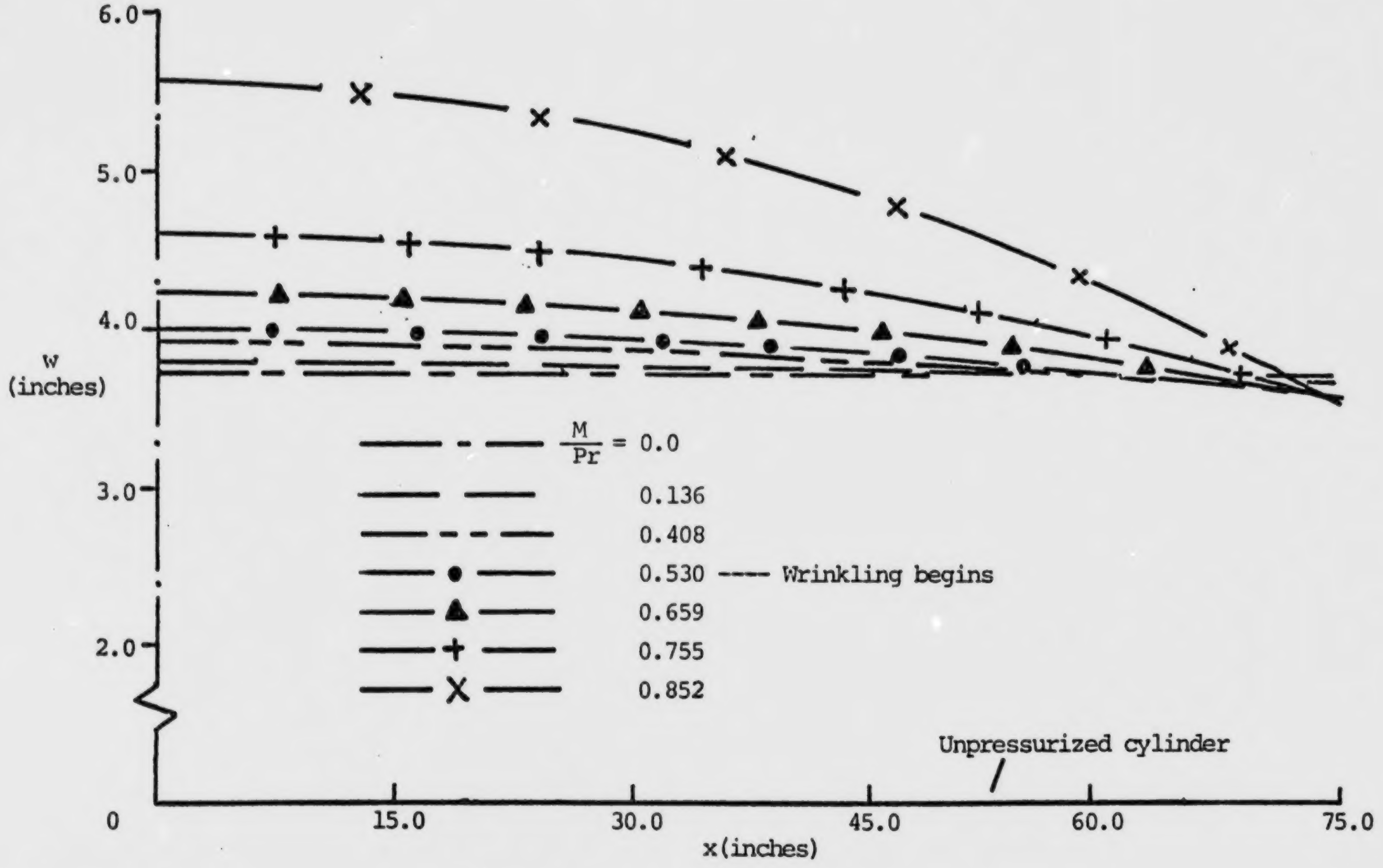

FIG. 5.28 NORMAL DISPLACEMENT VERSUS AXIAL COORDINATE ALONG TOP OF CYLINDER.

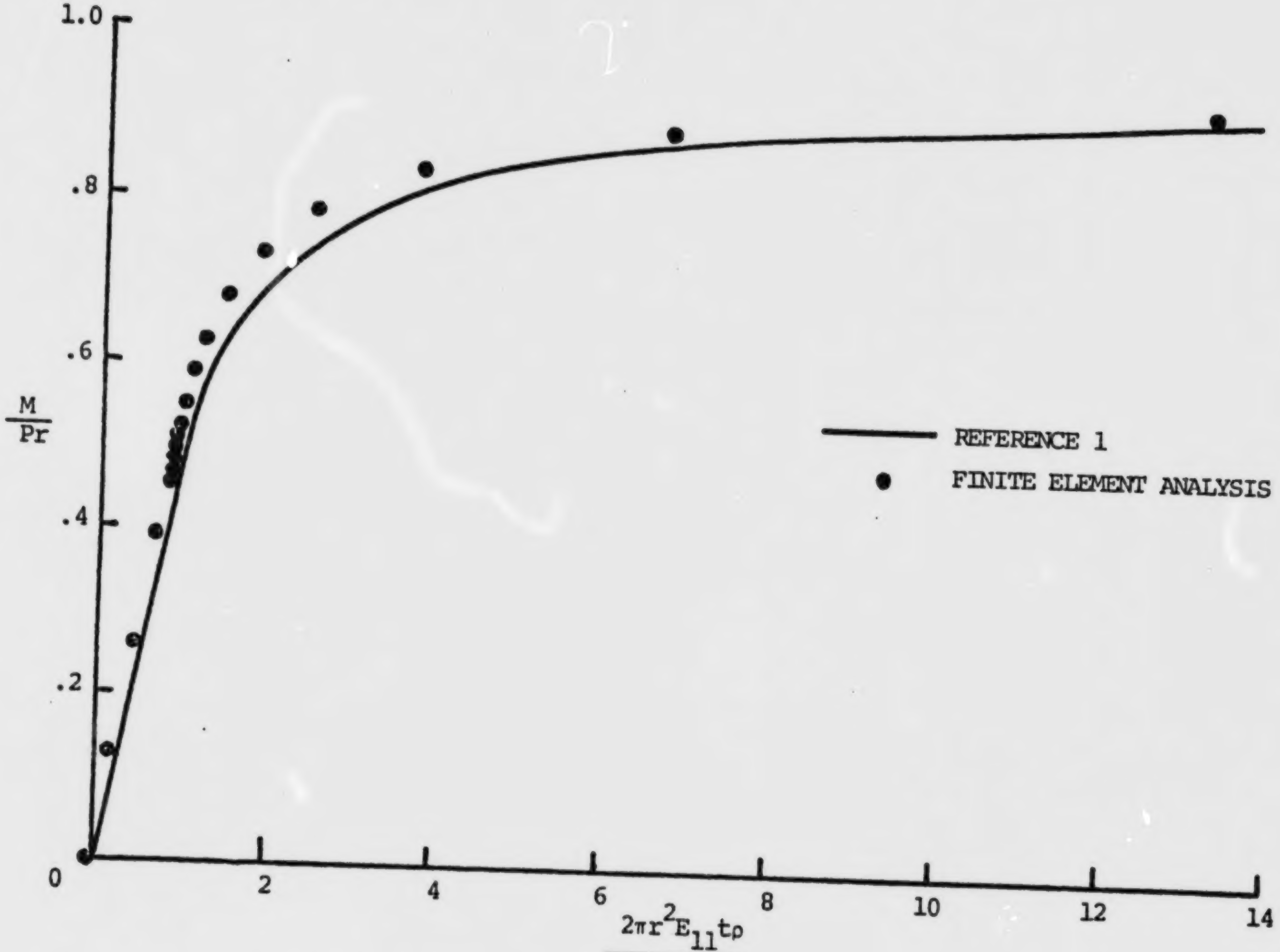

FIG. 5.29 MOMENT-CURVATURE RELATIONSHIP FOR HJ-15 CELL.

MATERIAL PROPERTIES: $E_{11} = E_{22} = 2.21\ (10^8)$ Pa; $t = 0.127$ mm;

$\nu_{12} = \nu_{21} = 0.4$.

DIMENSIONS: $p = 896.4$ Pa; $P_{ax} = 0.0$; $r = 0.914$m; $L/r = 1$.

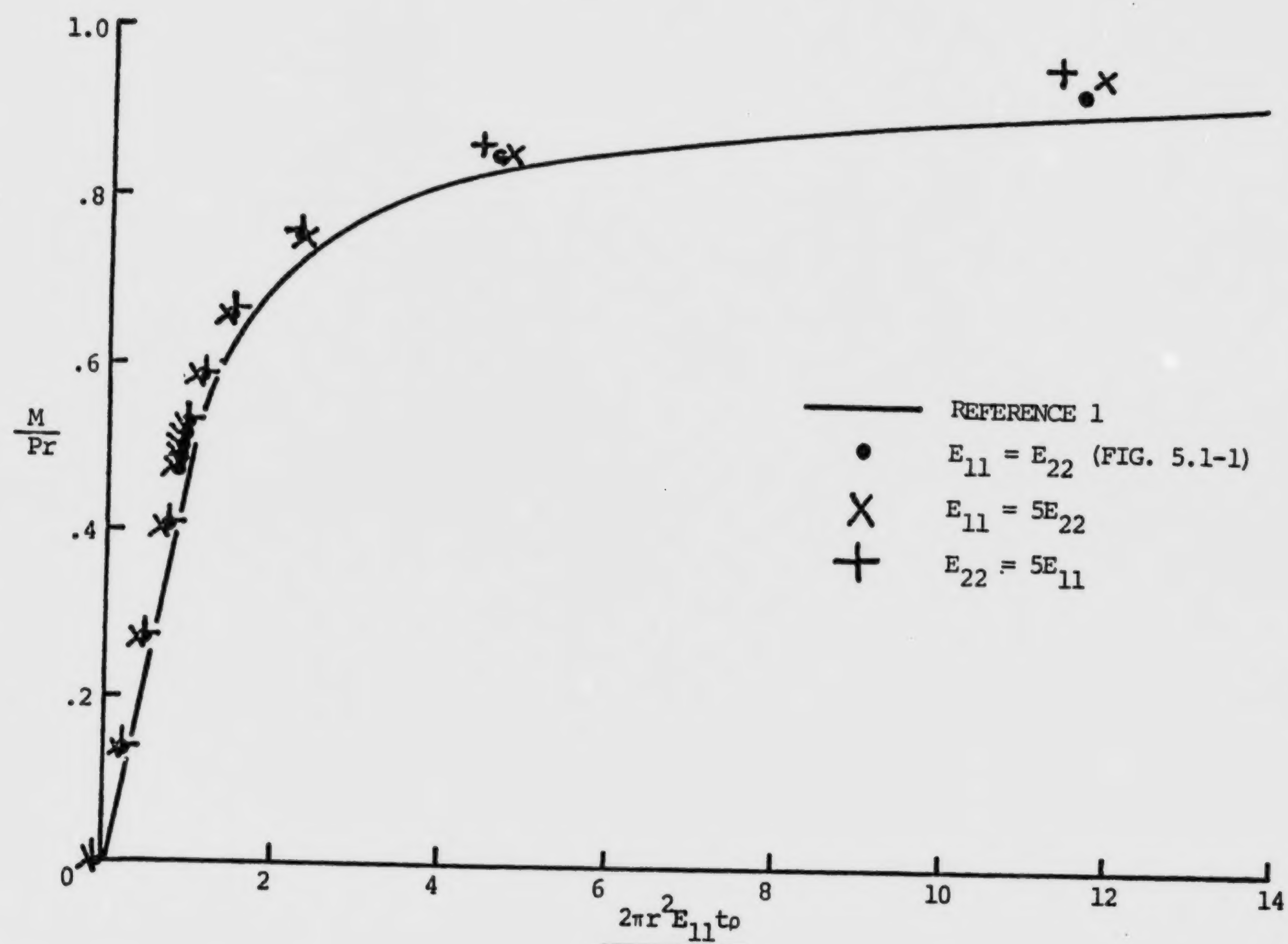

FIG. 5.30 MOMENT-CURVATURE RELATIONSHIP FOR ORTHOTROPIC CYLINDER.

MATERIAL PROPERTIES: $E_{11} = E_{22} = 2.28\ (10^9)$ Pa; $t = 0.3556$ mm; $\nu_{12} = \nu_{21} = 0.3$.

DIMENSIONS: $p = 3.5\ (10^4)$ Pa; $P_{ax} = 1.8\ (10^5)$ N; $r = 1.524$m; $L/r = 2.5$.

$$E_{11} = E_{22} \quad \text{(Figure 5.24)}$$

$$E_{11} = 5E_{22} \tag{45}$$

$$E_{22} = 5E_{11}$$

with the Stein and Hedgepeth curve. For the orthotropic material the shear modulus is approximated by

$$G_{12} = \frac{\sqrt{E_{11}E_{22}}}{2(1 + \sqrt{\nu_{21}\nu_{12}})} \tag{46}$$

All other relevant data were kept the same. Again, we obtain excellent agreement with the standard analytical curve.

appears that there is no effect of varying the moduli as given in equations (45). On the contrary, if one considers the displacements for the three cases one would find that they are completely different. As an example, the normal displacement for the three cases of equation (45) under pressure load only are 0.0946m, 0.0946m and 0.0189m respectively. The x and y displacements are different for all three cases.

This effect is due to the dimensionless curvature parameter

$$\frac{2\pi r^2 t E_{11} \rho}{P} \tag{47}$$

If E_{22} and the applied bending moment are kept constant, as we increase or decrease the modulus in the x-direction, the cylinder will resist more or less the applied moment since the cylinder is stiffer in the x-direction if E_{11} is increased. As it resists more, the curvature of the cylinder tends to be smaller and if it resists less, the curvature will be larger. Therefore, it is a combined $E_{11}\rho$ effect and equation (47) remains constant as E_{11} is varied, keeping everything else constant.

5.5.3) Rectilinear Anisotropic Case

When the material axes do not coincide with the structural axes, the cylinder behaves in a distinctive manner. If the cylinder is only pressurized, it takes a hyperboloidal configuration. Figure 5.31 shows the effect of varying ψ (which is the angle between the material and structural axes). The curvature is extremely high and positive at the top of the cylinder which implies the configuration shown in Figure 5.31 (which is exaggerated for clarification). This effect is also observed for a cylindrical shell under a uniform temperature load [Ref. 5.18]. As ψ is increased from zero (the orthotropic case), the circumferential displacement and the rotations increase drastically compared to the orthotropic material. The circumferential displacement is constrained at the right end of the cylinder and as we approach the mid-length of the cylinder, it increases very quickly. In other words, the material twists as we approach the mid-length of the cylinder. If we could cut the cylinder at various stations along its length and looked at the cross section, approaching from the end, ε would increase from '0' to its highest value at the mid-length (see Figure 5.32). This effect is similar to stretching a rope which is composed of a number of twisted strands.

Due to this twisting effect, half the cylinder must be used to analyze the anisotropic material. The hoop and longitudinal stresses are also nonuniform under a pressure load only. For the isotropic and orthotropic material, the hoop stress resultant is calculated from the simple formula

$$N_\theta = pr \tag{48}$$

and the longitudinal stress resultant by

$$N_x = \frac{pr}{2} - \frac{P_{AX}}{2\pi r} \tag{49}$$

These equations are no longer valid for the anisotropic material. As ψ is increased further from zero, the stresses become more nonuniform.

As we start applying the bending moment, it tends to untwist the cylinder and reduce the curvature slowly. If the moment is further increased, some elements will go in compression. The compression region is also nonuniform. For the isotropic and orthotropic cases, the compression region is always uniform if the l/r ratio is not too high. This is not the case for the anisotropic material. A typical compression region is shown in Figure 5.33. The half cylinder is plotted in the $\tilde{y}$ coordinate system. Since half the cylinder is utilized, both the upper and lower edges of the elements shown in Figure 5.33 represent the bottom centreline of the cylinder. The case shown is for $\psi = 5^\circ$. The increasing numbers shown in different elements demonstrate which elements went into compression as the applied bending moment was increased. If ψ is further increased the compression region can also grow in a band (the X's in Figure 5.33).

This nonuniformity of the compression region complicates matters. A few attempts in the line of Section 5.3.3 of putting different moduli to zero was found to be fruitless and should be a subject for further investigation.

5.6) Suggestions for Future Work

The following are suggestions for future work.

(i) Nonuniformity of Compression Region

A suitable wrinkling criterion for nonuniform wrinkled regions should be investigated due to widespread use of fabric material in ACV skirt systems. This condition is primarily the principal stresses normal to the wrinkled region being zero.

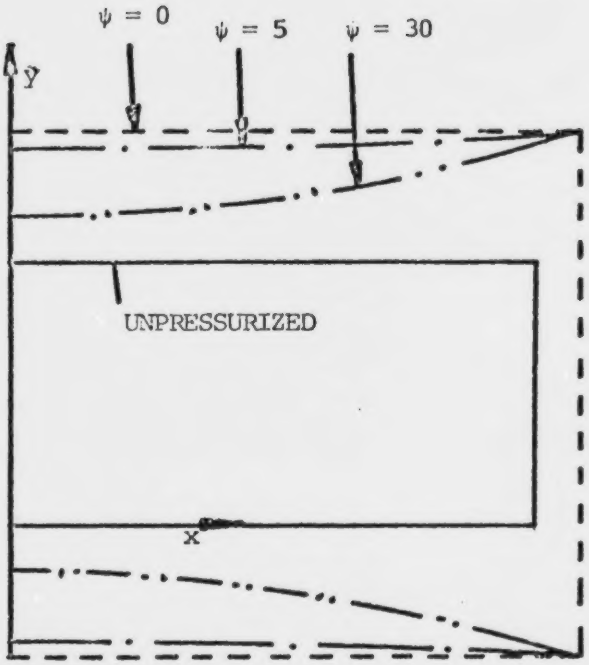
ψ = 0
ψ = 5
ψ = 30
ȳ
UNPRESSURIZED
x

FIG. 5.31 HYPERBOLOIDAL CONFIGURATION OF ANISOTROPIC CYLINDER

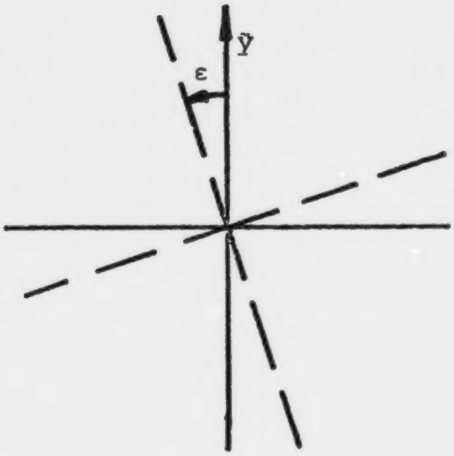

FIG. 5.32 TWISTING OF ANISOTROPIC CYLINDER

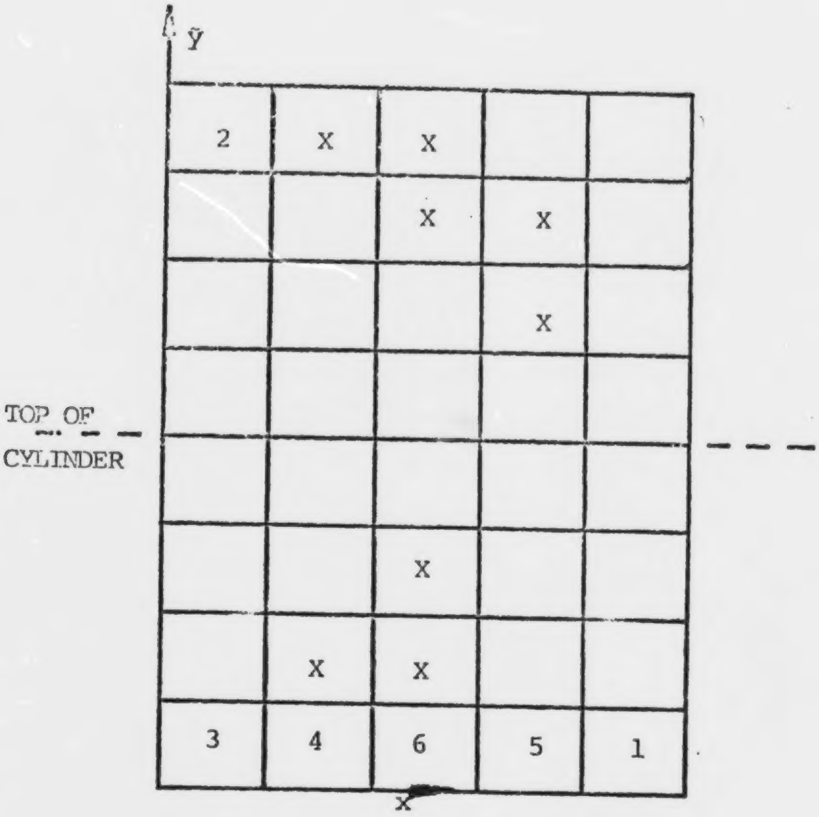
ȳ
2
X
X
X
X
X
TOP OF
CYLINDER
X
X
X
3
4
6
5
1
x̄

FIG. 5.33 NONUNIFORMITY OF COMPRESSION REGION FOR ANISOTROPIC CYLINDER

MATERIAL PROPERTIES: $E_{11} = 1.14\ (10^{10})$Pa; $E_{22}=2.28((10^{9})$; $\nu_{21} = 0.3$;
$G_{12} = 1.53\ (10^{9})$Pa; $t = 0.3556$ mm; $\psi = 5^{0}$

DIMENSIONS: SEE FIG. 5.1-1

(ii) Cone Analysis

One should extend the finite element capability to include the wrinkling analysis of slightly tapered conical shells for isotropic, orthotropic and rectilinear anisotropic materials. Special attention should be given to the bottom boundary condition for this shell since skirt-ground contact tends to stabilize the shell as discussed by Sullivan [Ref. 5.11] and an extension of which is presented in [Ref. 5.22].

(iii) Segmented Skirt

One should study the behaviour of segmented skirts under typical ACV loading. Since most segmented skirts comprise a combination of flat, cylindrical and tapered sections, one should be able to take the analysis of this report in conjunction with item (ii) and study the static case quite easily.

(iv) Dynamic Analysis

As was observed in the experimental study of the conical shell [Ref. 5.11] and the cylinder [Refs. 5.5, 5.6], there appears to be a "creep-wrinkling effect" before collapse occurs. That is, without further loading, the wrinkled region continues to expand until collapse occurs. This may involve viscoelastic phenomena in conjunction with the wrinkling criterion and deserves further attention.

5.7 Conclusions

A finite element analysis for wrinkling of thin pressurized cylindrical shells was developed and the major conclusions are:

(i) The analysis is more general than the Stein and Hedgepeth model since the bending stiffness of the material is retained and small compressive stresses are permissible before wrinkling occurs.

(ii) For length-to-radius ratios less than five, excellent agreement is obtained with the Stein and Hedgepeth model for both isotropic and orthotropic materials. For l/r ratios greater than five the Jahsman effect is observed. This effect can be neglected for ACV applications since the l/r ratios of typical conical cells (HJ-15 and Bertin cell) are of order one.

(iii) The nonuniformity of the compression region, a conical shell configuration and segmented skirt analysis should be subjects for future work.

6) HEAVE STABILITY OVER WATER

6.1) Introduction

When an air cushion vehicle is hovering statically over water, it depresses the water surface, according to Archimedes' principle, as shown in Figure 6.1. If the vehicle is heaving, it will act as a pneumatic wave maker. This is because the heaving motion will cause the pressure acting over the water free-surface directly beneath the vehicle to oscillate, and by classical linearized water wave theory [Refs. 6.1, 6.2] waves will form which travel outward. This wave motion has an associated energy radiation which must be included in a heave stability analysis.

One cannot assume that this energy radiation always has a stabilizing effect on cushion dynamics, or equivalently, that a cushion hovering over water will be stable if it is shown to be stable on land. Recently, Fowler has demonstrated that the converse can be true [Ref. 6.3]. It is noted that this particular stability problem occurs only for cushions hovering at rest or moving forward at very slow speeds. For a vehicle at a high enough speed the water has no time to react to the vehicle motion.

6.2) Pressure-Water Surface Interaction

It is assumed that the cushion pressure-water surface interaction can be dealt with using classical linearized water wave theory [Ref. 6.2], and that the air cushion vehicle can be approximated by the two dimensional inverted box configuration shown schematically in Figure 6.2. This is the air cushion model used by Ogilvie [Ref. 6.4], who studied the frequency response of the water free surface directly beneath the model when it was subjected to a sinusoidal cushion pressure variation. He considered both zero and nonzero lip immersion cases and suggested that for large low pressure air cushion vehicles the zero lip immersion analysis should be adequate. He noted that nonzero lip immersion generally reduces the amplitude of generated waves but for certain wave lengths there can be wave amplitude augmentation or resonance.

The frequency response function developed by Ogilvie [Ref. 6.4] for the 'zero' lip immersion case is used here to examine the heave stability of an air cushion vehicle hovering over water. As noted above, the frequency response function is based on classical linearized water wave theory, which is in turn based on potential flow theory for an incompressible ideal fluid where one is interested in finding a velocity potential Φ which satisfies Laplace's equation

$$\nabla^2\Phi = 0 \quad \text{for } y < 0 \tag{1}$$

subject to the dynamical free surface or pressure condition

$$\Delta\eta = -\frac{1}{g}\Phi_t - \frac{\Delta p}{\rho_w g} \tag{2}$$

and to the kinematic free surface or displacement condition

$$\Delta\eta_t = \Phi_y \tag{3}$$

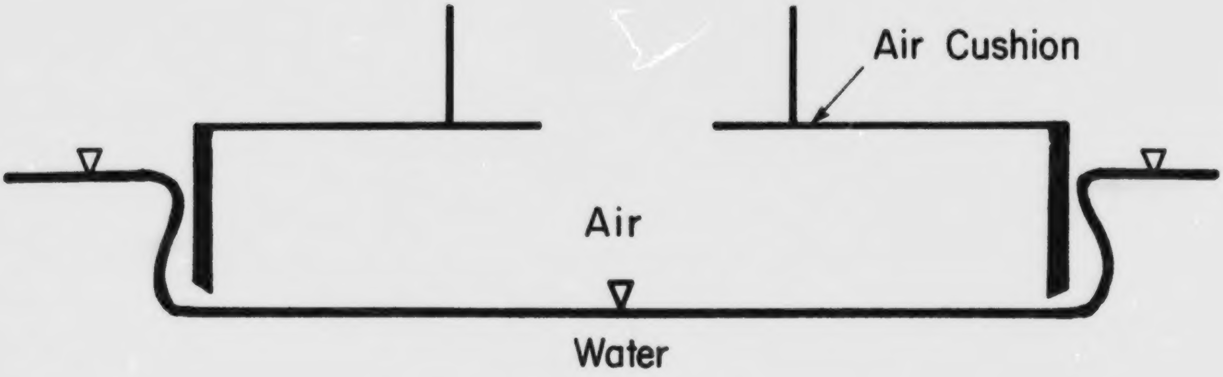
Air Cushion
Air
Water

FIGURE 6.1 AIR CUSHION HOVERING OVER WATER AT ZERO FORWARD SPEED.

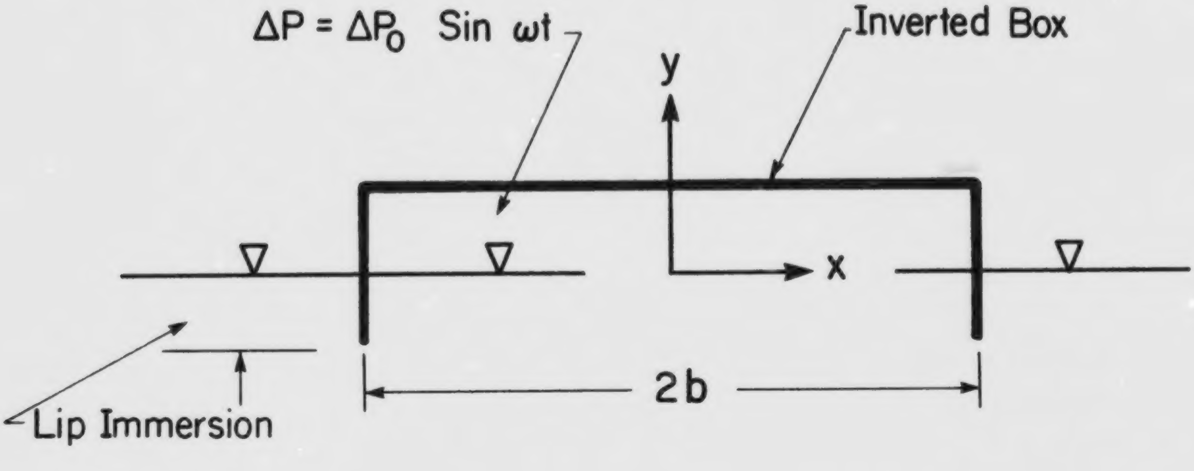
$\Delta P = \Delta P_0$ Sin ωt
Inverted Box
y
x
2b
Lip Immersion

FIGURE 6.2 INVERTED BOX AT THE SURFACE OF AN INFINITELY DEEP INFINITE EXPANSE OF WATER.

where

$$\begin{aligned} \Delta p &= \Delta p_c \sin\omega t \qquad |x| < b \\ &= 0 \qquad\qquad\quad\; |x| > b \end{aligned} \tag{4}$$

where $\Delta\eta$ is the deflection of the water surface from its reference $(y = 0)$ position, b is the vehicle semi-width, Δp_c is the amplitude of the cushion pressure oscillation, g is the acceleration due to gravity, and ρ_w is the density of water. The subscripts t and y indicate partial derivatives with respect to time and the vertical coordinate respectively. By letting

$$\Phi(x, y, t) = \Phi_1(x, y)\sin\omega t + \Phi_2(x, y)\cos\omega t \tag{5}$$

it follows that

$$\Phi_{1y} - \nu\Phi_1 = 0 \qquad -\infty < x < \infty,\ y = 0 \tag{6.1}$$

$$\begin{aligned} \Phi_{2y} - \nu\Phi_2 &= \frac{-\omega\ \Delta p_c}{\rho_w g} \qquad |x| < b,\ y = 0 \\ &= 0 \qquad\qquad\quad |x| > b,\ y = 0 \end{aligned} \tag{6.2}$$

where

$$\nu = \frac{\omega^2}{g} \tag{7}$$

is the wave number of generated waves. The latter is related to the wavelength λ by

$$\lambda = \frac{2\pi}{\nu} \tag{8}$$

To obtain a unique solution, Ogilvie [Ref. 6.4], following Stoker's work [Ref. 6.1], assumed the water to be initially at rest and enforced the condition that there be only outgoing waves at $|x| = \infty$. This is in contrast to Lamb [Ref. 6.2] who assumed fictitious damping forces in order to be rid of free oscillations and thus achieve a unique solution. The above conditions together with the requirement that the fluid velocity must vanish as $y \to -\infty$ gave [Ref. 6.4]

$$\Phi_1(x, y) = \frac{-2\Delta p_c}{\rho_w \omega} \sin\nu b\ e^{\nu y} \cos\nu x \tag{9.1}$$

$$\Phi_2(x, y) = \mathrm{Re}[f(z)] - \frac{2\Delta p_o}{\rho_w \omega} \sin\nu b \; e^{\nu y} \sin\nu x \tag{9.2}$$

where

$$f(z) = \frac{-\omega \, \Delta p_o}{\pi \rho_w g} e^{-j\nu z} \int_{j\infty}^{z} e^{j\nu t} \, \mathrm{Ln} \frac{t - b}{t + b} \, dt \tag{10}$$

and

$$z = x + jy \tag{11}$$

Substitution into the dynamical condition gave for $|x| < b$ the water surface deflection [Ref. 6.4]

$$\Delta\eta(x, t) = \left[\frac{-\Delta p_o}{\rho_w g} (1 + 2\sin\nu b \, \sin\nu x) + \frac{\omega}{g} \mathrm{Re}[f(x - jo)] \right] \sin\omega t$$

$$+ \left[\frac{2\Delta p_o}{\rho_w g} \sin\nu b \, \cos\nu x \right] \cos\omega t \tag{12}$$

This expression is singular at each of the lips. However, as noted by Ogilvie [Ref. 6.4], the singularities are very weak, and the errors introduced should be local in scope. Ogilvie [Ref. 6.4] showed how for the air cushion problem one could integrate from $x = -b$ to $x = b$ to obtain an average piston-like deflection

$$\overline{\Delta\eta}(t) = \frac{1}{2b} \int_{-b}^{b} \Delta\eta(x, t) dx = \frac{2\Delta p_o}{\rho_w g \, \nu b} \Big[\sin^2 \nu b \, \cos\omega t$$

$$+ \frac{1}{2\pi} [C_e + \mathrm{Ln}(2\nu b) + g(2\nu b)] \sin\omega t$$

$$- \sin\nu b \, \cos\nu b \, \sin\omega t \Big] \tag{13}$$

where C_e = Euler's constant = 0.577216 and

$$g(x) = \int_{0}^{\infty} \frac{u e^{-xu}}{u^2 + 1} \, du \tag{14}$$

Equation (13) can be rewritten in complex notation as

$$\frac{\overline{\Delta\eta}(j\omega)}{\Delta p(j\omega)} = N(j\omega) \tag{15}$$

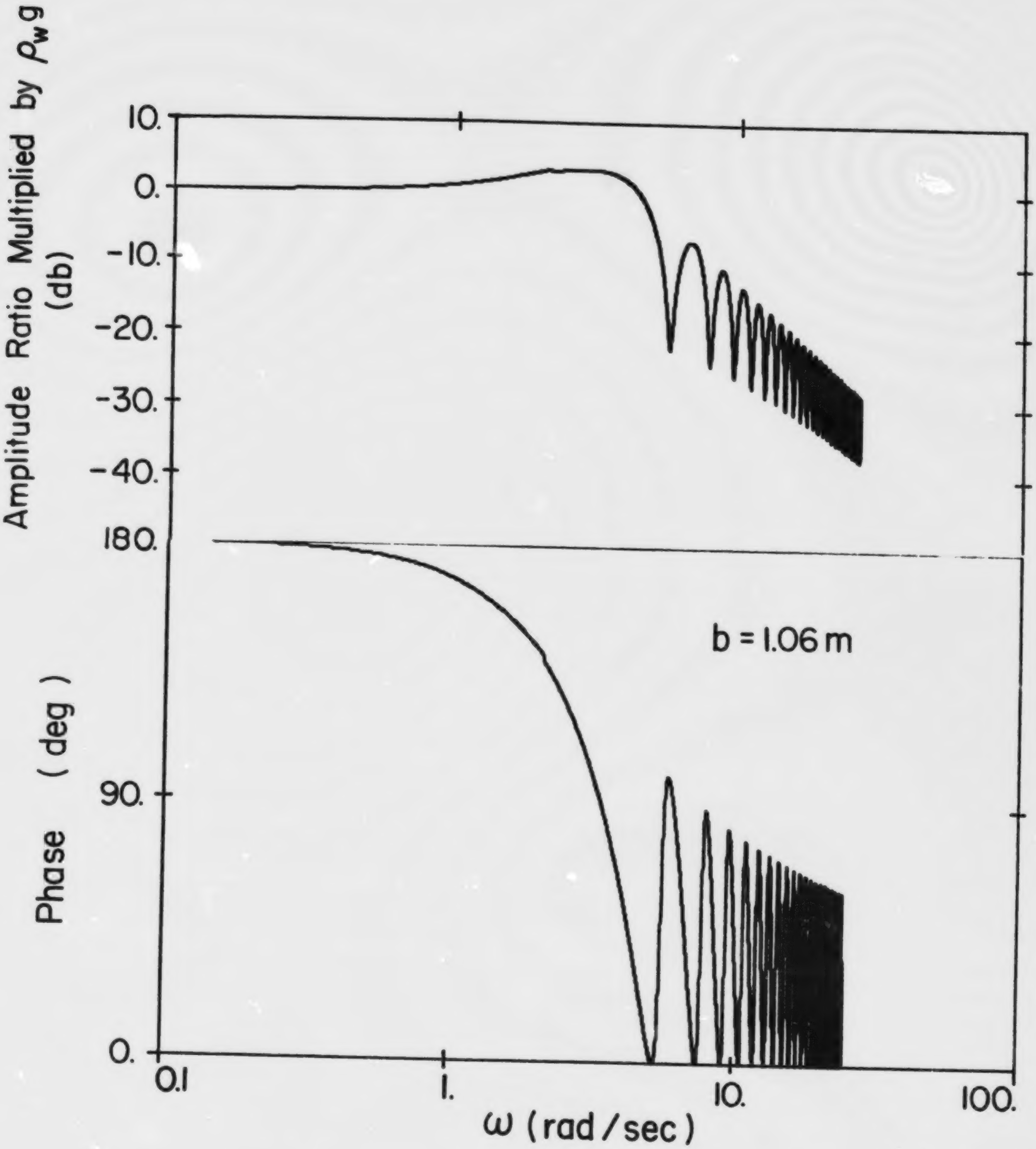

FIGURE 6.3 WATER COMPLIANCE FREQUENCY RESPONSE FUNCTION.

where

$$N(j\omega) = A + Bj \tag{16}$$

where

$$A = \frac{2}{\rho_w g \nu b}\left[\frac{1}{2\pi}\left[C_e + \mathrm{Ln}(2\nu b) + g(2\nu b)\right] - \sin\nu b\,\cos\nu b\right] \tag{17.1}$$

$$B = \frac{2}{\rho_w g \nu b}\sin^2\nu b \tag{17.2}$$

6.3) Lip Flow

The flow under the lip of an air cushion vehicle hovering over water usually consists of an air-water spray. It may also be inherently unsteady because of water surface deflections at the lip; the flow modulation produced by these deflections would cause cushion pressure oscillations which in turn would produce more deflections. Probably, the simplest conceptual model for steady lip flow is that shown in Figure 6.4. There it is assumed that the water-free surface forms a channel through which the cushion air flows and the hydrostatic pressure impresses itself along the channel. If the latter is the case, then the air in the channel must accelerate according to Bernoulli's law, and this in turn implies that the channel must be converging as shown. If this model gave an adequate representation of the actual flow, then one could write for steady flow

$$Q_a = C_m \ell h \sqrt{\frac{2p_c}{\rho_a}} \tag{18}$$

where C_m could be measured experimentally. Here, it is assumed that this is the case. In fact, to study the effect of the pressure-water surface interaction on heave stability, it is further assumed that the model is also adequate for unsteady operation. Also, to simplify, the direct modulation of the flow by the water surface motion at the lip is ignored, even though equation (12) could be used to take this modulation into account. However, the latter step is questionable because the analysis upon which equation (12) is based is suspect for the near lip region [Ref. 6.4].

6.4 Stability Considerations

The linear lumped capacitance-resistance model for a unit length of an infinite length vehicle is used; its governing equations are:

$$C_c\frac{d\Delta p_c}{dt} = (\Delta Q_c - \Delta Q_a) - 2b\left(\frac{d\Delta h}{dt} - \frac{d\overline{\Delta\eta}}{dt}\right) \tag{19}$$

$$m\frac{d^2\Delta h}{dt^2} = 2b\,\Delta p_c + \text{Damping Forces} \tag{20}$$

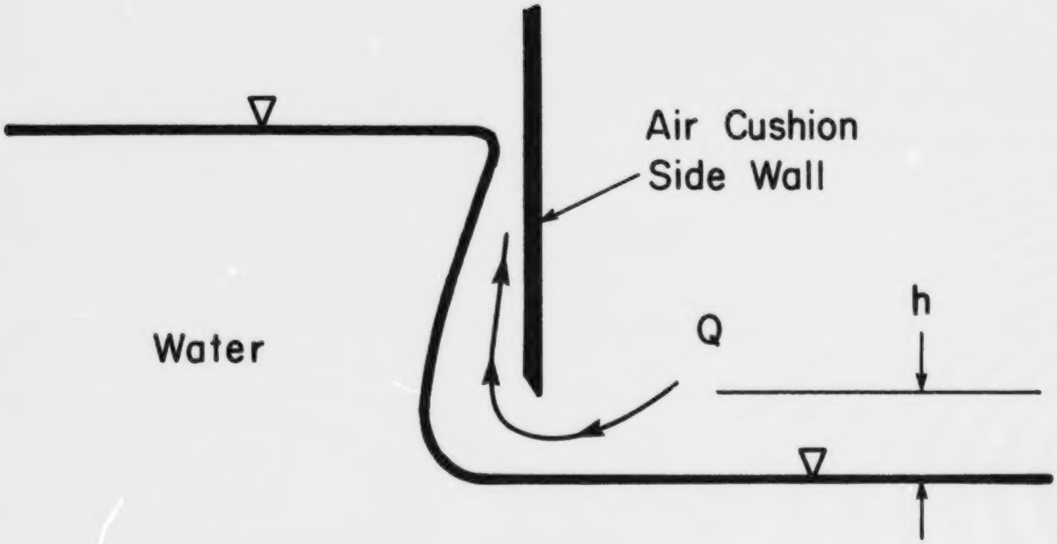
Air Cushion
Side Wall
Water
Q
h

FIGURE 6.4 SIMPLE MODEL OF AIR ESCAPE UNDER CUSHION LID.

where

$$C_c = \frac{\forall_{cc}}{\rho_a a^2} \qquad \text{Lumped Capacitance} \qquad (21.1)$$

$$a = \sqrt{\gamma RT} \qquad \text{Air Sound Speed} \qquad (21.2)$$

$$\Delta Q_c = \frac{-\Delta p_c}{R_c - C_{PQ}} \qquad \text{Inlet Flow} \qquad (21.3)$$

$$\Delta Q_a = \frac{\Delta p_c}{R_a} + \frac{\Delta h}{\alpha_a} \qquad \text{Lip Flow} \qquad (21.4)$$

where

$$R_c = \frac{2(p_{fe} - p_{ce})}{Q_e}, \quad R_a = \frac{2p_{ce}}{Q_e}, \quad \alpha_a = \frac{h_e}{Q_e} \qquad (22)$$

Due to a lack of information concerning the damping forces in equation (20), for the present work they are assumed to be negligible. However, in practice, they may be quite significant. Possible sources for these include spray formation, skirt deflections with hysteresis, and skirt-water contact.

Now, by introducing the Laplace variable s and noting that at a stability boundary $s = j\omega$, equations (19) and (20) reduce to

$$C_c j\omega \, \Delta p_c(j\omega) = \frac{-\Delta p_c(j\omega)}{R_c - C_{PQ}} - \frac{\Delta p_c(j\omega)}{R_a} - \frac{\Delta h(j\omega)}{\alpha_a} - 2b \, j\omega[\Delta h(j\omega) - \overline{\Delta\eta}(j\omega)] \qquad (23)$$

$$-m\omega^2 \Delta h(j\omega) = 2b \, \Delta p_c(j\omega) \qquad (24)$$

The water compliance model gives

$$\overline{\Delta\eta}(j\omega) = (A + Bj)\Delta p_c(j\omega) \qquad (25)$$

Substitution of equations (25) and (24) into equation (23) gives

$$\left[\left(A2b\omega + \frac{(2b)^2}{m\omega} - C_c\omega \right) j - \left(\frac{1}{R_c - C_{PQ}} + \frac{1}{R_a} - \frac{2b}{m\omega^2}\frac{1}{\alpha_a} + B2b\omega \right)\right] \Delta p_c(j\omega) = 0 \qquad (26)$$

For a nontrivial solution, both the real and imaginary parts of the expression in square brackets must vanish. Thus one must have

$$A2b\omega + \frac{(2b)^2}{m\omega} - C_c\omega = 0 \tag{27.1}$$

$$\frac{1}{R_c - C_{PQ}} + \frac{1}{R_a} - \frac{2b}{m\omega^2}\frac{1}{\alpha_a} + B2b\omega = 0 \tag{27.2}$$

When the equilibrium hover-gap h_e is specified, the remaining unknowns in equations (27) are p_{ce} and ω. A numerical search of the (p_{ce}-ω) plane is used to obtain a solution. For this, p_{ce} is increased in small steps from a very small value, and for each discrete value the values of the left hand side of equations (27) are calculated for a range of frequencies. Unfortunately, the technique of setting $s = j\omega$ to find a stability boundary has a number of limitations, one of which is associated with the fact that equations (27) are satisfied when any root of the system characteristic equation lies on the imaginary axis in the s-plane, which implies that the solution of equations (27) does not necessarily represent a stability boundary. This problem circumvented here by multiplying the coefficients A and B of the water compliance function by a factor β. With $\beta = 0$, the water compliance effect is effectively removed and one is left with the case of an air cushion vehicle hovering over a rigid surface. The value of p_{ce} for critical stability for this case as obtained by the Routh Hurwitz criteria should agree with the prediction of equations (27). This was found to be the case.

6.5) Results for HEX-5

The theory was applied to a unit length of the HEX-5 amphibious air cushion vehicle [Ref. 6.3]. As the HEX-5 has a finite length, it is to be expected that the theoretical results can at best be of only a qualitative value. For the hover-gaps considered it was generally found that the effect of the water surface-pressure interaction was a sometimes many-fold increase in critical stability pressure relative to overland operation. However, as noted above [Ref. 6.3], the HEX-5, which has never been unstable overland, is often unstable over water. This would lead one to conclude that either the stability analysis is incorrect or some important parameter has been excluded.

The frequencies obtained from typical numerical solutions are of the order of 3 Hz. At such frequencies, $N(j\omega)$ can be used to show that the average water surface motion is often in phase with cushion pressure. In other words, when the cushion pressure is increasing, the average water surface is actually moving upward. This is very much like a skirt flexibility where an increase in cushion pressure causes the cushion volume to decrease. As shown in [Ref. 6.5] such a flexibility is stabilizing, so this explains why, for some hover-gaps at any rate, the water surface-pressure interaction model has a stabilizing influence. This point can be further illustrated by rearranging equations (27) to obtain

$$(A2b - C_c)\omega^2 + \frac{(2b)^2}{m} = 0 \tag{28.1}$$

and

$$\omega^2 = \frac{\dfrac{2b}{m\alpha_a}}{\left(\dfrac{1}{R_c - C_{PQ}} + \dfrac{1}{R_a} + B2b\omega \right)} \qquad (28.2)$$

Equation (28.2) into equation (28.1) gives after some simplification

$$\underbrace{\frac{A2b - C_c}{\left(\dfrac{1}{R_c - C_{PQ}} + \dfrac{1}{R_a} + B2b\omega \right)}}_{I} + \underbrace{2b\alpha_a}_{II} = 0 \qquad (29)$$

For frequencies of the order of 3 Hz, both A and B are positive. This implies that the effect of the water surface compliance model is a reduction in the magnitude of the first term relative to overland operation. But, in [6.5],where overland operation was treated, the first term was shown to be effectively a negative damping term. As the water surface compliance model tends to reduce this term, one would expect increased stability.

6.6) Discussion

Two important assumptions which may be responsible for the discrepancy between predicted and observed behaviour are the lip flow assumption and the lip immersion assumption. One could use equation (12) to deal with the direct modulation of the lip flow by the water surface motion. However, such a step is questionable because the potential flow analysis is suspect near the lip. Nevertheless it could possibly predict trends adequately and therefore should be attempted.

REFERENCES

Section 1

1.1 Sullivan, P. A., Hinchey, M. J., Delaney, R. G., "An Investigation of the Roll Stiffness Characteristics of Three Flexible Skirted Systems", UTIAS Report No. 213, March 1977; TDC Contract D-500-203-1.

1.2 Sullivan, P. A.,Hinchey, M. J., Murra, I., Parravano, G. J., "Research on the Stability of Air Cushion Systems", TDC File D 500-308, UTIAS Report No. 238, Nov. 1979.

1.3 Sullivan, P. A., Hinchey, M. J., Hartmann, P. V., Dupuis, A., "Research into Air Cushion Stability: 1978 Report", Jan. 1981, TDC Contract D-500-431-1, TP 1760.

1.4 Ribner, D., "A Remote Data Acquisition and Control System", M.A.Sc. Thesis, Dept. of Electrical Engineering, University of Toronto, July 1980.

Section 2

2.1 Sullivan, P. A., Hinchey, M. J., Hartman, P. V., and Dupuis, A., "Research on Air Cushion Stability - 1978", Transportation Development Centre, Contract Report TP 1760, TDC-File D-500-431-1.

2.2 Sweet, L. M., Richardson, H. H., and Wormley, D. N., "Plenum Air Cushions/Compressor-Duct Interactions", American Society of Mechanical Engineers, Paper 75-WA/AUT-23, 1975.

2.3 Hinchey, M. J., "Heave Instabilities of Amphibious Air Cushion Suspension Systems", University of Toronto, Institute for Aerospace Studies, Report No. 246, November 1980.

2.4 Fowler, H. S., "The Caspar Research Project: The Multicell Skirt, A Summary", National Research Council of Canada Associate Committee on Air Cushion Technology, Report 5-76, 1976

2.5 Durkin, J., and Langhi, W., "An Investigation of the Performance of a Centrifugal Lift Fan Operating Against a Sinusoidally Varying Back Pressure", Presented at the Sixth Canadian Symposium on Air Cushion Technology, Canadian Aeronautics and Space Institute, September 1974.

2.6 Wheeler, R., "Recent United Kingdom Hovercraft Development", Journal of Hydronautics, Vol. 12, No. 1, pp. 3-17, January 1978.

2.7 Goldschmied, F. R., and Wormley, D. N., "Frequency Response of Blower/Duct Plenum Fluid Systems", Journal of Hydronautics, Vol. 11, No. 1, pp. 18-27, January 1977.

2.8 Thompson, W. C., Boghani, A. B., and Leland, T. J. W., "Experimental and Analytical Dynamic Flow Characteristics of an Axial-Flow Fan from an Air Cushion Landing System Model", National Aeronautics and Space Administration, Technical Note TN D-8413, July 1977.

2.9 Hinchey, M., and Sullivan, P. A., "Duct Effects on the Dynamic Fan Characteristics of Air Cushions", Journal of Hydronautics, Vol. 13, No. 1, pp. 28-29, January 1979.

2.10 Ohashi, H., "Analytical and Experimental Study of the Dynamic Characteristics of Turbopumps", National Aeronautics and Space Administration, Technical Note TN D-4298, April 1968.

2.11 Benson, R., and Whitfield, A., "An Experimental Investigation of the Non-Steady Flow Characteristics of a Centrifugal Compressor", University of Manchester, IST 1965.

2.12 Wylie, E. B., and Streeter, V. L., Hydraulic Transients, McGraw-Hill, New York, 1978.

2.13 Gosman, A., and Ideriah, F., "Teach-T: A General Computer Program for Two-Dimensional Turbulent, Recirculating Flows", Department of Mechanical Engineering, Imperial College, London, 1976.

2.14 Ribich, W. A. and Richardson, H. H., "Dynamic Analysis of Heave Motion for a Transport Vehicle Fluid Suspension", Department of Mechanical Engineering, Massachusetts Institute of Technology, Contract C-85-65, 1967.

2.15 Birkhoff, G., and Zarantonello, E., Jets, Wakes and Cavities, Academic Press, New York, 1957.

2.16 Sullivan, P. A., and Parravano, G. J., "A Theoretical and Experimental Investigation of a Hinged Lip Tracked Air Cushion Vehicle Suspension System", Transportation Development Centre, Contract Report D-[illegible]00-210-2, March 1977.

2.17 Ower, E., and Pankhurst, R., The Measurement of Air Flow, Pergamon Press, Oxford, 1966.

2.18 ———— "Flow Meter Computation Handbook", American Society of Mechanical Engineers, New York, 1961.

2.19 Green, G., "Measurement of Heave Stability Boundaries of a Duct-Plenum System", University of Toronto, Faculty of Applied Science and Engineering, Bachelor's Thesis, 1979.

2.20 Graham, T. A., "The Effects of Skirt Material Choice on the Heave Stability of an Air Cushion", M.A.Sc. Thesis, University of Toronto, Institute for Aerospace Studies, 1980.

Section 3

3.1 Sullivan, P. A., Hinchey, M. J., and Delaney, R. G., "An Investigation of the Roll Stiffness Characteristics of Three Flexible Skirted Cushion Systems", University of Toronto, Institute for Aerospace Studies, Report No. 213, March 1977, TDC Contract D-500-201.

3.2 Rapson, J. E., Hovercraft Development Limited, U.K., Private Communication.

3.3 Fowler, H. S., National Research Council of Canada, Private Communication.

3.4 Sullivan, P. A., Hinchey, M. J., Murra, I., and Parravano, G. J., "Research on the Stability of Air Cushion Systems", University of Toronto, Institute for Aerospace Studies, Report No. 238, November 1979.

3.5 Elsely, G. H., and Devereaux, A. J., Hovercraft Design and Construction, David and Charles, London, England, 1968.

Section 4

4.1 Ribner, D. B., "A Remote Data Acquisition and Control System", University of Toronto, Institute for Aerospace Studies, M.A.Sc. Thesis, July 1980.

4.2 Sullivan, P. A., Hinchey, M. J. and Delaney, R. G., "An Investigation of the Roll Stiffness Characteristics of Three Flexible Skirted Cushion Systems", UTIAS Report No. 213, March 1977, Transportation and Development Centre, Contract D-500-203-1

4.3 Sullivan, P. A., Hinchey, M. J., Murra, I., and Parravano, G. J. "Research on the Stability of Air Cushion Systems , UTIAS Report No. 238, November 1979, Transportation and Development Centre, Contract D-500-308.

4.4 Hartmann, P. V., "Application of System Parameter Identification Methods to the Determination of Dynamic Pitch-Heave Characteristics of an ACV", M.A.Sc. Thesis, University of Toronto, Institute for Aerospace Studies, June 1979.

Section 5

5.1 Stein, M., and Hedgepeth, J. M., "Analysis of Partly Wrinkled Membranes", National Aeronautics and Space Administration, TN D-813, 1961.

5.2 McComb, H. G. Jr., Zender, G. W., and Mikulas, M. M. Jr., "The Membrane Approach to Bending Instability of Pressurized Cylindrical Shells", Collected Papers on Instability of Shell Structures, National Aeronautics and Space Administration, TN D-1510, pp. 229-237, 1962.

5.3 Peery, J. D., "Post-Buckling Strength of a Pressurized Cylinder", Rep. GD/A-DDG-024A, General Dynamics/Astronautics, National Aeronautics and Space Administration, CR-54802, October 1964.

5.4 Wang, C., Applied Elasticity, McGraw-Hill, New York, pp. 350-352, 1953.

5.5 Jahsman, W. E., "Combined Bending and Compression of a Pressurized Cylindrical Membrane Column", Transactions of the ASME, Journal of Engineering for Industry, pp. 372-378, August 1965.

5.6 Leaumont, N. J. Jr., "Collapse Tests of Pressurized Membrane-Like Circular Cylinder for Combined Compression and Bending", National Aeronautics and Space Administration, TN D-2814, May 1965.

5.7 Miller, R. P., "Experimental Bending Strength of an ATLAS LV-3C Booster Beyond Compression Skin Wrinkling", National Aeronautics and Space Administration, TN D-5156, April 1969.

5.8 Webb, J., "Moment-Curvature Relationship of Inflated 'Mattress' Type Beams with Nonlinear Material Properties", Cranfield Institute of Technology, Cranfield, Memo No. S1, July 1971.

5.9 Mikulas, M. M. Jr., "Behaviour of a Flat Stretched Membrane Wrinkled by the Rotation of an Attached Hub", National Aeronautics and Space Administration, TN D-2456, September 1964.

5.10 Gerden, J. C., and Sazawal, V. K., "A Review of Creep Instability in High-Temperature Piping and Pressure Vessels", Welding Research Council, Bulletin 195, pp. 33-55, 1974.

5.11 Sullivan, P. A., Hinchey, M. J., Murra, I., and Parravano, G. J., "Research on the Stability of Air Cushion Systems", University of Toronto, Institute for Aerospace Studies, Report No. 238, November 1979.

5.12 Flugge, W., Stresses in Shells, Springer-Verlag, Berlin, 1962.

5.13 Seide, P., "A Survey of Buckling Theory and Experiments for Circular Conical Shells of Constant Thickness", National Aeronautics and Space Administration, TN D-1510, pp. 401-426, 1962.

5.14 Heppler, G. H., "Report on the Development of a 24 Degree of Freedom Curvilinear Shell Finite Element for Use in Analyzing Linear Elastic Isotropic Thin Shell Structures", Course AER 2057S, University of Toronto, June 1980.

5.15 Nanyaro, P. A., "Curvilinear Thin Plate Orthotropic Finite Element", Course AER 2057S, University of Toronto, June 1980.

5.16 Timoshenko, S., and Woinowsky-Krieger, S., Theory of Plates and Shells, McGraw-Hill, New York, p. 471, 1959.

5.17 Krauss, H., Thin Elastic Shells, John Wiley and Sons Inc., New York, pp. 89-94, 1967.

5.18 Hansen, J. S., University of Toronto, Institute for Aerospace Studies, Private Communication.

5.19 Hinchey, M. J., "Heave Stability of Amphibious Air Cushion Suspension Systems", Ph.D. Thesis, *University of Toronto*, 1979.

5.20 Bogner, F. K., Fox, R. L., and Schmit, L. A. Jr., "The Generation of Inter-Element-Compatible Stiffness and Mass Matrices by Use of Interpolation Formulas", Proc. Conf. Matrix Methods in Struc. Mech., Air Force Flight Dynamics Laboratory, Air Institute of Technology, AFFDL-TR-66-80.

5.21 Ashton, J. E., Halpin, J. C., and Petit, P. H., *Primer on Composite Materials: Analysis*, Technomic Publishing Co., *U.S.A., 1969.*

5.22 Sullivan, P. A., Hinchey, M. J., Hartmann, P. V., and Dupuis, A., "Research into Air Cushion Stability - 1978", *Transportation Development Centre*, Contract Report TP 1760, TDC-File D-500-431-1.

Section 6

6.1 Stocker, J. J., *Water Waves - The Mathematical Theory with Applications*, Interscience Publishers, Pure and Applied Mathematics Series, Vol. IV, 1957.

6.2 Lamb, H., "On Deep Water Waves", *Proceedings of the London Mathematical Society*, Ser. 2, Vol. 2, 1904.

6.3 Fowler, H., "An Experiment on the Heave Oscillation of a Light Air Cushion Vehicle over Water", *Canadian Aeronautics and Space Journal*, Vol. 2, No. 2, Second Quarter, 1980.

6.4 Ogilvie, T. F., "Oscillating Pressure Fields on a Free Surface", Department of Naval Architecture and Marine Engineering, *College of Engineering, University of Michigan*, Sept. 1969.

6.5 Hinchey, M. J., "Heave Instabilities of Amphibious Air Cushion Suspension Systems, Ph.D. Thesis, *University of Toronto*, 1979.

Appendix D

D.1 Pellegrin, M. T., and Bajura, R. A., "Pulsating Flow of an Incompressible Fluid Through a Sharp-Edge Orifice Meter", *West Virginia University* Report ENG-74-10399-A, 1976.

D.2 Kinsler, L. E., and Frey, A. R., *Fundamentals of Acoustics*, John Wiley & Sons, 1962, p. 186.

D.3 Ingard, V., and Ising, H., "Acoustic Nonlinearity of an Orifice", *Journal of the Acoustical Society of America*, Vol. 42, No. 1, 1967.

APPENDIX A

CONTRACT WORK STATEMENT

A.1 OBJECTIVES

The objectives of the program specific to each of three projects to be carried out are:

A.1.1 Provide stability limits of vehicle equipped with HDL type segmented skirts, as designed by Hoverlift Systems Ltd., with regard to vehicle inertias, cushion air flow and vehicle forward speed.

A.1.2 Provide mathematical criteria predicting flow instability in the pneumatic circuit of air cushion vehicles, with regard to specific features such as restrictions, resonators and friction losses.

A.1.3 Provide a description and mathematical treatment of the stability of flexible skirt material, as applied specifically to a conical skirt layout, and, generally to air cushion skirting.

A.2 WORK STATEMENT

The program of research is divided for convenience into three main projects, for which description of tasks follow. However the Contractor shall carry out such work as deemed necessary by TDC to successfully complete each projects, but not specifically spelled out at this stage. Such additional work shall be accommodated within the overall time and financial resources allocated.

A.2.1 HDL Stability Limits

Models of Hoverlift Systems Ltd. air cushion system shall be built as scale models of HSL 101 and/or CASPAR, to be tested on the heave table and on the circular track.

Limits shall be investigated by modifying speed, mass, and/or inertias along pitch or roll axis.

Responses shall be compared to that of other air cushion systems, already tested by UTIAS in previous contracts. Additional tests of these systems may have to be re-run in order to validate comparison basis.

A.2.2. Pneumatic Circuit Stability

This project is to be concerned with internal aerodynamics of cushion systems. However inertias of the complete systems are to be considered in as much as they bear on oscillatory phenomena.

Specifically the following subjects are to be investigated in the course of this project:

i) Effect of ducting on instability and damping.

ii) Cushion cell internal flow effect on stability.

iii) Limit oscillations (non-linear)

iv) Effect of orifice area and resonator volume on stability and damping.

v) Effect of hovering over water on stability limits.

These topics are to be studied theoretically and experimentally. Inasmuch as possible these studies are to be paralleled with similar work conducted elsewhere and to which UTIAS has access.

A.2.3. Buckling of Skirt Material

This project is to resume and extend work performed previously at UTIAS for TDC, its object being to provide a complete description of the behaviour of pressure stabilized flexible structures, with particular regard to the buckling of Bertin type conical skirt system.

This project is to address skirt material, strength and stiffness, such that results may be applied generally to other skirt geometries.

APPENDIX B

SCALING ARGUMENTS FOR GEOMETRICALLY SIMILAR AIR CUSHION SYSTEMS

The scaling arguments presented are based on the Routh-Hurwitz stability criteria.

B.1 Rigid Plenum Air Cushion with a Constant Pressure Source

The characteristic equation for this case, based on the lumped capacitance-resistance model, is of the form

$$As^3 + Bs^2 + Cs + D = 0 \tag{B.1}$$

where

$$\begin{aligned} A &= C_c \\ B &= 1/R_c + 1/R_a \\ C &= S_a{}^2/m \\ D &= S_a/(m\alpha_a) \end{aligned} \tag{B.2}$$

where the parameters are as defined previously. The Routh-Hurwitz criteria for this case indicate that at a stability boundary,

$$AD - BC = 0 \tag{B.3}$$

or

$$\frac{C_c S_a}{m\alpha_a} - \frac{S_a{}^2}{m}\left(\frac{1}{R_c} + \frac{1}{R_a}\right) = 0 \tag{B.4}$$

which reduces to,

$$\frac{C_c}{\alpha_a} - S_a\left(\frac{1}{R_c} + \frac{1}{R_a}\right) = 0 \tag{B.5}$$

Now, for geometrically similar systems operating at the same cushion pressure,

$$
\begin{aligned}
S_a &\propto D_p^{\,2} \\
R_c &\propto 1/D_p^{\,2} \\
R_a &\propto 1/D_p^{\,2} \qquad\qquad (B.6) \\
C_c &\propto D_p^{\,3} \\
\alpha_a &\propto 1/D_p
\end{aligned}
$$

Substitution into each term in Eq. (B.5) yields:

$$\frac{C_c}{\alpha_a} \propto D_p^{\,4} \qquad S_a \quad \frac{1}{R_c} + \frac{1}{R_a} \propto D_p^{4} \qquad\qquad (B.7)$$

thus, each term is proportional to the same power of D_p, the criteria scale. In other words, geometrically similar systems operating at a geometrically similar hover-gap will be unstable at the same cushion pressure. A similar conclusion is reached when geometrically similar box-plenum systems are considered provided the characteristic equation is again based on the lumped capacitance-resistance model. Note that when arbitrary fan slope coefficient is taken into consideration, Eq. (B.5) becomes:

$$[illegible] \frac{1}{R_c + C_{PQ}} + \frac{1}{R_a}) = 0 \qquad\qquad [illegible].5$$

In this case, one finds that for geometrically similar systems to be unstable at the same cushion pressure C_{PQ} must scale according to $1/D_p^{\,2}$.

B.2 Rigid Plenum Air Cushion with a Duct and a Constant Pressure Source

The characteristic equation for this case, based on a lumped capacitance-resistance model for the plenum and a lumped inertance model for the duct, is:

$$(I_d s + R_c) \quad \left[C_c s^3 + \frac{s^2}{R_a} + \frac{S_a^{\;2}}{m} s + \frac{S_a}{m\alpha_a} \right] + s^2 = 0 \qquad \text{(B.8)}$$

Expanding this equation gives:

$$s^4 + \left(\frac{R_c}{I_d} + \frac{1}{R_a C_c} \right) s^3 + \left(\frac{S_a^{\;2}}{mC_c} + \frac{1}{I_d C_c} + \frac{R_c}{R_a} \frac{1}{I_d C_c} \right) s^2 +$$

$$\left(\frac{S_a}{\alpha_a m} \frac{1}{C_c} + R_c \frac{S_a^{\;2}}{m} \frac{1}{I_d C_c} \right) s + R_c \frac{S_a}{\alpha_a m} \frac{1}{I_d C_c} = 0 \qquad \text{(B.9)}$$

This is of the form,

$$s^4 + C_o s^3 + C_1 s^2 + C_2 s + C_3 = 0 \qquad \text{(B.10)}$$

where

$$\begin{aligned} C_o &= \left(\frac{R_c}{I_d} + \frac{1}{R_a C_c} \right) \\ C_1 &= \left(\frac{S_a^{\;2}}{mC_c} + \frac{1}{I_d C_c} + \frac{R_c}{R_a} \frac{1}{I_d C_c} \right) \\ C_2 &= \left(\frac{S_a}{\alpha_a m} \frac{1}{C_c} + R_c \frac{S_a^{\;2}}{m} \frac{1}{I_d C_c} \right) \\ C_3 &= R_c \frac{S_a}{\alpha_a m} \frac{1}{I_d C_c} \end{aligned} \qquad \text{(B.11)}$$

The routh Hurwitz criteria for this case indicate that at a stability boundary,

$$C_2 C_o C_1 - C_2^{\;2} - C_o^{\;2} C_3 = 0 \qquad \text{(B.12)}$$

Now, for geometrically similar duct plenum systems operating at the same cushion pressure,

$$C_o \propto 1/D_p$$

$$C_2 \propto 1/D_p^{2} \qquad \text{(B.13)}$$

$$C_3 \propto 1/D_p^{3}$$

whereas the first term in C_1 is proportional to $1/D_p$ while the second and third terms are proportional to $1/D_p^2$. This implies that for geometrically similar duct plenum systems, the Routh-Hurwitz criteria do not scale. In practice, the lack of scaling is very small and could possibly be ignored for engineering purposes. It is an inertance effect.

APPENDIX C

DERIVATION OF A 24 DEGREE OF FREEDOM CURVILINEAR SHELL FINITE ELEMENT FOR A RECTILINEAR ANISOTROPIC MATERIAL

A rectilinear anisotropic material is one where the material itself is of an orthotropic character but where the material axes do not coincide with the structural axes (Figure A1). If there is an angle ψ between these two sets of axes, the stress-strain relations are given by [Ref. 5.21]:

$$\begin{bmatrix} \sigma_x \\ \sigma_y \\ \tau_{xy} \end{bmatrix} = \begin{bmatrix} \bar{Q}_{11} & \bar{Q}_{12} & \bar{Q}_{16} \\ \bar{Q}_{12} & \bar{Q}_{22} & \bar{Q}_{26} \\ \bar{Q}_{16} & \bar{Q}_{26} & \bar{Q}_{66} \end{bmatrix} \begin{bmatrix} \epsilon_x \\ \epsilon_y \\ \gamma_{xy} \end{bmatrix} \qquad \text{(C-1)}$$

where

$$\begin{aligned}
\bar{Q}_{11} &= Q_{11}m^4 + 2(Q_{12} + 2Q_{66})n^2m^2 + Q_{22}n^4 \\
\bar{Q}_{22} &= Q_{11}n^4 + 2(Q_{12} + 2Q_{66})n^2m^2 + Q_{22}m^4 \\
\bar{Q}_{12} &= (Q_{11} + Q_{22} - 4Q_{66})n^2m^2 + Q_{12}(n^4 + m^4) \\
\bar{Q}_{66} &= (Q_{11} + Q_{22} - 2Q_{12} - 2Q_{66})n^2m^2 + Q_{66}(n^4 + m^4) \\
\bar{Q}_{16} &= (Q_{11} - Q_{12} - 2Q_{66})nm^3 + (Q_{12} - Q_{22} + 2Q_{66})n^3m \\
\bar{Q}_{26} &= (Q_{11} - Q_{12} - 2Q_{66})n^3m + (Q_{12} - Q_{22} + 2Q_{66})nm^3
\end{aligned} \qquad \text{(C-2)}$$

with

$$m = \cos\psi, \qquad m = \sin\psi$$

and

$$Q_{11} = \frac{E_{11}}{(1 - \nu_{12}\nu_{21})} \quad , \qquad Q_{22} = \frac{E_{22}}{(1 - \nu_{12}\nu_{21})} \qquad \text{(C-3)}$$

$$Q_{12} = \frac{\nu_{21}E_{11}}{(1 - \nu_{12}\nu_{21})} = \frac{\nu_{12}E_{22}}{(1 - \nu_{12}\nu_{21})} \;, \; Q_{66} = G_{12} \qquad \text{(C-4)}$$

$$\frac{\nu_{21}}{E_{22}} = \frac{\nu_{12}}{E_{11}} \tag{C-5}$$

when $\psi = 0$, we get the case for an orthotropic material, and if $E = E_{11} = E_{22}$; $\nu = \nu_{12} = \nu_{21}$ and $G_{12} = E/2(1+\nu)$ the isotropic case follows.

The strain-displacement relationships are given in curvilinear coordinates by

$$\begin{aligned} \epsilon_x &= e_x + zk_x \\ \epsilon_y &= e_y + zk_y \\ \gamma_{xy} &= e_{xy} + zk_{xy} \end{aligned} \tag{C-6}$$

where

$$\begin{aligned} e_x &= u_{,x} + \frac{1}{2} w^2_{,x} \\ e_y &= v_{,y} + \frac{w}{r} + \frac{1}{2} w^2_{,y} \\ e_{xy} &= v_{,x} + u_{,y} + w_{,x} w_{,y} \end{aligned} \tag{C-7}$$

and

$$\begin{aligned} k_x &= -w_{,xx} \\ k_y &= -w_{,yy} \\ k_{xy} &= -2w_{,xy} \end{aligned} \tag{C-8}$$

A variable followed by a comma denotes partial differentiation with the following subscripts:

$$\left(w_{,xx} = \frac{\partial^2 w}{\partial x^2} \right)$$

The following restrictions are imposed on the analysis:

- normals to the middle surface of the shell remain normal throughout the deformation;
- transverse shear deformation is neglected;
- the strains [equation (C-6)] are linear in z;
- the quadratic terms in u, v are small compared to the quadratic terms in $w_{,x}$ and $w_{,y}$;

- the effects of u and v on k_x, k_y and k_{xy} are negligible.

The strain energy for a rectilinear anisotropic, linearly elastic shell in cylindrical coordinates is

$$U = \frac{r}{2} \iiint_V (\sigma_x \epsilon_x + \sigma_\theta \epsilon_\theta + \tau_{x\theta} \gamma_{x\theta}) dx d\theta dz \qquad \text{(C-9)}$$

Rewriting this expression in curvilinear coordinates ($y = r\theta$) yields

$$U = \frac{1}{2} \iiint (\sigma_x \epsilon_x + \sigma_y \epsilon_y + \tau_{xy} \gamma_{xy}) dx dy dz \qquad \text{(C-10)}$$

The total potential energy is therefore

$$\Pi_p = U - W \qquad \text{(C-11)}$$

where W is the work done by external loading which can be written as

$$W = \iint_A (P_u u + P_v v + P_w w) dx dy \qquad \text{(C-12)}$$

where P_u, P_v and P_w are external loads and are functions of x and y.

The shell structure is now decomposed into a collection of curved rectangular elements (see Figure C2) each having a different assumed displacement pattern such that

$$\Pi_p = \sum_{k=1}^{N} \Pi_p^{(k)} \qquad \text{(C-13)}$$

where $\Pi_p^{(k)}$ is the potential energy of the k^{th} element.

C.1) Strain Energy

Substituting from equations (C-1) and (C-6) into (C-10), the strain energy becomes

$$U = \frac{1}{2} \iiint_V [\bar{Q}_{11} e_x^2 + 2\bar{Q}_{12} e_x e_y + 2\bar{Q}_{16} e_x e_{xy} + 2\bar{Q}_{26} e_y e_{xy} + \bar{Q}_{22} e_y^2 + \bar{Q}_{66} e_{xy}^2] dx dy dz$$

$$+ \frac{1}{2} \iiint_V z[2\bar{Q}_{11} e_x k_x + 2\bar{Q}_{22} e_y k_y + 2\bar{Q}_{66} e_{xy} k_{xy} + 2\bar{Q}_{12} (e_x k_y + e_y k_x)$$

$$+ 2\bar{Q}_{16} (e_x k_{xy} + e_{xy} k_x) + 2\bar{Q}_{26} (e_y k_{xy} + e_{xy} k_y)] dx dy dz$$

Contd...

$$+ \frac{1}{2} \iiint_V z^2[\bar{Q}_{11}k_x{}^2 + \bar{Q}_{22}k_y{}^2 + \bar{Q}_{66}k_{xy}^2 + 2\bar{Q}_{12}k_xk_y + 2\bar{Q}_{16}k_xk_{xy}$$

$$+ 2\bar{Q}_{26}k_yk_{xy}]dxdydz \qquad \text{(C-14)}$$

Since we will consider only shells of uniform thickness h, we can perform the integration over z from -(h/2) to (h/2), which will cancel the second integral of equation (C-14). The strain energy, upon performing the integration becomes

$$U = \frac{1}{2} \iint_A h[\bar{Q}_{11}e_x{}^2 + 2\bar{Q}_{12}e_xe_y + 2\bar{Q}_{16}e_xe_y + 2\bar{Q}_{26}e_ye_{xy} + \bar{Q}_{22}e_y{}^2 + \bar{Q}_{66}e_{xy}^2]dA$$

$$+ \frac{1}{2} \iint_A \frac{h^3}{12} [\bar{Q}_{11}k_x{}^2 + \bar{Q}_{22}k_y{}^2 + \bar{Q}_{66}k_{xy}^2 + 2\bar{Q}_{12}k_xk_y + 2\bar{Q}_{16}k_xk_{xy} + 2\bar{Q}_{26}k_yk_{xy}]dA \qquad \text{(C-15)}$$

Substituting the linearized form of equations (C-7), and equations (C-8) into the above, the strain energy can be expressed as

$$U = U_m + U_{mc} + U_B \qquad \text{(C-16)}$$

where

$$U_m = \frac{1}{2} \iint [Q^*_{11}u^2_{,x} + Q^*_{22}v^2_{,y} + 2Q^*_{12}u_{,x}v_{,y} + Q^*_{66}(v_{,x} + u_{,y})^2$$

$$+ \underline{2Q^*_{26}(v_{,y}v_{,x} + v_{,y}u_{,y})} + \underline{2Q^*_{16}(u_{,x}v_{,x} + u_{,x}u_{,y})}]dA \qquad \text{(C-17)}$$

$$U_{mc} = \frac{1}{2} \iint_A \left[Q^*_{22}\left(\frac{w^2}{r^2} + 2v_{,y}\frac{w}{r}\right) + 2Q^*_{12}u_{,x}\frac{w}{r} + \underline{2Q^*_{26}\left(v_{,x}\frac{w}{r} + u_{,y}\frac{w}{r}\right)}\right] dA \qquad \text{(C-18)}$$

$$U_B = \frac{1}{2} \iint_A [\overset{+}{Q}_{11}w^2_{,xx} + \overset{+}{Q}_{22}w^2_{,yy} + 2\overset{+}{Q}_{12}w_{,xx}w_{,yy} + 4\overset{+}{Q}_{66}w^2_{,xy} + \underline{4\overset{+}{Q}_{16}w_{,xx}w_{,xy}}$$

$$+ \underline{4\overset{+}{Q}_{26}w_{,yy}w_{,xy}}]dA \qquad \text{(C-19)}$$

For convenience, we set $\overset{*}{Q}_{ij} = h\bar{Q}_{ij}$ and $\overset{+}{Q}_{ij} = (h^3/12)\bar{Q}_{ij}$. The underlined terms are the extra terms due to the anisotropy of the material.

U_B is the strain energy due to bending and will provide a stiffness matrix that can be used in the finite element analysis of a flat plate subject to out of plane or bending loads.

U_m is the strain energy due to in-plane forces, or membrane forces, and will yield a stiffness matrix suitable for analysis of a flat plate subject to in-plane loading.

U_{mc} is the strain energy expression arising from the curvilinear coordinates (for plane coordinates $r \to \infty$) and serves to couple the in-plane and out-of-plane displacements. The stiffness matrix obtained from U_{mc}, used with those from U_B and U_m, allows analysis of curved panels or circular cylinders.

Each stiffness matrix shall be derived independently.

C.2) Stiffness Matrix Derivation

C.2.1) Trial Functions

We will consider a rectangular element of dimensions a and b (see Figure C2). At each node of the element, we specify the following degrees of freedom: u, v, w, $w_{,x}$, $w_{,y}$ and $w_{,xy}$. The choice of trial function is the same as Bogner et al [Ref. 5.20] and Heppler [Ref. 5.14]. They are:

$$u(x,y) = \left(\frac{a-x}{a}\right)\left(\frac{b-y}{b}\right)u_{11} + \left(\frac{a-x}{a}\right)\left(\frac{y}{b}\right)u_{12} + \left(\frac{x}{a}\right)\left(\frac{b-y}{b}\right)u_{21} + \left(\frac{x}{a}\right)\left(\frac{y}{b}\right)u_{22} \tag{C-20}$$

$$v(x,y) = \left(\frac{a-x}{a}\right)\left(\frac{b-y}{b}\right)v_{11} + \left(\frac{a-x}{a}\right)\left(\frac{y}{b}\right)v_{12} + \left(\frac{x}{a}\right)\left(\frac{b-y}{b}\right)v_{21} + \left(\frac{x}{a}\right)\left(\frac{y}{b}\right)v_{22} \tag{C-21}$$

$$w(x,y) = \sum_{i=0}^{3}\sum_{j=0}^{3} a_{ij}\, x^i\, y^j \tag{C-22}$$

The choices for the trial function are fully explained in References [5.14] and [5.20] and will not be repeated here.

C.2.2) Membrane Stiffness Matrix

Differentiating equations (C-20) and (C-21), substituting into (C-17), performing the integration over the rectangle and differentiating with respect to the nodal degrees of freedom, we obtain

$$[K_m]\{\delta_m\} = \{P_m\} \tag{C-23}$$

where $[K_m]$ is given by

$$[K_m] = \left[\begin{array}{cccccccc}
2A_1+B_1 & & & & & \text{SYMMETRIC} & & \\
A_3+2B_3 & 2A_2+B_2 & & & & & & \\
A_5 & -A_4+B_4 & 2A_1-B_1 & & & & & \\
A_4+B_4 & A_7 & -A_3+2B_3 & 2A_2-B_2 & & & & \\
-A_1-B_1 & -A\ -B_3 & A_6 & -A_4+B_5 & 2A_1+B_1 & & & \\
-A_3-B_3 & -A_2-B_2 & A_4+B_5 & A_8 & A_3+2B_3 & 2A_2+B_2 & & \\
A_6 & A_4+B_5 & -A_1+B_1 & A_3-B_3 & A_5 & -A_4+B_4 & 2A_1-B_1 & \\
-A_4+B_5 & A_8 & A_3-B_3 & -A_2+B_2 & A_4+B_4 & A_7 & -A_3+2B_3 & 2A_2-B_2
\end{array}\right] \qquad \text{(C-24)}$$

and

$$A_1 = \frac{1}{6}\frac{b}{a}Q^*_{11} + \frac{1}{6}\frac{a}{b}Q^*_{66} \qquad A_2 = \frac{1}{6}\frac{a}{b}Q^*_{22} + \frac{1}{6}\frac{b}{a}Q^*_{66}$$

$$A_3 = \frac{1}{4}Q^*_{12} + \frac{1}{4}Q^*_{66} \qquad A_4 = -\frac{1}{4}Q^*_{12} + \frac{1}{4}Q^*_{66}$$

$$A_5 = \frac{1}{6}\frac{b}{a}Q^*_{11} - \frac{1}{3}\frac{a}{b}Q^*_{66} \qquad A_6 = -\frac{1}{3}\frac{b}{a}Q^*_{11} + \frac{1}{6}\frac{a}{b}Q^*_{66}$$

$$A_7 = -\frac{1}{3}\frac{a}{b}Q^*_{22} + \frac{1}{6}\frac{b}{a}Q^*_{66} \qquad A_8 = \frac{1}{6}\frac{a}{b}Q^*_{22} - \frac{1}{3}\frac{b}{a}Q^*_{66}$$

$$B_1 = \frac{Q^*_{16}}{2} \qquad B_2 = \frac{Q^*_{26}}{2} \qquad B_3 = \frac{1}{6}\frac{a}{b}Q^*_{26} + \frac{1}{6}\frac{b}{a}Q^*_{16}$$

$$B_4 = -\frac{1}{3}\frac{a}{b}Q^*_{26} + \frac{1}{6}\frac{b}{a}Q^*_{16} \qquad B_5 = \frac{1}{6}\frac{a}{b}Q^*_{26} - \frac{1}{3}\frac{b}{a}Q^*_{16}$$

$$\{\delta_m\} = [u_{11}\ v_{11}\ u_{12}\ v_{12}\ u_{22}\ v_{22}\ u_{21}\ v_{21}]^T \qquad \text{(C-25)}$$

$\{P_m\}$ is the load vector arising from the work done due to external membrane loading and some examples are given in Section C3.

C.2.3) Bending Stiffness Matrix

The energy expression is given by equation (C-18) as:

$$U_B = \frac{1}{2}\int_0^b\int_0^a [Q_{11}^{+} w_{,xx}^2 + Q_{22}^{+} w_{,yy}^2 + 2Q_{12}^{+} w_{,xx} w_{,yy} + 4Q_{66}^{+} w_{,xy}^2$$

$$+ \underline{4Q_{16}^{+} w_{,xx} w_{,xy}} + \underline{4Q_{26}^{+} w_{,yy} w_{,xy}}]dxdy$$

and the trial function by equation (C-22),

$$w(x,y) = \sum_{i=0}^{3} \sum_{j=0}^{3} a_{ij}\, x^i\, y^j$$

Rewriting these equations in terms of nondimensional coordinates,

$$\xi = \frac{x}{a} \qquad\qquad \eta = \frac{y}{b} \qquad\qquad \text{(C-26)}$$

we obtain

$$U_B = \frac{1}{2ab}\int_0^1\int_0^1 \Bigg[Q_{11}^{+} \left(\frac{b}{a}\right)^2 w_{,\xi\xi}^2 + Q_{22}^{+} \left(\frac{a}{b}\right)^2 w_{,\eta\eta}^2 + 2Q_{12}^{+} w_{,\xi\xi} w_{,\eta\eta}$$

$$+ 4Q_{66}^{+} w_{,\xi\eta}^2 + 4Q_{16}^{+} \left(\frac{b}{a}\right) w_{,\xi\xi} w_{,\xi\eta} + 4Q_{26}^{+} \left(\frac{a}{b}\right) w_{,\eta\eta} w_{,\xi\eta} \Bigg] d\xi d\eta \quad \text{(C-27)}$$

and

$$w(\xi,\, \eta) = \sum_{i=0}^{3} \sum_{j=0}^{3} \bar{a}_{ij}\, \xi^i\, \eta^i \qquad \text{(C-28)}$$

This implies

$$w_{,\xi\xi} = \sum_{i=0}^{3} \sum_{j=0}^{3} \bar{a}_{ij}\, i(i-1)\xi^{i-2}\, \eta^j$$

$$w_{,\eta\eta} = \sum_{i=0}^{3} \sum_{j=0}^{3} \bar{a}_{ij}\, j(j-1)\xi^i\, \eta^{j-2} \qquad \text{(C-29)}$$

$$w_{,\xi\eta} = \sum_{i=0}^{3} \sum_{j=0}^{3} \bar{a}_{ij}\, ij\, \xi^{i-1}\, \eta^{j-1}$$

Taking equation (C-27) term by term and using equations (C-29), the following integral forms are found:

$$
\begin{aligned}
&Q_{11}^{+}\left(\frac{b}{a}\right)^{2}\int_{0}^{1}\int_{0}^{1} w_{,\xi\xi}^{2}\, d\xi d\eta = Q_{11}^{+}\left(\frac{b}{a}\right)^{2}\sum_{i=j=k=\ell=0}^{3}\frac{ik(i-1)(k-1)\bar{a}_{ij}\bar{a}_{k\ell}}{(i+k-3)(j+\ell+1)}\\
&Q_{22}^{+}\left(\frac{a}{b}\right)^{2}\int_{0}^{1}\int_{0}^{1} w_{,\eta\eta}^{2}\, d\xi d\eta = Q_{22}^{+}\left(\frac{a}{b}\right)^{2}\sum_{i=j=k=\ell=0}^{3}\frac{j\ell(j-1)(\ell-1)\bar{a}_{ij}\bar{a}_{k\ell}}{(i+k+1)(j+\ell-3)}\\
&4Q_{66}^{+}\int_{0}^{1}\int_{0}^{1} w_{,\xi\eta}^{2}\, d\xi d\eta = 4Q_{66}^{+}\sum_{i=j=k=\ell=0}^{3}\frac{ikj\ell\ \bar{a}_{ij}\ \bar{a}_{k\ell}}{(i+k=1)(j+\ell-1)} \qquad \text{(C-30)}\\
&2Q_{12}^{+}\int_{0}^{1}\int_{0}^{1} w_{,\xi\xi}\, w_{,\eta\eta}\, d\xi d\eta = 2Q_{12}^{+}\sum_{i=j=k=\ell=0}^{3}\frac{i(i-1)\ell(\ell-1)\bar{a}_{ij}\ \bar{a}_{k\ell}}{(i+k-1)(j+\ell-1)}\\
&4Q_{16}^{+}\left(\frac{b}{a}\right)\int_{0}^{1}\int_{0}^{1} w_{,\eta\xi}\, w_{,\xi\xi}\, d\xi d\eta = 4Q_{16}^{+}\left(\frac{b}{a}\right)\sum_{i=j=k=\ell=0}^{3}\frac{i(i-1)k\ell\ \bar{a}_{ij}\ \bar{a}_{k\ell}}{(i+k-2)(j+\ell)}\\
&4Q_{26}^{+}\left(\frac{a}{b}\right)\int_{0}^{1}\int_{0}^{1} w_{,\eta\eta}\, w_{,\xi\eta}\, d\xi d\eta = 4Q_{26}^{+}\left(\frac{a}{b}\right)\sum_{i=j=k=\ell=0}^{3}\frac{j(j-1)k\ell\ \bar{a}_{ij}\ \bar{a}_{k\ell}}{(i+k)(j+\ell-2)}
\end{aligned}
$$

Equations (C-30) can be expressed in vector-matrix notation, so that equation (C-27) becomes

$$
\begin{aligned}
U_B = \frac{1}{2ab}\Bigg[\, & Q_{11}^{+}\left(\frac{b}{a}\right)^{2} \langle a'\rangle [M_1]\{a'\} + Q_{22}^{+}\left(\frac{a}{b}\right)^{2} \langle a'\rangle [M_2]\{a'\}\\
& + 4Q_{66}^{+} \langle a'\rangle [M_3]\{a'\} + 2Q_{12}^{+} \langle a'\rangle [M_4]\{a'\} + 4Q_{16}^{+}\left(\frac{b}{a}\right)\langle a'\rangle [M_5]\{a'\}\\
& + 4Q_{26}^{+}\left(\frac{a}{b}\right)\langle a'\rangle [M_6]\{a'\}\Bigg] \qquad \text{(C-31)}
\end{aligned}
$$

where $[M_i]$ $i = 1, 6$ are obtained from equations (C-30). It should be noted that $[M_1]$, $[M_2]$ and $[M_3]$ are symmetric while $[M_4]$, $[M_5]$ and $[M_6]$ are non-symmetric. The vector $\{a'\}$ is the vector of coefficients of the trial function with normalized coordinates. By evaluating $w(\xi,\eta)$; $w_{,\xi}(\xi,\eta)$; $w_{,\eta}(\xi,\eta)$ and $w_{,\xi\eta}(\xi,\eta)$ at the nodal coordinates, we can obtain a matrix equation of the form

$$
\{\delta_B(\xi,\eta)\} = [A]^{-1}\ \{a'\} \qquad \text{(C-32)}
$$

where [A] is given in Table C1.

Table C1

$$[A] = \begin{bmatrix}
1 & 0 & 0 & 0 & 0 & 0 & 0 & 0 & 0 & 0 & 0 & 0 & 0 & 0 & 0 & 0 \\
0 & 0 & 1 & 0 & 0 & 0 & 0 & 0 & 0 & 0 & 0 & 0 & 0 & 0 & 0 & 0 \\
-3 & 0 & -2 & 0 & 3 & 0 & -1 & 0 & 0 & 0 & 0 & 0 & 0 & 0 & 0 & 0 \\
2 & 0 & 1 & 0 & -2 & 0 & 1 & 0 & 0 & 0 & 0 & 0 & 0 & 0 & 0 & 0 \\
0 & 1 & 0 & 0 & 0 & 0 & 0 & 0 & 0 & 0 & 0 & 0 & 0 & 0 & 0 & 0 \\
0 & 0 & 0 & 1 & 0 & 0 & 0 & 0 & 0 & 0 & 0 & 0 & 0 & 0 & 0 & 0 \\
0 & -3 & 0 & -2 & 0 & 3 & 0 & -1 & 0 & 0 & 0 & 0 & 0 & 0 & 0 & 0 \\
0 & 2 & 0 & 1 & 0 & -2 & 0 & 1 & 0 & 0 & 0 & 0 & 0 & 0 & 0 & 0 \\
-3 & -2 & 0 & 0 & 0 & 0 & 0 & 0 & 0 & 0 & 0 & 0 & 3 & -1 & 0 & 0 \\
0 & 0 & -3 & -2 & 0 & 0 & 0 & 0 & 0 & 0 & 0 & 0 & 0 & 0 & 3 & -1 \\
9 & 6 & 6 & 4 & -9 & -6 & 3 & 2 & 9 & -3 & -3 & 1 & -9 & 3 & -6 & 2 \\
-6 & -4 & -3 & -2 & 6 & 4 & -3 & -2 & -6 & 2 & 3 & -1 & 6 & -2 & 3 & -1 \\
2 & 1 & 0 & 0 & 0 & 0 & 0 & 0 & 0 & 0 & 0 & 0 & -2 & 1 & 0 & 0 \\
0 & 0 & 2 & 1 & 0 & 0 & 0 & 0 & 0 & 0 & 0 & 0 & 0 & 0 & -2 & 1 \\
-6 & -3 & -4 & -2 & 6 & 3 & -2 & -1 & -6 & 3 & 2 & -1 & 6 & -3 & 4 & -2 \\
4 & 2 & 2 & 1 & -4 & -2 & 2 & 1 & 4 & -2 & -2 & 1 & -4 & 2 & -2 & 1
\end{bmatrix}$$

Noting that

$$\begin{aligned}
w(x,y;\ a_{ij}) &= w(\xi,\eta;\ \bar{a}_{ij}) \\
w_{,x}(x,y;\ a_{ij}) &= \frac{1}{a}\, w_{,\xi}(\xi,\eta;\ \bar{a}_{ij}) \\
w_{,y}(x,y;\ a_{ij}) &= \frac{1}{b}\, w_{,\eta}(\xi,\eta;\ \bar{a}_{ij}) \\
w_{,xy}(x,y;\ a_{ij}) &= \frac{1}{ab}\, w_{,\xi\eta}(\xi,\eta;\ \bar{a}_{ij})
\end{aligned} \qquad \text{(C-33)}$$

and defining [D] as a diagonal matrix whose diagonal is

$$[1;\ a;\ b;\ ab;\ 1;\ a;\ b;\ ab;\ 1;\ a;\ b;\ ab;\ 1;\ a;\ b;\ ab] \qquad \text{(C-34)}$$

we have

$$[D]\{\delta_B(x,y)\} = \{\delta\ (\xi,\eta)\} = [A]^{-1}\{a'\} \qquad \text{(C-35)}$$

or

$$\{a'\} = [A][D]\{\delta_B(x,y)\} \tag{C-36}$$

we define

$$[A_w] = [A][D] \tag{C-37}$$

so that equation (C-38) becomes

$$\{a'\} = [A_w]\{\delta_B\} \tag{C-38}$$

Now

$$\{a'\}^T = <a'> = \{\delta_B\}^T[A_w]^T$$

or

$$<a'> = <\delta_B> [A_w]^T \tag{C-39}$$

From equations (C-31), (C-37) and (C-38), it follows that

$$\begin{aligned} U_B = \frac{1}{2ab} \Bigl[& Q^+_{11} \left(\frac{b}{a}\right)^2 <\delta_B> [A_w]^T[M_1][A_w]\{\delta_B\} + Q^+_{22} \left(\frac{a}{b}\right)^2 <\delta_B> [A_w]^T[M_2][A_w]\{\delta_B\} \\ & + 4Q^+_{66} <\delta_B> [A_w]^T[M_3][A_w]\{\delta_B\} + 2Q^+_{12} <\delta_B> [A_w]^T[M_4][A_w]\{\delta_B\} \\ & + 4Q^+_{16} \left(\frac{b}{a}\right) <\delta_B> [A_w]^T[M_5][A_w]\{\delta_B\} + 4Q^+_{26} \left(\frac{a}{b}\right) <\delta_B> [A_w]^T[M_6][A_w]\{\delta_B\} \Bigr] \end{aligned} \tag{C-40}$$

Differentiation of this energy expression with respect to the nodal degrees of freedom, the stiffness bending matrix for a flat plate is given by

$$\begin{aligned} [k_B] = \frac{1}{ab} \Bigl[& Q^+_{11} \left(\frac{b}{a}\right)^2 [A_w]^T [M_1][A_w] + Q^+_{22} \left(\frac{a}{b}\right)^2 [A_w]^T[M_2][A_w] \\ & + 4Q^+_{66} [A_w]^T[M_3][A_w] + Q^+_{12}[A_w]^T([M_4] + [M_4]^T)[A_w] \\ & + 2Q^+_{16} \left(\frac{b}{a}\right) [A_w]^T([M_5] + [M_5]^T)[A_w] \\ & + 2Q^+_{26} \left(\frac{a}{b}\right) [A_w]^T([M_6] + [M_6]^T)[A_w] \Bigr] \end{aligned} \tag{C-41}$$

The last three terms of equation (C-41) arise from the non-symmetry of $[M_4]$, $[M_5]$ and $[M_6]$. Therefore, for the bending of a flat plate, we have

$$[k_B]\{\delta_B\}\ ,\ \{P_B\} \tag{C-42}$$

where $[k_B]$ is of order 16x16, and

$$\{\delta_B\} = [w_{11}\ w_{,x11}\ w_{,y11}\ w_{,xy11}\ w_{12}\ w_{,x12}\ w_{,y12}\ w_{,xy12}\ w_{22}\ w_{,x22}\ w_{,y22}$$
$$w_{,xy22}\ w_{21}\ w_{,x21}\ w_{,y21}\ w_{,xy21}]^T \tag{C-43}$$

$\{P_B\}$ is the load vector arising from the work done due to external bending loading and some examples are given in Section C3.

C.2.4) Curvilinear Coupling Stiffness Matrix

The stiffness matrix for this case is derived from equation (C-18),

$$U_{mc} = \frac{1}{2} \int_0^b\int_0^a \left[Q^*_{22} \left(\frac{w^2}{r^2} + 2v_{,y} \frac{w}{r} \right) + 2Q^*_{12}\, u_{,x} \frac{w}{r} + \underline{2Q^*_{26} \left(v_{,x} \frac{w}{r} + u_{,y} \frac{w}{r} \right)} \right] dxdy \tag{C-44}$$

We require the derivatives $u_{,x}$, $v_{,y}$ and $u_{,y}$ which can be obtained from equations (C-20) and (C-21) as

$$\begin{aligned}
u_{,x}(x,y) &= \frac{(-u_{11}+u_{21})}{a} + (u_{11} - u_{12} + u_{22} - u_{21}) \frac{y}{ab} \\
v_{,y}(x,y) &= \frac{(-v_{11}+v_{12})}{b} + (v_{11} - v_{12} + v_{22} - v_{21}) \frac{x}{ab} \\
v_{,x}(x,y) &= \frac{(-v_{11}+v_{21})}{a} + (v_{11} - v_{12} + v_{22} - v_{21}) \frac{y}{ab} \\
u_{,y}(x,y) &= \frac{(-u_{11}+u_{12})}{b} + (u_{11} - u_{12} + u_{22} - u_{21}) \frac{x}{ab}
\end{aligned} \tag{C-45}$$

They can be cast in the form

$$\begin{aligned}
u_{,x} &= \sum_{i=0}^{1} b'_i\, y^i & \qquad v_{,y} &= \sum_{i=0}^{1} c_i x^i \\
u_{,y} &= \sum_{i=0}^{1} f_i\, x^i & \qquad v_{,x} &= \sum_{i=0}^{1} g_i y^i
\end{aligned} \tag{C-46}$$

or in nondimensional coordinates by the use of equation (C-26),

$$u_{,x} = \sum_{i=0}^{1} \bar{b}_i' \eta^i \qquad v_{,y} = \sum_{i=0}^{1} \bar{c}_i \xi^i$$

$$u_{,y} = \sum_{i=0}^{1} \bar{f}_i \xi^i \qquad v_{,x} = \sum_{i=0}^{1} \bar{g}_i \eta^i \tag{C-47}$$

From equations (C-22) and (C-28),

$$w(x,y) = \sum_{i=0}^{3} \sum_{j=0}^{3} a_{ij} x^i y^i = \sum_{i=0}^{3} \sum_{j=0}^{3} \bar{a}_{ij} \xi^i \eta^j \tag{C-48}$$

From equations (C-47) and (C-48), we form the products required in equation (C-44),

$$v_{,y} w = \sum_{i=0}^{1} \sum_{j=0}^{3} \sum_{k=0}^{3} \bar{c}_i \bar{a}_{jk} \xi^{i+j} \eta^k$$

$$u_{,x} w = \sum_{i=0}^{1} \sum_{j=0}^{3} \sum_{k=0}^{3} \bar{b}_i' \bar{a}_{jk} \xi^j \eta^{i+k}$$

$$w^2 = \sum_{i=0}^{3} \sum_{j=0}^{3} \sum_{k=0}^{3} \sum_{\ell=0}^{3} \bar{a}_{ij} \bar{a}_{k\ell} \xi^{i+k} \eta^{j+\ell} \tag{C-49}$$

$$v_{,x} w = \sum_{i=0}^{1} \sum_{j=0}^{3} \sum_{k=0}^{3} \bar{g}_i \bar{a}_{jk} \xi^j \eta^{i+k}$$

$$u_{,y} w = \sum_{i=0}^{1} \sum_{j=0}^{3} \sum_{k=0}^{3} \bar{f}_i \bar{a}_{jk} \xi^{i+j} \eta^k$$

Integration of (C-44) term by term leads to

$$I_1 = \int_0^b \int_0^a v_{,y} w \, dxdy = ab \sum_{i=0}^{1} \sum_{j=0}^{3} \sum_{k=0}^{3} \frac{\bar{c}_i \bar{a}_{jk}}{(i+j+1)(k+1)}$$

$$I_2 = \int_0^b \int_0^a u_{,x} w \, dxdy = ab \sum_{i=0}^{1} \sum_{j=0}^{3} \sum_{k=0}^{3} \frac{\bar{b}_i' \bar{a}_{jk}}{(j+1)(i+k+1)} \tag{C-50}$$

Contd...

$$I_3 = \int_0^b \int_0^a w^2 \, dxdy = ab \sum_{i=0}^{3} \sum_{j=0}^{3} \sum_{k=0}^{3} \sum_{\ell=0}^{3} \frac{\bar{a}_{ij} \, \bar{a}_{k\ell}}{(i+k+1)(j+\ell+1)}$$

$$I_4 = \int_0^b \int_1^a v_{,x} w \, dxdy = ab \sum_{i=0}^{1} \sum_{j=0}^{3} \sum_{k=0}^{3} \frac{\bar{g}_{\ell} \, \bar{a}_{jk}}{(j+1)(i+k+1)} \qquad \text{(C-50)}$$

$$I_5 = \int_0^b \int_0^a u_{,y} w \, dxdy = ab \sum_{i=0}^{1} \sum_{j=0}^{3} \sum_{k=0}^{3} \frac{\bar{f}_i \, \bar{a}_{jk}}{(i+j+1)(k+1)}$$

These equations can be put in matrix vector form as

$$I_1 = ab \, \langle c \rangle \, [Z] \{a'\}$$

$$I_2 = ab \, \langle b' \rangle \, [Y] \{a'\}$$

$$I_3 = ab \, \langle a' \rangle \, [X] \{a'\} \qquad \text{(C-51)}$$

$$I_4 = ab \, \langle g \rangle \, [Y] \{a'\}$$

$$I_5 = ab \, \langle f \rangle \, [Z] \{a'\}$$

where

$$Z_{i,jk} = \frac{1}{(i+j+1)(k+1)} \qquad \text{(C-52)}$$

$$Y_{i,jk} = \frac{1}{(j+1)(k+i+1)} \qquad \text{(C-53)}$$

$$X_{ij,k\ell} = \frac{1}{(i+k+1)(j+\ell+1)} \qquad \text{(C-54)}$$

Matrices [Y] and [Z] are of order (2x16), [X] of order (16x16), <c>, <b'>, <g> and <f> of order (1x2) and as before {a'} of order (16x1). The vectors {a'}, {b'}, {c}, {g} and {f} are vectors of the coefficients of the nondimensional coordinates in w, $u_{,x}$, $v_{,y}$, $v_{,x}$ and $u_{,y}$ respectively. By evaluating these at the nodal coordinates, a relationship between {a'}, {b'}, {c}, {g}, {f} and the nodal degrees of freedom can be found. They are given as

$$\{C\} = [C_v]\{\delta\}$$

$$\{b'\} = [B_u]\{\delta\} \qquad \text{(C-55)}$$

Contd...

$$\{a'\} = [A'_w]\{\delta\}$$

$$\{g\} = [G_v]\{\delta\}$$

$$\{f\} = [F_u]\{\delta\} \qquad \text{(C-55)}$$

where $\{\delta\}$ is the nodal displacement vector of the form

$$\{\delta\} = [u_{ij} \; v_{ij} \; w_{ij} \; w_{,xij} \; w_{,yij} \; w_{,xyij}]^{T}_{\substack{i=1,2\\ j=1,2}} \qquad \text{(C-56)}$$

where i and j are permuted in the same manner as equation (C-42) for $\{\delta_B\}$.

$[A'_w]$ is the same matrix as $[A_v]$ only it has been expanded to be of order (16x24) to allow for the u and v degrees of freedom in $\{\delta\}$. Matrices $[C_v]$, $[B_u]$, $[G_v]$ and $[F_u]$ are all of order (2x24) and are given in Table C2 (a), (b), (c) and (d) respectively.

Table C2

$$[C_v] = \begin{bmatrix} 0 & \frac{-1}{b} & 0 & 0 & 0 & 0 & 0 & \frac{1}{b} & 0 & 0 & 0 & 0 & 0 & 0 & 0 & 0 & 0 & 0 & 0 & 0 & 0 & 0 & 0 & 0 \\ 0 & \frac{1}{b} & 0 & 0 & 0 & 0 & 0 & \frac{-1}{b} & 0 & 0 & 0 & 0 & 0 & \frac{1}{b} & 0 & 0 & 0 & 0 & 0 & \frac{-1}{b} & 0 & 0 & 0 & 0 \end{bmatrix}$$

(a)

$$[B_u] = \begin{bmatrix} \frac{-1}{a} & 0 & 0 & 0 & 0 & 0 & 0 & 0 & 0 & 0 & 0 & 0 & 0 & 0 & 0 & 0 & 0 & 0 & \frac{1}{a} & 0 & 0 & 0 & 0 & 0 \\ \frac{1}{a} & 0 & 0 & 0 & 0 & 0 & \frac{-1}{a} & 0 & 0 & 0 & 0 & 0 & \frac{1}{a} & 0 & 0 & 0 & 0 & 0 & \frac{-1}{a} & 0 & 0 & 0 & 0 & 0 \end{bmatrix}$$

(b)

$$[G_v] = \begin{bmatrix} 0 & \frac{-1}{a} & 0 & 0 & 0 & 0 & 0 & 0 & 0 & 0 & 0 & 0 & 0 & 0 & 0 & 0 & 0 & 0 & 0 & \frac{1}{a} & 0 & 0 & 0 & 0 \\ 0 & \frac{1}{a} & 0 & 0 & 0 & 0 & 0 & \frac{-1}{a} & 0 & 0 & 0 & 0 & 0 & \frac{1}{a} & 0 & 0 & 0 & 0 & 0 & \frac{-1}{a} & 0 & 0 & 0 & 0 \end{bmatrix}$$

(c)

$$[F_u] = \begin{bmatrix} \frac{-1}{b} & 0 & 0 & 0 & 0 & 0 & \frac{1}{b} & 0 & 0 & 0 & 0 & 0 & 0 & 0 & 0 & 0 & 0 & 0 & 0 & 0 & 0 & 0 & 0 & 0 \\ \frac{1}{b} & 0 & 0 & 0 & 0 & 0 & \frac{-1}{b} & 0 & 0 & 0 & 0 & 0 & \frac{1}{b} & 0 & 0 & 0 & 0 & 0 & \frac{-1}{b} & 0 & 0 & 0 & 0 & 0 \end{bmatrix}$$

(d)

Substituting equations (C-55) into equations (C-51), we obtain

$$I_1 = ab <\delta> [C_v]^T[Z][A_w'] \{\delta\}$$

$$I_2 = ab <\delta> [B_u]^T[Y][A_w'] \{\delta\}$$

$$I_3 = ab <\delta> [A_w']^T[X][A_w'] \{\delta\} \qquad \text{(C-57)}$$

$$I_4 = ab <\delta> [G_v]^T[Y][A_w'] \{\delta\}$$

$$I_5 = ab <\delta> [F_u]^T[Z][A_w'] \{\delta\}$$

Differentiating equations (C-57) with respect to the nodal degrees of freedom and with equation (C-44), the coupling stiffness matrix is

$$[K_{mc}] = ab \left[\frac{Q^*_{22}}{r^2} [K_3] + \frac{Q^*_{22}}{r} ([K_1] + [K_1]^T) + \frac{Q^*_{12}}{r} ([K_2] + [K_2]^T) + \frac{Q^*_{26}}{r} ([K_4] + [K_4]^T) + \frac{Q^*_{26}}{r} ([K_5] + [K_5]^T) \right] \qquad \text{(C-58)}$$

where

$$[K_1] = [C_v]^T[Z][A_w']$$

$$[K_2] = [B_u]^T[Y][A_w']$$

$$[K_3] = [A_w']^T[X][A_w'] \qquad \text{(C-59)}$$

$$[K_4] = [G_v]^T[Y][A_w']$$

$$[K_5] = [F_u]^T[Z][A_w']$$

We therefore have

$$[K_{mc}]\{\delta\} \qquad \text{(C-60)}$$

where $[K_{mc}]$ is the (24x24) matrix given by equation (C-58).

The total stiffness matrix for a rectangular shell element with 24 degrees of freedom is

$$[K_T] = [K_B] + [K_m] + [K_{mc}] \tag{C-61}$$

where $[K_B]$ and $[K_m]$ have been expanded to (24x24) matrices.

For the orthotropic case, we set $\psi = 0$ and the resulting stiffness matrices agree with the author's derivation. Furthermore, if $E = E_{11} = E_{22}$ which implies $\nu = \nu_{21} = \nu_{12}$ and $G_{12} = E/2(1+\nu)$ the isotropic case follows and the stiffness matrices agree with Heppler [Ref. 5.14].

C.3) Consistent Force Vector Calculation

Evaluation of the consistent force vector requires evaluating the work for every term of equation (C-12). For loads normal to the plate, we have

$$W_1 = \int_o^b \int_o^a P_w w dx dy \tag{C-62}$$

and for in-plane loads,

$$W_2 = \int_o^b \int_o^a P_u u dx dy \tag{C-63}$$

$$W_3 = \int_o^b \int_o^a P_v v dx dy \tag{C-64}$$

The load functions are in general functions of x and y.

We will evaluate equation (C-62) for various forms of $P_w(x,y)$ and equations (C-63) and (C-64) will be treated similarly.

If we assume that P_w is uniformly distributed over the element, say the internal pressure Q as an example, from equation (C-62),

$$W_1 = Q \int_o^b \int_o^a w dx dy \tag{C-65}$$

and substituting for w(x,y) from equations (C-48), we obtain

$$W_1 = Q\, a\, b \sum_{i=0}^{3} \sum_{j=0}^{3} \frac{\bar{a}_{ij}}{(i+1)\ (j+1)} \tag{C-66}$$

As before, $\{a'\} = [A_W]\{\delta_B\}$, so that equation (C-66) can be re-written as

$$W_1 = Q\ a\ b\ \langle a' \rangle\ \{S\} \tag{C-67}$$

or

$$W_1 = Q\ a\ b\ \langle \delta_B \rangle\ [A_W]^T \{S\} \tag{C-68}$$

where

$$S_{ij} = \frac{1}{(i+1)(j+1)} \tag{C-69}$$

Differentiating equation (C-68) with respect to the nodal degrees of freedom, we obtain

$$\frac{\partial W_1}{\partial \delta_B i} = Q\ a\ b [A_W]^T \{S\} = \{P_B\} \tag{C-70}$$

where $\{P_B\}$ is given in Table C3.

Table C3

BENDING LOAD CONSISTENT FORCE VECTOR

	UNIFORMLY DISTRIBUTED LOAD Q	DISTRIBUTED EDGE LOAD V			
		$x = 0$	$x = a$	$y = 0$	$y = b$
w_{11}	$Qab/4$	$bV/2$	0	$aV/2$	0
$w_{,x11}$	$Qa^2b/24$	0	0	$a^2V/12$	0
$w_{,y11}$	$Qab^2/24$	$b^2V/12$	0	0	0
$w_{,xy11}$	$Qa^2b^2/144$	0	0	0	0
w_{12}	$Qab/4$	$bV/2$	0	0	$aV/2$
$w_{,x12}$	$Qa^2b/24$	0	0	0	$a^2V/12$
$w_{,y12}$	$-Qab^2/24$	$-b^2V/12$	0	0	0
$w_{,xy12}$	$-Qa^2b^2/144$	0	0	0	0
w_{22}	$Qab/4$	0	0	0	$aV/2$
$w_{,x22}$	$-Qa^2b/24$	0	$bV/2$	0	$-a^2V/12$
$w_{,y22}$	$-Qab^2/24$	0	0	0	0
$w_{,xy22}$	$Qa^2b^2/144$	0	$-b^2V/12$	0	0
w_{21}	$Qab/4$	0	0	$aV/2$	0
$w_{,x21}$	$-Qa^2b/24$	0	$bV/2$	$-a^2V/12$	0
$w_{,y21}$	$Qab^2/24$	0	0	0	0
$w_{,xy21}$	$-Qa^2b^2/122$	0	$b^2V/12$	0	0

If P_w is an edge distributed load or moment, then equation (C-65) becomes a line integral and if P_w is a delta function at one of the nodes, evaluation of the integral is unnecessary as this corresponds to a point load or moment at that node.

In-plane loads are treated in a similar manner and some results for when P_u and P_v are uniformly distributed edge loads are given in Table C4.

Table C4

MEMBRANE LOAD CONSISTENT FORCE VECTOR

	DISTRIBUTED EDGE LOAD N			
	$x = 0$	$x = a$	$y = 0$	$y = b$
u_{11}	(bN)/2	0	0	0
v_{11}	0	0	(aN)/2	0
u_{12}	(bN)/2	0	0	0
v_{12}	0	0	0	(aN)/2
u_{22}	0	(bN)/2	0	0
v_{22}	0	0	0	(aN)/2
u_{21}	0	(bN)/2	0	0
v_{21}	0	0	(aN)/2	0

C.4) Stress Formulation

A typical problem consists of a cylinder under different kinds or combinations of loading. The cylinder is discretized as shown in Figure C3 for a quarter cylinder of length ℓ. The case shown consists of 72 nodes and 56 elements.

All individual elemental stiffness matrices (C-61) are stored in global matrix including boundary conditions. We solve a system of equations of the form

$$[K^*]\{\delta^*\} = \{P^*\} \qquad \text{(C-71)}$$

where $[K^*]$ is the global stiffness matrix, $\{\delta^*\}$ is a column matrix of all the nodal degrees of freedom and $\{P^*\}$ is a column matrix corresponding to the applied loads acting on the cylinder. After solving this set of equations, we obtain u, v, w, $w_{,x}$, $w_{,y}$ and $w_{,xy}$ at all the nodes of the cylinder.

The linearized form of the strain-displacements (C-6) are

$$\begin{aligned} \epsilon_x &= u_{,x} \\ \epsilon_y &= v_{,y} + \frac{w}{r} \\ \gamma_{xy} &= v_{,x} + u_{,y} \end{aligned} \tag{C-72}$$

from which the stress-resultants can be calculated (C-1):

$$\begin{aligned} N_x &= h(\bar{Q}_{11}\epsilon_x + \bar{Q}_{12}\epsilon_y + \bar{Q}_{16}\gamma_{xy}) \\ N_y &= h(\bar{Q}_{12}\epsilon_x + \bar{Q}_{22}\epsilon_y + \bar{Q}_{26}\gamma_{xy}) \\ N_{xy} &= h(\bar{Q}_{16}\epsilon_x + \bar{Q}_{26}\epsilon_y + \bar{Q}_{66}\gamma_{xy}) \end{aligned} \tag{C-73}$$

and when $\psi = 0$,

$$\begin{aligned} N_x &= h(Q_{11}\epsilon_x + Q_{12}\epsilon_y) \\ N_y &= h(Q_{12}\epsilon_x + Q_{22}\epsilon_y) \\ N_{xy} &= h\, Q_{66}\gamma_{xy} \end{aligned} \tag{C-74}$$

C.4.1) Stress Formulation at the Nodes

From equation (C-72) we must evaluate the derivatives $u_{,x}$, $v_{,x}$, $u_{,y}$ and $v_{,y}$ at all the nodes of Figure C3. From equations (C-45) the required derivatives are:

$$\begin{aligned} u_{,x} &= \frac{(u_{21} - u_{11})}{a} + (u_{11} - u_{12} + u_{22} - u_{21})\frac{y}{ab} \\ u_{,y} &= \frac{(u_{12} - u_{11})}{b} + (u_{11} - u_{12} + u_{22} - u_{21})\frac{x}{ab} \end{aligned} \tag{C-75}$$

and similarly for the v derivatives by replacing u with v in the above expressions. Evaluating the derivatives at the corner nodes of a typical element, with the aid of Figure C2(a), it follows that

$$\left.\frac{\partial u}{\partial x}\right|_{\substack{1,1\\x=0,y=0}} = \left.\frac{\partial u}{\partial x}\right|_{\substack{2,1\\x=a,y=0}} = \frac{1}{a}\left(u_{21} - u_{11}\right) \tag{C-76a}$$

$$\left.\frac{\partial u}{\partial x}\right|_{\substack{1,2\\x=0,y=b}} = \left.\frac{\partial u}{\partial x}\right|_{\substack{2,2\\x=a,y=b}} = \frac{1}{a}\left(u_{22} - u_{12}\right) \tag{C-76b}$$

$$\left.\frac{\partial u}{\partial y}\right|_{\substack{1,1\\x=0,y=0}} = \left.\frac{\partial u}{\partial y}\right|_{\substack{1,2\\x=0,y=b}} = \frac{1}{b}\left(u_{12} - u_{11}\right) \tag{C-76c}$$

$$\left.\frac{\partial u}{\partial y}\right|_{\substack{2,1\\x=a,y=0}} = \left.\frac{\partial u}{\partial y}\right|_{\substack{2,2\\x=a,y=b}} = \frac{1}{b}\left(u_{22} - u_{21}\right) \tag{C-76d}$$

Since the derivatives with respect to x vary linearly in y and the derivatives with respect to y vary linearly with x, there are jump discontinuities in evaluating the derivatives at the different nodes of Figure C3. The jump discontinuities with respect to x will occur at all the nodes except along $\bar{x} = 0$, and with respect to y at all the nodes except along $\bar{y} = 0$.

Table C5 shows which equations to use to calculate the derivatives for a typical mesh as in Figure C3.

Table C5

Nodes	$\frac{\partial u}{\partial x}$	$\frac{\partial u}{\partial y}$
all 1,1 nodes in element (x=0, y=0)	C-76a	C-76c
along $\bar{y}=\pi r$ except node 72 (x=0, y=b)	C-76b	node directly under it
along $\bar{x}$ = 1/2 except node 72 (x=a, y=0)	node directly to its left	C-76d
node 72 (x=a, y=b)	node 63	node 71

Special care must be used when evaluating the derivatives with respect to y along $\bar{y} = r\pi$ and with respect to x along $\bar{x} = \ell/2$, and at the last node. As an example along $\bar{y} = r\pi$ for node 18, its derivative with respect to y is equal to the derivative with respect to y of node 17 as can be seen by equation (C-76c). Similarly, along $\bar{x} = \ell/2$, the derivative with respect to x of node 66 is equal to the derivative with respect to x of node 57 from equation (C-76a). For the last node, the derivative with respect to x of node 63 by equation (C-76b), and the derivative with respect to y of node 72 is equal to the derivative with respect to y of node 71 by equation (C-76d).

For the derivative of v we exchange u with v and the same comments mentioned above apply also to v.

Since w is explicitly calculated at every node in $\{\delta^*\}$, the strains and stress resultants are readily calculated from equations (C-72) and (C-73) respectively at every node.

C.4.2) Stress Formulation at the Centre of the Element

From equations (C-23) and (C-75) the displacement u and the necessary derivatives evaluated at the centre of the element ($x = a/2$ and $y = b/2$) are:

$$\begin{aligned} u\left(\frac{a}{2}, \frac{b}{2}\right) &= \frac{1}{4}\,(u_{11} + u_{12} + u_{21} + u_{22}) \\ u_{,x}\left(\frac{a}{2}, \frac{b}{2}\right) &= \frac{1}{2a}\,(u_{22} + u_{21} - u_{12} - u_{11}) \qquad \text{(C-77)} \\ u_{,y}\left(\frac{a}{2}, \frac{b}{2}\right) &= \frac{1}{2b}\,(u_{22} + u_{12} - u_{21} - u_{11}) \end{aligned}$$

and similarly for v by interchanging u with v. The u and v displacements evaluated at the centre consist of taking the average of the four displacements given at the nodes for that particular element.

To evaluate the normal displacement at the centre of the element we proceed as follows. w is given by equation (C-22) as

$$w(x, y) = \sum_{i=0}^{3} \sum_{j=0}^{3} a_{ij}\, x^i y^j \qquad \text{(C-78)}$$

which can be rewritten as

$$w(x, y) = \langle \bar{P} \rangle \{\alpha\} \qquad \text{(C-79)}$$

where

$$\langle \bar{P} \rangle = [1\ x\ y\ x^2\ xy\ y^2\ x^3\ x^2y\ xy^2\ y^3\ x^3y\ x^2y^2\ xy^3\ x^3y^2\ x^2y^3\ x^3y^3] \qquad \text{(C-80)}$$

Substituting this equation into (C-79), it follows that

$$w(x,\ y) = \langle\bar{P}\rangle\ [C]^{-1}\ \{\delta_B\} \qquad \text{(C-85)}$$

$\{\delta_B\}$ is known at every node of the element since it is given by $\{\delta^*\}$.

Therefore, to calculate the normal displacement at the centre of element, we let $x = a/2$ and $y = b/2$ in equations (C-80) and (C-85).

Now since all the necessary derivatives and displacements are known at the centre of the element, the strains and stress resultants are readily calculated at the centre of the element from equations (C-72) and (C-73) respectively.

C.4.3) Curvature Calculation

To calculate the curvature of the cylindrical shell, from equation (C-85),

$$w_{,xx}(x,\ y) = \langle\bar{P}'\rangle\ [C]^{-1}\{\delta_B\} \qquad \text{(C-86)}$$

where, from equation (C-80),

$$\langle\bar{P}'\rangle = [0\ 0\ 0\ 2\ 0\ 0\ 6x\ 2y\ 0\ 0\ 6xy\ 2y^2\ 0\ 6xy^2\ 2y^3\ 6xy^3] \qquad \text{(C-87)}$$

We calculate the curvature along the top of the cylinder (Figure C3, $\bar{y} = \pi r$) at $x = a/2$ and $y = b$ at the elemental level by averaging the individual curvature of the first three elements (elements 8, 16 and 24 of Figure C3). A negative curvature implies that the cylinder bends downward.

APPENDIX D

UNSTEADY ORIFICE FLOW

The lumped capacitance-resistance model assumes that an inviscid steady orifice flow law can be applied quasi-statically in time. The steady flow law is resistive or jet-like and for incompressible flow is,

$$Q_o = C_m A_o v_o = C_m A_o \sqrt{\frac{2p_c}{\rho}} \qquad \text{(D-1)}$$

Equation (D-1) follows from Euler's equation,

$$\underbrace{\frac{\partial v}{\partial t}}_{\text{Local}} + \underbrace{v\frac{\partial v}{\partial s}}_{\text{Convective}} + \frac{1}{\rho}\frac{\partial p}{\partial s} = 0 \qquad \text{(D-2)}$$

when the local or unsteady term is ignored. This appendix presents an order of magnitude argument which suggests that in some cases ignoring the local term may not be justified. Use is made of the fact that at one characteristic length L upstream of an orifice steady flow is very much like sink flow or flow in converging channels (Fig. D1). The argument assumes that Eq. (D-1) is valid and uses it, together with simple geometrical considerations, to estimate both acceleration terms in the converging channels when the pressure p_o is oscillating sinusoidally according to,

$$p_o = p_{oe} + \Delta p_o \sin\omega t \qquad \text{(D-3)}$$

where Δp_o is small. The analysis is linear.

Consider first a slot orifice. From geometry, one can write for the local term,

$$\frac{\partial v_s}{\partial t} = \frac{\partial \Delta v_s}{\partial t} = \frac{2C_m L}{\pi r}\frac{d\Delta v_o}{dt} \qquad \text{(D-4)}$$

where v_s is the velocity in the converging channels and v_o is the velocity at the vena contracta of the orifice. Using Eqs. (D-1) and (D-3) and linearizing, Eq. (D-4) reduces to,

$$\frac{\partial \Delta v_s}{\partial t} = \frac{2C_m L}{\pi r}\frac{\omega}{\rho v_{oe}}\Delta p_o \cos\omega t \qquad \text{(D-5)}$$

where the maximum value over one cycle is,

$$\frac{2C_m L}{\pi r}\frac{\omega}{\rho v_{oe}}\Delta p_o \qquad \text{(D-6)}$$

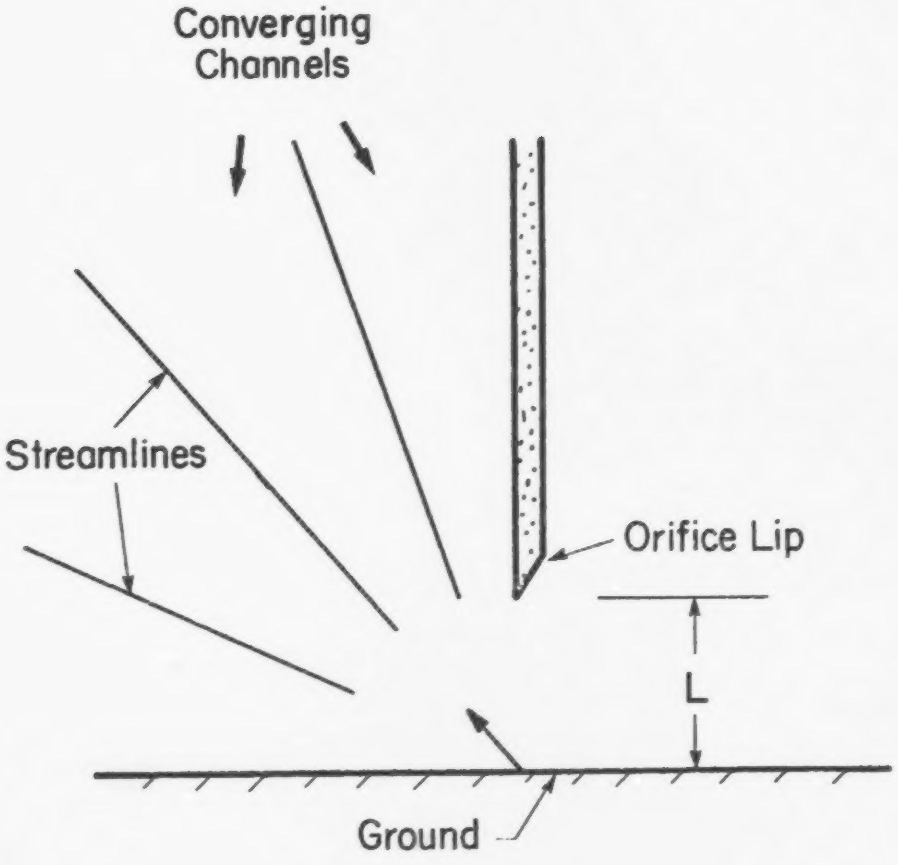
Converging Channels
Streamlines
Orifice Lip
L
Ground

FIG. D1 SLOT ORIFICE FLOW APPROXIMATION

Similarly, for the perturbations in the convective term,

$$\frac{\partial v_{se}}{\partial s} \Delta v_s + v_{se} \frac{\partial \Delta v_s}{\partial s} \qquad \text{(D-7)}$$

geometry considerations give,

$$- \frac{8C_m^2 L^2}{\pi^2 r^3} \frac{1}{\rho} \Delta p_o \sin\omega t \qquad \text{(D-8)}$$

where, in this case, the maximum value over one cycle is,

$$\frac{8C_m^2 L^2}{\pi^2 r^3} \frac{1}{\rho} \Delta p_o \qquad \text{(D-9)}$$

Forming the ratio of the maximum values gives the Strouhal-like number,

$$R = \frac{\text{Local}}{\text{Convective}} = \frac{\pi}{4C_m} \frac{r^2}{L} \frac{\omega}{v_{oe}}$$

$$\cong 1.3 \frac{r^2}{L} \frac{\omega}{v_{oe}} \qquad \text{(D-10)}$$

Similar calculations for a circular orifice give,

$$R = \frac{1}{2C_m} \frac{r^3}{L^2} \frac{\omega}{v_{oe}}$$

$$\cong 0.82 \frac{r^3}{L^2} \frac{\omega}{v_{oe}} \qquad \text{(D-11)}$$

The above analysis is restricted to the converging channels. With this restriction, the minimum value of each ratio occurs at r = L and is,

$$R_m \cong 1.3 \frac{L\omega}{v_{oe}} \text{ Slot Orifice} \qquad \text{(D-12-A)}$$

$$R_m \cong 0.82 \frac{L\omega}{v_{oe}} \text{ Circular Orifice} \qquad \text{(D-12-B)}$$

Assuming that a value at r = L is typical for the orifice region, R_m much less than unity would imply that Eq. (D-1) is adequate. However, R_m of the order of unity would suggest that use of Eq. (D-1) is questionable. In the latter case, the lumped reactance-resistance model proposed by Pellegrin et al (Ref. D.1), or some extension of it, would probably be more appropriate. Note that when P_{oe}, or equivalently V_{oe}, tends to zero, R_m tends to infinity, which indicates that in this limit, Eq. (D-1) would be totally inadequate for a linear analysis; in fact, a purely lumped reactance or slug flow model (Ref. D-2) would be more appropriate. However, in this limit, Eq. (D-1) may be adequate for large amplitude or nonlinear oscillations because during a typical oscillation the flow may be predominantly jet-like. This is an area for future work. Specifically, the transition from reactive to resistive behaviour must be clarified (Ref. D.3).

APPENDIX E

SEQUENCE OF FUNCTIONS

USED IN HSL ROLL AND PITCH STIFFNESS ANALYSIS

This appendix gives the series of geometric functions g_1, g_2, g_3, ..., which are used to describe the detailed geometry of the flexible skirt and produce the cushion stiffness, and leakage area functions which are used in roll and pitch stiffness theory. The geometries are diagrammed in figures 3.2 to 3.8 of the main text and include rounded sections at the corners, triangular segments at the sides and the central rectangular region. The equations must be applied with care as several members of the "g" series will tend towards infinity as θ approaches 0 unless $H\cos\theta - h_p$ approaches zero faster; for cases at high flow this will not occur, however this condition can be enforced with suitable leak height addition during computer calculation. Subsequently a similar geometry has been developed which treats the area near $\theta = 0$ as a special case and eliminates this problem.

For geometry I:

$$g_1 = H - h_p \sec\alpha; \quad \text{Define } H \triangleq H_s + H_p \tag{E-1}$$

$$g_2 = (H - h_p \sec\alpha) \cot\alpha \tag{E-2}$$

$$g_3 = (H - h_p \sec\alpha) \operatorname{cosec}\alpha \tag{E-3}$$

$$g_4 = \frac{B_s}{2} - H \cot\alpha + h_p \operatorname{cosec}\alpha \tag{E-4}$$

$$g_5 = \frac{B_s}{2} \sin\alpha - H \cos\alpha + h_p \tag{E-5}$$

$$g_6 = \frac{B_s}{2} \cdot \cos\alpha - H \frac{\cos^2\alpha}{\sin\alpha} + h_p \cot\alpha \tag{E-6}$$

$$g_7 = \frac{B_s}{2} \cdot \sin\alpha + H \cos\alpha - h_p \tag{E-7}$$

$$g_8 = \left(\frac{B_s}{2} \cdot \sin\alpha + H \cos\alpha - h_p\right) \cot(\Phi-\alpha) \tag{E-8}$$

$$g_9 = \frac{B_s}{2} \cdot \cos\alpha - H \sin\alpha + h_p \tan\alpha \tag{E-9}$$

$$g_{10} = \frac{1}{2} (g_6 + g_3 + g_9 + g_8) \tag{E-10}$$

$$g_{11} = g_{10} - g_6 - g_3 \tag{E-11}$$

$$g_{12} = h_p \tan\alpha - g_{11} \tag{E-12}$$

$$\begin{aligned} g_{13} = {} & H_p \sin\alpha + \frac{B_s}{4} \cdot \sin\alpha \cot(\Phi-\alpha) \\ & + H\left(\frac{1}{2} \cos\alpha \cot(\Phi-\alpha) - \sin\alpha\right) - \frac{h_p}{2} \cot(\Phi-\alpha) \end{aligned} \tag{E-13}$$

Note: g_{13} can be positive or negative depending on location of centre line of ground contact.

For Geometry II: (g_1-g_7 and g_9 similar to geometry I):

$$g_8 = -g_1 \sin\alpha - H_p (\sin\alpha + \cos\alpha \tan\theta) + 2H \sin\alpha + h_p \tan\theta - H_{s_3} (\sin\alpha + \cos\alpha \tan\theta) + \frac{B}{2} (\cos\alpha - \sin\alpha \tan\alpha) - \frac{B_s}{2} \cos\alpha - h_p \tan\alpha \qquad \text{(E-14)}$$

$$g_{10} = \frac{1}{2} (g_6 + g_3 + g_9 + g_8) \qquad \text{(E-15)}$$

$$g_{11} = g_{10} - g_6 - g_3 \qquad \text{(E-16)}$$

$$g_{12} = h_p \tan\alpha - g_{11} \qquad \text{(E-17)}$$

$$g_{13} = \frac{B}{4} (\cos\alpha - \sin\alpha \tan\theta) - \frac{B_s}{4} \cos\alpha - \frac{H}{2} \sin\alpha + \frac{H_p}{2} (2\sin\alpha - \cos\alpha \tan\theta + \frac{h_p}{2} \tan\theta - \frac{H_{s_3}}{2} (\sin\alpha + \cos\alpha \tan\theta) \qquad \text{(E-18)}$$

For Geometry III:

$$g_1 = h_p \sec\alpha - H \qquad \text{(E-19)}$$

$$g_2 = g_1 \cot\alpha \qquad \text{(E-20)}$$

$$g_3 = g_2 \cos\alpha - H \sin\alpha \qquad \text{(E-21)}$$

$$g_4 = \frac{B_s}{2} + g_2 \qquad \text{(E-22)}$$

$$g_5 = g_4 \sin\alpha \qquad \text{(E-23)}$$

$$g_6 = g_4 \cos\alpha \qquad \text{(E-24)}$$

$$g_7 = (\frac{B_s}{2} - g_2) \sin\alpha \qquad \text{(E-25)}$$

$$g_8 = g_7 \cot (\phi - \alpha) \qquad \text{(E-26)}$$

$$g_9 = g_7 \cot\alpha \qquad \text{(E-27)}$$

$$g_{10} = \frac{1}{2} (g_8 + g_9 + g_6) \qquad \text{(E-28)}$$

$g_{11} = g_{10} - (g_8 + g_9 + g_3)$ (E-29)

~~$g_{13} = H_p \sin\alpha - g_{11}$~~ $g_{12} = h_p \tan\alpha - g_{11}$ (E-30)

$g_{13} = H_p \sin\alpha - g_{12}$ (E-31)

APPENDIX F

VAMPIRE 1 STEADY STATE FAN CHARACTERISTIC

The lift fan installed in Vampire 1 is based on a Hartzell VB29B, 29 in (73.66cm) diameter fixed pitch axial rotor. The choice of this system, as opposed to a centrifugal fan usually used for ACV lift systems, reflected two perceived advantages: weight savings and transmission simplifications. Furthermore, the manufacturer's steady state characteristic for delivery pressure p_f as a function of volume flow Q_f showed that $dp_f/dQ_f < 0$ over the entire operating range of volume flows. This slope condition is required for static stability. The geometry of the installation in Vampire 1 is shown in Figure F1. As an economy measure, an available contoured inlet for a 30 in diameter rotor was used, and connected to the fan housing by a short tapered section. To spread the flow into the vehicle's plenum box, a turning annulus was installed below the fan. Its geometry was initially chosen to have a reduction in cross sectional area of about 10% from the inlet to the outlet; this was intended to prevent boundary layer separation and associated dynamic losses. However, it was subsequently found that, as installed, the actual cross-sectional area increased by about 4%.

The manufacturer's characteristic curve for the fan is shown in Figure F2. This was obtained under standard test conditions for axial fans, which included the use of downstream stator blades. The manufacturer indicated that, in the absence of stators, the pressure at the exit of the annulus, which is the effective delivery pressure in the plenum box p_f, might be 10% to 20% lower than the values given in Figure F2 [Ref. F1].

This fan system has a number of attendant disadvantages. The first is that it does not provide enough Q_f to correctly scale the relatively high values used on high speed amphibious vehicles such as those built by the British Hovercraft Corporation [Ref. F2]. Secondly, it stalls at values of Q_f corresponding to normal equilibrium cushion pressures. In addition to causing low fan efficiencies, this greatly complicates the task of measuring the installed pressure-volume flow characteristic, since the flow upstream of the rotor is then partly recirculating. The presence of reversed flow in the inlet at low cushion flow rates was first detected by using appropriately located tufts. The originally preferred method of measuring Q_f, four sets of total head pitot rakes, was therefore ruled out for most of the operating regime. Thirdly, it was subsequently decided that the location of the inlet rake at the junction between the inlet and the tapered section was unsatisfactory for the volume flow measurements, owing mainly to uncertainties introduced in the measurement of the local static pressure. However, there was no suitable alternative location. Finally, as is discussed in Section 2, it is now clear that the response of the fan to unsteady cushion pressures arising from vehicle motion can cause large deviations from the steady state characteristic. Indeed, the flow in the inlet of Vampire 1 has been observed to reverse momentarily during a pitch or roll oscillation of large enough amplitude.

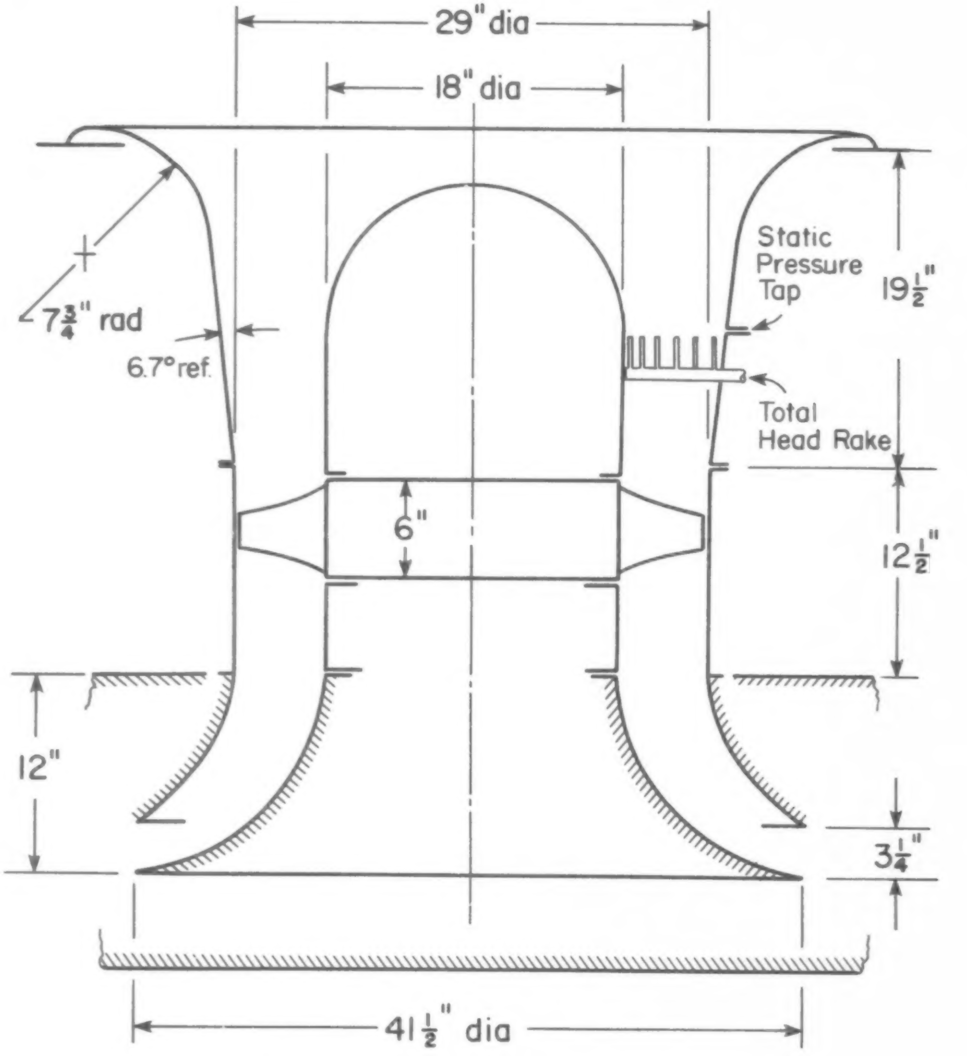
29" dia
18" dia
$7\frac{3}{4}$" rad
6.7° ref.
Static Pressure Tap
Total Head Rake
$19\frac{1}{2}$"
6"
$12\frac{1}{2}$"
12"
$3\frac{1}{4}$"
$41\frac{1}{2}$" dia

FIG. F1 GEOMETRY OF ORIGINAL LIFT FAN INSTALLATION IN VAMPIRE 1.

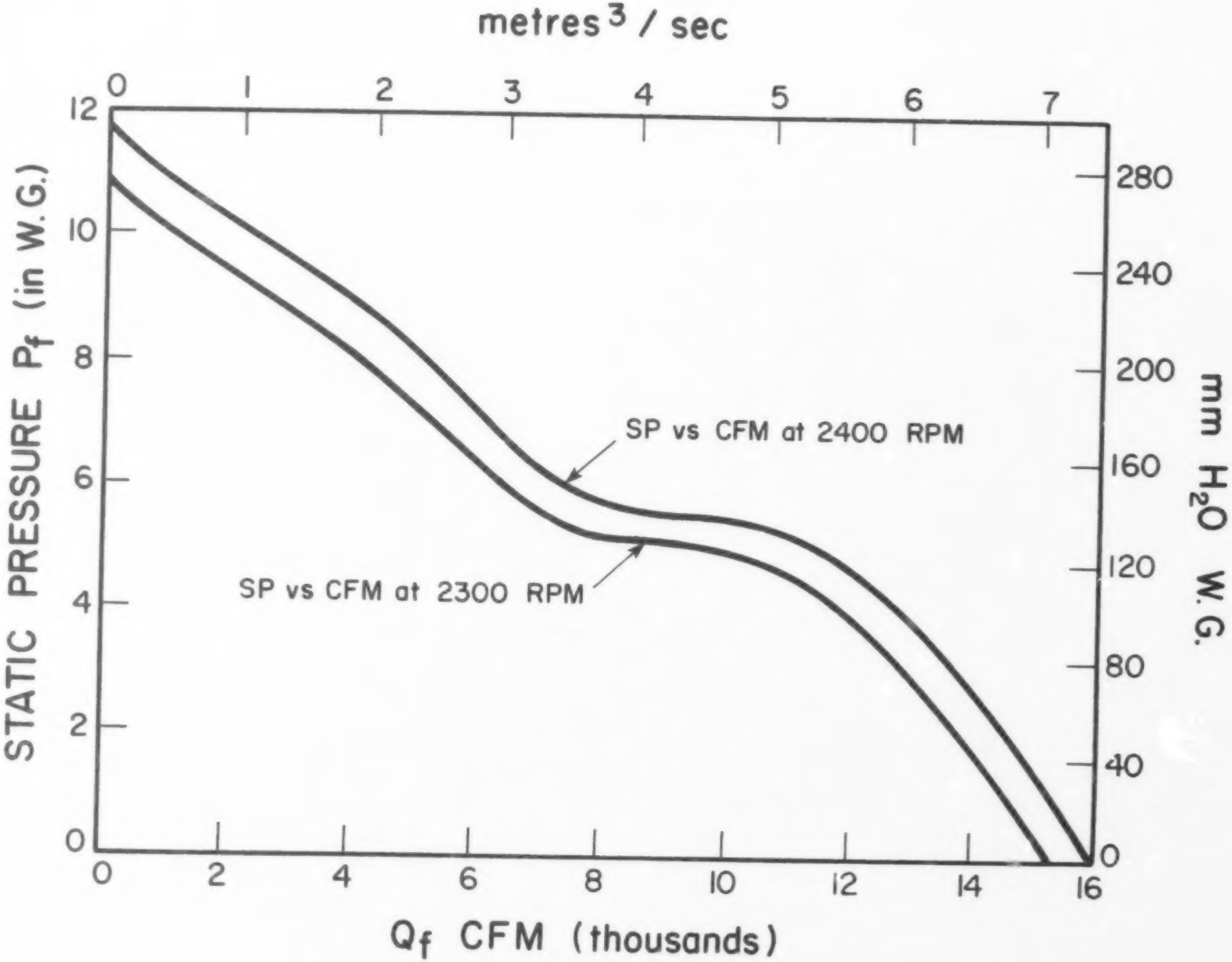

FIG. F2 VAMPIRE 1 FAN CHARACTERISTIC AS SUPPLIED BY MANUFACTURER, AIR DENSITY = 0.075 LB_m/FT^3

For vehicle dominated motion, the unsteady effects arise from air inertia in the inlet, fan annulus and delivery ducting; unsteady blade aerodynamic effects are usually negligible [see Section 2.2.2.1]. It is currently believed that the geometry of the present fan system greatly complicates the task of devising accurate mathematical models of these unsteady effects.

Various methods of determining Q_f for the installed fan have been employed since 1974. Miller [Ref. F1] used the inlet rakes for flows which were unstalled, and pitot cylinder probes, located both immediately below the fan rotor and at the outlet of the turning annulus, for the entire flow regime. A pitot cylinder probe consists of a small diameter cylinder mounted with its axis transverse to the flow direction. Two static pressure taps are located at 90° apart around the periphery. By rotating the cylinder about its axis and monitoring the static pressures on these two taps, one can find the local flow direction, the total head, and with adequate calibration, the local static pressure. Hence, in principle at least, one can compute local velocities and flows. However, the determination of local static pressure can be subject to considerable error because the calibration factors are very sensitive to Reynolds number and other parameters [Ref. F2].

The uncertainties associated with these flow measurement techniques led to a search for alternatives. Ultimately a procedure which was initially thought to be very cumbersome was adopted. This was to shut off all the holes delivering air from the plenum box to the cushion, attach two 0.3048m diameter ducts to the rear of the plenum box, and install ASME standard orifice plate meters in these ducts [Ref. F3]. Previous experience has shown this technique to be very reliable and, once the required hardware had been assembled, the most convenient.

Figures F3 and F4 give typical results for the nondimensional delivery pressure $C_{FP} = p_f/\rho N^2D^2$ as a function of $C_{FQ} = Q_f/ND^3$. The results in Fig. F3 are the most recent data, obtained using the orifice plate meter; and this gives pressures significantly in excess of the manufacturer's curve, in contrast to what was expected. This may be contrasted with earlier data given in Fig. F4. The data obtained in the stall regime by Miller [Ref. F1] using the pitot cylinder was the first to be obtained and it coincided with the expectations of the manufacturer. The discrepancy first appeared with the first use of the orifice plate installation in June of 1977, and because it was much larger than would be expected in routine fan calibrations (up to 30%) was a source of considerable concern. Measurements obtained in February, 1982, by using the orifice plate meter by a different operator agreed with the first orifice plate measurements so the data in Fig. F3 is believed to be the most reliable.

As part of the process of designing and installing a new high efficiency fan, the possible role of the turning annulus in generating the high delivery pressures is being investigated.

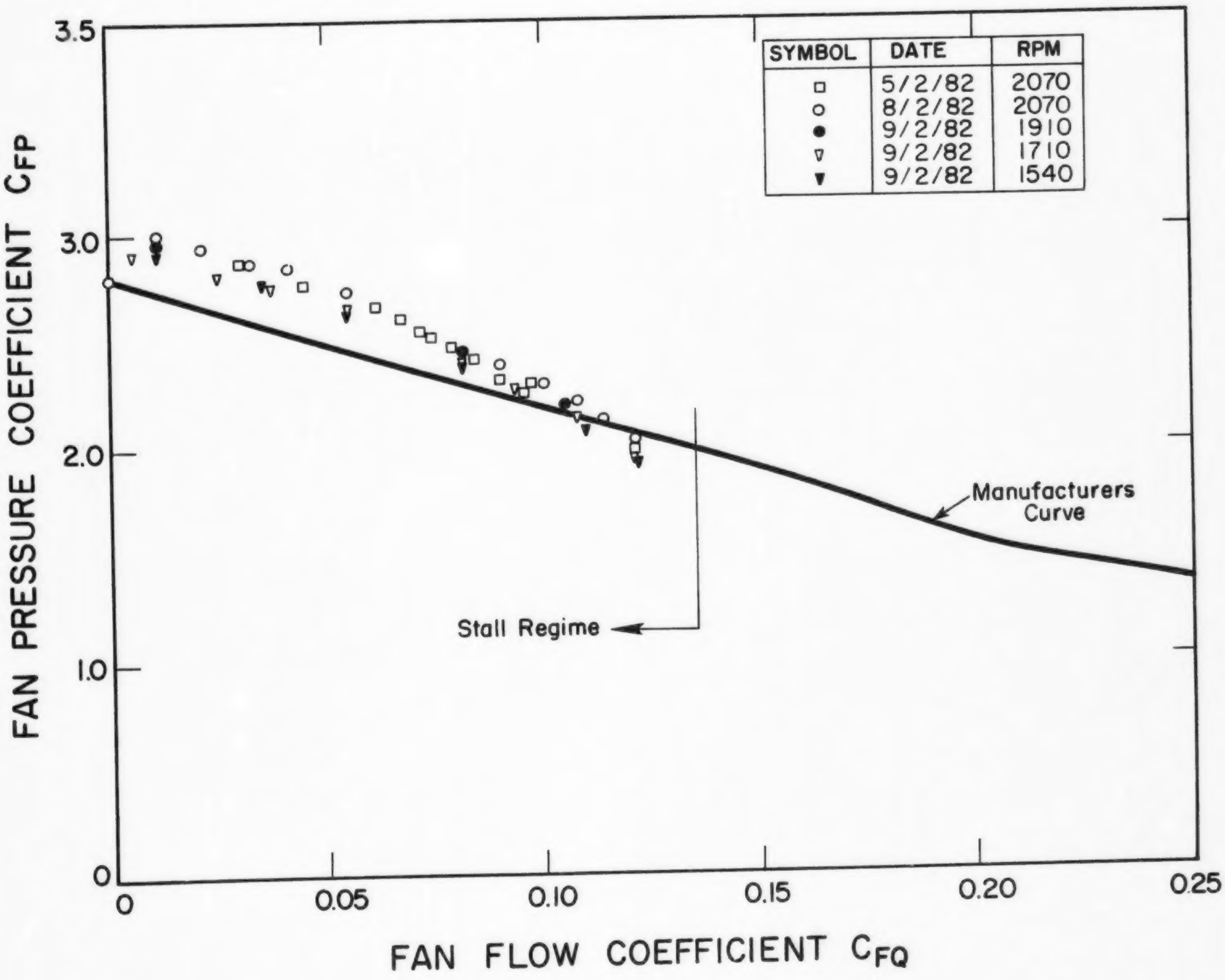

FIG. F3 RECENT DATA OBTAINED IN THE STALLED REGIME BY USING ASME ORIFICE PLATE INSTALLATION.

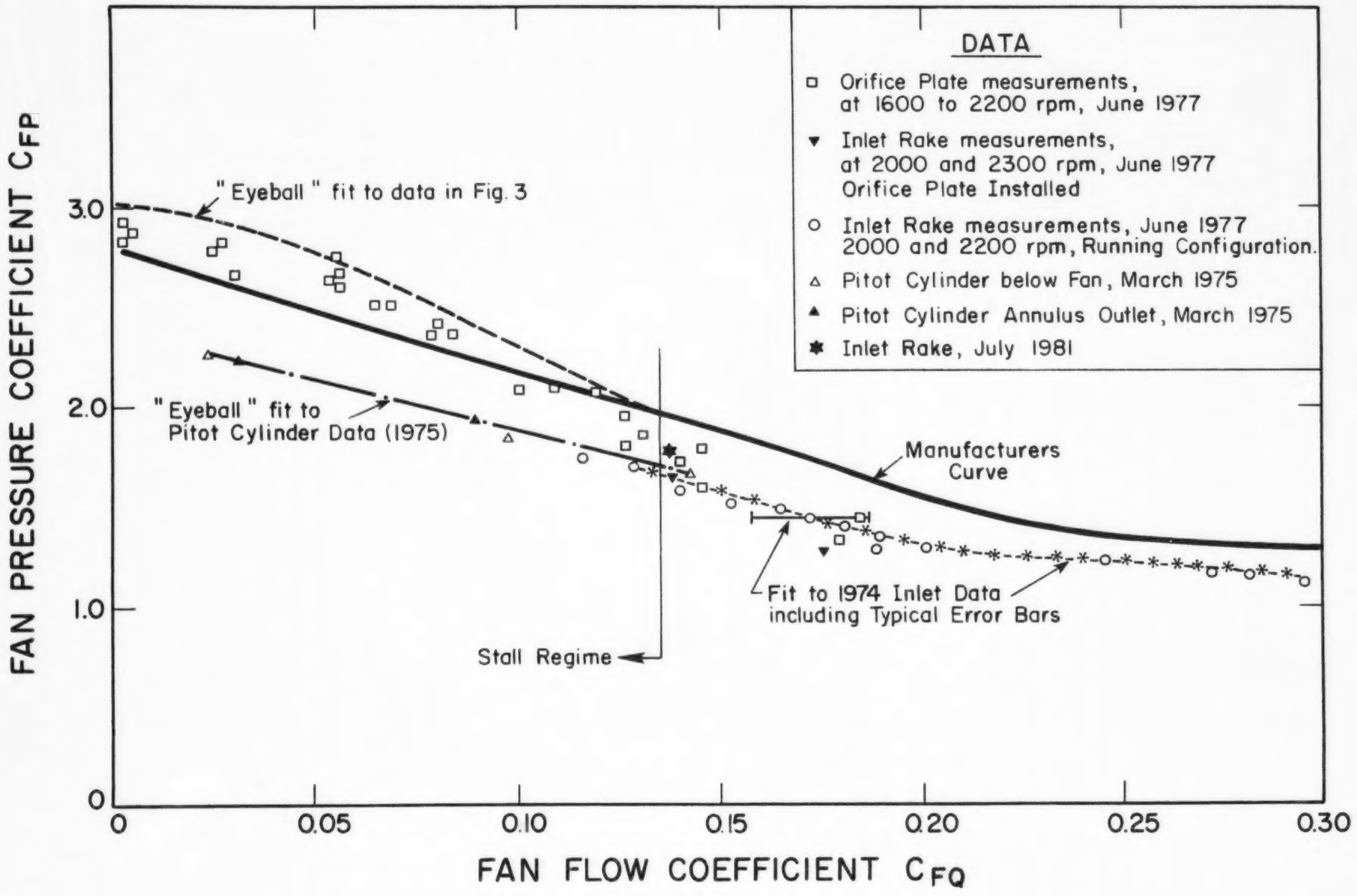

FIG. F4 COMPARISON OF DATA OBTAINED BY VARIOUS METHODS FROM 1974 TO 1981.

References

F1 Miller, E. J., "The Calibration of the Vampire 1 Axial Flow Lift System", M.A.Sc. Thesis, University of Toronto, May 1975.

F2 Fowler, H. S., "On the Lift-Air Requirements of Air Cushion Vehicles and Its Relation to the Terrain and Operational Mode". National Research Council of Canada, Division of Mechanical Engineering, Ottawa, Canada, Report No. ME-246, May 1979.

F3 Flowmeter Computation Handbook. American Society of Mechanical Engineers, New York, 1961.

APPENDIX G

THE UTIAS CIRCULAR TRACK FACILITY

Introduction

The UTIAS circular track facility was developed as part of an air cushion technology program with the aid of a Negotiated Development Grant awarded by the National Research Council of Canada (NRC). The facility consists of 3 major components, the track and building, the test vehicle, and the instrumentation and data recording system. These components are described in the following sections.

Track and Building

The circular track consists of a plywood floor 4.87m wide with a centre line diameter of 42.7m. Incorporated into the track is a pair of hydraulically operated ramps 2.7m long x 1.8m wide each, and controllable to a maximum height of 0.2m. The ramps can be operated in unison or separately. Thus various combinations of heave, pitch and roll inputs can be obtained.

The track is enclosed by a large geodectic dome to remove wind interference effects. Peripheral buildings include a model bay for work on the model in a controlled climate environment, a control room to allow observation and remote control of the hydraulics and vehicle when running and a room containing the hydraulic power system.

The Test Vehicle

The basic test vehicle, VAMPIRE I, (Variable Air Cushion Model Producing Intermediate Range Experiments) has platform dimensions of approximately 4m x 2m with an all up weight (AUW) of 700 kg. The vehicle layout is shown schematically in Fig. G-1. The major components of the vehicle are the plenum box, incorporating the main structural frame which carries both the propulsion and lifting units, instrumentation box and a tether suspension assembly. The power for the propulsion and the 0.74m dia. lift fan is supplied by two 11 kW Briggs and Stratton four-cycle, single-cylinder engines. The tether suspension assembly is designed in such a way that the suspension point as well as the box containing rate gyros and accelerometers can be located exactly at the CG of the vehicle in order to eliminate tether cable induced moments and errors in acceleration measurements. The instrumentation box contains power supplies, power and signal distribution busses and signal multiplexing and transmitting circuitry. The bottom of the plenum box is designed to allow relatively easy removal so that changes of skirt systems can be made simply.

The test vehicle is tethered to the centre post by a 3/16" diameter steel cable which also supports power supply, vehicle control and signal cables running from the vehicle to the slip rings in the centre post. The vehicle is controlled from a control room (Fig. G-2), where separate controls are provided for both the propulsion and lift engine throttles. Other controls and monitoring devices include tachometers for both engines, closed circuit TV (CCTV) with a video camera mounted on top of the centre post, separate controls for both ramps and an emergency shutdown switch.

Four motorcycle type wheels are installed for power-off handling of the vehicle, as well as for protection against damage in case of hard structure contact with ground.

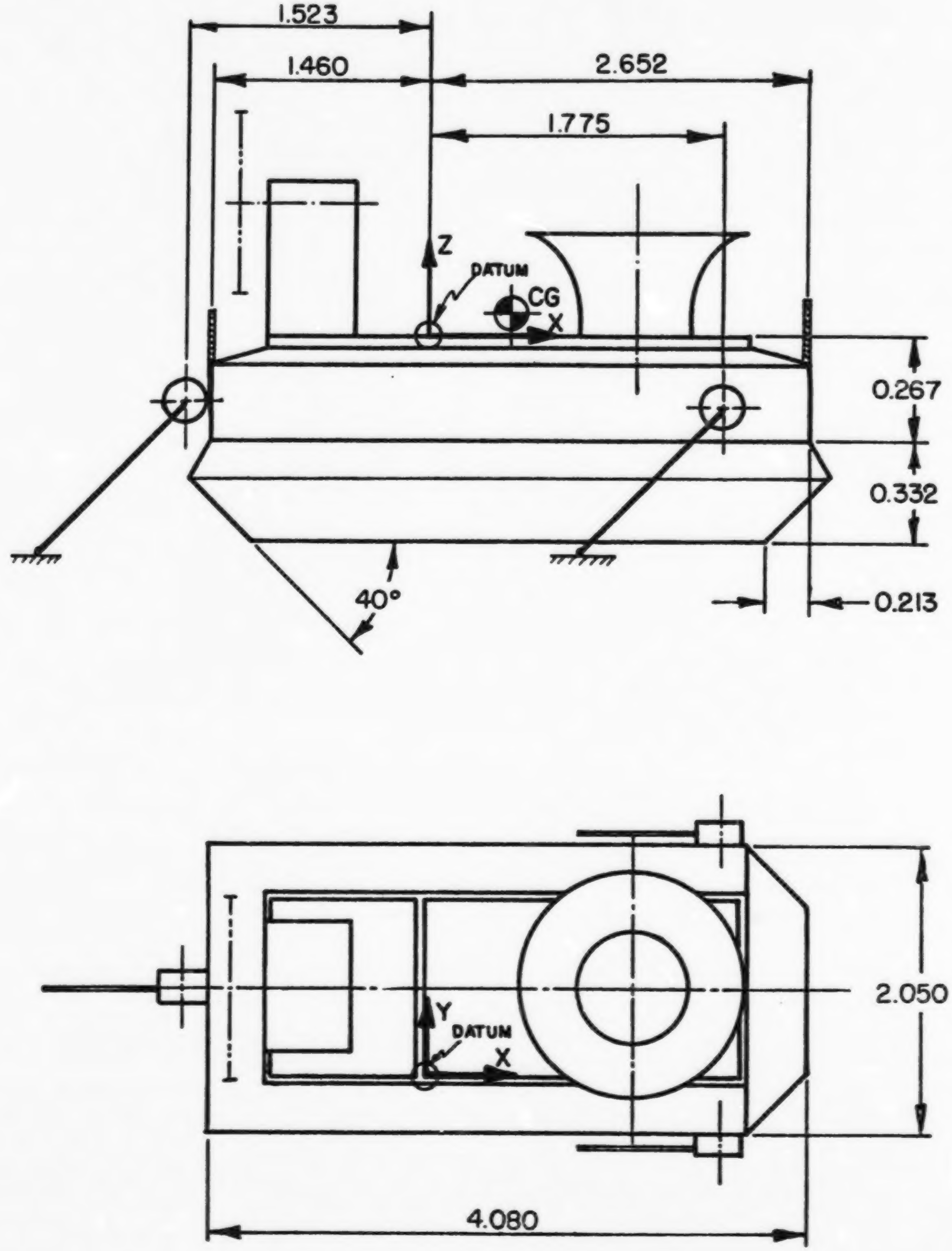
1.523
1.460
2.652
1.775
Z
DATUM
CG
X
0.267
0.332
40°
0.213
Y
DATUM
X
2.050
4.080

FIG. G.1 VAMPIRE I BASIC DIMENSIONS (m).

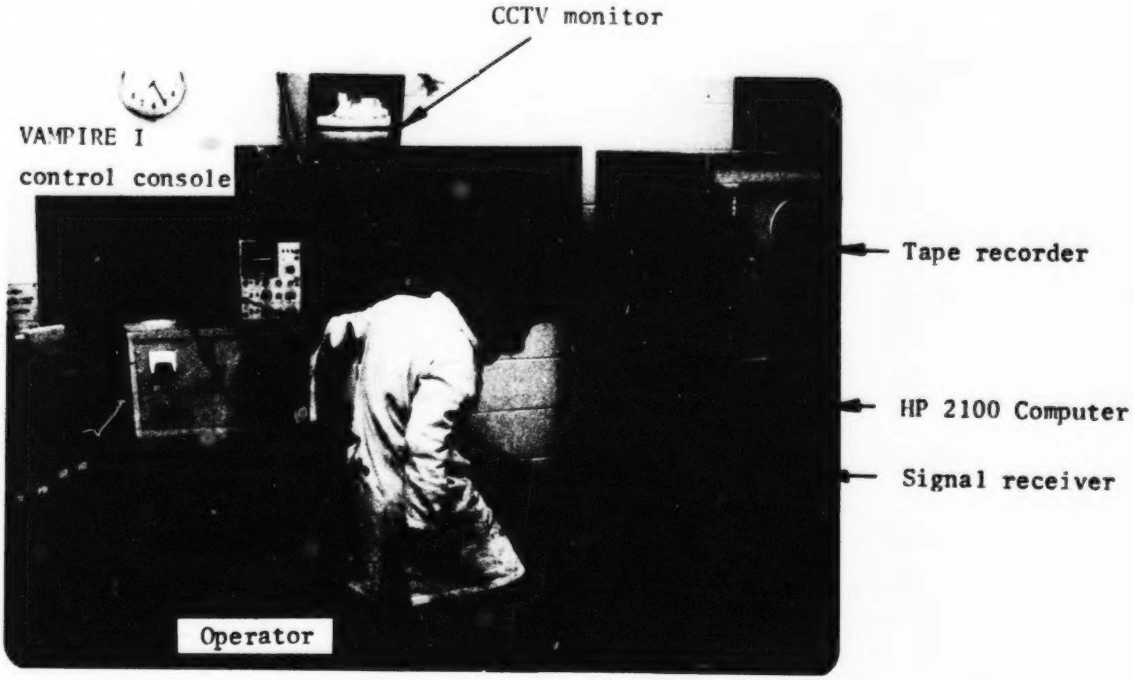
CCTV monitor
VAMPIRE I
control console
Tape recorder
HP 2100 Computer
Signal receiver
Operator

FIG. G.2 UTIAS CIRCULAR TRACK CONTROL ROOM.

Instrumentation

The electronic instrumentation package is being continually developed and is now in what could be termed the second stage. The original system used a heavy cable with a large number of wires to send analog signals from various sensors on board the vehicle to the slip rings in the centre post, from where the signals were taken via an underground cable to an analog-to-digital (A/D) converter and then to a computer for recording on a magnetic tape. Apart from significant attenuation of signals and susceptibility to pick up noise, the weight of the cable significantly affected the dynamic characteristics of the test vehicle. For these reasons the system was modified in the second stage of development by eliminating the heavy signal cable and installing a signal multiplexing and digitizing circuitry directly on board the vehicle. Thus only a single pair of wires is now needed for transmission of all the signals in multiplexed form.

The sensors on board the vehicle available for present experiments include three accelerometers and three rate gyros for measurement of accelerations and rates of rotation about all three axes. They are installed in a box which is located at the CG of the vehicle and which is heated to a constant 60°C to eliminate temperature dependency of the instruments. There are also three trailing arm sensor (TAS) assemblies, one installed on the centre line of the vehicle at the aft end, the other two TAS assemblies being installed at the front end, one on each side of the vehicle. Each TAS assembly consists of an arm fabricated from aluminium tubes, a small nylon wheel at one end of the arm and a precision multitap potentiometer assembly with the shaft of the potentiometer connected to the trailing arm. Two torsion springs of equal stiffness and acting opposite each other impose a constant torque on the trailing arm to keep it in contact with the ground. The output signal from the potentiometer is linearly proportional to the angular position of the trailing arm and if the locations and geometries of all three trailing arms are known, the pitch and roll angles and heave can be calculated.

Problems arise when the ramps are used, since the trailing arms indirectly feed back the height of their respective potentiometer axes above the ramp surface rather than from the ground reference plane. To eliminate this effect, a relatively complicated computer program is required. This must take into account the situations of the moving vehicle that occur when all three trailing arms are on the ground reference, when the front trailing arms begin to climb the ramps, when the front trailing arms fall off the end of the ramp, when the rear trailing arm climbs the ramp and when the rear trailing arm falls off the end of the ramp bringing the trailing arms all back to the ground reference; at this point the vehicle has cleared the ramps. This effect is illustrated in Fig. 4.15 of the main text.

The signals from all the sensors are fed into sample-and-hold amplifiers which are then multiplexed at a rate of 100 samples per second per channel, digitized by a 12-bit A/D converter and transmitted in serial form via a twisted-pair cable, centre-post slip rings and an underground cable to a receiver in the control room. There are altogether 16 channels available for signal transmission with 9 channels being used at the present. The A/D converter digitizes analog voltages in a ± 10 volt range with 11 bit accuracy and 1 sign bit, though only 8 bits of information plus 1 sign bit and 1 parity bit are transmitted since the existing computer software is designed for 8 bit words.

The signal receiver in the control room converts serial stream of data into parallel form, checks parity of each word and sends the data to an HP2100 minicomputer. The data are then processed to allow recording on a magnetic tape in a form compatible with the Univeristy of Toronto IBM 370 computer.